DISCOVERY AND BIOLOGICAL EVALUATION OF FERROPTOCIDE

BY

EVIJOLA LLABANI

DISSERTATION

Submitted in partial fulfillment of the requirements
for the degree of Doctor of Philosophy in Chemistry
in the Graduate College of the
University of Illinois at Urbana-Champaign, 2019

Urbana, Illinois

Doctoral Committee:

Professor Paul J. Hergenrother, Chair
Assistant Professor Jefferson Chan
Professor Wilfred van der Donk
Professor Steven C. Zimmerman

ABSTRACT

The chemical diversification of natural products provides a robust and general method for creation of stereochemically complex and structurally diverse small molecules. The resulting compounds have physicochemical traits different from those in most screening collections, and as such are a rich source for biological discovery. Herein, we subject the complexity-to-diversity library of compounds to an anticancer phenotypic screen. This effort resulted in identification of an active class of compounds derived from pleuromutilin natural product. Biological evaluation identified the novel compound ferroptocide, a small molecule that rapidly and robustly induces ferroptotic death of cancer cells. Target identification efforts and CRISPR knockout studies reveal that ferroptocide has a different target from other known pro-ferroptotic agents; it is an inhibitor of thioredoxin, a key component of the thioredoxin antioxidant system in the cell. Ferroptocide shows the ability to positively modulate the immune system in a murine model of breast cancer and will be a useful tool to study the utility of pro-ferroptotic agents for treatment of cancer.

ACKNOWLEDGEMENTS

This has been an incredible journey, and I do want to take a moment and thank all the people that helped and supported me throughout my time here. I feel very fortunate that I had the opportunity to work on discovery and translational science projects. The ferroptocide discovery project was challenging to say the least, but I loved every moment of it. I learned and grew so much as a scientist and as a person. Resilience is key! The Carle project has been such a humbling and rewarding experience. Working with clinicians and cancer patients reminded me of how important our science is and how thankful we should be for all the joys in our lives. These experiences would not have been possible without the help and support of my advisor, Paul. Thank you, I will forever be grateful. Thank you for all your patience and guidance, for encouraging my ideas, for letting me run with them, and for being there whenever I needed you. Many thanks also go to my committee members for all their helpful insights and advice throughout the years. Thank you for always being willing to help!

I also would like to thank all my coworkers (previous and current) for making this place a fun space to work in and a home away from home. Thank you for all the hugs and laughers, Fridays on campus town, volleyball matches, coffee chats, dinners, and lab trips. I will really miss you. I am very thankful to all my collaborators, especially Rob Hicklin. Thank you for being a great collaborator, an amazing friend, and introducing me to the Vine House. I made some of my best memories there. Special thanks go to all my roommates, and of course to the best bay mate ever, Sarah T.

Lastly, I want to thank all my friends and family. Fei Fei, Haider, Malvi, Ina, Brenda, and Lisa thank you; you all are my family here, and I would have not done this without you. Thank you for keeping me sane and making sure I had a life outside lab. Very special thanks go to my grandparents, parents, and sisters for supporting my life choices even if that meant not seeing me for 10 years. I can never repay you, and I hope you think it was worth it as much as I do. Finally, I would like to thank my partner, Kea, for all the delicious food, all the fun memories, and for always being there every step of the away. You have been my constant all these years, and I am excited for what the future holds.

Thank you to each and every one of you that were a part of my journey.

Table of Contents

Chapter 1: Ferroptosis: Current Landscape 1
  1.1 Modes of cell death 1
  1.2 Ferroptosis RCD and its pathways 2
    1.2.1 Hallmarks of ferroptosis 2
    1.2.2 Pathways implicated in ferroptosis 5
    1.2.3 Execution of ferroptosis 7
  1.3 Small molecule inducers and inhibitors of ferroptosis 8
    1.3.1 Inducers of ferroptosis 8
    1.3.2 Inhibitors of ferroptosis 11
  1.4 Ferroptosis and oxytosis 12
  1.5 Therapeutic targeting of ferroptosis 14
  1.6 Cell death and immunity 16
  1.7 Conclusions and outlook 18
  1.8 References 19
Chapter 2: Discovery of Ferroptocide 27
  2.1 Phenotypic screening 27
  2.2 Library considerations: CtD library 29
  2.3 Anticancer phenotypic screening of the CtD library 33
  2.4 Structure–activity relationship studies 34
    2.4.1 SAR studies of 85-2 hit compound 34
    2.4.2 SAR studies of P4 hit compound 36
    2.4.3 SAR studies of lead compound ferroptocide 37

2.4.4 Synthesis and evaluation of tool compounds 39
2.4.5 Investigation of other α-chloro esters 40
2.4.6 Assessing ferroptocide reactivity with glutathione 42
2.5 Assessing hemolysis of compounds of interests 46
2.6 Compound activity in a panel of cell lines 47
2.7 Mode of action studies 48
2.7.1 Ferroptocide speed of cell death 48
2.7.2 Ferroptocide is non-apoptotic 51
2.7.3 Ferroptocide co-localizes to mitochondria 53
2.7.4 Ferroptocide induces cellular ROS formation 54
2.7.5 Ferroptocide is a pro-ferroptotic agent 57
2.8 Additional studies 67
2.8.1 Cell cycle studies 67
2.9 Target ID and validation studies 73
2.9.1 Covalent binding in cells 73
2.9.2 Chemical proteomics: 1D Gel 75
2.9.3 Mitochondrial fractionation 76
2.9.4 2D-gel target ID studies 79
2.9.5 Target validation from 2D-gel analysis 84
2.9.6 Target ID: Biotin-streptavidin pulldown 92
2.9.7 siRNA and CRISPR KO studies of putative targets 94
2.9.8 Thioredoxin as a putative target of ferroptocide 96
2.10 Evaluation *in vivo* 104

2.10.1 MTD and PK studies ... 104
2.10.2 Efficacy model in 4T1 ... 105
2.10.3 Activity in immunocompetent and immunocompromised mice ... 106
2.11 Conclusions ... 108
2.12 Supplementary figures ... 110
2.13 Materials and methods ... 113
2.14 References ... 132
Chapter 3: Personalized Therapy for Late-Stage Patients ... 143
3.1 Personalized medicine approaches ... 143
3.1.1 Genomic precision medicine ... 143
3.1.2 Functional precision medicine ... 145
3.2 Metastatic breast cancer no standard of care ... 148
3.3 Non-interventional prospective study at Carle hospital ... 149
3.4 Results and analysis ... 151
3.5 Future technology PCEM ... 155
3.6 Conclusion and outlook ... 156
3.7 Methods and materials ... 158
3.8 References ... 160

Chapter 1: Ferroptosis: Current Landscape

1.1 Modes of cell death

Cell death is, counterintuitively, an essential step in the continued life of an organism. Because of this critical role, it is a detailed genetic process carried through specific cellular mechanisms targeting harmful and irreversibly damaged cells. Cells die either via accidental cell death (ACD) due to severe external stimuli such as physical, chemical, and mechanical insults, or regulated cell death (RCD), which relies on defined intrinsic signaling mechanisms and can be modulated in a pharmacological or genetic manner.[4]

Regulated cell death was synonymous for decades with an apoptotic death phenotype; however, other regulated forms of cell death with characteristic molecular mechanisms and morphological features have recently emerged. Due to distinctive morphological changes, RCD can be categorized into three types (**Fig. 1.1**): Type I is referred to as apoptosis (characterized by membrane blebbing, chromatin condensation, nuclear fragmentation, caspase activation, cytochrome c release, cleavage of PARP, etc.), Type II is referred to as autophagy (extensive cytoplasmic vacuolization, phagocytosis, and lysosomal degradation), and Type III is referred to as necrosis (membrane rupturing and release of cellular contents in the extracellular matrix, **Fig 1.1)**.[4,7] Such modes of cell death reside between the two cell death extremes (apoptosis and

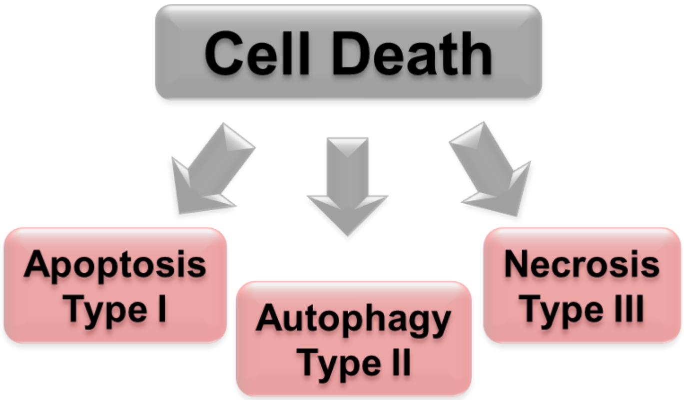

Figure 1.1. Spectrum of cell death. Cell death is categorized in three types: type I or apoptosis, type II or autophagy, and type III or necrosis.

necrosis) depending on their caspase dependency as shown in **Figure 1.2**. The focus of this chapter will be on ferroptosis, its relevant pathways, activators and inhibitors, as well as its evolutionary role in disease.

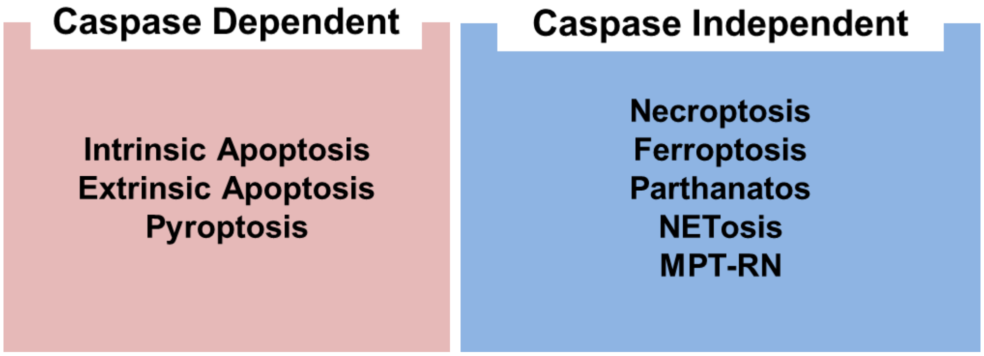

Figure 1.2. Various types of cell death based on caspase dependency. Apoptosis and pyroptosis are the only caspase dependent forms of cell death.

1.2 Ferroptosis RCD and its pathways

1.2.1 Hallmarks of ferroptosis

Coined in 2012, ferroptosis is a newly discovered mode of regulated cell death that relies on accumulation of iron-dependent lipid peroxidation to lethal levels resulting in cell demise.[3,6,8,9] This ferroptotic death phenotype involves unique morphological, biochemical, and genetic core features that are distinctive from any other form of cell death. Indeed, the cell death committee has recently highlighted these key characteristics such as: accumulation of general reactive oxygen species (ROS), iron-dependent lipid ROS, and protection against ferroptotic cell death via iron-chelators (deferoxamine), lipophilic antioxidants (trolox, α-tocopherol), ferroptosis-specific inhibitors (ferrostain-1, liproxstatin), and inhibitors of lipid peroxidation.[7] These guidelines are highly recommended in mechanistic studies aimed at elucidating the mode of cell death of small molecules suspected of displaying a ferroptotic profile.

Comparison of the cell death hallmarks between ferroptosis and other RCDs (apoptosis, necroptosis, autophagy, and parthanatos) result in no overlap between these pathways, emphasizing the uniqueness of ferroptosis as a regulated form of cell death (**Table 1.1**). It is important to note that some of these hallmarks (phosphatidylserine exposure, executioner caspase -3, -7, -9 activation, membrane depolarization, DNA damage, etc.) offer invaluable information in tracking cell death *in vivo*, and current efforts are focusing on developing detection agents for use of these biomarkers in the clinic.[10] Unfortunately, to date, there are no suitable biomarkers of ferroptosis *in vivo*. These markers are mainly limited to assessing the abundance of NADP(H)[11], mRNA levels of prostaglandin E synthase 2 (PTGES2)[12] and ChaC glutathionespecific gamma-glutamylcyclotransferase 1 (CHAC1) in cells, which can predict sensitivity to ferroptosis. Further in-depth studies and biocompatible probes are needed to identify predictable hallmarks of ferroptosis, which could be necessary to bridge the gap between basic biology and medicinal applications.

Table 1.1. A comparison of features of apoptotic and non-apoptotic forms of cell death. Abbreviations: TNF, tumor necrosis factor; MMP, mitochondrial transmembrane potential; MOMP, mitochondrial outer membrane potential; TRADD, tumor necrosis factor receptor type 1-associated DEATH domain protein; FADD, Fas-associated protein with death domain; Atg, autophagy-related genes; PARP-1, poly (ADP-ribose) polymerase 1; GCL, glutamate-cysteine ligase. This table is adopted with permission from Springer Nature (2016).[3]

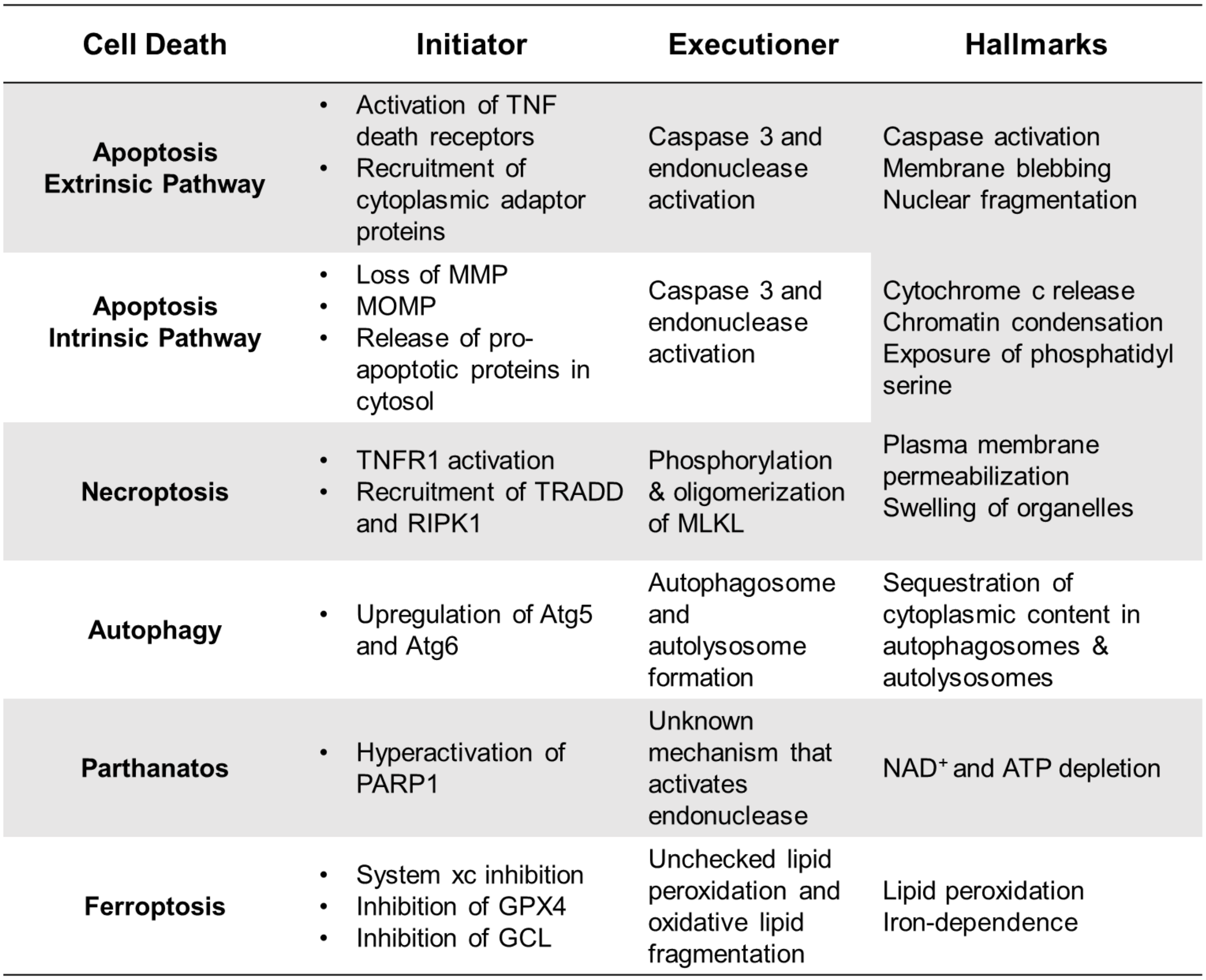

Cell Death	Initiator	Executioner	Hallmarks
Apoptosis Extrinsic Pathway	• Activation of TNF death receptors • Recruitment of cytoplasmic adaptor proteins	Caspase 3 and endonuclease activation	Caspase activation Membrane blebbing Nuclear fragmentation
Apoptosis Intrinsic Pathway	• Loss of MMP • MOMP • Release of pro-apoptotic proteins in cytosol	Caspase 3 and endonuclease activation	Cytochrome c release Chromatin condensation Exposure of phosphatidyl serine
Necroptosis	• TNFR1 activation • Recruitment of TRADD and RIPK1	Phosphorylation & oligomerization of MLKL	Plasma membrane permeabilization Swelling of organelles
Autophagy	• Upregulation of Atg5 and Atg6	Autophagosome and autolysosome formation	Sequestration of cytoplasmic content in autophagosomes & autolysosomes
Parthanatos	• Hyperactivation of PARP1	Unknown mechanism that activates endonuclease	NAD^+ and ATP depletion
Ferroptosis	• System xc inhibition • Inhibition of GPX4 • Inhibition of GCL	Unchecked lipid peroxidation and oxidative lipid fragmentation	Lipid peroxidation Iron-dependence

1.2.2 Pathways implicated in ferroptosis

The current understanding in the field outlines two main pathways as key inducers of ferroptosis: 1) inhibition of system X_C^-, 2) direct or indirect inactivation of a glutathione-dependent enzyme, GPX4, as shown in **Figure 1.3**. Critical processes of these routes include glutathione biosynthesis, amino acid-, lipid-, and iron-metabolism. In the advent of system X_C^- failure, cells use the transsulfuration pathway to biosynthesize cysteine from methionine, bypassing the system X_C^- and displaying resistance to ferroptosis-inducing compounds.[6,13] A genome-wide siRNA screen identified cysteinyl-t-RNA synthase (CARS) as a genetic suppressor, whose loss results in upregulation of the transsulfuration pathway, inhibition of lipid ROS generation, leading to resistance to ferroptosis, and thus linking transsulfuration to this mode of cell death.[14,15]

Lipid metabolism is another essential process in the execution of ferroptosis. The presence of

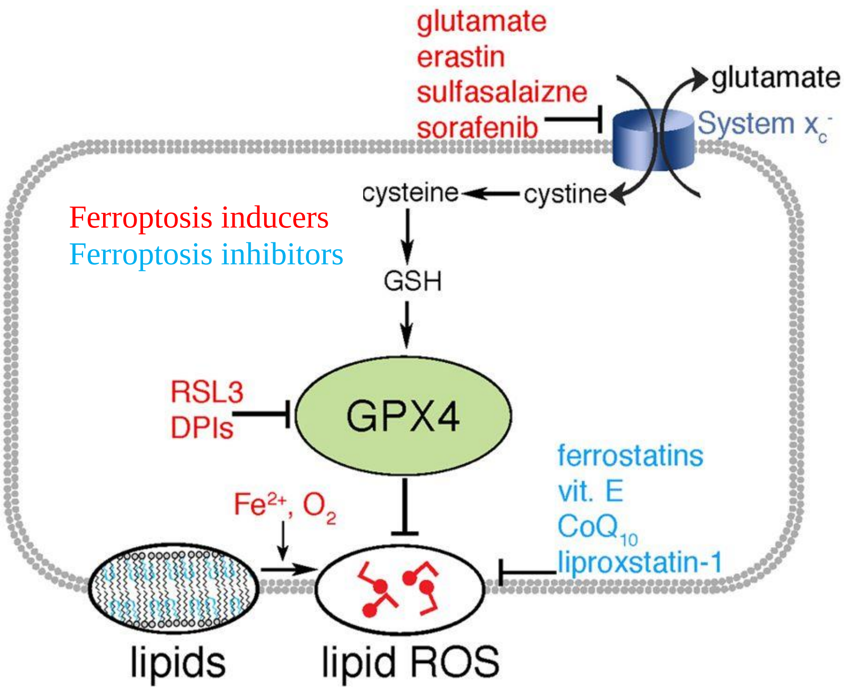

Figure 1.3. Inhibition of system X_C^-, and GPX4 results in generation of iron-dependent lipid peroxides. Images are adapted with permission from Agmon and coworkers.[1]

labile bis-allylic hydrogens in polyunsaturated fatty acids (PUFAs) renders them susceptible to enzymatic and non-enzymatic oxidation that results in lipid peroxidation and generation of ferroptotic death signals.[6,16] Free PUFAs must be esterified to membrane phospholipids and undergo oxidation to signal ferroptosis.[17] Importantly, abundance and localization of highly oxidizable PUFAs is correlated with sensitivity to ferroptosis-inducing compounds. The most commonly depleted PUFAs in ferroptotic cells are arachidonic acid (AA) and adrenic acid phospholipids supported by lipidomic studies.[18-20]

Furthermore, enzymes involved in PUFA-biosynthesis and remodeling such as acyl-coA synthetase long chain family member 4 (ACSL4) and lysophosphatidylcholine acyltransferase 3 (LPCAT3) can modulate a response to ferroptosis. Genetic knockdown of these enzymes confers resistance to ferroptosis while treatment with excess AA increases ferroptotic sensitivity.[17,21,22] Other enzymes that mediate induction of ferroptosis include lipoxygenase (LOX) and cyclooxygenase (COX), which directly catalyze the formation of lipid peroxides. Genetic knockdown[23] and small molecule inhibition of LOXs[24] such as LOX-12 and LOX-15 result in

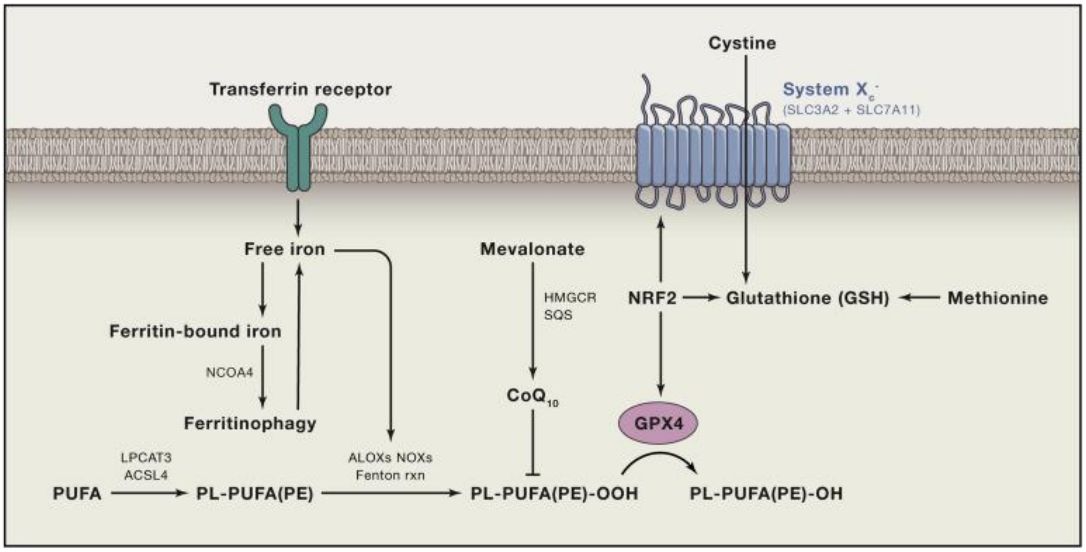

Figure 1.4. Relevant pathways involved in ferroptosis. Images are adapted with permission from Stockwell and coworkers.[6]

increased resistance to compound-induced ferroptosis. Taken together, these studies emphasize the importance of lipids and their relevant enzymes in modulation of this form of cell death.

In addition, glutamine can trigger ferroptosis due to glutaminolysis. This process enables glutamine degradation, which is a carbon-source for the tricarboxylic acid (TCA) cycle and lipid biosynthesis, rendering it invaluable in ferroptosis.[3,6] To support this hypothesis, Gao and coworkers demonstrated that α-ketoglutarate, a product of the TCA cycle can overcome the need for glutamine in ferroptosis.[25] The only other enzyme of glutaminolysis that is required in ferroptosis is mitochondrial glutaminase GLS2, which catalyzes the first step of glutaminolysis,[6,25] thus connecting this process to ferroptotic cell death.

Another important driver of ferroptosis is the mevalonate pathway (**Fig 1.4**). This pathway plays a vital role in selenocysteine synthesis—required for GPX4 maturation, and production of coenzyme Q10 (CoQ10), which is an endogenous inhibitor of ferroptosis as observed from its antioxidant function in membranes.[26,27] A typical selenoprotein, GPX4, contains a selenocysteine in its catalytic site and uses it to detoxify lipid peroxides. The mevalonate pathway is the primary source of generation of isopentenyl pyrophosphate (IPP), which regulates a Sec transfer RNA overseeing the maturation of GPX4.[26,28,29] In addition, a ferroptosis-inducing compound (FIN56) was shown to decrease the levels of coenzyme Q10, a mevalonate-derived lipophilic antioxidant, further establishing the interplay between the mevalonate pathway and ferroptosis.[27]

1.2.3 Execution of ferroptosis

Ferroptotic cell death is likely executed via fragmentation of lipid peroxides into electrophilic reactive species such as aldehydes and conjugate acceptors that can covalently react with plasma membrane proteins, other essential proteins, and nucleic acids. Sequencing of erastin-resistant cells revealed upregulation of aldo-keto reductase family 1-member C (AKR1C) family genes, which convert reactive end-products of lipid peroxidation to unreactive species, thus supporting this hypothesis.[30,31] Furthermore, NRF2 has been shown to specifically modulate the gene transcription of this family gene among other functions, and promote resistance to ferroptosis.[32-34]

Another key player in execution of ferroptosis is iron. Iron storage, transport, and metabolism in cells together with the pathways that tightly regulate them govern the sensitivity to ferroptosis.[35] In addition, the pool of free labile iron in cells can generate ROS via the Fenton reaction.[35,36] This pool is modulated by ferritin, an iron storage protein, whose degradation via ferritinophagy increases iron availability and renders cells sensitive to ferroptosis (**Fig. 1.5**).[37,38] Iron chelation by the addition of exogeneous small molecules or genetic alterations of iron-dependent enzymes blocks ferroptosis and rescues cells from death, thus emphasizing the importance of this element in the ferroptotic cell death modality.

1.3 Small molecule inducers and inhibitors of ferroptosis

1.3.1 Inducers of ferroptosis

All reported ferroptosis inducers share one common feature, their ability to breach the glutathione-dependent lipid peroxidation defense network in cells. Nonetheless, as eluded to previously, they can be categorized into two main classes: Class I includes compounds that cause inhibition of system X_C^-, which results in depletion of glutathione, and Class II activators that cause inactivation of GPX4 either via direct alkylation [RSL3, ML162] or indirectly due to degradation of GPX4 (FIN56) or inhibition of its enzymatic activity [$FINO_2$] shown in **Figure 1.5**. Dixon and coworkers were the first to assess induction of ferroptosis with small molecule compounds.[8] The genesis of this work stemmed from identification of small molecules that were selectively lethal for RAS mutant tumor cells. This promising work captured the interest in the field given that 30% of cancers possess mutations of the RAS family of small GTPases.[8,39]

A high throughput screen for compounds that displayed synthetic lethality with oncogenic RAS ($HRAS^{G12V}$) discovered erastin (**Fig. 1.5 A**) in engineered cell lines of fibroblasts (BJ-TERT/LT/ST/RAS^{V12}).[40,41] These cells (BJ) were engineered to express in a systematic fashion the catalytic subunit of human telomerase (hTERT), the SV40 large T and small T antigens (LT and ST), and the oncogenic allele of HRAS ($HRAS^{G12V}$), thus enabling generation of isogenic cell line pairs. Mechanistic studies elucidated mitochondrial voltage dependent anion channels (VDAC) as direct targets of erastin while its ferroptotic profile was attributed to inhibition of system X_C^-, that leading to depletion of glutathione.[8,41] Given this activity, erastin is considered a class I ferroptotic inducer.

RSL3[42] and ML162[43] (**Fig. 1.5 B**) are class II inhibitors that were identified in two separate synthetic lethal screens in the same BJ cell system, but displaying potency and selectivity in HRAS and KRAS mutant cancer cells. Counter-screening with bioactive compounds that suppressed cell death induced by erastin and RSL3 elucidated details of the mechanism of action of these compounds and revealed the importance of cellular iron in promoting selective lethality with oncogenic RAS. Notably, GPX4 was identified as the direct target of the RSL3 covalent inhibitor in a subsequent study, which established the role of GPX4 as a central regulator of ferroptosis.[12]

Further efforts utilizing modulatory profiling to map cell death and identify small molecules with regulated non-apoptotic death phenotype in HT-1080 and engineered BJ cells, discovered FIN56 as a new type of class II ferroptosis activators (**Fig. 1.5 B**).[27] In contrast to erastin and RSL3, FIN56 causes degradation of GPX4 enzyme via modulation of squalene synthase of the mevalonate pathway. This study was pivotal in elucidating the role of lipid metabolism in ferroptosis and the consequences of its dysregulation in cells.

Additionally, a successful collaboration between the Woerpel laboratory and the National Cancer Institute (NCI) identified another class II inducer, $FINO_2$, via NCI's *in vitro* cell screening project (**Fig. 1.5 B**).[44] This small molecule displayed a non-apoptotic phenotype that was determined to be ferroptotic in nature *without* modulating the known protein targets of ferroptosis. A follow up study unraveled the complex role of this small molecule in ferroptosis, encompassing the indirect inhibition of GPX4 enzymatic activity and direct oxidation of iron, thus resulting in generation of massive lipid peroxidation.[45]

Despite our understanding of ferroptosis as a mode of regulated cell death being in its infancy, to date there have been at least seven ferroptosis-inducing small molecules introduced to the chemical biologist's tool box. These probes have been instrumental in discovering many of the key ferroptotic pathways and central regulators mentioned above, which can be grouped in one overarching theme—glutathione-dependent lipid peroxidation. Yet, many uncharted territories including its relevance to other cellular antioxidant systems exist in ferroptosis, and

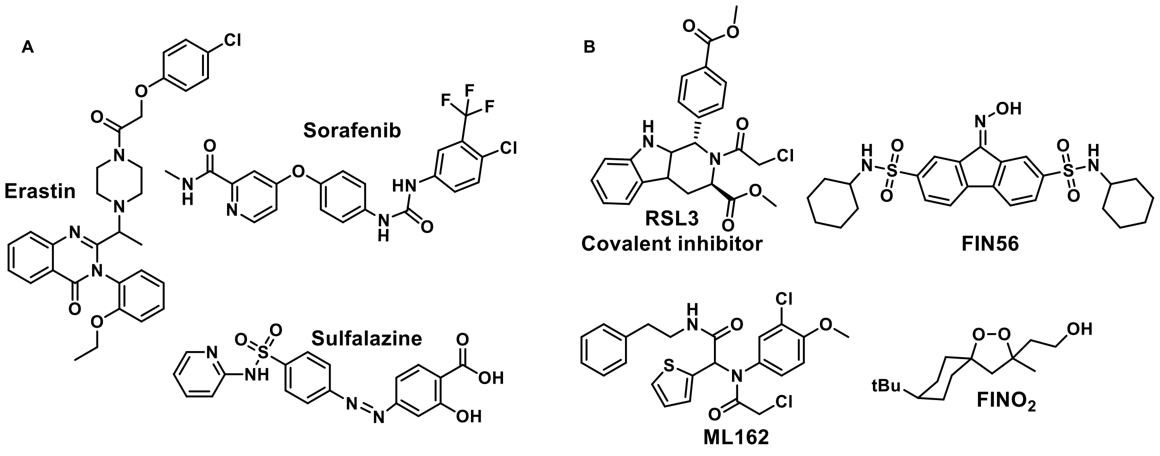

Figure 1.5. Current ferroptosis-inducing compounds can be categorized in: (A) class I inhibitors that cause depletion of glutathione (B) class II inhibitors that inactivate directly or indirectly the glutathione-dependent enzyme, GPX4.

discovery of novel ferroptosis-inducing tool compounds is needed as they can help uncover new biology and molecular pathways relevant to this cell death modality.

1.3.2 Inhibitors of ferroptosis

Multiple reports have also investigated the pharmacological *inhibition* of ferroptosis via small molecule compounds. These molecules serve as protectants against ferroptosis and are crucial tools for investigating ferroptosis-inducing compounds (**Fig. 1.6**). These inhibitors act as iron chelators (deferoxamine) or antioxidants (ferrostatin-1, liproxstatin-1, Trolox, vitamin E) and are readily available for cell studies. Deferoxamine is a membrane-impermeable compound that localizes in lysosomes via endocytosis and chelates lysosomal iron. The current hypothesis is that lysosomal iron is directed to other compartment of the cells and disruption of its delivery results in reduction of the overall iron levels and thus prevention of ferroptosis.[3]

Despite the ability of various compounds to act as radical scavengers, in fact not all can rescue cells from ferroptotic cell death. A combination of lipophilic antioxidants (vitamin E and Trolox) and ferroptosis-specific inhibitors is needed to protect cells from the lethal ferroptotic phenotype. Assessment of cell death using this combination is required to provide sufficient evidence in determining if a novel compound triggers ferroptosis.

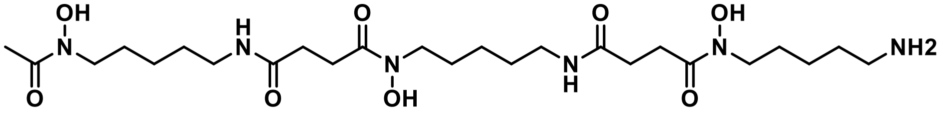

Deferoxamine

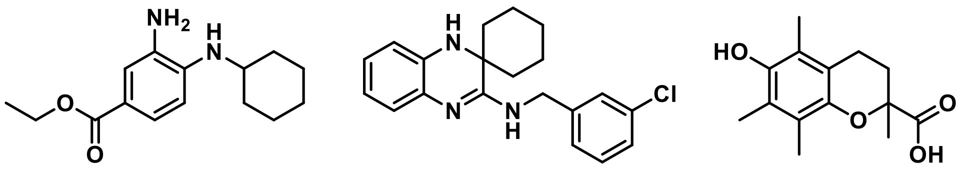

Ferrostatin-1 **Liproxstatin-1** **Trolox**

Figure 1.6. A limited series of compounds are known to inhibit ferroptosis. Deferoxamine is an iron chelator while the other compounds possess antioxidant activity.

In conclusion, after surveying the ferroptosis landscape of its inducers and inhibitors, the major limitation in the field lies in the scarcity of chemical tools currently at our disposal. All the ferroptotic discoveries described above were conducted in a limited set of cell lines (i.e. HT-1080, BJ-RAS mutated engineered cell systems). Selection of such cells proved problematic; for example, when attempting to link RAS mutation to compound activity in a panel of diverse cancer cell lines.[12] Erastin and RSL3 showed minimal to no activity. These data challenged the relevance of RAS-mutational status and the selective synthetic lethal ability of these compounds in cancer treatment. Despite this glaring lack of mechanistic understanding, erastin and RSL3 remain the two gold-standard small molecules for studying ferroptosis.

Furthermore, the bioactivity of these reported probes is linked to specific cell lines and is limited to HT-1080 or BJeLR xenograft studies *in vivo*[12]. For example, erastin is not active in breast cancer (4T1), lung cancer (A549) or colon cancer (HCT 116) cell lines as we will explore in chapter 2 of this thesis. Due to its low water-solubility, erastin is not used in animal models; piperazine analogue is used instead but a comprehensive ferroptotic data profile is missing for this analogue.[12] While RSL3 displays activity, it suffers from lack of quantitative cell death, slow reactivity in cells and limited cell line activity in mice[12]. As a practical consideration, fast-acting, reliable, and bioavailable compounds are critical when performing biological experiments and animal work. However, the reported ferroptotic inducers are unable to do so, demonstrating the need for development of new chemical probes with broad bioactivity to further investigate ferroptosis and its underlying mechanisms not only in cells but also *in vivo*.

1.4 Ferroptosis and oxytosis

A closely related mode of cell death to ferroptosis is oxytosis, which was reported in 2001. Treatment of neuroblastoma cells with glutamate and glutamate analogues, resulted in ROS generation and glutathione depletion followed by a lethal calcium influx.[9] The first two events are core ferroptotic features and highlight the parallel between these two cell death modalities and their dependency on system X_C^-. This system transports extracellular cysteine inside cells for production of glutathione in a 1:1 exchange rate with intracellular glutamate (**Fig. 1.7**).[5]

Indeed, high extracellular levels of glutamate behave similarly to treatment with the ferroptosis-inducing compound erastin; they both cause inhibition of system X_C^-, leading to depletion of glutathione and inactivation of GPX4. This process results in accumulation of lipid hydroperoxides, massive accumulation of reactive oxygen species (ROS), mitochondrial ROS, and other dysfunctions in cells.[46] Despite the similarities in the initiation phase (system X_C^- inhibition), the termination phase of these two forms of cell death is drastically different. Oxidative glutamate toxicity (oxytosis) requires additional downstream events that involve apoptotic features and are dependent on calcium intake instead of iron, especially in neuronal cells; meanwhile, calcium is not needed in ferroptosis though its role is not well understood.[9,36,47] A high degree of overlap of these cell death mechanisms is observed in other cell types.[3] However, more functional studies are needed to further substantiate the distinction between these two cell death mechanisms.

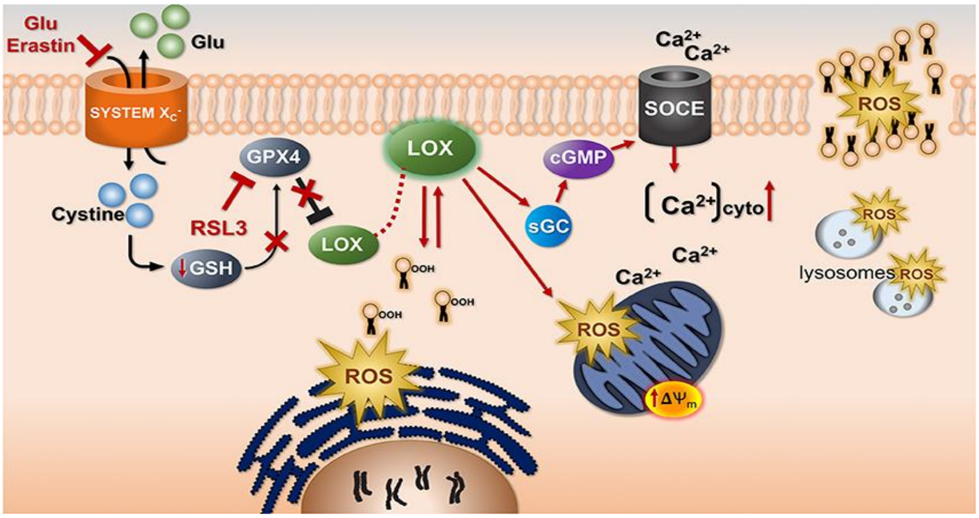

Figure 1.7. Common pathways in oxytosis and ferroptosis. Image is adapted with permission from Lewerenz and coworkers.[5]

1.5 Therapeutic targeting of ferroptosis

The continual accumulation of compelling evidence highlights ferroptosis as a potential novel and efficient inducer of cell death for anticancer treatment that can be achieved via two strategies: 1) identification of small molecule inhibitors with broad anticancer activity 2) inhibition of key molecular targets in multiple pathways that activate ferroptosis. Most of the ferroptotic-inducers were discovered in synthetic lethal screens with selectivity towards RAS mutated engineered cells. Nonetheless, subjecting 117 cell lines isolated from diverse tissues (leukemia, lung, colon, CNS, melanoma, ovarian, kidney, and breast) and the NCI-60 panel to erastin and RSL3 revealed no selective preference of such compounds for RAS mutated versus RAS wild type cancer cells.[12] This study unveiled that diffuse, large B cell lymphomas and renal cell carcinomas appear to be particularly sensitive to ferroptosis. Notably, sorafenib, an FDA-approved multikinase inhibitor for renal carcinomas, was found to display a ferroptotic profile due to inhibition of system X_C^-.[30] Tumors resistant to sorafenib contain high levels of the negative regulators of ferroptosis (Nrf2 and MT-1G) and can be re-sensitized to the this kinase inhibitor upon pharmacological or genetic inhibition of these regulators *in vitro* and in xenograft mouse models.[32,48]

Furthermore, targeting of tumors dependent on system X_C^- (ideally in systems with inactive transsulfuration pathways) could be a viable anticancer approach to promote cancer cell death. Triple negative breast cancers (TNBC) are an excellent model, as they survive on the interaction of this cysteine/glutamate transporter with MUC1-C transmembrane oncoprotein and directly respond to sulfasalazine or erastin treatment displaying a ferroptotic phenotype.[49] Combination of class I inhibitors, especially the FDA-approved examples (sorafenib and sulfalazine) with chemotherapeutics currently used for treatment of TNBC is an underexplored area of research. A phase II clinical study evaluated sorfenib with taxane/anthracycline chemotherapeutics in HER2 negative patients and reported no drug–drug interactions for the sorafenib/epirubicin combination.[50] In another trial, HER2 negative trial sorafenib/capecitabine combination resulted in significant progression free survival but had to be discontinued due to compound toxicity.[51] These trials were not selective for TNBC patients per se, but do offer insights into the potential of developing new combinations specifically for TNBC patients, based on our sorafenib-ferroptosis knowledge.

In addition, expression of the system X_C^- is correlated with the malignancy grade of brain tumors.[52,53] Savaskan and coworkers demonstrated that pharmacological and genetic inhibition of this system causes ferroptosis and disrupts the neurodegenerative and toxic environment of gliomas.[54,55] Combination of temolozomide (TMZ) with erastin (not sorafenib) potentiates the sensitivity of gliomas to TMZ, prompting a new multitoxic approach in treatment of brain tumors. Given the drastically low patient response rate to TMZ treatment,[56] and lack of other treatment options for brain cancers,[57] combination of TMZ with reliable ferroptotic compounds could be useful, of course pending sufficient blood-brain barrier (BBB) penetrance for these compounds. Currently, there is no data on the ability of ferroptotic compounds to cross the BBB, so future efforts will need to explore this area in the context of assessing combination therapy in brain cancers. As described earlier, glutaminolysis is another crucial system in ferroptosis that can be exploited as an anticancer strategy. The combination of ferroptosis dependence on this vital metabolic process for cancer cell proliferation and targeting of glutaminolysis molecular components for inhibition could serve as another potential therapeutic avenue.[54]

A limited number of studies have investigated the potential link of ferroptosis to pathological cell death, particularly in neurodegenerative disease models. Oxidative damage, lipid oxidation, iron accumulation, dysregulation of GSH and decrease GPX activity are the common features found in brains of patients with Parkinson's (PD)[58-60], Alzheimer's (AD)[61], Hungtington's (HD)[62-64], periventricular leukomalacia (cerebral white matter injury)[65,66], and ischemic stroke[67-69], thus connecting ferroptosis to brain disease. Iron chelation, administration of vitamin E or ferrostatin-1/liproxstatin-1 was shown to reduce the neurodegeneration levels in the mouse models of PD[70,71], AD[72], and HD[18,64]. Other reports have demonstrated that ferroptosis is involved in tissue/organ injury due to ischemia/reperfusion, and inhibition of ferroptosis is effective in treatment of organ damage.[73,74]

These reports provide evidence for use and exploration of ferroptosis-inducing compounds in multiple disease areas outside the realm of oncology. This is highly attractive as it creates new frontiers for investigation of ferroptosis as an important biological process in a broad range of disease areas, meaning it is not just another form of non-apoptotic cell death. Induction of ferroptosis can be a powerful anticancer strategy and it appears to be a key process in neurological disorders. Therefore, compounds that reliably trigger ferroptosis in various systems (cell lines and/or animal models) are of paramount importance, particularly considering our current array of imperfect ferroptotic tool compounds.

1.6 Cell death and immunity

Historically, apoptosis has been the most studied form of regulated cell death and is thought to be tolerogenic since it is the main method of clearance of abnormal cells via phagocytosis (also known as efferocytosis), thus preventing inflammation.[75-77] However, recent studies have provided evidence of other regulated non-apoptotic forms of cell death with well-defined initiation and execution mechanisms. Such modes of cell death *can* release damage-associated molecular patterns (DAMPs), triggering activation of the neighboring macrophages and dendritic cells via Toll-Like-Receptor signaling and other signaling pathways.[78] This activation involves expression of tumor infiltrating lymphocytes and/or initiation of an adaptive immune response, both of which are highly attractive strategies in the clinic.[77]

Given the scientific community's appreciation of the role of the immune system in cancer and the potential of immunology in the clinic, there is an increased interest in methods that will activate the immune system to elicit an immune response. The most developed approach thus far, is immunotherapy, which relies on biologics such as antibodies, bispecific T-cell engagers, antibody drug conjugates (ADCs), and vaccines, to activate the immune system to kill cancer cells. A different strategy is to obliterate these malignant cells via small molecules that induce non-apoptotic cell death and can thus release DAMPS to signal an immune response.

Conventional chemotherapeutics (doxorubicin, taxanes, Pt-based compounds, methotrexate, and gemcitabine, to name a few) have been shown to display immunological effects in a dose-dependent manner, as discovered through metronomic chemotherapy—chronic administration of chemotherapy at low, minimally toxic doses, with no prolonged drug-free periods—yet their primary mechanism of action is some form of apoptosis.[79,80] Additionally, numerous efforts have focused on developing small molecules with immunostimulatory effects, but most of these are in the early stages of development (**Table 1.2**).[2] Therefore, identification of non-apoptotic compounds that can directly elicit an immune response or enhance the effect of immunotherapy are highly desirable in the clinic. In the later chapters, we will demonstrate how a small molecule discovered in our laboratory can potentially play a part in developing this frontier.

Table 1.2. Categories of small molecule compounds with immunomodulatory functions in solid tumors. Abbreviations: DC: dendritic cell, DNMT: DNA methyltransferase, HDAC: histone deacetylase complex. IDO: indoleamine-2, 3-dioxygenase, RORɣt: Retinoic acid receptor-related orphan nuclear receptor gamma, TNFα: tumor necrosis factor α. This table is adapted with permission from Murphy and coworkers.[2]

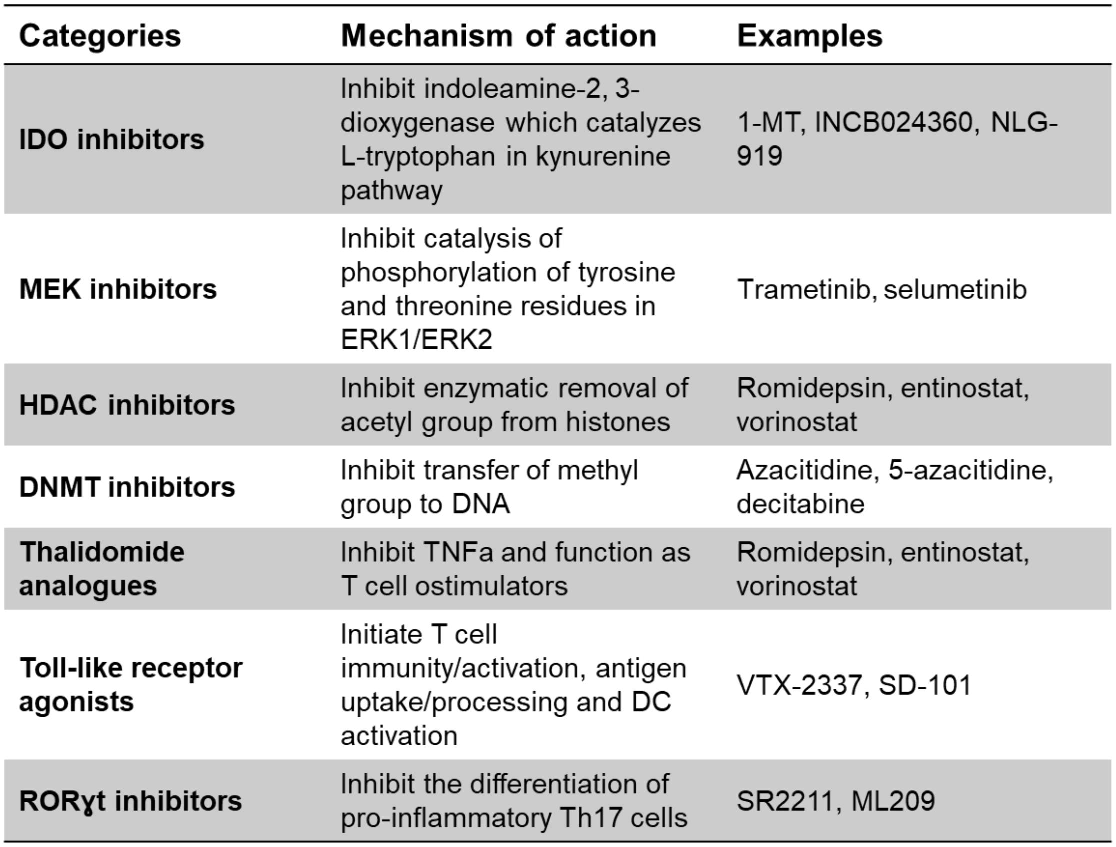

Categories	Mechanism of action	Examples
IDO inhibitors	Inhibit indoleamine-2, 3-dioxygenase which catalyzes L-tryptophan in kynurenine pathway	1-MT, INCB024360, NLG-919
MEK inhibitors	Inhibit catalysis of phosphorylation of tyrosine and threonine residues in ERK1/ERK2	Trametinib, selumetinib
HDAC inhibitors	Inhibit enzymatic removal of acetyl group from histones	Romidepsin, entinostat, vorinostat
DNMT inhibitors	Inhibit transfer of methyl group to DNA	Azacitidine, 5-azacitidine, decitabine
Thalidomide analogues	Inhibit TNFa and function as T cell ostimulators	Romidepsin, entinostat, vorinostat
Toll-like receptor agonists	Initiate T cell immunity/activation, antigen uptake/processing and DC activation	VTX-2337, SD-101
RORɣt inhibitors	Inhibit the differentiation of pro-inflammatory Th17 cells	SR2211, ML209

1.7 Conclusions and outlook

In this chapter, I have surveyed non-apoptotic forms of cell death with a focus on ferroptosis, a new mode of regulated cell death. An overview of all the pathways currently involved in ferroptosis as well as its hallmarks were presented to help the reader better understand where ferroptosis stands in the landscape of other RCDs. Despite its partial overlap with oxytosis, ferroptosis is morphologically, biochemically, and genetically different from other known cell death modalities, and thus is an important biological process for future study and applications.

Multiple groups have directed their attention towards ferroptosis, generating several ferroptosis-activators and inhibitors. However, activity of these compounds is limited to specific cell lines and currently target one of two ferroptotic pathways: depletion of glutathione or inactivation of GPX4. Discovery of tool compounds that would further elucidate the molecular mechanism of ferroptosis, identify biomarkers of ferroptosis in vivo, and have broad activity is of paramount importance. Furthermore, ferroptosis-inducing compounds have the potential to activate the immune system via the release of DAMP signals to combat cancer; however, more in-depth studies are needed to prove or disprove this hypothesis.

1.8 References

1 Agmon, E., Solon, J., Bassereau, P. & Stockwell, B. R. Modeling the effects of lipid peroxidation during ferroptosis on membrane properties. *Sci. Rep.* **8**, 5155–5165, (2018).

2 Murphy, A. G. & Zheng, L. Small molecule drugs with immunomodulatory effects in cancer. *Hum. Vaccin. Immunother.* **11**, 2463–2468, (2015).

3 Cao, J. Y. & Dixon, S. J. Mechanisms of ferroptosis. *Cell. Mol. Life Sci.* **73**, 2195–2209, (2016).

4 Fuchs, Y. & Steller, H. Live to die another way: modes of programmed cell death and the signals emanating from dying cells. *Nat. Rev. Mol. Cell Biol.* **16**, 329–344, (2015).

5 Lewerenz, J. *et al.* The cystine/glutamate antiporter system x(c)(-) in health and disease: from molecular mechanisms to novel therapeutic opportunities. *Antioxid. Redox Signal.* **18**, 522–555, (2013).

6 Stockwell, B. R. *et al.* Ferroptosis: A regulated cell death nexus linking metabolism, redox biology, and disease. *Cell* **171**, 273–285, (2017).

7 Galluzzi, L. *et al.* Molecular mechanisms of cell death: Recommendations of the Nomenclature Committee on Cell Death 2018. *Cell Death Differ.* **25**, 486–541, (2018).

8 Dixon, Scott J. *et al.* Ferroptosis: An iron-dependent form of nonapoptotic cell death. *Cell* **149**, 1060–1072.

9 Lewerenz, J. *et al.* Oxytosis/Ferroptosis—(Re-) Emerging Roles for Oxidative Stress-Dependent Non-apoptotic Cell Death in Diseases of the Central Nervous System. *Front. Neurosci.* **12**, 214, (2018).

10 Neves, A. A. & Brindle, K. M. Imaging Cell Death. *J. Nucl. Med.* **55**, 1–4, (2014).

11 Shimada, K., Hayano, M., Pagano, N. C. & Stockwell, B. R. Cell-Line Selectivity Improves the Predictive Power of Pharmacogenomic Analyses and Helps Identify NADPH as Biomarker for Ferroptosis Sensitivity. *Cell Chem. Biol.* **23**, 225–235, (2016).

12 Yang, W. S. *et al.* Regulation of ferroptotic cancer cell death by GPX4. *Cell* **156**, 317–331, (2014).

13 Hayano, M. *et al.* Loss of cysteinyl-tRNA synthetase (CARS) induces the transsulfuration pathway and inhibits ferroptosis induced by cystine deprivation. *Cell Death Differ.* **23**, 270–278, (2016).

14 Hayano, M. *et al.* Loss of cysteinyl-tRNA synthetase (CARS) induces the transsulfuration pathway and inhibits ferroptosis induced by cystine deprivation. *Cell Death Differ.* **23**, 270–280, (2015).

15 Shimada, K. & Stockwell, B. R. tRNA synthase suppression activates de novo cysteine synthesis to compensate for cystine and glutathione deprivation during ferroptosis. *Mol. Cell Oncol.* **3**, e1091059, (2015).

16 Yang, W. S. *et al.* Peroxidation of polyunsaturated fatty acids by lipoxygenases drives ferroptosis. *Proc. Natl. Acad. Sci.* **113**, E4966–E4975, (2016).

17 Kagan, V. E. *et al.* Oxidized arachidonic and adrenic PEs navigate cells to ferroptosis. *Nat. Chem. Biol.* **13**, 81–90, (2016).

18 Skouta, R. *et al.* Ferrostatins Inhibit Oxidative Lipid Damage and Cell Death in Diverse Disease Models. *J. Am. Chem. Soc.* **136**, 4551–4556, (2014).

19 Friedmann Angeli, J. P. *et al.* Inactivation of the ferroptosis regulator Gpx4 triggers acute renal failure in mice. *Nat. Cell Biol.* **16**, 1180–1191, (2014).

20 Kagan, V. E. *et al.* Oxidized arachidonic and adrenic PEs navigate cells to ferroptosis. *Nat. Chem. Biol.* **13**, 81–90, (2017).

21 Dixon, S. J. *et al.* Human Haploid Cell Genetics Reveals Roles for Lipid Metabolism Genes in Nonapoptotic Cell Death. *ACS Chem. Biol.* **10**, 1604–1609, (2015).

22 Doll, S. *et al.* ACSL4 dictates ferroptosis sensitivity by shaping cellular lipid composition. *Nat. Chem. Biol.* **13**, 91–98, (2016).

23 Shintoku, R. *et al.* Lipoxygenase-mediated generation of lipid peroxides enhances ferroptosis induced by erastin and RSL3. *Cancer Sci.* **108**, 2187–2194, (2017).

24 Wang, H. *et al.* 12-Lipoxygenase plays a key role in cell death caused by glutathione depletion and arachidonic acid in rat oligodendrocytes. *Eur. J. Neurosci.* **20**, 2049–2058, (2004).

25 Gao, M. *et al.* Glutaminolysis and Transferrin Regulate Ferroptosis. *Mol. Cell* **59**, 298–308, (2015).

26 Hao, S. *et al.* Metabolic networks in ferroptosis. *Oncol. Lett.* **15**, 5405–5411, (2018).

27 Shimada, K. *et al.* Global survey of cell death mechanisms reveals metabolic regulation of ferroptosis. *Nat. Chem. Biol.* **12**, 497–503, (2016).

28 Kryukov, G. V. *et al.* Characterization of Mammalian Selenoproteomes. *Science* **300**, 1439–1443, (2003).

29 Warner, G. J. *et al.* Inhibition of Selenoprotein Synthesis by Selenocysteine tRNA[Ser]Sec Lacking Isopentenyladenosine. *J. Biol. Chem.* **275**, 28110–28119, (2000).

30 Dixon, S. J. *et al.* Pharmacological inhibition of cystine–glutamate exchange induces endoplasmic reticulum stress and ferroptosis. *eLife* **3**, e02523, (2014).

31 Magtanong, L., Ko, P. J. & Dixon, S. J. Emerging roles for lipids in non-apoptotic cell death. *Cell Death Differ.* **23**, 1099–1109, (2016).

32 Sun, X. *et al.* Activation of the p62-Keap1-NRF2 pathway protects against ferroptosis in hepatocellular carcinoma cells. *Hepatology (Baltimore, Md.)* **63**, 173–184, (2016).

33 Sun, X. *et al.* Metallothionein-1G facilitates sorafenib resistance through inhibition of ferroptosis. *Hepatology* **64**, 488–500, (2016).

34 Sun, X. *et al.* Activation of the p62-Keap1-NRF2 pathway protects against ferroptosis in hepatocellular carcinoma cells. *Hepatology* **63**, 173–184, (2016).

35 Xie, Y. *et al.* Ferroptosis: process and function. *Cell Death Differ.* **23**, 369–379, (2016).

36 Dixon, S. J. & Stockwell, B. R. The role of iron and reactive oxygen species in cell death. *Nat. Chem. Biol.* **10**, 9–17, (2013).

37 Masaldan, S. *et al.* Iron accumulation in senescent cells is coupled with impaired ferritinophagy and inhibition of ferroptosis. *Redox Biol.* **14**, 100–115, (2017).

38 Gao, M. *et al.* Ferroptosis is an autophagic cell death process. *Cell Res.* **26**, 1021–1032, (2016).

39 Vigil, D., Cherfils, J., Rossman, K. L. & Der, C. J. Ras superfamily GEFs and GAPs: validated and tractable targets for cancer therapy? *Nat. Rev. Cancer* **10**, 842–857, (2010).

40 Dolma, S., Lessnick, S. L., Hahn, W. C. & Stockwell, B. R. Identification of genotype-selective antitumor agents using synthetic lethal chemical screening in engineered human tumor cells. *Cancer Cell* **3**, 285–296, (2003).

41 Yagoda, N. *et al.* RAS-RAF-MEK-dependent oxidative cell death involving voltage-dependent anion channels. *Nature* **447**, 864–868, (2007).

42 Yang, W. S. & Stockwell, B. R. Synthetic lethal screening identifies compounds activating iron-dependent, nonapoptotic cell death in oncogenic-RAS-harboring cancer cells. *Chem. Biol.* **15**, 234–245, (2008).

43 Bittker, J. A., Weiwer, M., Shimada, K., et al. . in *In: Probe Reports from the NIH Molecular Libraries Program* (National Center for Biotechnology Information Bethesda (MD), 2010).

44 Abrams, R. P., Carroll, W. L. & Woerpel, K. A. Five-Membered Ring Peroxide Selectively Initiates Ferroptosis in Cancer Cells. *ACS Chem. Biol.* **11**, 1305–1312, (2016).

45 Gaschler, M. M. *et al.* FINO2 initiates ferroptosis through GPX4 inactivation and iron oxidation. *Nat. Chem. Biol.* **14**, 507‒515, (2018).

46 Shirlee, T., David, S. & Pamela, M. Oxytosis: A Novel Form of Programmed Cell Death. *Curr. Top. Med. Chem.* **1**, 497–506, (2001).

47 Fearnhead, H. O., Vandenabeele, P. & Vanden Berghe, T. How do we fit ferroptosis in the family of regulated cell death? *Cell Death Differ.* **24**, 1991–1998, (2017).

48 Houessinon, A. *et al.* Metallothionein-1 as a biomarker of altered redox metabolism in hepatocellular carcinoma cells exposed to sorafenib. *Mol. Cancer* **15**, 28–38, (2016).

49 Hasegawa, M. *et al.* Functional interactions of the cystine/glutamate antiporter, CD44v and MUC1-C oncoprotein in triple-negative breast cancer cells. *Oncotarget* **7**, 11756–11769, (2016).

50 Loibl, S. *et al.* Sorafenib in the Treatment of Early Breast Cancer: Results of the Neoadjuvant Phase II Study - SOFIA*. *Breast Care* **9**, 169–174, (2014).

51 Baselga, J. *et al.* Sorafenib in Combination With Capecitabine: An Oral Regimen for Patients With HER2-Negative Locally Advanced or Metastatic Breast Cancer. *J. Clin. Oncol.* **30**, 1484–1491, (2012).

52 Robert, S. M. *et al.* SLC7A11 expression is associated with seizures and predicts poor survival in patients with malignant glioma. *Sci. Transl. Med.* **7**, 289ra286, (2015).

53 Savaskan, N. E. *et al.* Small interfering RNA–mediated xCT silencing in gliomas inhibits neurodegeneration and alleviates brain edema. *Nat. Med.* **14**, 629–632, (2008).

54 Sehm, T. *et al.* Temozolomide toxicity operates in a xCT/SLC7a11 dependent manner and is fostered by ferroptosis. *Oncotarget* **7**, 74630–74647, (2016).

55 Chen, D. *et al.* The oxido-metabolic driver ATF4 enhances temozolamide chemo-resistance in human gliomas. *Oncotarget* **8**, 51164–51176, (2017).

56 Lee, S. Y. Temozolomide resistance in glioblastoma multiforme. *Genes & Diseases* **3**, 198–210, (2016).

57 Davis, M. E. Glioblastoma: Overview of Disease and Treatment. *Clin J. Oncol. Nurs.* **20**, S2–S8, (2016).

58 Dixon, S. J. & Stockwell, B. R. The Hallmarks of Ferroptosis. *Annu. Rev. Cancer Biol.* **3**, null, (2019).

59 Dexter, D. *et al.* Lipid Peroxidation as Cause of Nigral Cell Death in Parkinson's Disease. *The Lancet* **328**, 639–640, (1986).

60 Cassarino, D. S. *et al.* Elevated reactive oxygen species and antioxidant enzyme activities in animal and cellular models of Parkinson's disease. *Biochim. Biophys. Acta, Mol. Basis Dis.* **1362**, 77–86, (1997).

61 Castellani, R. J. *et al.* Iron: The Redox-active Center of Oxidative Stress in Alzheimer Disease. *Neurochem. Res.* **32**, 1640–1645, (2007).

62 Browne, S. E., Ferrante, R. J. & Beal, M. F. Oxidative Stress in Huntington's Disease. *Brain Pathol.* **9**, 147–163, (1999).

63 Lee, J. *et al.* Modulation of lipid peroxidation and mitochondrial function improves neuropathology in Huntington’s disease mice. *Acta Neuropathol.* **121**, 487–498, (2011).

64 Chen, J. *et al.* Iron Accumulates in Huntington’s Disease Neurons: Protection by Deferoxamine. *PLoS One* **8**, e77023, (2013).

65 Back, S. A. *et al.* Selective vulnerability of preterm white matter to oxidative damage defined by F2-isoprostanes. *Ann. Neurol.* **58**, 108–120, (2005).

66 Inder, T. *et al.* Elevated Free Radical Products in the Cerebrospinal Fluid of VLBW Infants with Cerebral White Matter Injury. *Pediatric Res.* **52**, 213–218, (2002).

67 Tuo, Q. z. *et al.* Tau-mediated iron export prevents ferroptotic damage after ischemic stroke. *Mol. Psychiatry* **22**, 1520–1530, (2017).

68 Brouns, R. & De Deyn, P. P. The complexity of neurobiological processes in acute ischemic stroke. *Clin. Neurol. Neurosurg.* **111**, 483–495, (2009).

69 Dietrich, R. B. & W G Bradley, J. Iron accumulation in the basal ganglia following severe ischemic-anoxic insults in children. *Radiology* **168**, 203–206, (1988).

70 Kabiraj, P. *et al.* The Neuroprotective Role of Ferrostatin-1 Under Rotenone-Induced Oxidative Stress in Dopaminergic Neuroblastoma Cells. *Protein J.* **34**, 349-358, (2015).

71 Do Van, B. *et al.* Ferroptosis, a newly characterized form of cell death in Parkinson's disease that is regulated by PKC. *Neurobiol. Dis.* **94**, 169–178, (2016).

72 Hambright, W. S. *et al.* Ablation of ferroptosis regulator glutathione peroxidase 4 in forebrain neurons promotes cognitive impairment and neurodegeneration. *Redox Biol.* **12**, 8–17, (2017).

73 Friedmann Angeli, J. P. *et al.* Inactivation of the ferroptosis regulator Gpx4 triggers acute renal failure in mice. *Nat. Cell Biol.* **16**, 1180–1191, (2014).

74 Linkermann, A. *et al.* Synchronized renal tubular cell death involves ferroptosis. *Proc. Natl. Acad. Sci.* **111**, 16836–16841, (2014).

75 Garg, A. D., Romano, E., Rufo, N. & Agostinis, P. Immunogenic versus tolerogenic phagocytosis during anticancer therapy: mechanisms and clinical translation. *Cell Death Differ.* **23**, 938–951, (2016).

76 Nagata, S. & Tanaka, M. Programmed cell death and the immune system. *Nat. Rev. Immunol.* **17**, 333, (2017).

77 Linkermann, A., Stockwell, B. R., Krautwald, S. & Anders, H.-J. Regulated cell death and inflammation: an auto-amplification loop causes organ failure. *Nat. Rev. Immunol.* **14**, 759–767, (2014).

78 Kono, H. & Rock, K. L. How dying cells alert the immune system to danger. *Nat. Rev. Immunol.* **8**, 279, (2008).

79 Galluzzi, L., Senovilla, L., Zitvogel, L. & Kroemer, G. The secret ally: Immunostimulation by anticancer drugs. *Nat. Rev. Drug Discov.* **11**, 215–233, (2012).

80 Lesterhuis, W. J., Haanen, J. B. A. G. & Punt, C. J. A. Cancer immunotherapy – revisited. *Nat. Rev. Drug Discov.* **10**, 591–600, (2011).

Chapter 2: Discovery of Ferroptocide

2.1 Phenotypic screening

Phenotypic screening, also known as forward chemical genetics, is the historical mode of screening in drug discovery.[1-3] It consists of subjecting a library of compounds to a target agnostic screen and monitoring disease-linked phenotypes. The compounds that elicit the desired phenotype are considered small molecule hits. Conducting hit-to-lead studies is a significant challenge, however, as the target of each hit is unknown. The rate limiting step thus becomes target identification and elucidation of the mode of action of the compound of interest. Recent advances in chemical biology techniques have enabled rapid target discovery and shortened this timeline to months instead of years, but the intricacies involved in identifying the underlying biology still require significant technical expertise.[4]

Some of the inherent advantages of phenotypic screening include: screening in physiologically relevant contexts (minimally cell-based or animal-based models), uncovering new targets or molecular mechanisms of actions (MMOA), and identifying cell permeable hit compounds.[3,5] Most of the commonly prescribed drugs in the clinic (anthracyclines [i.e. doxorubicin], paclitaxel, vinca alkaloids, etc.) were discovered through phenotypic screening efforts conducted in animal models of leukemia and lymphomas in the 1960s[6], which speaks to the utility and value of phenotypically discovered drugs. Furthermore, a detailed analysis by Swinney and Anthony of all 75 first-in-class FDA approved drugs from 1999–2008 revealed that 28 of these drugs were discovered through phenotypic screening approaches, while 17 came from target-based approaches (**Fig. 2.1**).[1] At the time, this study questioned the industry's heavy focus and investment on target-based technologies since the mid-1980s. Sequencing of the human genome, advancements in high throughput screening technologies and modern biological techniques, coupled to progress in combinatorial and parallel chemistry had inspired a target and hypothesis-based approach to drug discovery, and yet the industry was facing the challenge of low productivity in research and development (R&D). This study shed light into the problems observed in industry. An updated survey of first-in-class drugs approved from 1999–2013 indicated that from 113 first-in-class drugs, 78 were developed from target-based screens (45 small molecules and 33 biologics) and 33 from system-based approaches in direct contrast to the initial report.[7] The reasons for the apparent discrepancy were attributed to the additional 5-year period of the second analysis and the semantic distinctions in the definition of phenotypic screen vs chemocentric and/or active pharmacophore screens.

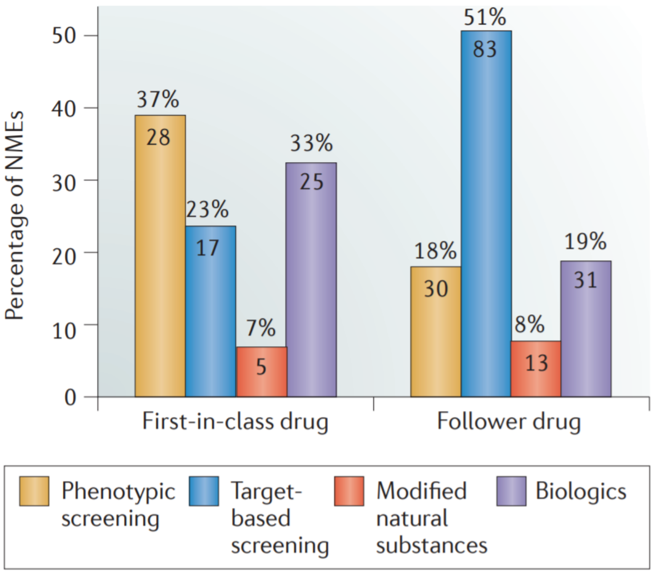

Figure 2.1. Distribution of first in class drugs approved from 1999–2008. Phenotypic screens generated more first in class drugs than target-based screens. Image is reproduced with permission from Nature[1].

The high attrition rates of compounds in the clinic, especially due to lack of efficacy attributed to the reductionist approach to disease biology (focusing on insufficiently validated targets and lacking consideration for target engagement in vivo)[8] have recently instigated a "resurrection" of phenotypic screens in oncology R&D programs throughout the US.[9-11] The modern phenotypic assays aim to incorporate clinically relevant biological systems with a clear link to disease such as induced pluripotent stem cells (iPSC), patient-derived primary cells, 3D systems, and cell co-culturing models.[3,9]

Other important considerations are the assay stimuli and readouts. Ideally, the readout is a translational biomarker close to a clinical endpoint such as muscle contraction, contraction of heart tissues for beta blocker development, patient-derived airway epithelial cells in the case of cystic fibrosis coupled to measurement of channel activity and the airway surface liquid release, etc.[11] The future of phenotypic assays lies in screening libraries of compounds with unique physiochemical properties (different from the current commercial screening libraries) in a clinically relevant endpoint assay using patient-derived models.

2.2 Library considerations: CtD library

Of critical importance when conducting a phenotypic screen is the compound collection. Commercially available libraries (Chembridge, Microformat, PNAS CC) are mainly comprised of flat, aromatic compounds possessing a low number of stereogenic centers, sp3-hybridized carbons (Fsp_3), and ring complexity (**Fig. 2.2**).[1,12] Assessment of the complexity of approved oncology drugs by these three metrics indicates that FDA-approved anticancer drugs are more complex than compounds in commercial libraries. Therefore, there is a critical need for complex and diverse small molecules. The Hergenrother lab’s approach to addressing this challenge is coined complexity-to-diversity (CtD), where complex and readily available natural products are subjected to short ($\leq$ 7) synthetic steps to arrive at complex and diverse scaffolds (**Fig. 2.3**). Evaluation of the complexity of the CtD library demonstrates that the resultant compounds have a high number of chiral centers, high Fsp_3, and enhanced ring complexity similar to FDA-approved oncology drugs as shown in **Fig 2.2**.

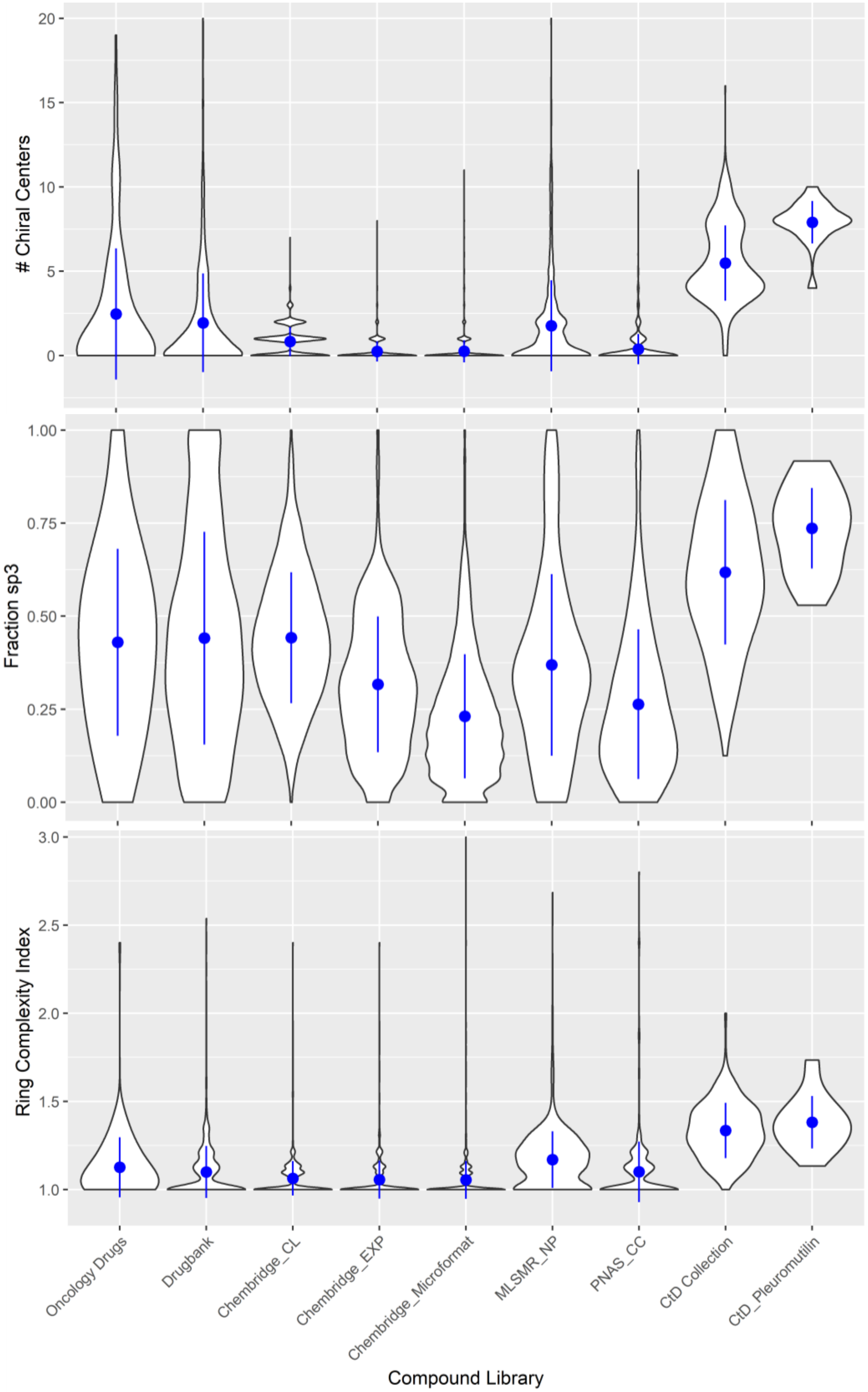

Figure 2.2. Comparison of complexity metrics (chiral centers, Fsp3, and ring complexity) of pleuromutilin compounds with various small molecule libraries. Violin plots shown, where width represents the distribution while the blue dot and line represent the mean and standard deviation.

Currently, there are >600 compounds synthesized via the CtD strategy applied to adrenosterone,[13] gibberellic acid,[13] quinine,[13,14] abietic acid,[15] sinomenine,[16] pleuromutilin, and lycorine[17] in our lab. Additionally, various academic labs have adopted and applied this approach to several natural products such as yohimbine,[18] haemanthabine,[19] nitrogenous steroids of dutasteride and abiraterone acetate,[20] ilimaquinone,[21] and others. The resulting collections of complex compounds have been used to discover small molecules with anticancer and antimicrobial activities, autophagy inhibitors,[18,22,23] and to identify predictive guidelines for broad-spectrum antibiotic discovery.[24] We hypothesized that subjecting our in-house CtD library to a cytotoxicity phenotypic screen would enable discovery of compounds with new MMOA.

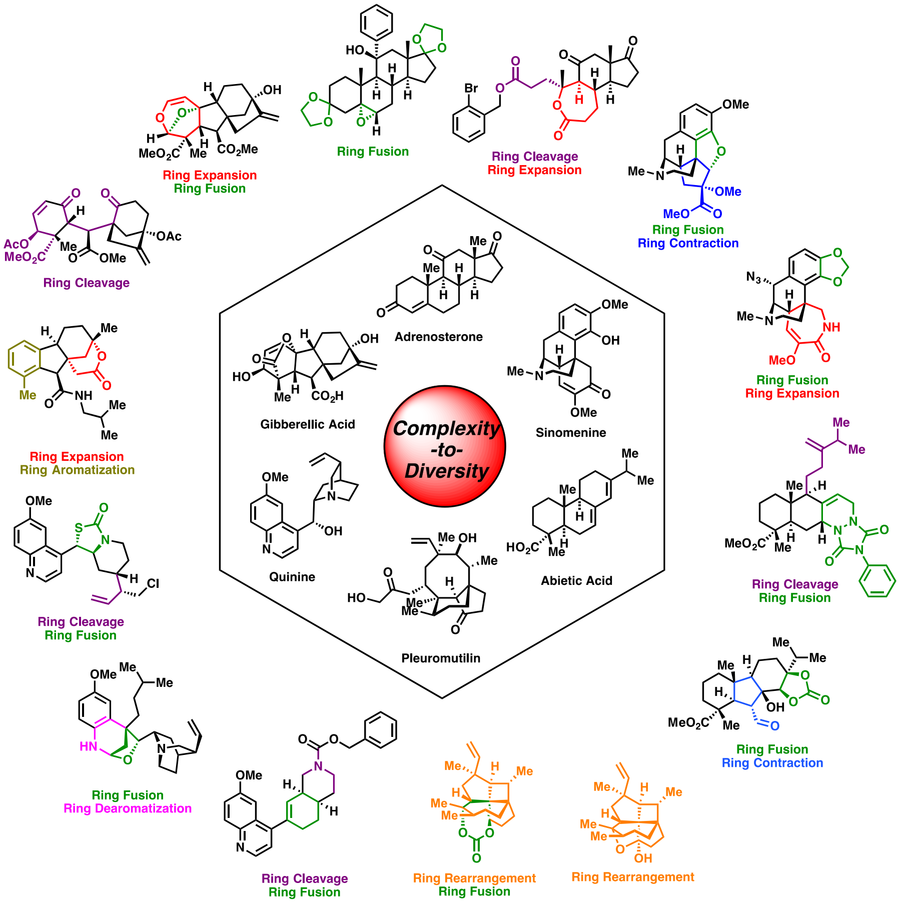

Figure 2.3. Following the Complexity-to-Diversity strategy six natural product are transformed in short synthetic sequences to comprised of a 341member library.

Table 2.1. Hit compounds identified through an anticancer phenotypic screen and their respective IC_{50} values.

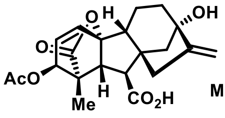

KCM-VI-118
False positive

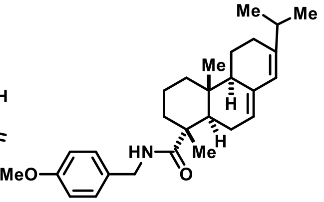

RJR-III-014Y
Weak Activity

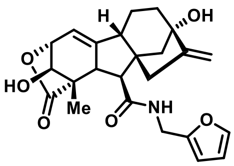

MFR-I-93
False positive

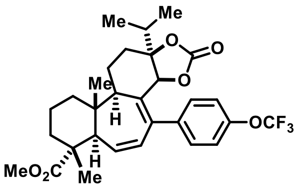

RH2-4-87B-2
Active compound

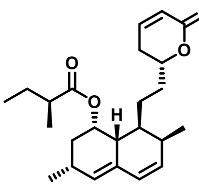

HR-05-225
Weak activity

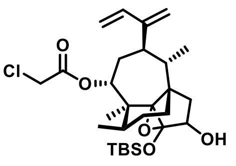

RH2-5-85-2
Active compound

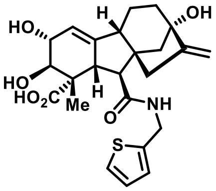

MFR-II-262
False positive

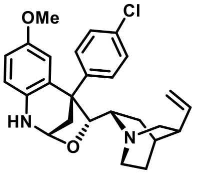

RH2-1-213-D
False positive

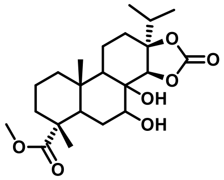

RJR-II-136
False positive

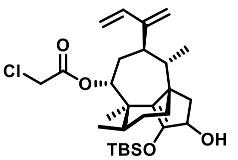

RH2-5-93-1
Active compound

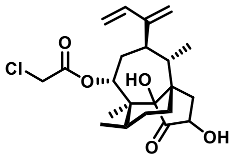

P4
Active Compound

Name	Percent Dead	IC_{50}
KCM VI-118	**HCT 116**: 84.8 %	>100
	ES-2: 65.4%	>100
	Mia PaCa-2: 69.4%	>100
RJR-III-014Y	**HCT 116**: N/A	-
	ES-2: N/A	-
	Mia PaCa-2: 50.8 %	16.7
MFR-I-93	**HCT 116**: 68.5 %	>100
	ES-2: 71%	>100
	Mia PaCa-2: 71%	>100
RH2-4-87B-2	**HCT 116**: 68.5 %	> 16.6
	ES-2: 71%	21.5
	Mia PaCa-2: 71%	5.1 ± 2.2
HR-05-225	**HCT 116**: 62.9 %	10.6
	ES-2: 51%	>100
	Mia PaCa-2: 60.9%	>100
RH2-5-85-2	**HCT 116**: 47.2 %	6.3 ± 2.5
	ES-2: 73.7 %	2.0 ± 0.4
	Mia PaCa-2: 54 %	5.0 ± 2.6
MFR II-262	**HCT 116**: 53%	>100
	ES-2: N/A	-
	Mia PaCa-2: N/A	-
RH2-1-213-D	**HCT 116**: N/A	-
	ES-2: 65.8 %	>100
	Mia PaCa-2: N/A	-
RJR-II-136	**HCT 116**: N/A	-
	ES-2: 65.8 %	>100
	Mia PaCa-2: N/A	-
RH2-5-93-1	**HCT 116**: N/A	13.4 ±
	ES-2: 49.5 %	4.8 ± 3.3
	Mia PaCa-2: N/A	18.2
	Mia PaCa-2: N/A	9.1 ± 3.4
P4	**HCT 116**: 63.4 %	19.7 ±
	ES-2: 53.2 %	6.7 ± 0.4

2.3 Anticancer phenotypic screening of the CtD library

Compounds from CtD were evaluated in whole-cell assays for their ability to rapidly kill cancer cell lines in a primary screen against the ES-2 (ovarian cancer), HCT 116 (colon cancer), and Mia PaCa2 (pancreatic cancer) cell lines. Such cell lines were selected as representatives of challenging-to-treat cancers. All compounds were assessed at 12 µM, with cell viability determined using the Alamar Blue viability assay. Compounds that elicited at least 50% cell death were considered hit compounds and were then evaluated through full dose-response curves (**Table 2.1**). From these assessments, four compounds were identified as having promising activity, with rapid induction of cell death (characterized further below). Three of the most active compounds were derived from the pleuromutilin (P) natural product and thus were prioritized for further investigation.

Pleuromutilin is a diterpenoid that was first isolated from basidiomycetes in 1951 by Kavanagh and co-workers.[25] The natural product **P** is found in several species of fungi and is a potent inhibitor of the bacterial 50S ribosome.[26-28] **P** is composed of 5-, 6-, and 8-membered rings and contains eight contiguous stereogenic centers. Several semisynthetic derivatives of **P** are used to treat Gram-positive pathogens in humans (retapamulin) and in veterinary medicine (tiamulin, valnemulin),[26,29] and recently epi-mutilin derivatives have been developed as antibiotics with activity against some Gram-negative bacteria.[30-33] Investigation of the antibacterial activity of **P** and its derivatives has inspired several endeavors in its total synthesis[31,32,34-36] that, combined with previous work on structure elucidation[37,38] and structure–activity relationship studies (SAR),[39-41] provide a wealth of synthetic information about the chemical reactivity of the **P** ring system. Such data was critical in constructing a small set of highly complex and structurally diverse compounds using **P** as a starting material (**Fig. 2.2**).

2.4 Structure–activity relationship studies

2.4.1 SAR studies of 85-2 hit compound

Upon dose-response validation of hit compounds as shown in **Table 2.1**, two compounds were prioritized for additional SAR studies (**85-2** and **P4**). Compound **85-2** is certainly a non-conventional lead compound due to the TBS-protecting functional group. Uses of silicon as a carbon isostere is one approach of discovering new drug-like entities with favorable biological properties in medicinal chemistry.[42] Literature reports indicate that silicon can be used as a carbon bioisostere (as in silaproline),[43] and similar silicon-containing compounds can display activity against influenza proton channels and CNS receptors (azasilines),[43] inhibit p38 MAP kinase activity (BIRB-796 Si-analogue),[44] function as opioid receptor agonists (sila-loperamide),[45] and display anticancer activity (5-tert-butyl-2-furylmethylidene-aniline silicon analogues, 3i)[46] as shown in **Figure 2.4**. Head-to-head comparisons of biological properties of silicon and carbon analogues demonstrate that silicon does not pose metabolic, efflux, or drug–drug interaction liabilities and can potentially improve oral bioavailability as shown for selective azasilanes.[43]

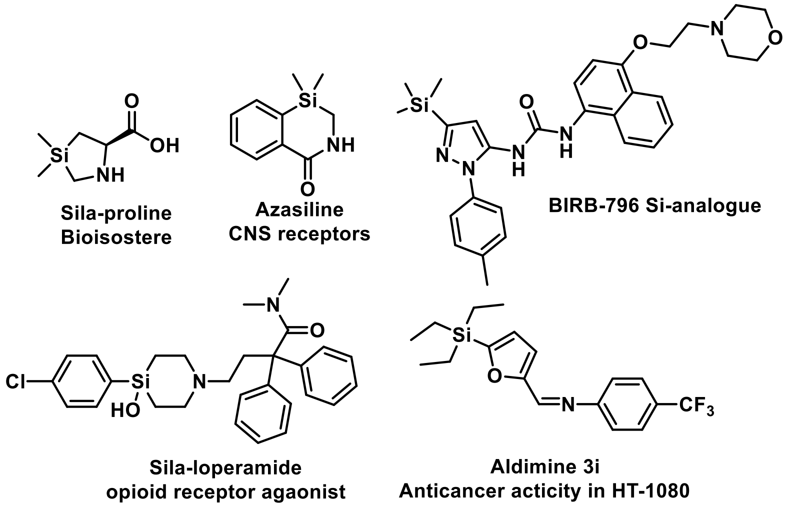

Figure 2.4. A subset of Silicon containing compounds with biological activity.

Despite the fact that **85-2** possesses a TBS protecting group and is not a silicon analogue, this scaffold was advanced for minimal SAR studies as shown in **Fig 1.5**. Substitution of the α-choro ester with an acetate (**5-259**) or furoic ester (**6-69**) results in loss of anticancer activity, while insertion of an azido group (**1-47**) improves activity in HCT 116 colon cancer cells and retains activity in an ovarian cancer cell line (ES-2). Modification of the secondary alcohol (**295-1**) is not tolerated while [4+2] cycloaddition of the diene resulted in the most active derivative of the series (**5-271**). To investigate the importance of the TBS group, TES derivatives (**6-45, 6-93C, 6-87**) were synthesized and tested for biological activity. Dose-response studies revealed that TES derivatives had diminished anticancer activity compared to their TBS- analogues, suggesting a potential interference in target engagement due to the bulkiness of the ethyl groups.

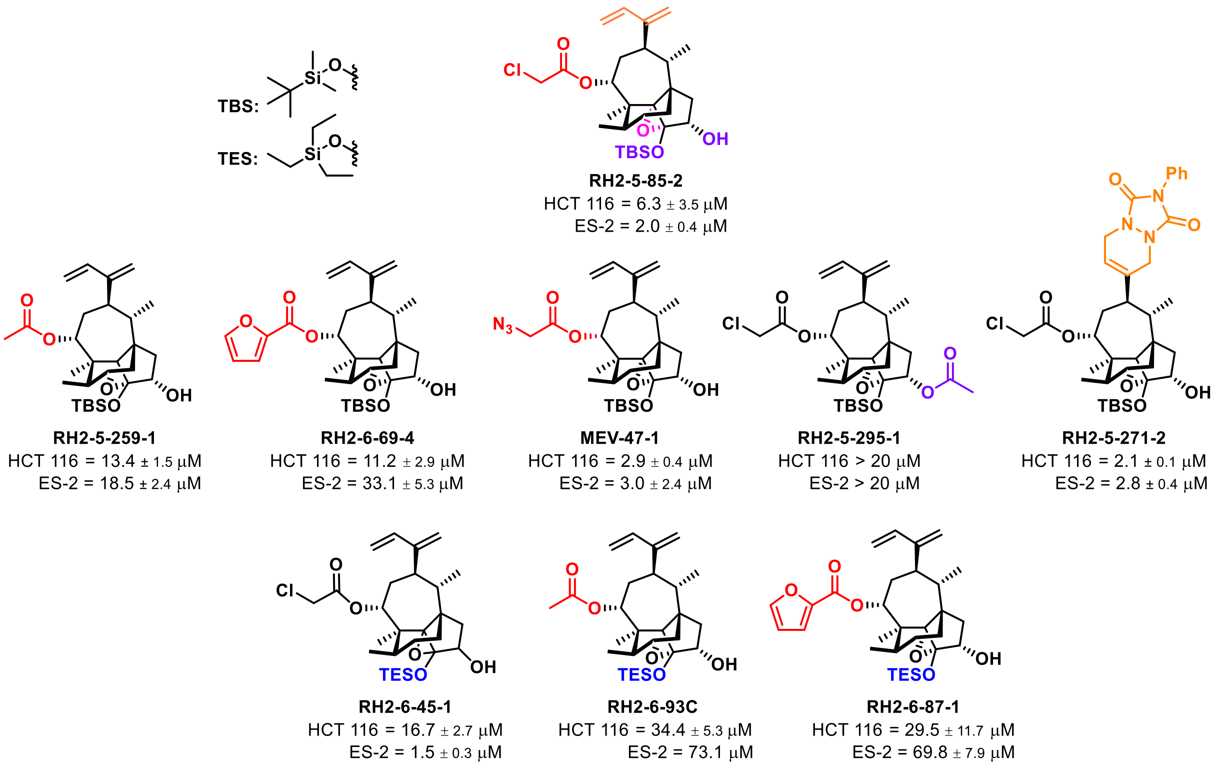

Figure 2.5. SAR studies of **85-2** scaffold discovered through an anticancer phenotypic screen of CtD library.

2.4.2 SAR studies of P4 hit compound

Another key compound discovered through the anticancer phenotypic screening effort was compound **P4**. Given the interest in **P**-derived compounds for antibacterial treatment, the discovery of **P4**'s anticancer activity warranted further pursuit. **P4** was a favorable hit compound due to the many functional group handles present in the molecule (color-coded in **Fig. 2.6**). In collaboration with Dr. Rob Hicklin (all SAR compounds) and undergraduate Mike Vinyard (for the azido derivatives), a series of compounds were synthesized and tested for activity (**Fig. 2.6**).

Methylation (**6-147**) and acetylation (**5-287**) of the secondary alcohol is moderately tolerated while modification of the diene (**5-267**) is highly favorable. The α-chloro ester moiety is deemed to be a key handle for activity. Indeed, removal of the α-chloro ester (**5-227**) as well as substitution with an acetate-, fluoro-, furan-, azido group results in loss of bioactivity (compounds **5-227**, **5-261**, **6-197**, **6-89**, **6-143** respectively). The most active compound from both SAR campaigns was **5-267**, hereafter referred to as **ferroptocide**. This scaffold was prioritized as a lead compound and subjected to further SAR analysis.

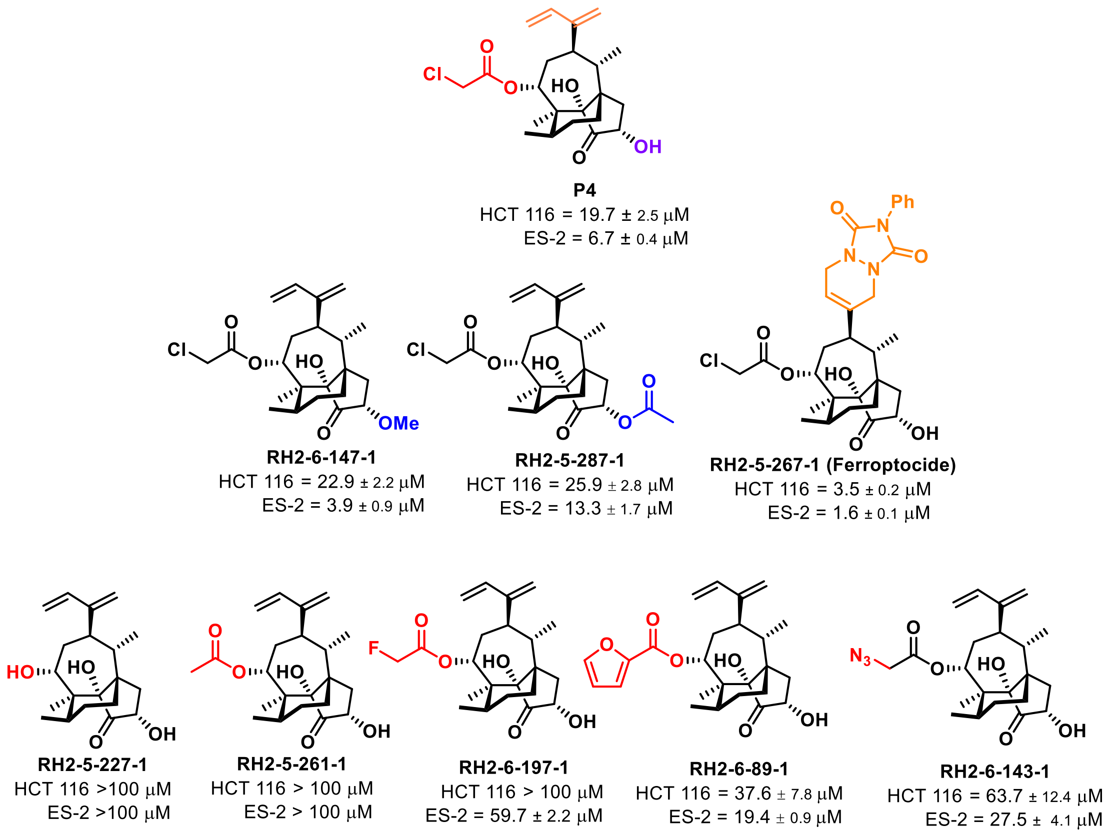
P4
HCT 116 = 19.7 ± 2.5 μM
ES-2 = 6.7 ± 0.4 μM

RH2-6-147-1
HCT 116 = 22.9 ± 2.2 μM
ES-2 = 3.9 ± 0.9 μM

RH2-5-287-1
HCT 116 = 25.9 ± 2.8 μM
ES-2 = 13.3 ± 1.7 μM

RH2-5-267-1 (Ferroptocide)
HCT 116 = 3.5 ± 0.2 μM
ES-2 = 1.6 ± 0.1 μM

RH2-5-227-1
HCT 116 >100 μM
ES-2 >100 μM

RH2-5-261-1
HCT 116 > 100 μM
ES-2 > 100 μM

RH2-6-197-1
HCT 116 > 100 μM
ES-2 = 59.7 ± 2.2 μM

RH2-6-89-1
HCT 116 = 37.6 ± 7.8 μM
ES-2 = 19.4 ± 0.9 μM

RH2-6-143-1
HCT 116 = 63.7 ± 12.4 μM
ES-2 = 27.5 ± 4.1 μM

Figure 2.6. Investigating the functional groups need for activity of **P4** hit compound.

2.4.3 SAR studies of lead compound ferroptocide

Ferroptocide is more potent than hit compound **P4**, with an IC_{50} = 1.6 μM against ES-2 cells. Further modification of the secondary alcohol and the α-chloro ester of **ferroptocide** unveiled structural features important for activity. While methylation and acetylation of the secondary alcohol of **ferroptocide** (**P19** and **P20**, respectively) did not change the activity (**Fig. 2.7**), replacement of the α-chloro ester with an acetate group (**P21**) eliminated activity. To investigate other electrophilic groups the fluoro- (**P22**) and iodo- (**P23**) compounds were synthesized. While **P22** had greatly diminished anticancer activity, the iodo analogue (**P23**) showed greater potency in cells at the expense of biological selectivity (**Fig. 2.8**). Additional compounds with poor leaving groups such as α-acetate ester (**P24**), α,α dichloro ester (**P25**), furoic ester (**P26**), and azido ester (**6-127**) exhibited no anticancer activity (**Fig. 2.7**). Another highly used group in medicinal chemistry and present in many approved drugs is the acrylate functional group. Synthesis of the acrylate analogue (**7-103**) did not improve nor diminished bioactivity. **Ferroptocide** remained the most active derivative after this extensive SAR analysis.

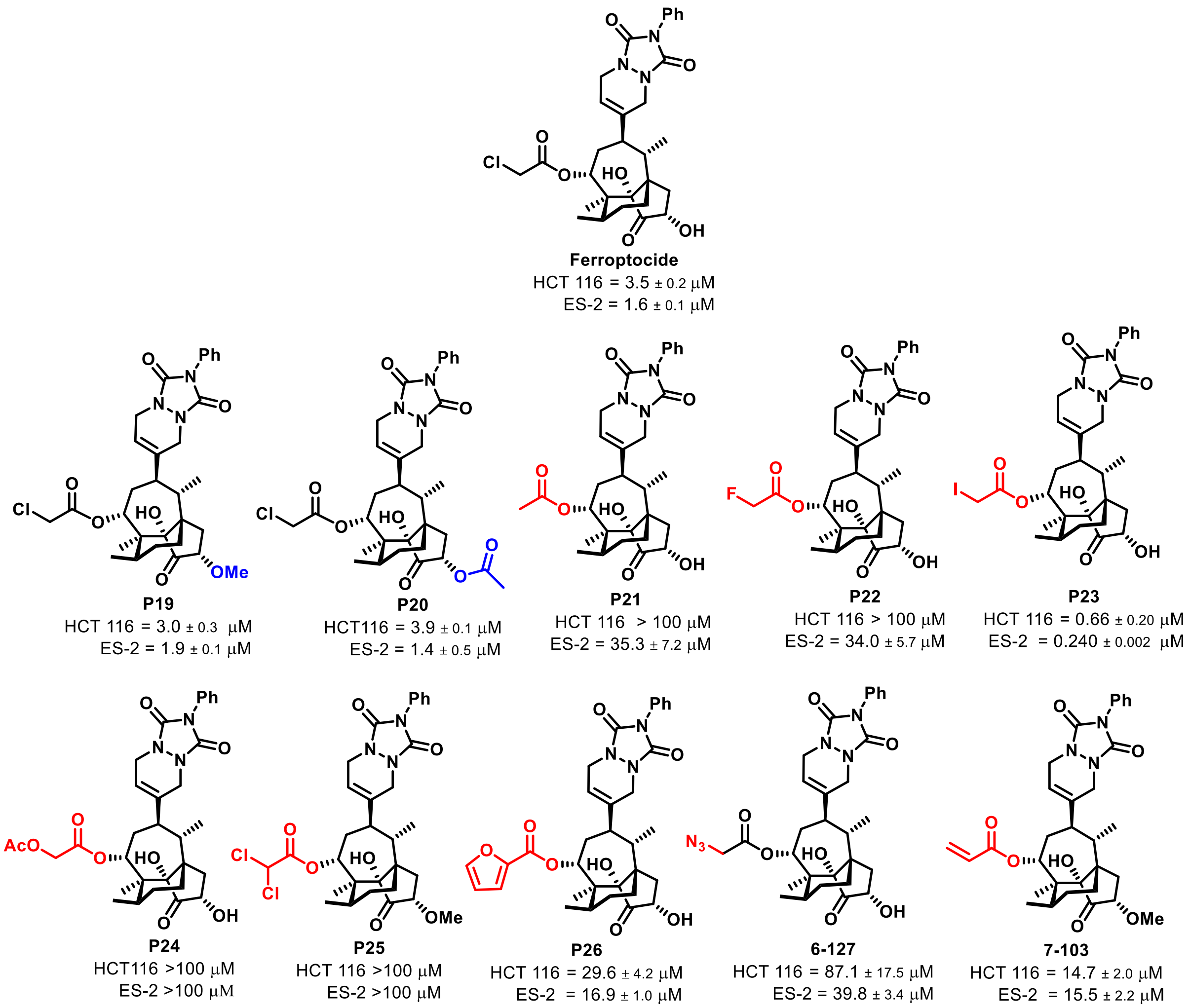

Ferroptocide
HCT 116 = 3.5 ± 0.2 μM
ES-2 = 1.6 ± 0.1 μM

P19
HCT 116 = 3.0 ± 0.3 μM
ES-2 = 1.9 ± 0.1 μM

P20
HCT116 = 3.9 ± 0.1 μM
ES-2 = 1.4 ± 0.5 μM

P21
HCT 116 > 100 μM
ES-2 = 35.3 ± 7.2 μM

P22
HCT 116 > 100 μM
ES-2 = 34.0 ± 5.7 μM

P23
HCT 116 = 0.66 ± 0.20 μM
ES-2 = 0.240 ± 0.002 μM

P24
HCT116 >100 μM
ES-2 >100 μM

P25
HCT 116 >100 μM
ES-2 >100 μM

P26
HCT 116 = 29.6 ± 4.2 μM
ES-2 = 16.9 ± 1.0 μM

6-127
HCT 116 = 87.1 ± 17.5 μM
ES-2 = 39.8 ± 3.4 μM

7-103
HCT 116 = 14.7 ± 2.0 μM
ES-2 = 15.5 ± 2.2 μM

Figure 2.7. SAR analysis of lead compound ferroptocide.

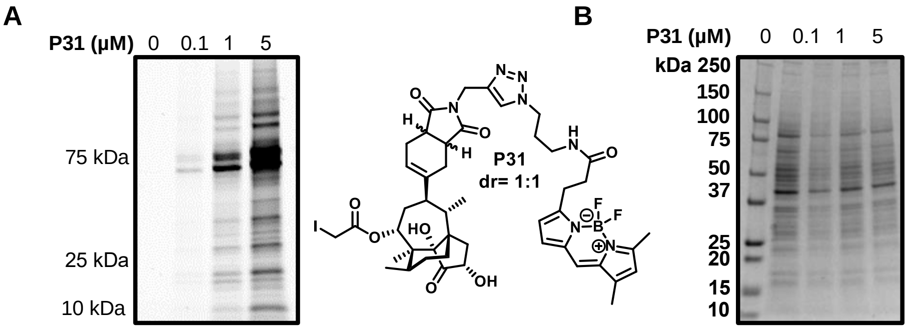

Figure 2.8. **(A)** Promiscuous bioactivity of the Iodo fluorescent analogue (**P31**) upon 30 min dose-dependent treatment with compound. **(B)** Coomassie stain of gel demonstrates equal loading.

2.4.4 Synthesis and evaluation of tool compounds

Additional synthesis and evaluation revealed that the two bridgehead nitrogens in the urazole ring of **ferroptocide** could be removed (**P28**, **Fig. 2.9**) with minimal loss in activity. This discovery allowed for the construction of the alkyne tool compound **P29** (**Fig. 2.9**), which was further modified via a 1,3-dipolar cycloaddition resulting in fluorescent compound **P30**. Both **P29** and **P30** retained anticancer activity similar to **ferroptocide** (**Fig. 2.9**), and **P30** was used as a probe compound to explore subcellular localization. As shown by confocal microscopy, **P30** localizes to the cytoplasm in ES-2 cells. Additionally, a biotin analogue of

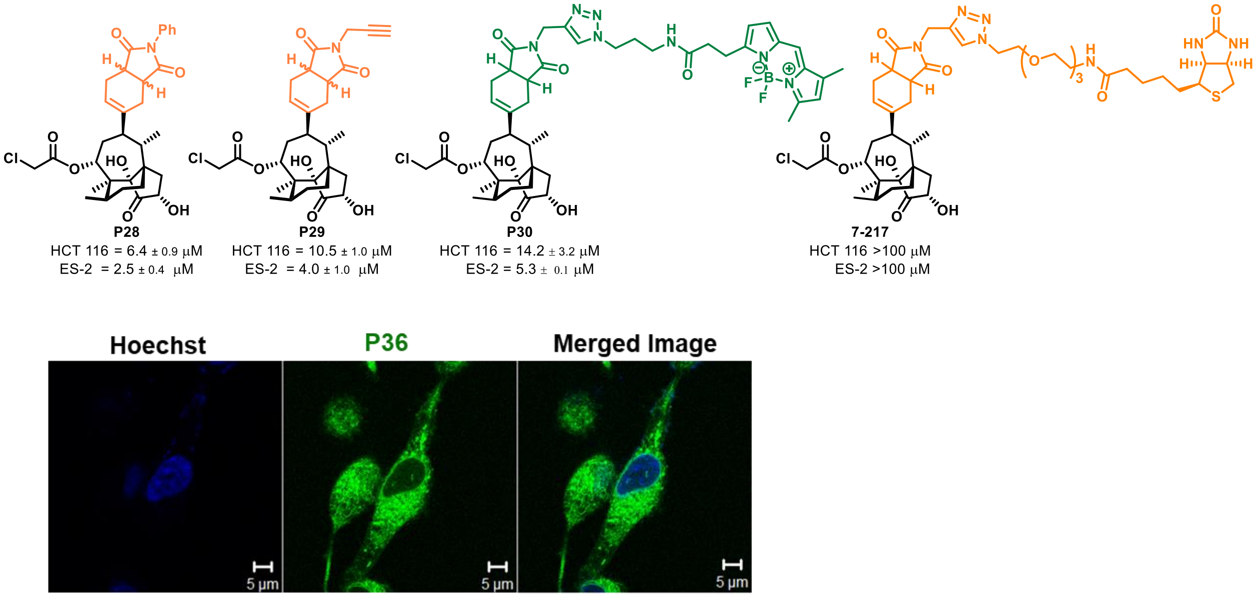

Figure 2.9. Synthesis of tool compounds and their biological activity. **P30** compound localizes in the cytoplasm of ES-2 cells after 30 min treatment. Hoechst dye is used to stain the nucleus.

ferroptocide (**7-217**) was synthesized but displayed diminished bioactivity potentially due to lack of cell permeability as observed from the large molecular weight of such scaffold.

2.4.5 Investigation of other α-chloro esters

α-Chlorocarbonyl electrophiles are expected to be reactive towards nucleophilic substrates due to their high reactivity.[47] Such scaffolds including chloroacetamides, chloromethyl ketones, p-chloronitrobenze electrophiles and others, tend to react with cysteine thiols in cells due to the polarizability and electron-rich nature of sulfur. The main cysteine-rich endogenous nucleophiles include glutathione (the most abundant nucleophile in cells), gamma glutamyl cysteine (precursor of glutathione), and la antigen (RNA chaperone that facilitates correct processing and maturation of RNA polymerase III transcript) among others. In addition, residues such as serine, lysine, tyrosine, threonine, aspartate, and glutamate have the potential to be nucleophilic and react with these electrophilic compounds depending on the protein environment.

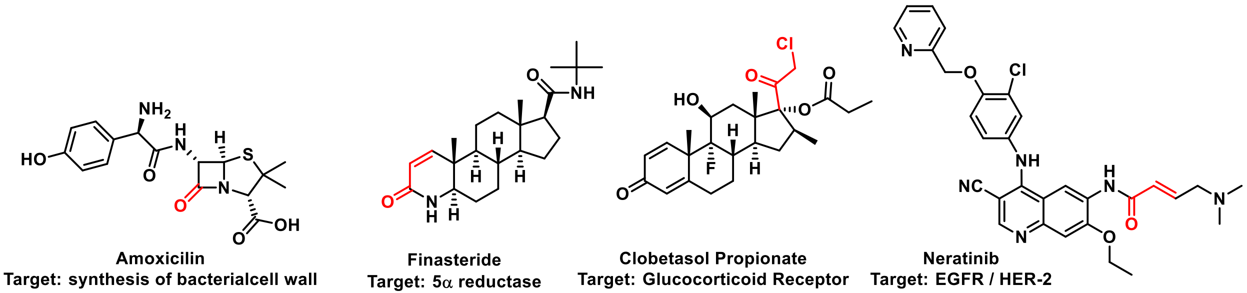

Amoxicilin
Target: synthesis of bacterialcell wall
Antibacterial Drug
FDA Approved 1982

Finasteride
Target: 5α reductase
Anticancer Drug
FDA Approved 1992

Clobetasol Propionate
Target: Glucocorticoid Receptor
Anti-Inflammatory Drug
FDA Approved 2007

Neratinib
Target: EGFR / HER-2
Anticancer Drug
FDA Approved 2017

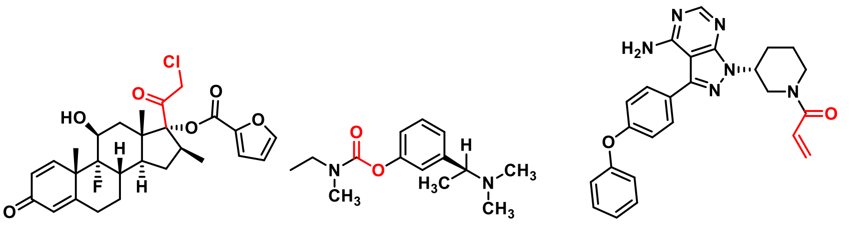

Mometasome Furoate
Target: Glucocorticoid Receptor
Anti-Inflammatory Drug
FDA Approved 1997

Rivastigmine
Target: Cholinesterase Inibitor
Dementia Drug
FDA Approved 2006

Ibrutinib
Target: Bruton's Kinase Inibitor
Anticancer Drug
FDA Approved 2013

Figure 2.10. A subset of FDA approved drugs containing carbonyl electrophiles

A detailed report by Klein and co-workers[48] demonstrated via an extensive study of the biochemical reactivity of 72 compounds containing diverse electrophilic groups towards 11 pharmacologically relevant targets, that chlorocarbonyl electrophiles exhibit surprisingly low off-target reactivity and minimal activity towards glutathione (GSH, k_{GSH}~0.1 l·mol^{-1}·s^{-1}). The authors concluded that these functional groups can be suitable warheads for designing targeted covalent inhibitors. Indeed, many covalent drugs (**Fig. 2.10**) that contain electrophiles such as

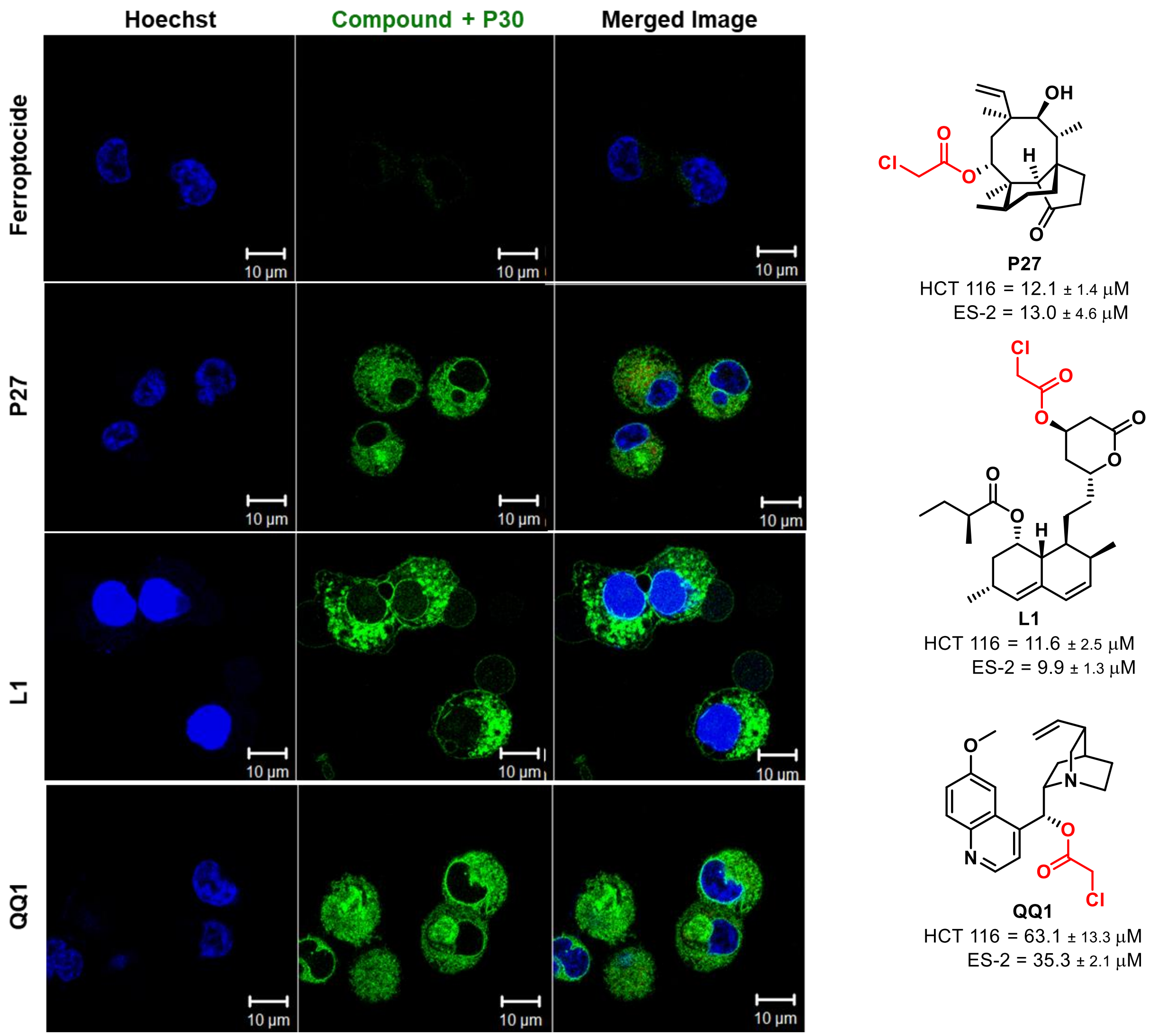

P27
HCT 116 = 12.1 ± 1.4 µM
ES-2 = 13.0 ± 4.6 µM

L1
HCT 116 = 11.6 ± 2.5 µM
ES-2 = 9.9 ± 1.3 µM

QQ1
HCT 116 = 63.1 ± 13.3 µM
ES-2 = 35.3 ± 2.1 µM

Figure 2.11. Fluorescent signal of **P30** is competed away upon pre-treatment with ferroptocide but not with the other three α-chloro esters. ES-2 cells were pre-treated at 3x IC_{50} value for 30 min followed by treatment with **P30** (5 µM). Nucleus was stained with Hoechst.

ibrutinib, finasteride, rivastigmine, and bortezomib are shown to be highly specific towards Bruton's kinase, 5α reductase, cholinesterase, and the proteasome, respectively.[49,50,51]

Importantly, installation of an α-chloro ester on pleuromutilin itself (**P27**), and other scaffolds such as lovastatin (**L1**), and quinine (**QQ1**), did not result in notable cell death or compete with **P30** in a confocal microscopy experiment as shown in **Figure 2.11**, demonstrating that the anticancer activity of **ferroptocide** is not attributed solely to the presence of an electrophilic functional group.

2.4.6 Assessing ferroptocide reactivity with glutathione

To further probe the selectivity of **ferroptocide**, compound reactivity with glutathione (GSH) was monitored at therapeutically relevant levels (5 mM). Such reactivity is a key feature of the pan-assay interference chemotypes.[47] Upon 2 hr treatment, **ferroptocide** did not display notable reactivity towards GSH even at 50 fold excess (**Fig. 2.12.A**). Time-course monitoring of **GSH-ferroptocide** adduct formation in a separate experiment, revealed that **ferroptocide** reacts relatively slow with glutathione over the course of 24 hr (30% remaining compound after 24 hr as shown in **Table 2.2.**). The highly electrophilic iodo analogue (**P23**) reacted immediately, while the less electrophilic dichloro analogue (**P25**) was non-reactive (**Fig. 2.12. B, C** respectively). These findings are consistent with the suspected S_N2-type reactivity as showcased during the SAR studies. Due to favorable selectivity and reactivity results, **ferroptocide** was prioritized for mode of action studies.

Table 2.2. Reactivity of ferroptocide with glutathione in a time-course LC/MS experiment.

Time (hr)	GSH-Ferroptocide Adduct %
0.5	4.9
1	18.2
2	33.2
3	38.1
24	72.5

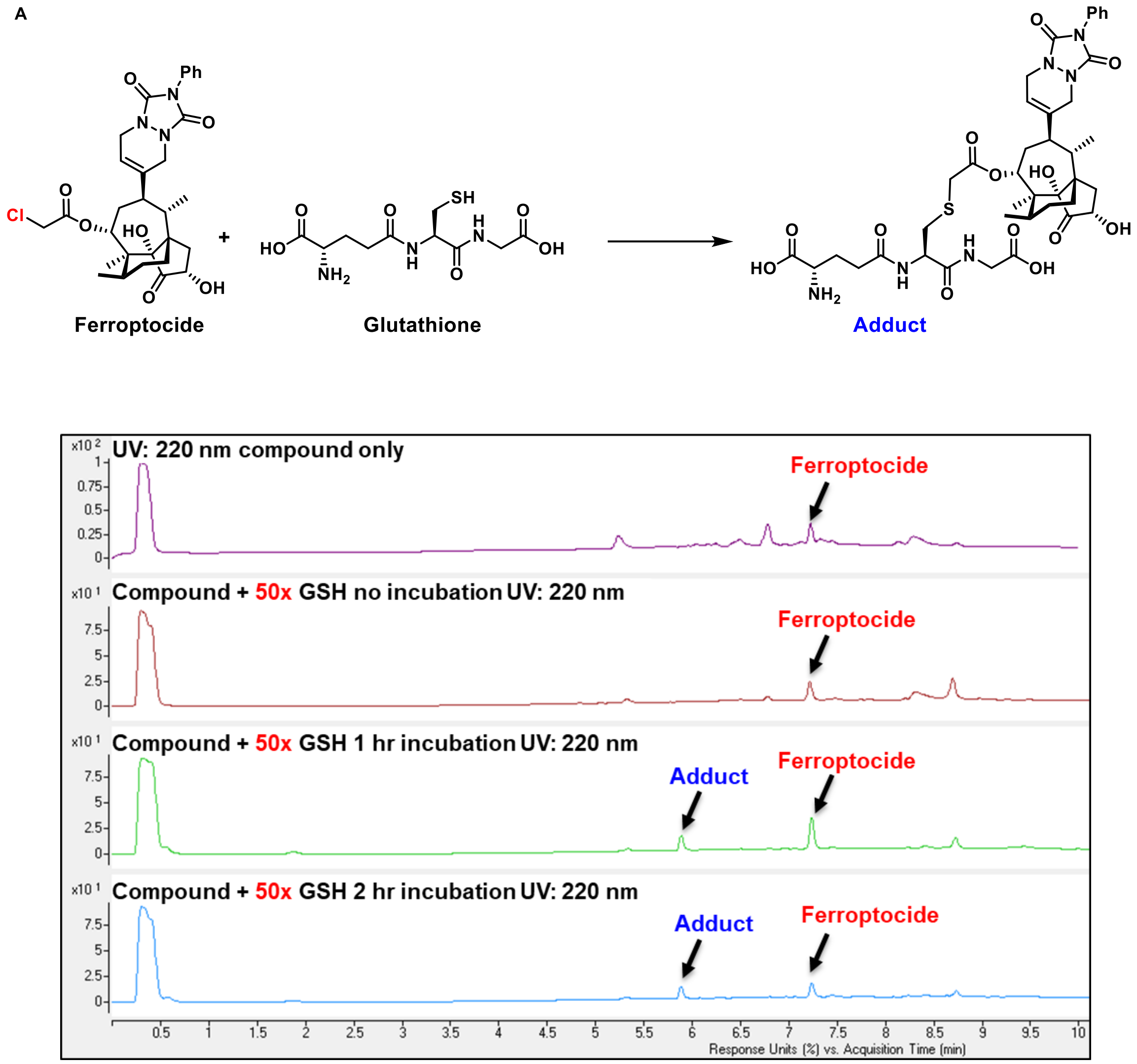

Figure 2.12. (cont.)

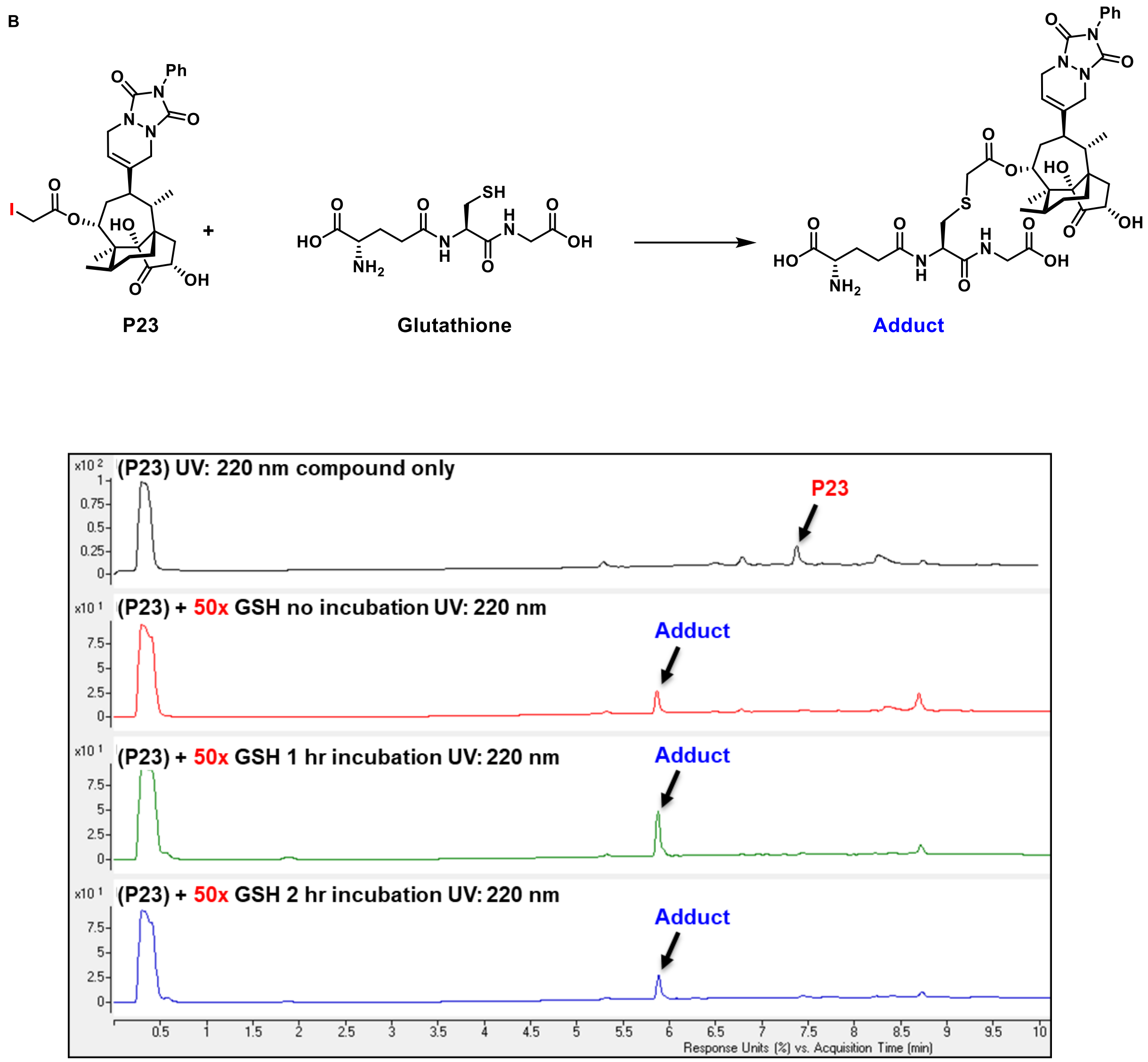

(P23) UV: 220 nm compound only

(P23) + 50x GSH no incubation UV: 220 nm

(P23) + 50x GSH 1 hr incubation UV: 220 nm

(P23) + 50x GSH 2 hr incubation UV: 220 nm

Figure 2.12. (cont.)

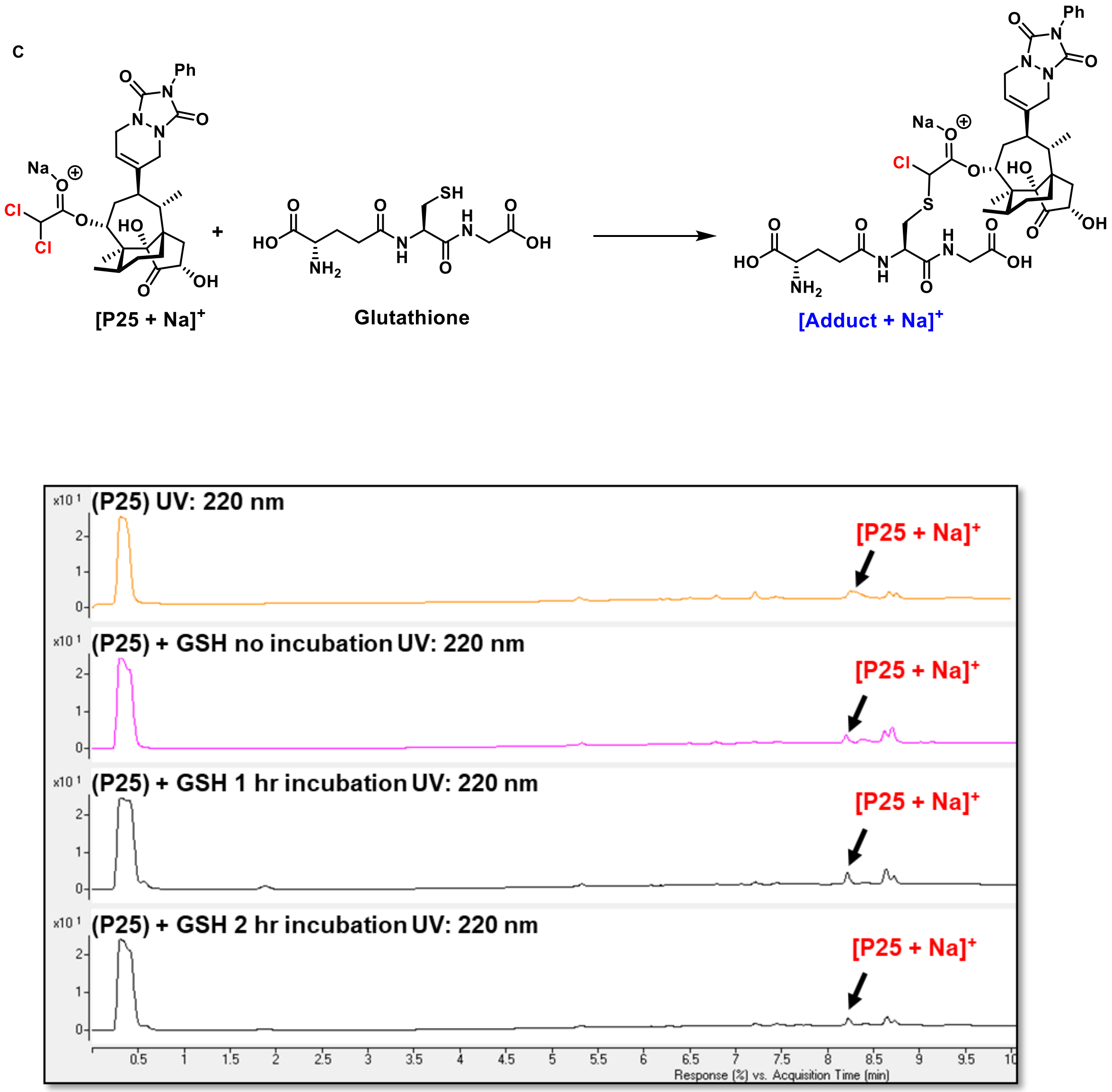

Figure 2.12. A–C. Monitoring the reactivity of 100 µM **ferroptocide**, **P23**, and **P25** respectively with 5 mM GSH at 37°C in PBS using an LC/MS-based method. **Ferroptocide** reacted at a slow rate, **P23** reacted immediately, while **P25** was completely non-reactive as suspected from S_N2 reactivity of the α-ester moiety.

2.5 Assessing hemolysis of compounds of interests

Ability of compounds to induce red blood cell lysing, also known as hemolysis, is a major safety hurdle for translation of compounds into the clinic as it is suggestive of broad cytotoxicity. Therefore, early in the discovery process, potential drug leads are rigorously assessed for their hemolytic ability to avoid investment of time and resources on risky compounds. To monitor hemolysis of compounds of interest, **P4** and **ferroptocide** were assessed in an *in vitro* assay using freshly purchased human blood. Both compounds did not induce lysing of red blood cells at 333 µM, as shown in **Fig. 2.13** suggesting therapeutic relevance and lack of broad toxicity. Further investigation of toxicity in animals (e.g. mice) must be performed to support these findings.

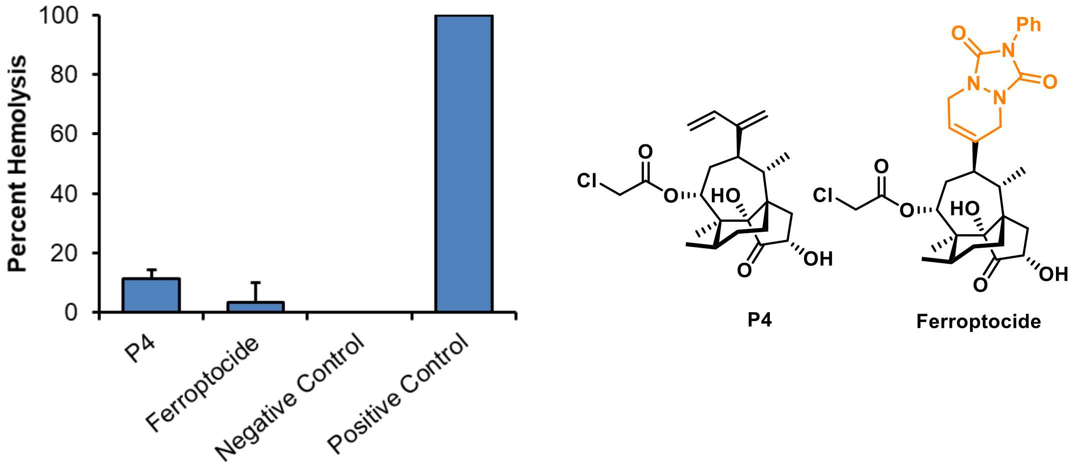

Figure 2.13. Assessment of the hemolytic ability of **P4** and **ferroptocide** at 333 µM. These compounds are non-hemolytic suggesting lack of broad toxicity. DMSO in water was used as a positive control and DMSO in red blood cell buffer was a negative control.

2.6 Compound activity in a panel of cell lines

Immortalized mammalian cancer cells are the workhorse of cancer research, and yet they are often poor surrogate models of cancer. They are susceptible to genetic variations (e.g. somatic mutations, chromosomal aberrations, etc.) and are neither clonal nor genetically stable.[52] A recent study investigated different types of commonly used breast cancer cells, MCF7, from 27 different sources and upon comprehensive sequencing identified rapid genetic discrepancies due to positive clonal selection sensitive to cell culture conditions.[52] Primary cancer cells on the other side are a more relevant testing model, but they are difficult to access as Institutional Review Board (IRB) approval and patient consent is needed; additionally, they are challenging to isolate and susceptible to contamination. A successful collaboration with oncologists at Carle Foundation hospital enabled access to multiple metastatic cancer patient biopsies and establishment of primary cancer cell lines temporarily.

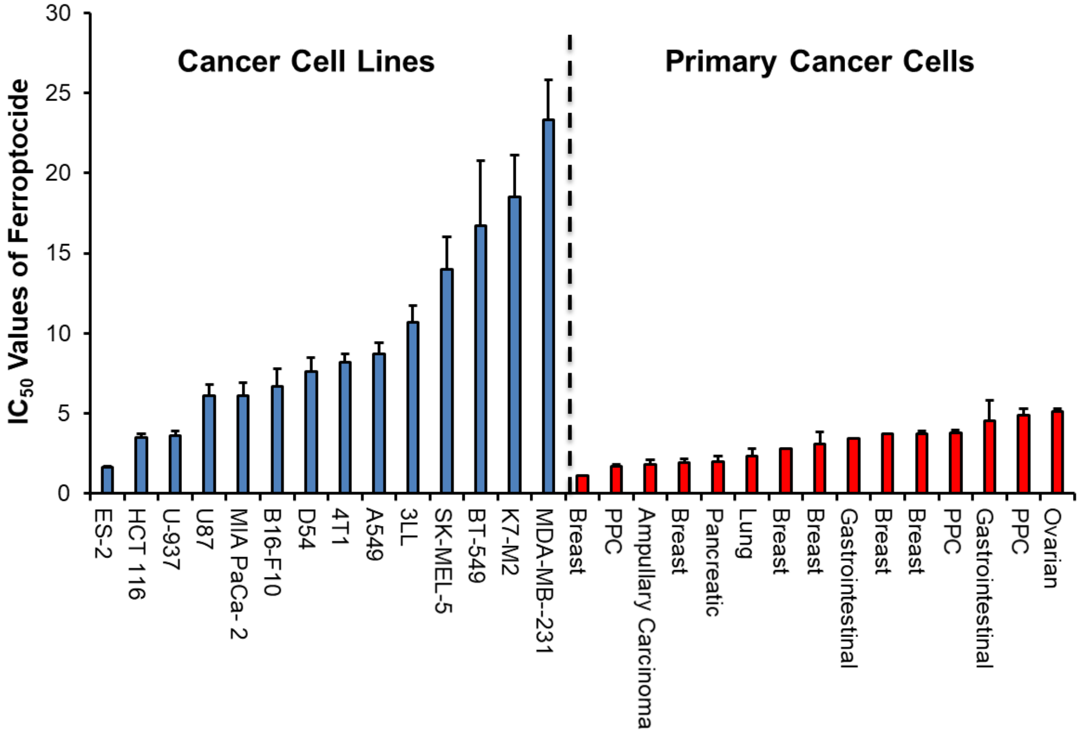

Figure 2.14. Ferroptocide displays broad activity (μM) in a 72 hr cell viability assay in immortalized cancer cells and in primary cells isolated from metastatic cancer patients. PPC: primary peritoneal carcinomas. Data represent the mean ± s.e.m., n≥3.

Evaluation of **ferroptocide** in a panel of cancer cell lines and primary cancer cells revealed broad activity across different types of cancer with an IC_{50} range of 1.6–24 μM for immortalized cancer cell lines and 1–5 μM for primary cancer cells obtained from metastatic patients, as shown in **Figure 2.14**. Interestingly, **ferroptocide** was more active in primary cancer cells than in immortalized cell lines supporting the therapeutic relevance of this lead compound. Such results inspired comparison studies of **ferroptocide** with FDA-approved drugs (5-FU, cisplatin, etoposide) and clinical drug candidate (PAC-1), which demonstrated a more active anticancer profile for **ferroptocide** than the other drugs in a 72 hr assay (**Fig. 2.15**).

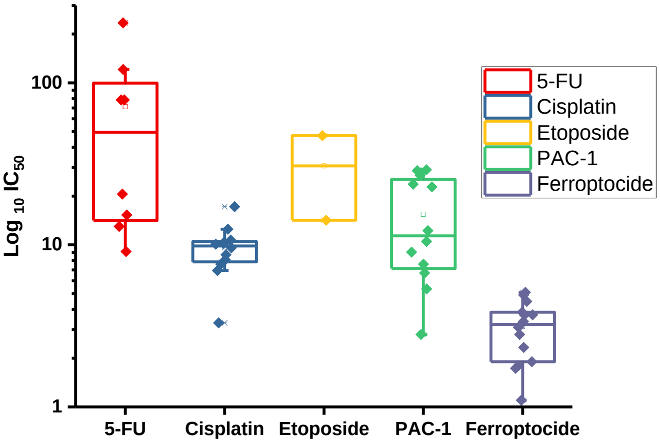

Figure 2.15. Effect of ferroptocide and approved and experimental chemotherapeutics (5-FU, Cisplatin, Etoposide, PAC-1) in primary patient-derived cells in a 72 hr cell viability Alamar Blue assay. Cells tested are those shown in **Fig. 2.14**. Data represent the mean ± s.e.m., n≥3.

2.7 Mode of action studies

2.7.1 Ferroptocide speed of cell death

In order to gain insights into the mode of anticancer activity, the speed of cell death of **ferroptocide** was compared to other approved chemotherapeutics and tool compounds with well-defined mechanisms including: procaspase-3 activators (PAC-1, 1541B),[53] nucleoside analogues (gemcitabine, 5-FU), DNA alkylators (MNNG, mitomycin C), topoisomerase inhibitors (etoposide, camptothecin, cycloheximide), ROS inducing agents (anitimycin A, IB-

DNQ,[54] rotenone), broad-spectrum kinase inhibitor (staurosporine), microtubule stabilizer (taxol), proteasome inhibitor (bortezomib), and a rapid apoptosis-inducing agent (Raptinal).[55] Cell death induced by **ferroptocide** was rapid in multiple cell lines derived from diverse cancer types, with a time to 50% cell death of 1 hour in ES-2 cells, (**Fig. 2.16 A**), 1.5 hr in Mia PaCa-2 (**Fig. 2.14B**), 7 hr in HCT 116 (**Fig. 2.16C**), and 7 hr in 4T1 (**Fig. 2.16D**). As the speed of cell death induced by **ferroptocide** was faster than the most rapid proapoptotic agent known (Raptinal), it was suspected to induce non-apoptotic cell death.

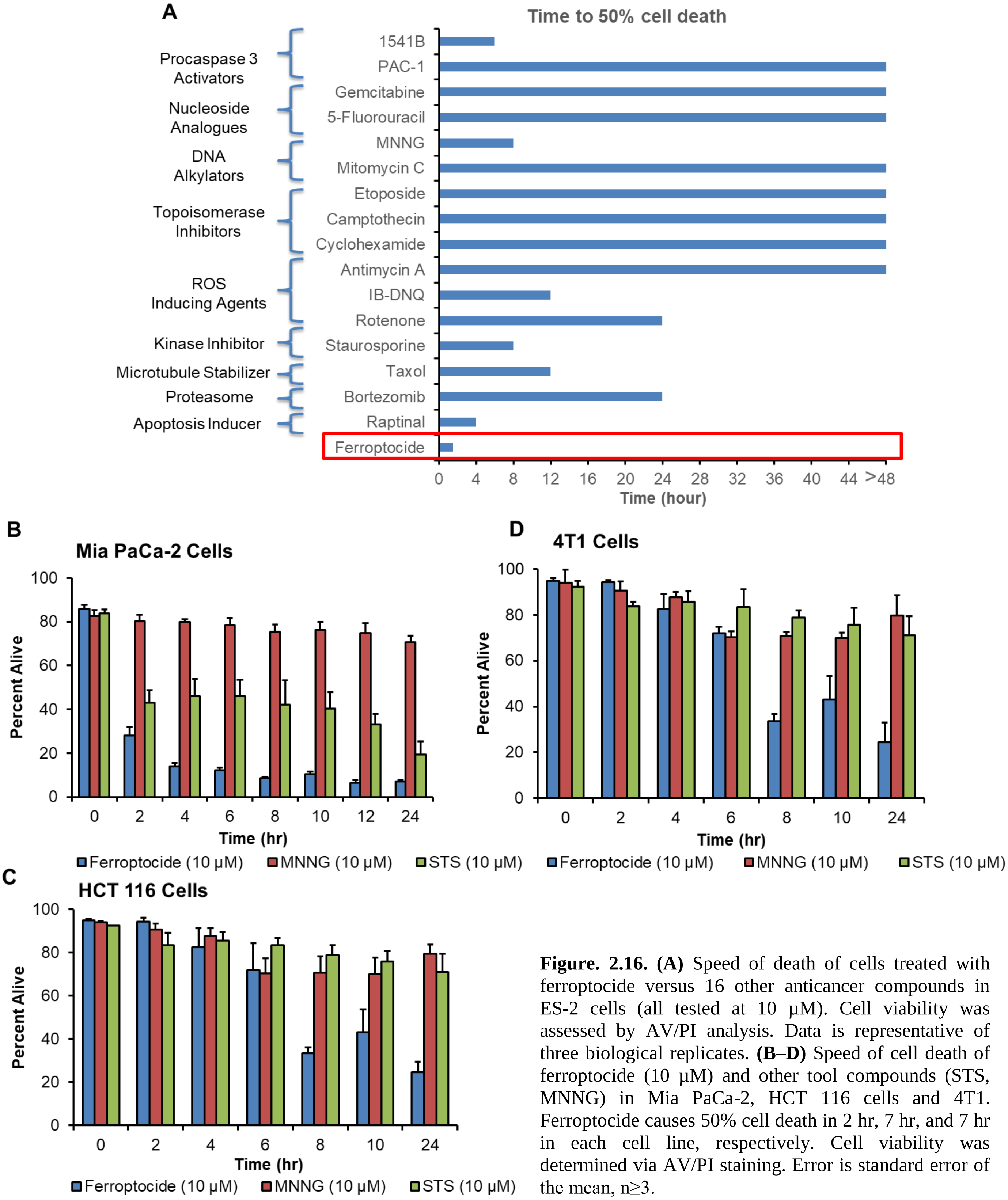

Figure. 2.16. (A) Speed of death of cells treated with ferroptocide versus 16 other anticancer compounds in ES-2 cells (all tested at 10 µM). Cell viability was assessed by AV/PI analysis. Data is representative of three biological replicates. **(B–D)** Speed of cell death of ferroptocide (10 µM) and other tool compounds (STS, MNNG) in Mia PaCa-2, HCT 116 cells and 4T1. Ferroptocide causes 50% cell death in 2 hr, 7 hr, and 7 hr in each cell line, respectively. Cell viability was determined via AV/PI staining. Error is standard error of the mean, n≥3.

2.7.2 Ferroptocide is non-apoptotic

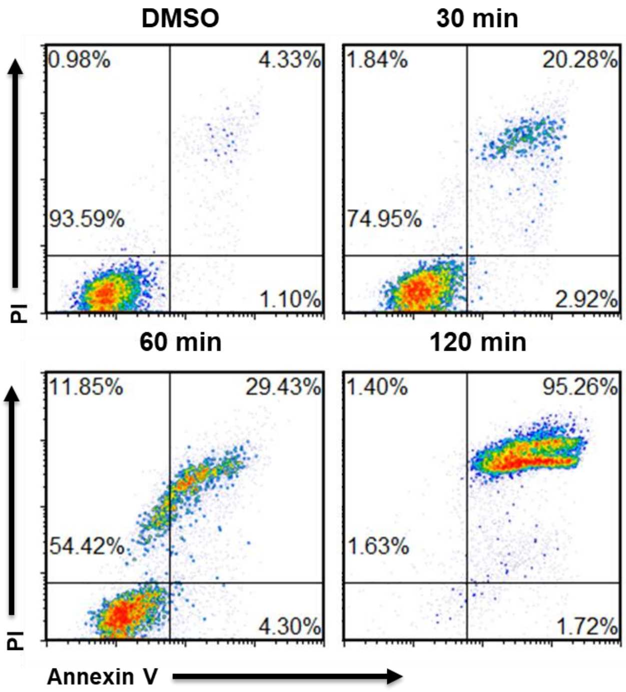

Figure 2.17. Time-course analysis of ES-2 cell viability upon treatment with ferroptocide (10 μM) indicates a non-apoptotic mode of cell death. AV/PI graphs are representative of three biological replicates.

To assess for early events of apoptosis, exposure of phosphatidylserine (PS) on the outer leaflet of the plasma membrane is monitored via flow cytometry using FITC-Annexin V and propidium iodide (PI) staining. Apoptotic cells are those that stain positive for FITC-Annexin V and negative for propidium iodide. Time course analysis of cells treated with **ferroptocide** followed by Annexin V/PI staining suggested a non-apoptotic mode of cell death as observed in **Figure 2.17**. The live cell population (FITC-Annexin V negative, PI-negative) migrates diagonally across the four quadrants instead of through the canonical apoptotic pathway. To further support these findings, protection experiments with the pan-caspase inhibitor Q-VD-OPh were performed. As shown in **Figure 2.18 A,B** Q-VD-OPh protects ES-2 and HCT 116 cells against the effect of the positive control Raptinal but has no effect against **ferroptocide**-induced cell death.

Additionally, cleavage of PARP-1 by caspase-3 is a common feature of apoptotic compounds in cells. Such marker was seen in Raptinal-treated ES-2 and HCT 116 cells but not in **ferroptocide**-treated cells as displayed by western blot analysis in **Figure 2.18 C** and **D**, respectively, suggesting non-apoptotic activity for our lead compound.

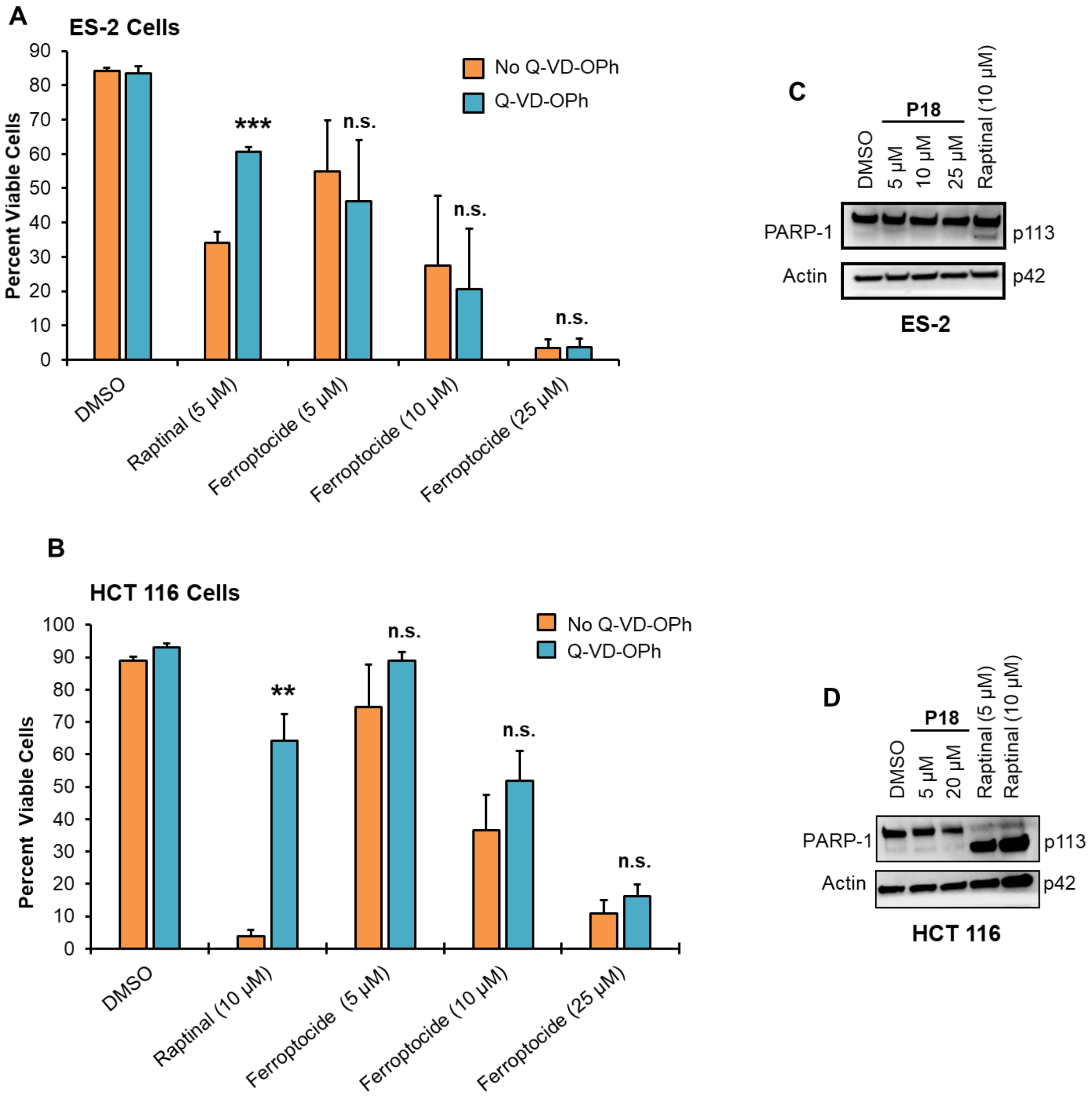

Figure 2.18. (A–B) Effect of pre-treatment with Q-VD-OPh (25 µM) for 2 hr followed by dose-response treatment with ferroptocide or positive control Raptinal (5 or 10 µM) for 13 hr in ES-2 and HCT 116 cells. Data are plotted as the mean ± s.e.m., n=3 biological replicates. *** $0.0001 \leq p < 0.001$, n.s. not significant. **(C–D)** Immunoblots of ES-2 and HCT 116 cells indicate no PARP-1 cleavage after 1 hr and 7 hr treatment (respectively) with ferroptocide (**P18**). The positive control, Raptinal, induces PARP-1 cleavage in both cell lines.

As further confirmation, cell morphological changes induced by **ferroptocide** and the positive control staurosporine (STS) were examined using transmission electron microscopy (TEM). Cells treated with **ferroptocide** exhibit none of the characteristics of apoptosis such as membrane blebbing, chromatin condensation, nuclear fragmentation, reduction of cellular volume, or rounding of the cell (**Fig. 2.19**).[56] Taken together, these data indicate that **ferroptocide** induces rapid, non-apoptotic cell death. As compounds with such a mode of cell death can have unique properties and advantages in vivo,[57-59] further elucidation of the mechanism of cell death of **ferroptocide** was of interest.

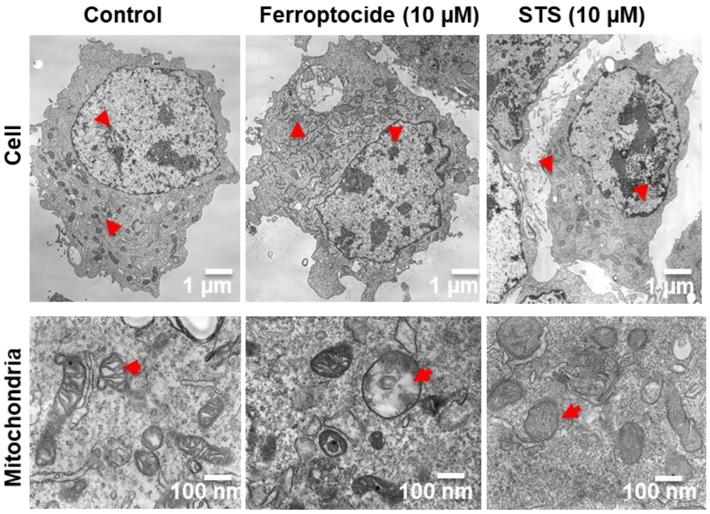

Figure 2.19. Transmission electron micrographs of ES-2 cells treated with DMSO (left), ferroptocide (10 μM, center) or staurosporine (STS, 10 μM, right) for 30 min. The images show lack of apoptotic morphological features and swelling of mitochondria upon ferroptocide treatment (red arrows) versus controls. TEM data are representative images.

2.7.3 Ferroptocide co-localizes to mitochondria

The TEM images (**Fig. 2.19**) reveal mitochondrial swelling as early as 30 minutes after **ferroptocide** treatment suggesting mitochondrial dysfunction due to compound treatment. To investigate this hypothesis, subsequent confocal microscopy

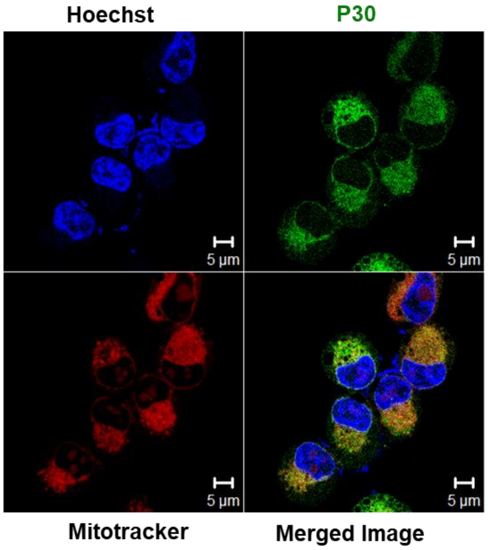

Figure 2.20. Co-localization analysis of ferroptocide with mitochondria. ES-2 cells were stained with MitoTracker Red (100 nM) followed by 30 min treatment with fluorescent analogue **P30** (10 μM). Nucleus was stained with Hoechst. Yellow dots indicate **P30** (green) on the mitochondria (red) in merged images.

experiments were conducted. These studies supported the prior TEM findings as the fluorescent analogue **P30** was found to co-localize with the Mitotracker dye in cells (**Fig. 2.20**). Localization of compounds to certain organelles can be informative when determining the mechanism of a compound. These data indicate a mitochondrial-based activity of **ferroptocide** directing our attention towards mitochondria for more in depth-mechanistic studies.

2.7.4 Ferroptocide induces cellular ROS formation

Mitochondria are an important source of reactive oxygen species (ROS), which can contribute to oxidative damage to mitochondrial proteins, membranes, DNA and redox signaling in mammalian cells.[60] Production of ROS in mitochondria can result in impairment of their synthesis of ATP and various metabolic processes such as tricarboxylic cycle, fatty acid oxidation, the urea cycle, amino acid metabolism, heme synthesis, and FeS center assembly. Other effects of mitochondrial ROS include release of cytochrome c to the cytosol via the mitochondria outer membrane permeabilization (MOMP) and activation of the apoptotic machinery, induction of mitochondrial

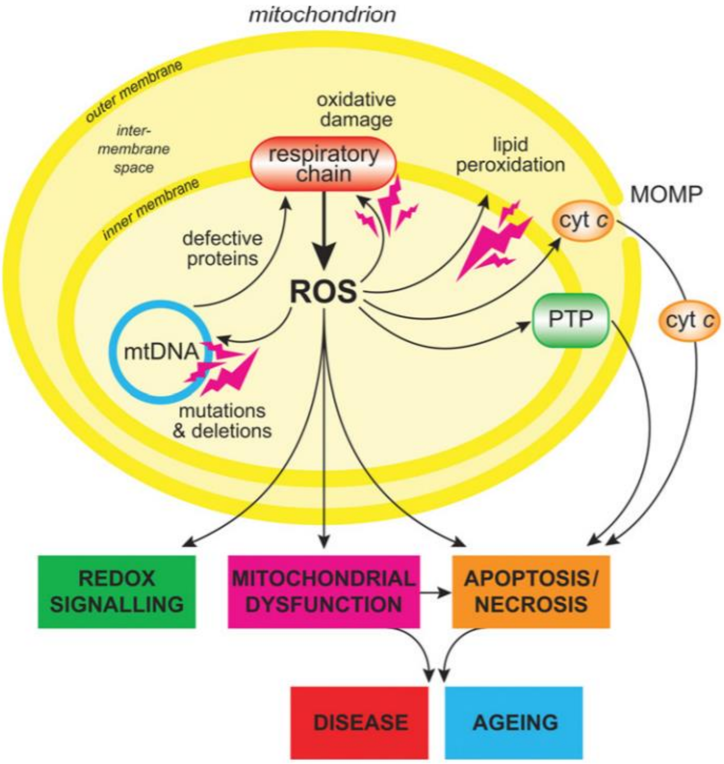

Figure 2.21. Mitochondrial ROS leads to oxidative damage of mitochondrial proteins, lipids, DNA, modulation of signaling pathways, and pathologies. Images from Murphy and coworkers.[50]

permeability transition pore (PPT) that increases susceptibility to ischemia and reperfusion injury, and modulation of redox signaling as shown in **Figure 2.21**. [61]

2.7.4.1 Ferroptocide causes ROS

Given the importance of reactive oxygen species (ROS) generation in mitochondria, ROS levels were monitored upon compound treatment using a ROS probe, carboxy-H_2CMFDA. Dose-dependent ROS production was observed in ES-2 (**Fig. 2.22A**) and HCT 116 cells treated with **ferroptocide** (**Fig. 2.22B**), similar to the positive control, *tert*-butyl hydroperoxide (TBHP) suggesting induction of oxidative cell death. To further investigate this hypothesis, protection studies with *N-acetylcysteine* (NAC-1) and a lipophilic antioxidant, trolox, were conducted in ES-2, HCT 116 cell lines as well as A549 lung cancer cells (**Fig. 2.23 A–E**).

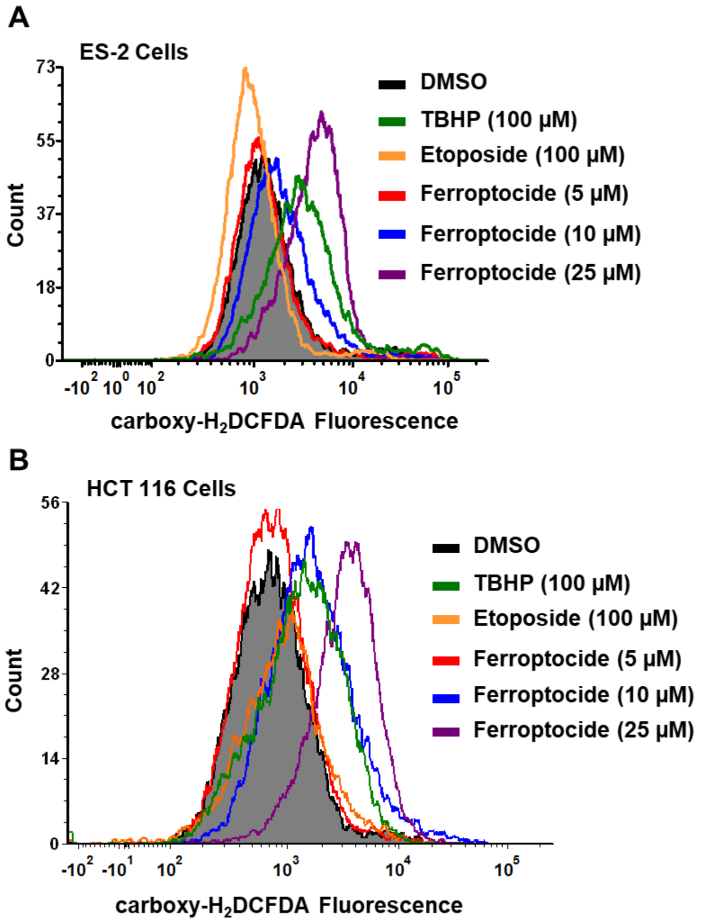

Figure 2.22. (A–B) Ferroptocide induces dose-dependent ROS generation within 1 hr similar to positive control TBHP in ES-2 and in HCT 116 cells respectively. DMSO and etoposide were included as negative controls. Data are representative of three independent experiments.

2.7.4.2 Antioxidant protection studies

As shown in **Figure 2.23.** both antioxidants (NAC-1 and Trolox) significantly rescue cancer cells upon dose-dependent treatment with **ferroptocide** (10, 25, 50 µM). A similar observation is made upon treatment with the positive control TBHP, while pre-treatment of cells with these antioxidants did not protect them against the apoptotic agent, Raptinal. These data are suggestive of a type of oxidative cell death induced by **ferroptocide**, requiring further investigation.

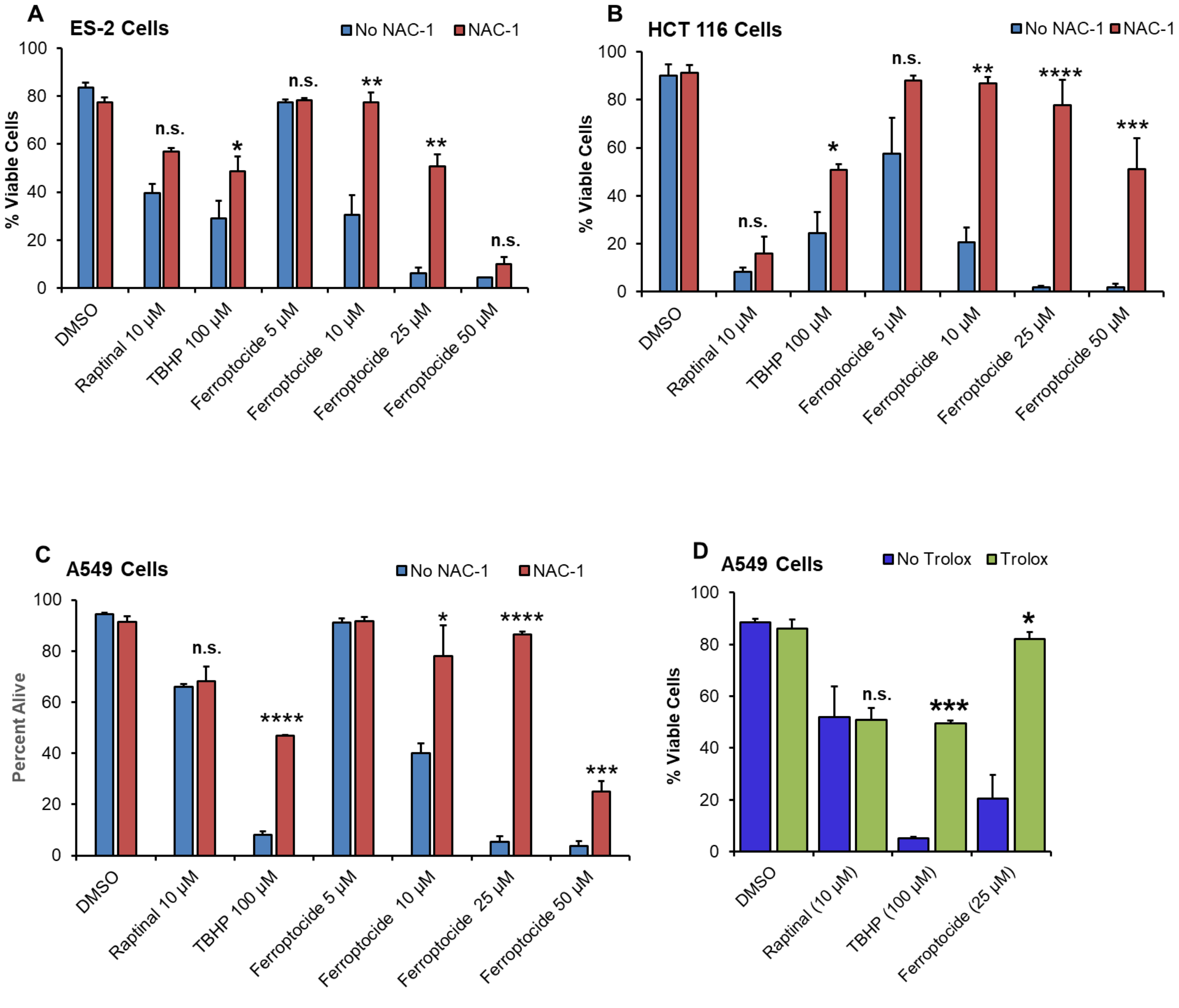

Figure 2.23 (cont.)

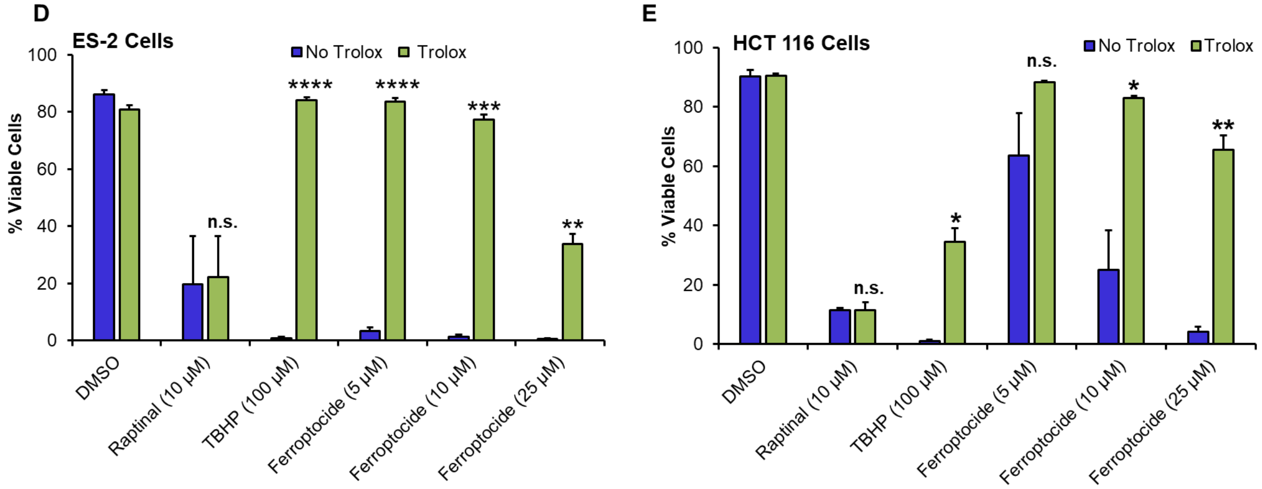

Figure 2.23. Antioxidant probes rescue cells from ferroptocide-induced cell death. NAC-1 (5 mM, 1 hr pre-treatment) protects cells from **ferroptocide** treatment for 24 hr in (**A**) ES-2, (**B**) HCT 116 and (**C**) A549 cells. (**D–F**) Lipophilic antioxidant Trolox (250 µM) rescues A549, ES-2, and HCT 116 cells from ferroptocide-induced cytotoxicity after 12, 14, and 10 hr incubation respectively. Data are plotted as the mean ± s.d., n=3 biological triplicates. **** $p < 0.0001$, *** $0.0001 \leq p < 0.001$, ** $0.001 \leq p < 0.01$, *$0.01 \leq p < 0.05$, n.s. $p > 0.05$.

2.7.5 Ferroptocide is a pro-ferroptotic agent

2.7.5.1 Ferroptocide induces lipid ROS

As described in chapter one of this thesis, one non-apoptotic mode of cell death that depends on production of lethal levels of iron-dependent lipid ROS is ferroptosis, a regulated process with distinct morphological, biochemical, and genetic characteristics.[62-66] The hallmarks of ferroptosis include generation of lipid hydroperoxides and cytoprotection by lipophilic antioxidants (trolox, butylated hydroxyltoluene [BHT]), ferroptosis inhibitors (ferrostatin-1, liproxstatin), and iron chelators (deferoxamine [DFO], ciclopirox olamine [CPX]).[62] Cellular effects of **ferroptocide**-induced ROS were investigated using a C11-BODIPY probe that detects lipid peroxidation.[63] **Ferroptocide** induces lipid ROS in ES-2 cells (**Fig. 2.25 A**), HCT 116 (**Fig. 2.25 B**), and 4T1 cells (**Fig. 2.25 C**) similar to known ferroptosis inducer, (1S,3R)-RSL3 (hereafter RSL3, **Fig. 2.24**)[67]; DFO pre-treatment of ES-2, HCT 116, and 4T1 cells protected them from **ferroptocide-** and RSL3-induced lipid ROS.

2.7.5.2 Protection studies with ferrostatin-1 and DFO

Given that generation of continuous lipid ROS is a functional requirement of ferroptosis,[62,63] additional experiments were performed to elucidate if ferroptosis was triggered by **ferroptocide**. Protection studies were conducted with ferrostatin-1 and DFO, and these inhibitors significantly protected against **ferroptocide**-induced cell death in ES-2, HCT 116, 4T1, and A549 cancer cells (**Fig. 2.26 A–E**, respectively). Additionally, these inhibitors rescued cells from the known ferroptosis inducers erastin (**Fig. 2.26 A–B**) and RSL3 (**Fig. 2.26 C–F**) respectively, while displaying no protection against Raptinal, an apoptosis-inducing agent. Taken together, these studies indicate that iron-dependent accumulation of lipid peroxidation (ferroptosis) upon **ferroptocide**-treatment is the cause of cell death.

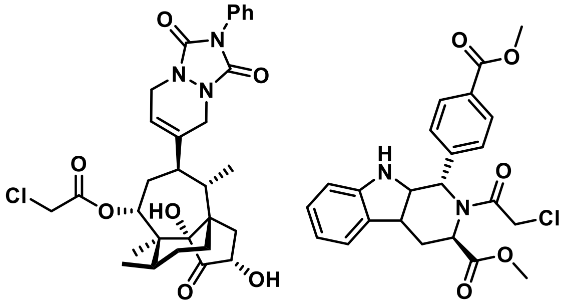

Ferroptocide
Lead Compound

RSL3
inducer of ferroptosis

Figure 2.24. Chemical structures of pro-ferroptotic tool compounds.

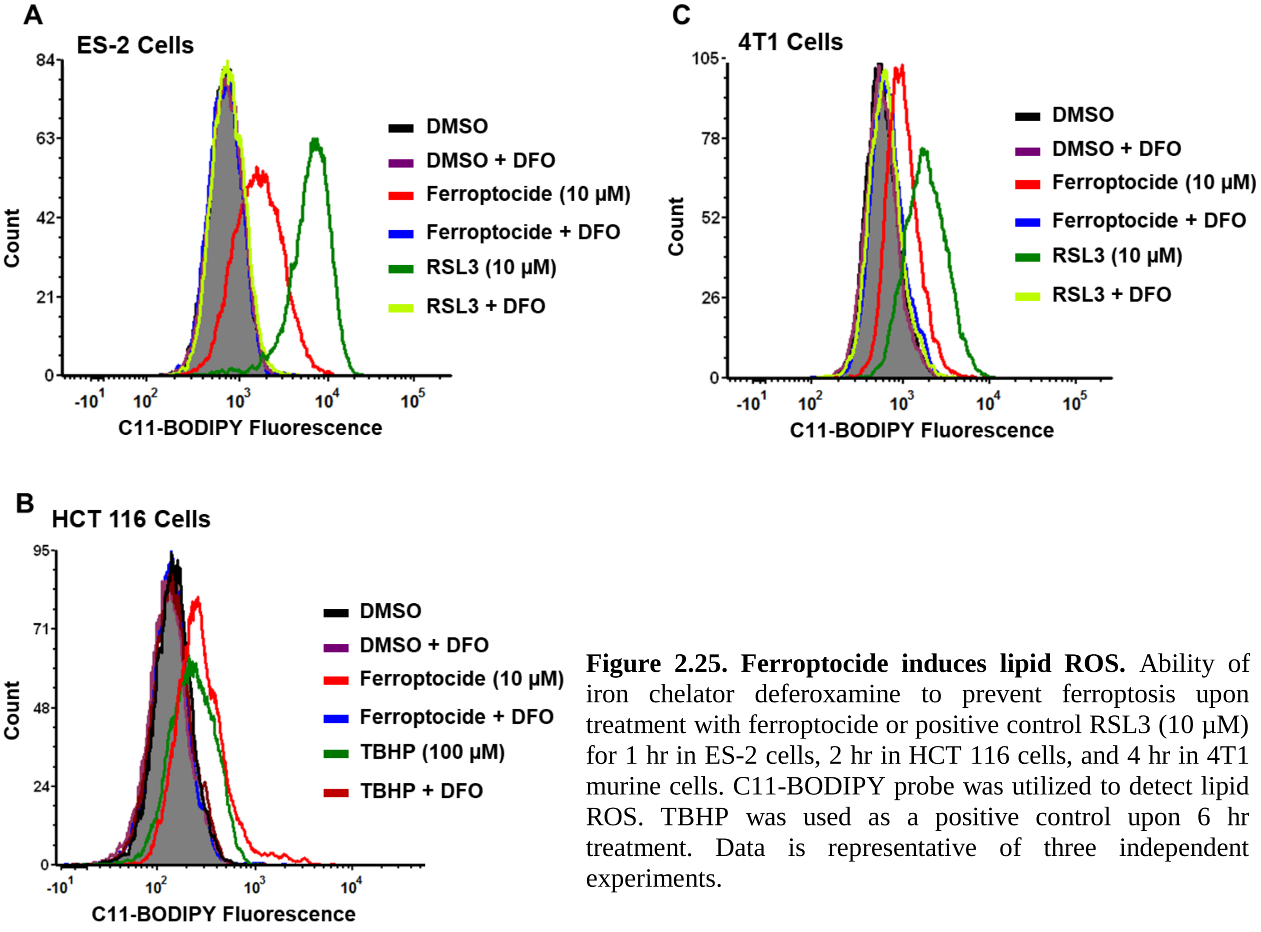

Figure 2.25. Ferroptocide induces lipid ROS. Ability of iron chelator deferoxamine to prevent ferroptosis upon treatment with ferroptocide or positive control RSL3 (10 μM) for 1 hr in ES-2 cells, 2 hr in HCT 116 cells, and 4 hr in 4T1 murine cells. C11-BODIPY probe was utilized to detect lipid ROS. TBHP was used as a positive control upon 6 hr treatment. Data is representative of three independent experiments.

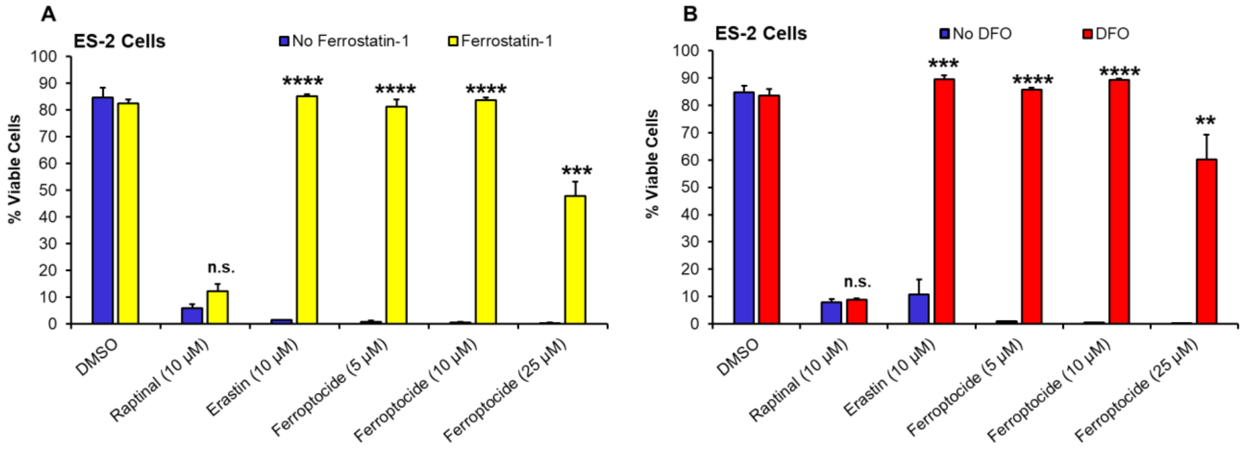

Figure 2.26 (cont.)

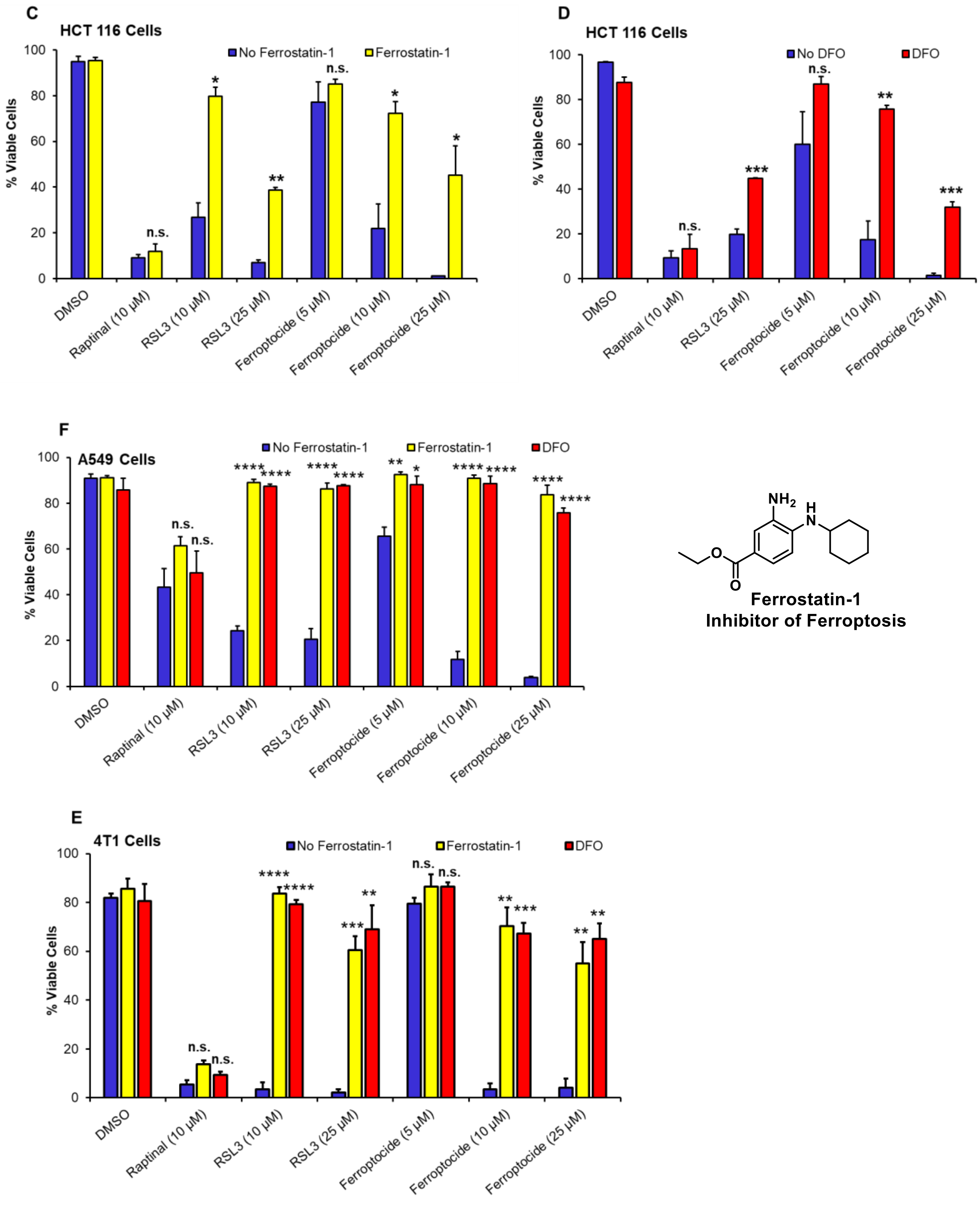

Figure 2.26. Ferroptocide is a ferroptotic agent. (A, C, E, F). Ability of ferroptosis inhibitor, ferrostatin (2 µM), to protect cells against ferroptocide treatment after 14 hr in ES-2, 24 hr in HCT 116, 18 hr in 4T1, and 12 hr in A549 cells respectively. **(B, D, E, F).** Effect of ferroptosis inhibitor, deferoxamine (100 µM) on viability of ES-2 cells, HCT 116, 4T1, and A549 cells after 14, 24, 18, 12 hr incubation with ferroptocide and erastin (positive control) respectively. Data are plotted as the mean ± s.d., n=3 biological triplicates. **** $p < 0.0001$, *** $0.0001 \leq p < 0.001$, ** $0.001 \leq p < 0.01$, *$0.01 \leq p < 0.05$, n.s. $p > 0.05$.

2.7.5.3 Head-to-head comparisons with Erastin and RSL3

Erastin and RSL3 were originally discovered as small molecules with RAS-selective lethality.[63] However, in our hands, the use of these tool compounds as positive controls for the ferroptosis studies described above revealed inconsistencies depending on the cell line. We set out to investigate the robustness of these compounds and ferroptocide. Monitoring the speed of cell death of **ferroptocide** versus erastin and RSL3, in HCT 116 and A549 cell lines (containing oncogenic K-RAS), demonstrates that **ferroptocide** is a fast-acting, robust pro-ferroptotic agent causing more quantitative cell death than the other two tool compounds (**Fig. 2.27**). This suggests that ferroptocide is a practical pro-ferroptotic tool compound that can be used reliably regardless of the cell line type.

Additionally, treatment of HCT 116 cells with the same concentration of **ferroptocide**, RSL3, and erastin results in generation of similar levels of lipid ROS upon **ferroptocide** and RSL3 treatment and a larger quantity compared to erastin-treatment, suggesting a rapid onset of lipid peroxidation for **ferroptocide** and RSL3 compounds (**Fig. 2.28**).

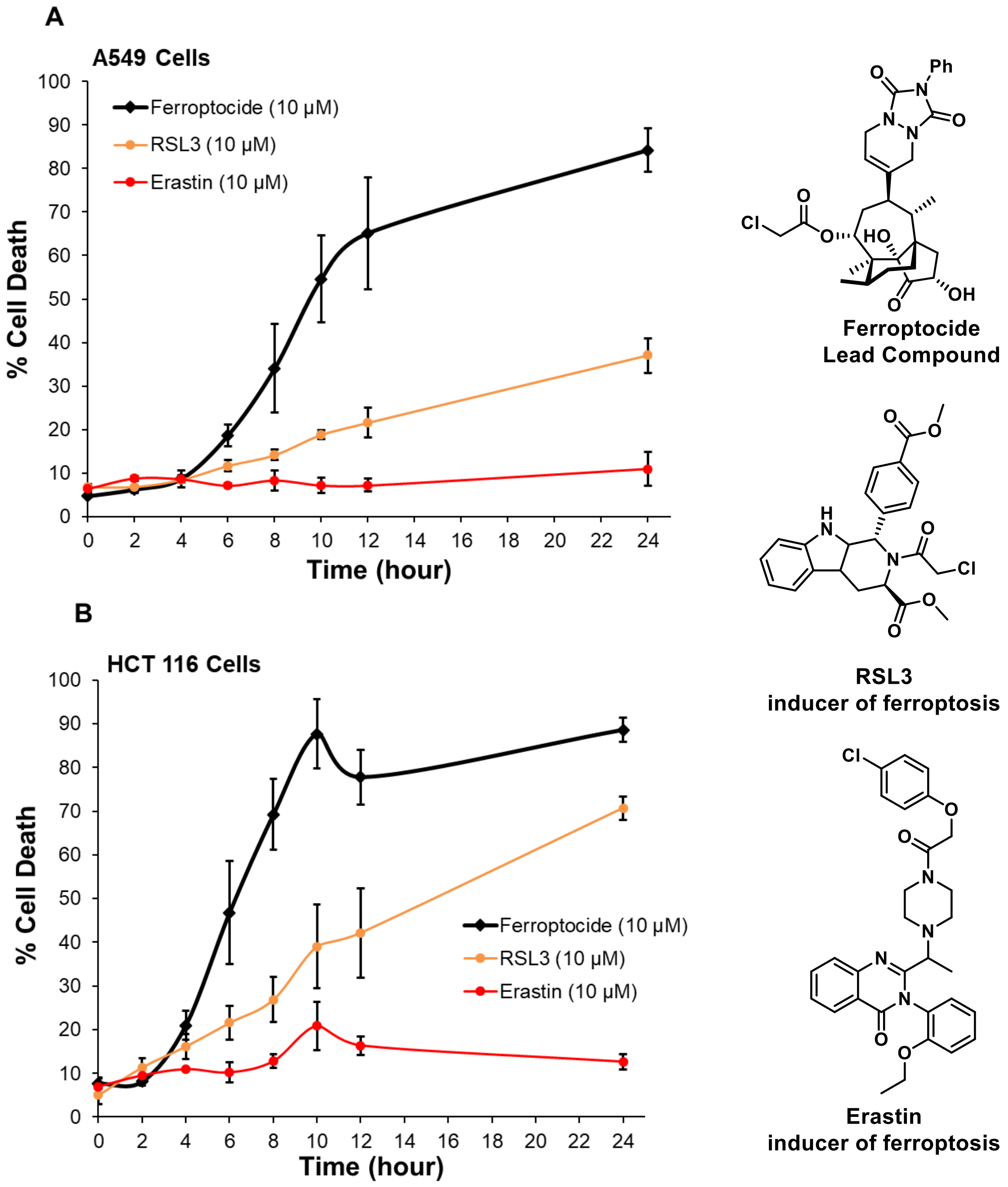

Figure 2.27. A–B. Ferroptocide is a robust pro-ferroptotic agent. Comparison of speed of cell death of ferroptocide, RSL3, and erastin, each at (10 μM) in HCT 116 and A549 (K-RAS mutant cell lines) respectively. Cell viability was determined with AV/PI staining. Data are plotted as the mean ± s.e.m., n=3 biological replicates.

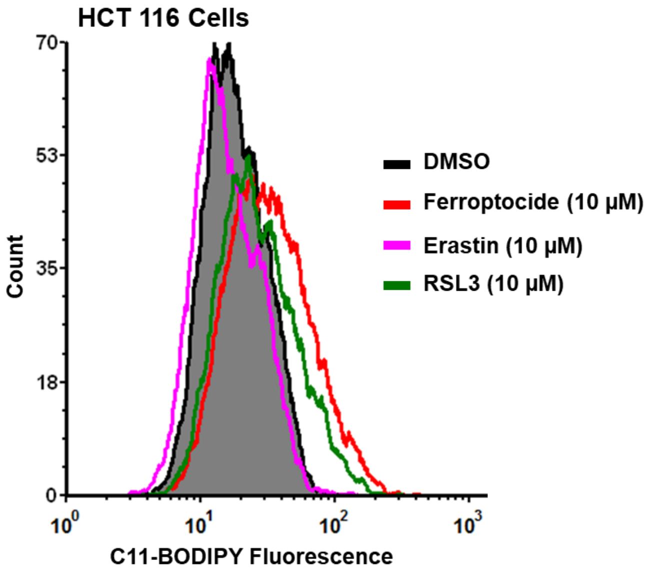

Figure 2.28. Generation of lipid ROS in HCT 116 cells upon 2 hr treatment using C11-bodipy probe for detection, n=3 biological replicates. DMSO is used as a negative control.

2.7.5.4 RNA-seq studies with Ferroptocide

Genetic methods for target identification and validation are increasingly incorporated in drug discovery projects due to the unparalleled advances in RNA interference (RNAi),[68] si/shRNA screens[69], and CRISPR Cas technologies.[70,71] One key advantage of utilizing RNA sequencing to investigate compound-induced changes at the transcript level is the lack of chemical modification needed for the compound of interest. The ability to receive a snapshot of genetic modulations occurring at the transcript level upon compound treatment is extremely powerful and can guide target discovery efforts as demonstrated for the polo-like kinase 1 (PLK1) inhibitor BI 2356. HCT 116 compound-resistant clones were sequenced and compared to the parental line to reveal PLK1 gene as the main gene mutated in more than one group with specific mutations at the BI 2356 binding site.[72]

We set out to monitor the effect of **ferroptocide** at the transcript level using genomic methods. RNA-seq data of **ferroptocide**-treated cells revealed that 35/40 genes involved in ferroptosis are modulated after 6 hr treatment in HT-29 colon cancer cells with false discovery rate (FDR) scores ≤ 0.05 (**Fig. 2.29 A**). This time point was selected to capture the primary mechanisms of the compound of interest on viable cells as described previously.[73] HT-29 cell viability was assessed via AV/PI analysis upon **ferroptocide**-treatment (**Fig. 2.29 B**).

Specific genes such as GCLC (3.5 fold), GCLM (4.9 fold), SLC7A11 (8.1 fold), and CHAC1 (9.8 fold), known to be upregulated in ferroptosis,[62,74] and AFT3 (11.5 fold), DDIT3 (22.5 fold), DDIT4 (11.3 fold), known to be upregulated upon ferroptosis were significantly overexpressed after **ferroptocide**-treatment, similar to RNA-seq results previously reported for erastin in HT-1080 cells.[74] Pathways affected by oxidative stress such as Keap1-Nrf2 ($p=7.8\ 10^{-10}$), unfolded protein response ($p=3.6\ 10^{-8}$), protein processing in endoplasmic reticulum ($p=2.4\ 10^{-10}$), amino acid transmembrane transporter activity ($p=1.7\ 10^{-5}$), and others were also modified upon compound treatment (**Fig. 2.30 A, B**). A detailed list of the top 30 upregulated genes and top 25 downregulated genes can be found in the general methods of this chapter (**Table S1, S2** respectively). These transcription profiles further support the hypothesis that **ferroptocide** induces oxidative stress and ferroptosis.

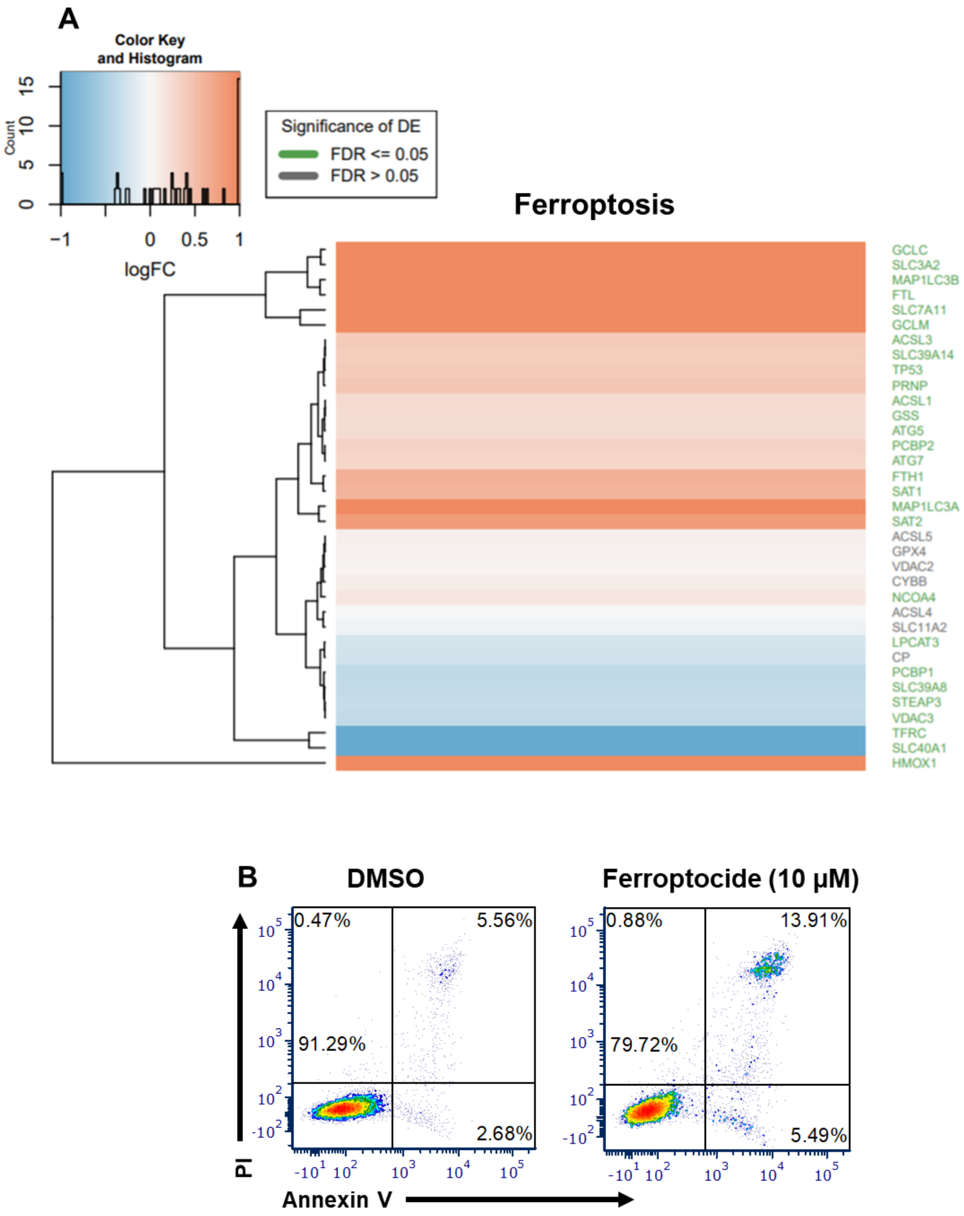

Figure 2.29. (A) Modulation of 35/40 genes involved in ferroptosis upon 6hr treatment of HT29 cells with 10 µM ferroptocide (FDR ≤ 0.05). **(B)** AnnexinV/PI graphs of HT-29 cells treated with ferroptocide (10 µM) for 6 hr. RNA of these cells was isolated and used for RNA seq data.

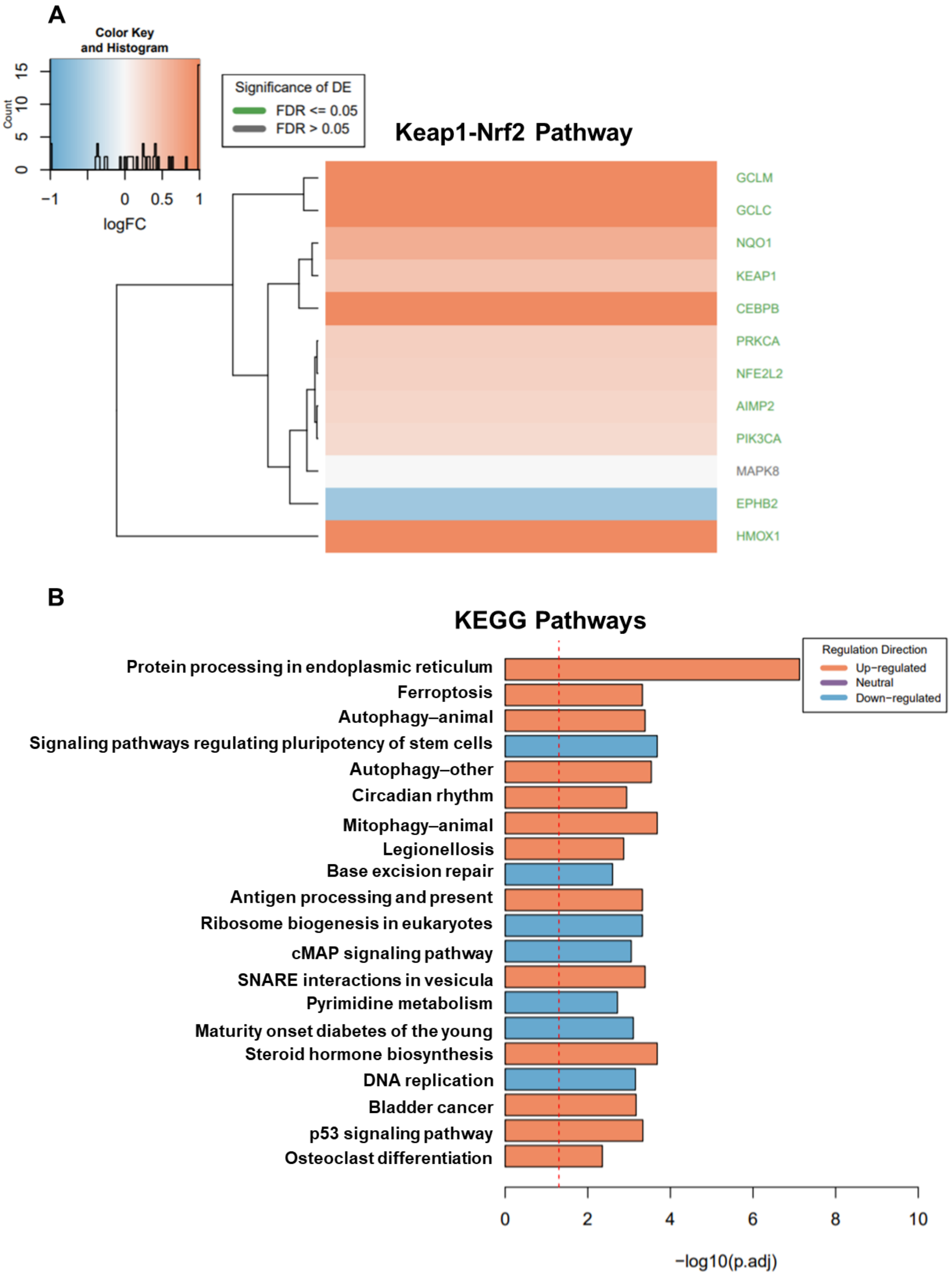

Figure 2.30. (A) Upregulation of KEAP1-Nrf2 pathway in ferroptocide-treated HT-29 cells. **(B)** Modulation of oxidative-stress pathways upon ferroptocide treatment, RNA-seq data of HT-29 cells.

2.8 Additional studies

2.8.1 Cell cycle studies

Cell cycle studies enable investigation of the overall effect of a cytotoxin in a specific phase of the cell cycle machinery. Information on disruption of a specific cell cycle phase provides insights and potential leads for mode of action studies. Propidium iodide (PI) dye is used to stain DNA of the fixed cells and asses if the compound effect (amount of PI signal) is localized in phase one (G1), two (G2/M), or synthesis phase (S).

Treatment of suspension cells (U-937) and adherent cells (ES-2) with dose-dependent concentrations of **ferroptocide** resulted in S-phase arrest as observed in **Figure 2.31** similar to the effect seen after treatment with the S-phase arrestor[75] doxorubicin. On the other hand, treatment of cells with Taxol caused arrest of cells in G2/M phase, consistent with literature reports.[76]

Additionally, time-course and G1-phase cell cycle synchronization studies of U-937 cells upon treatment with **ferroptocide** supported the S-phase arrestor observations (**Fig. 2.32 A, B** respectively). These data suggest that **ferroptocide** is not a microtubule stabilizer or destabilizer as observed from the lack of G2/M arrest but can potentially modulate a target that is implicated in DNA synthesis and causes S-phase arrest.

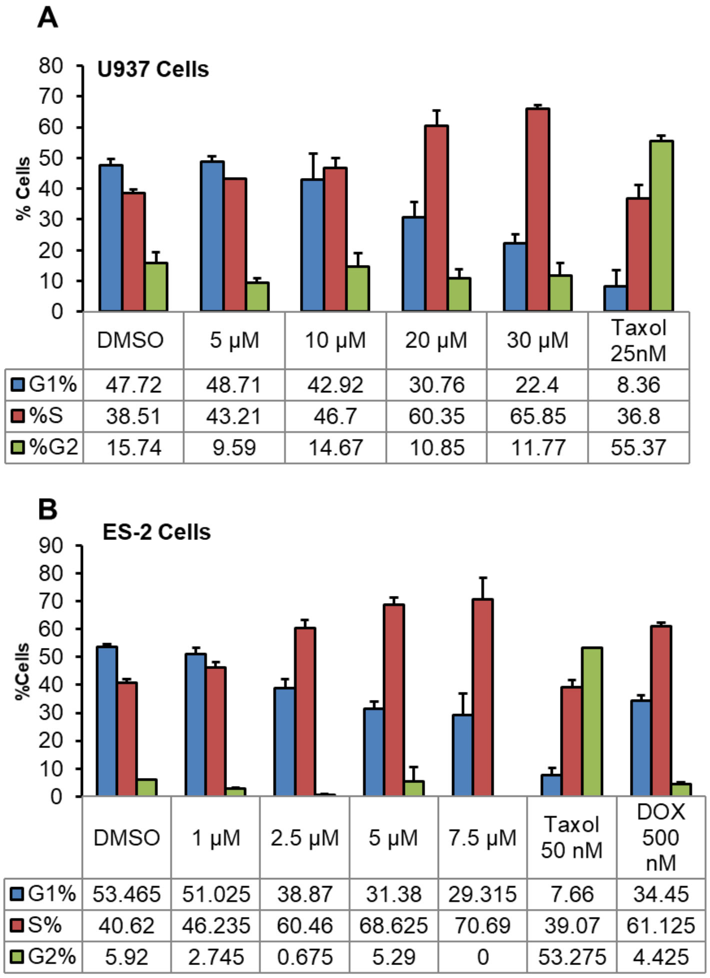

	DMSO	5 µM	10 µM	20 µM	30 µM	Taxol 25nM
🟦 G1%	47.72	48.71	42.92	30.76	22.4	8.36
🟥 %S	38.51	43.21	46.7	60.35	65.85	36.8
🟩 %G2	15.74	9.59	14.67	10.85	11.77	55.37

	DMSO	1 µM	2.5 µM	5 µM	7.5 µM	Taxol 50 nM	DOX 500 nM
🟦 G1%	53.465	51.025	38.87	31.38	29.315	7.66	34.45
🟥 S%	40.62	46.235	60.46	68.625	70.69	39.07	61.125
🟩 G2%	5.92	2.745	0.675	5.29	0	53.275	4.425

Figure 2.31. Ferroptocide is a S-phase arrester. (A–B) Cell cycle distribution of U-937 and ES-2 cells after 8 hr and 7 hr compound treatment respectively. The data was collected via flow cytometry (PI) and are plotted as the mean ± s.e.m., n=3 biological replicates.

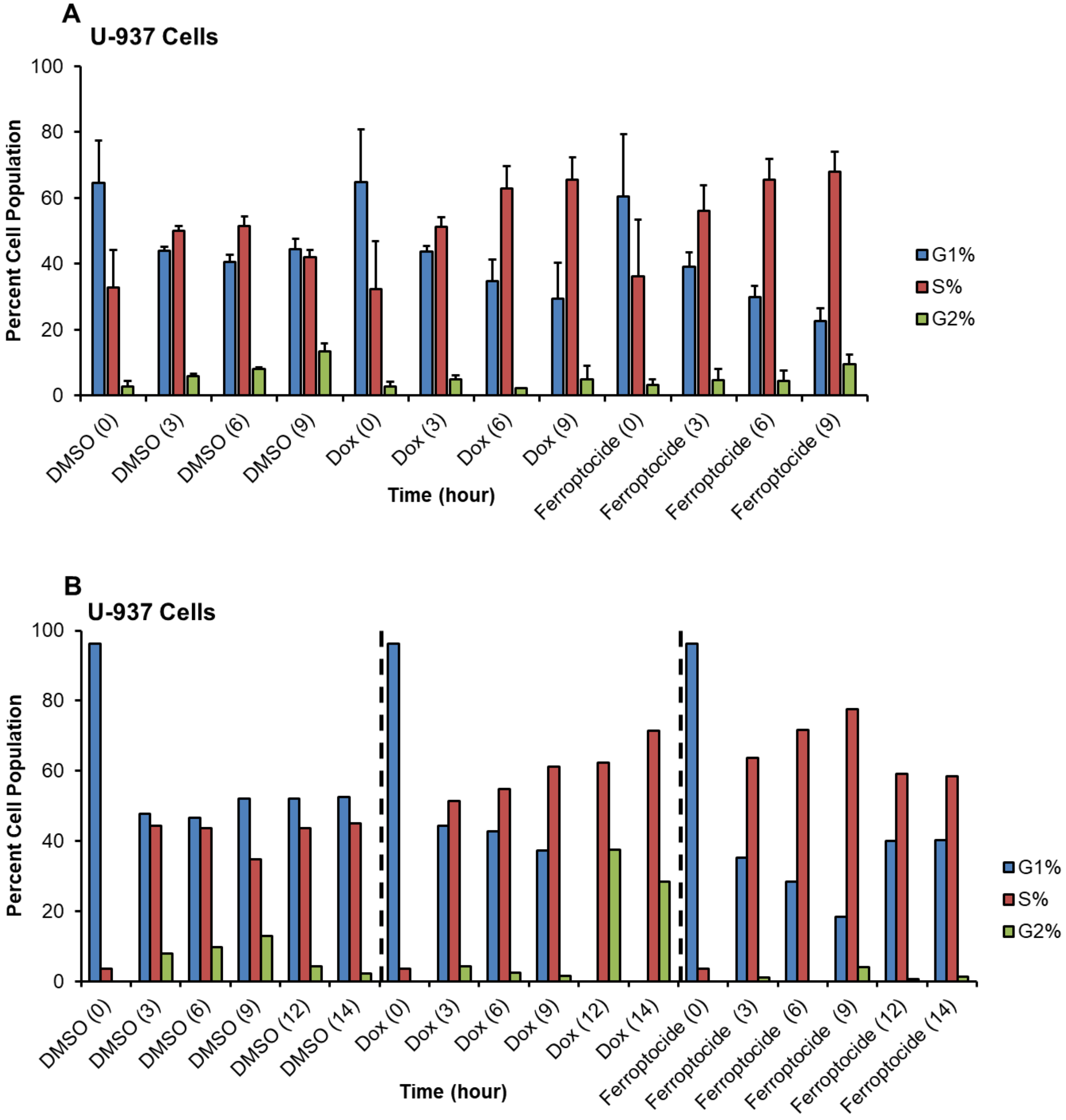

Figure 2.32. (A) Time course treatment of U-937 cells with 5 µM **ferroptocide** and 500 nM doxorubicin (Dox) at the indicated time points. Data are plotted as the mean ± s.e.m., n=3 biological replicates. **(B)** G1-cell synchronization studies. U-937 cells were starved for 24 hr with 0.2% FBS and then treated with 5 µM **ferroptocide** and 500 nM doxorubicin (Dox) for each specified time point. Data were collected via flow cytometry (PI) n=2.

To further investigate this hypothesis, we monitored the ability of **ferroptocide** to intercalate DNA and induce DNA damage. S-phase arrestor drugs can be categorized into topoisomerase inhibitors (i.e. etoposide, irinotecan, doxorubixin, daunoriubicin etc.), alkylating agents (Pt-agents), nucleoside analogues (gemcitabine, 5-FU), and DNA cleaving agents/minor grove binders (temoporfin, photopinantrin etc.) among a few others. Specific assays tailored to monitor the effect of each class are commercially available and were employed to assess the effect of **ferroptocide**. As shown in **Figure 2.33**, **ferroptocide** does not intercalate DNA similar to etoposide, while doxorubicin intercalates by displacing ethidium bromide, thus suggesting that our lead compound is not a DNA-intercalator.

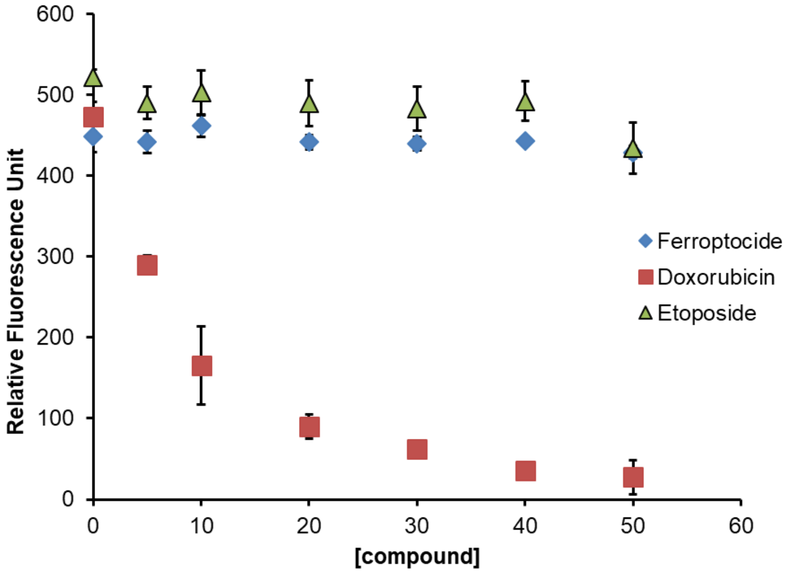

Figure 2.33. Ferroptocide is not a DNA-intercalator. Dose-dependent incubation of Herring DNA with **ferroptocide**, etoposide and doxorubicin for 30 min at r.t. Fluoresence was measured at Ex=300nm and Em= 590 nm in Gemini at IGB. Data are plotted as the mean ± s.e.m., n=3 biological replicates.

To further explore the effect of **ferroptocide** on DNA synthesis, its ability to induce DNA damage was assessed via flow cytometry and western blot analysis, monitoring for DNA damage markers such as gamma H2AX (ɣ-H2AX). This marker is correlated with the production of DNA double strand breaks, which are lethal to cells. As demonstrated in **Figure 2.34**, **ferroptocide**-treatment of ES-2 cells causes generation of ɣ-H2AX in a dose-dependent manner similar to the positive control gemcitabine. Collectively, the additional studies indicate that **ferroptocide** is an S-phase arrester that does not intercalate DNA, and directly or indirectly modulates a key target in DNA synthesis, resulting in generation of double stranded breaks. Other ferroptosis-inducers have not been reported to cause DNA damage; more experiments are needed to investigate if there is indeed a link between ferroptosis and the DNA repair machinery.

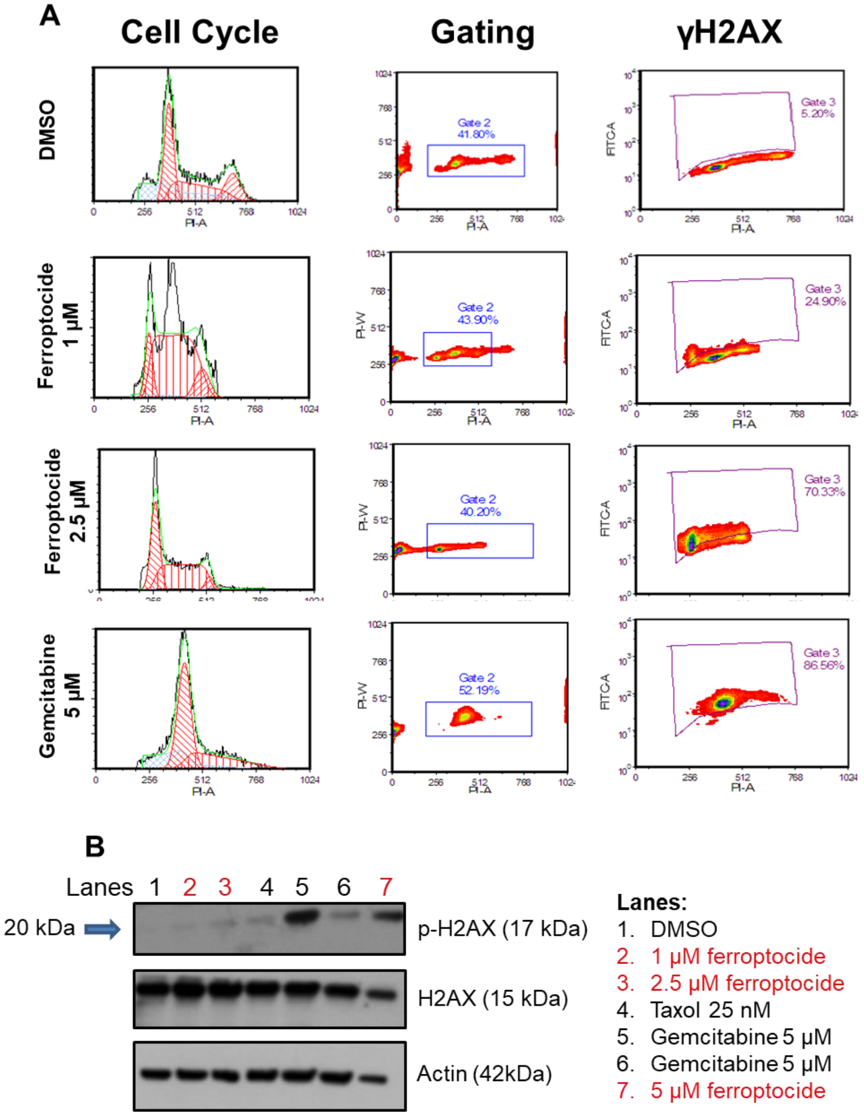

Figure 2.34. Ferroptocide generates double stranded breaks. (A) Monitoring the ability of ferroptocide to cause DNA damage in ES-2 cells after a 5 hr-incubation. Gemcitabine was used as a positive control after a 20 hr treatment. Data is representative of 4 independent biological experiments. **(B)** Western blot analysis of ferroptocide and control compounds to induce ɣH2AX in ES-2 cells after 5 hr and 20 hr treatment respectively, n=2.

2.9 Target ID and validation studies

2.9.1 Covalent binding in cells

SAR trends reveal that **ferroptocide** bioactivity depends on the presence of the electrophilic α-chloroester (**Fig. 2.7**), suggesting the possibility that it covalently modifies its target. To assess covalent modification in cells, in-gel fluorescence studies were performed in conjunction with competition studies. Treatment of cells with increasing concentrations of fluorescent analogue **P30** resulted in labeling of five main bands (**Fig. 2.35A**). Pre-treatment of cells with various concentrations of **ferroptocide**, followed by treatment with compound **P30** resulted in dose-dependent competition, primarily of two bands, in the in-gel fluorescence assay (bands B and D in **Fig. 2.35B**) implying specific compound interaction. A similar labeling and competition pattern was observed in multiple cancer cell lines including HCT 116, U937, BT-549, T47D, MDA-MB-231 (**Fig. 2.36A**), and primary cancer cells from patients (**Fig. 2.36B**). This finding suggests modulation of the same targets in immortalized cancer cell lines and in primary cancer cells. Next, we set out to identify these bands of interest.

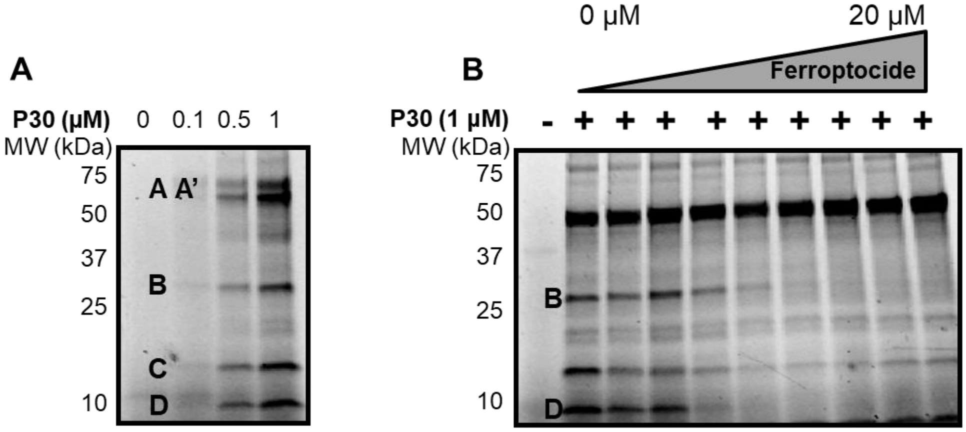

Figure 2.35. Ferroptocide is a covalent inhibitor in cells. (A) Proteomic profile for fluorescent analogue P30 in HCT 116 cells after 60 min treatment reveals labeling of five main bands. (Note: Band A and A' often appear as one band). Coomassie stain of gel demonstrates equal loading (Supplementary Fig. 2.1A). **(B)** Competitive profiling of the proteomic reactivity of P30 with parent compound ferroptocide. HCT 116 cells were pre-treated with DMSO or various concentrations of ferroptocide (30 min) followed by treatment with P30 (1 μM, 30 min) and analyzed by in-gel fluorescence assay. Specific competed proteins are marked as B and D. Coomassie stain of gel demonstrates equal loading (Supplementary Fig. 2.1B).

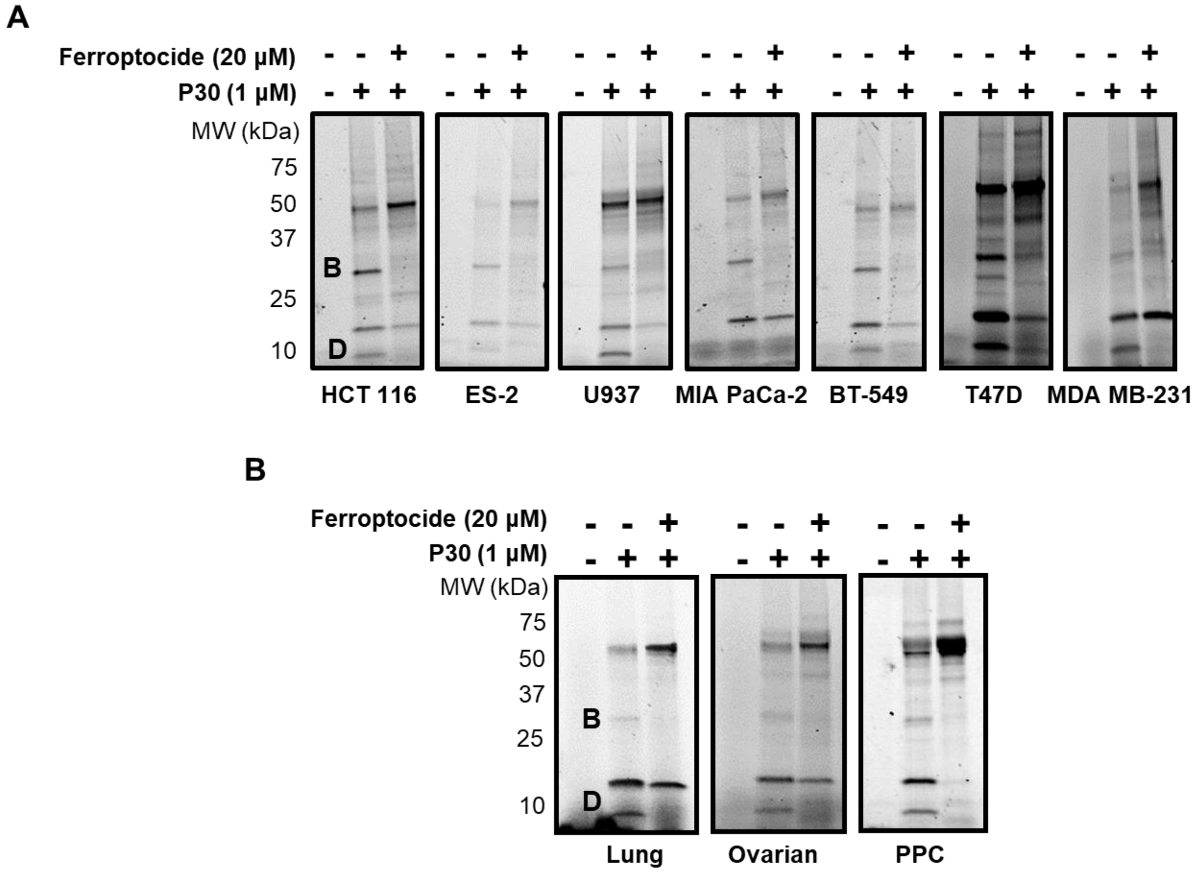

Figure 2.36. **(A)** Ferroptocide covalently modifies the same target(s) in multiple cell lines. Competition experiments were performed by treatment of cells with DMSO or ferroptocide (20 µM, 30 min) followed by **P30** incubation (1 µM, 30 min) and then analyzed using an in-gel fluorescence assay. Images are representative of three biological replicates. Coomassie stain of gels demonstrates equal loading (Supplementary Fig. 2.1C). **(B)** Ferroptocide causes the same proteomic competitive profile in primary cells isolated from metastatic cancer patient samples. Competition experiments were performed by treatment of cells with DMSO or ferroptocide (20 µM, 30 min) followed by **P30** incubation (1 µM, 30 min) and then analyzed using an in-gel fluorescence assay. Representative images of two biological replicates. PPC: primary peritoneal carcinomatosis. Coomassie stain of gels demonstrates equal loading (Supplementary Fig. 2.1D).

2.9.2 Chemical proteomics: 1D Gel

Chemical proteomics, specifically in-gel fluorescence studies, are well-characterized target identification methods that have been widely utilized to identify the target of many small molecule compounds such as pyrrolidine 1 (fumarate hydratase inhibitor),[77] 1,3,5 triazine RB-11ca (protein disulfide isomerase inhibitor),[78] and curcumin (casein kinase I gamma).[79,] In an attempt to elucidate the target of interest, protein identification via mass spectrometry was coupled with in-gel fluorescence (workflow shown in **Fig. 2.37**). Briefly, cells were incubated with compound **P30** and lysed before proteins were separated by SDS-PAGE, then subjected to in-gel fluorescence studies. Fluorescent bands were manually excised, trypsin-digested, and analyzed with LC–MS/MS.

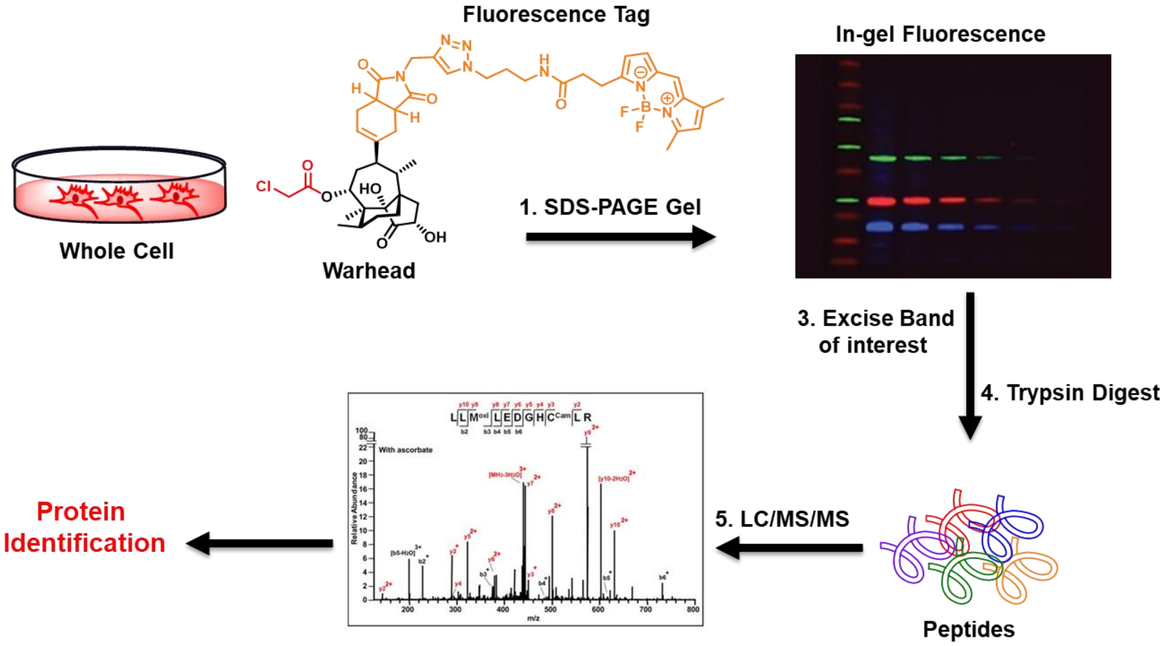

Figure 2.37. Chemical proteomics workflow for target ID in 1D gels.

2.9.3 Mitochondrial fractionation

As showcased in **Figure 2.36.** treatment of whole cells with **ferroptocide** followed by fluorescent analogue **P30** resulted in predominant competition of two bands, B and D, suggesting specific compound interaction. We set out to identify the protein target(s) corresponding to band B using chemical proteomics. Cell fractionation was employed to investigate if any of the potential proteins were associated with mitochondria from MOA studies. Indeed, the strongest fluorescent signal was observed in the membrane/organelle fraction (**Fig. 2.38A–B**)**,** implying compound activity in mitochondria, consistent with confocal microscopy and TEM images (**Fig. 2.19**).

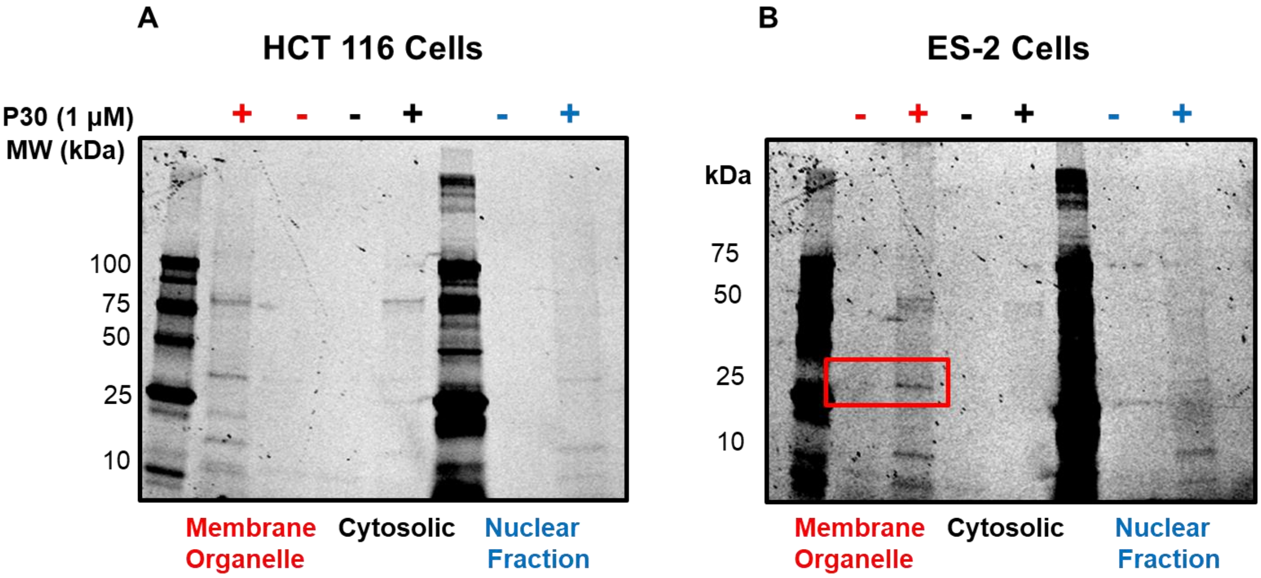

Figure 2.38. (A) Cell fractionation of HC T116 cells was subjected to in-gel fluorescence studies. Treatment with **P30** results primarily in labeling of mitochondrial proteins. **(B)** Cell fractionation of ES-2 cells treated with fluorescent analogue **P30** indicates labeling of mitochondrial proteins. Each gel is representative of three independent biological replicates. Coomassie stain of gels demonstrates equal protein loading.

To further explore this hypothesis, mitochondria of HCT 116 and ES-2 whole cells treated with **P30** were isolated. A similar fluorescence pattern was observed in whole cells for both cell lines (**Fig. 2.38 A–B**). The most intense fluorescent band that was competed away was excised and analyzed via LC–MS/MS. The analysis provided a list of 12 and 45 proteins detected between 25-37 kDa for HCT 116 and ES-2 cells, respectively (**Table 2.3**). However, only two proteins were present in both cell lines: a putative protein (unknown) and F-ATPase F1 mitochondrial complex gamma subunit. Compound modification was not observed in any of the peptides of interest, likely due to low protein coverage of < *30%*, thus warranting investigation of new target ID methods.

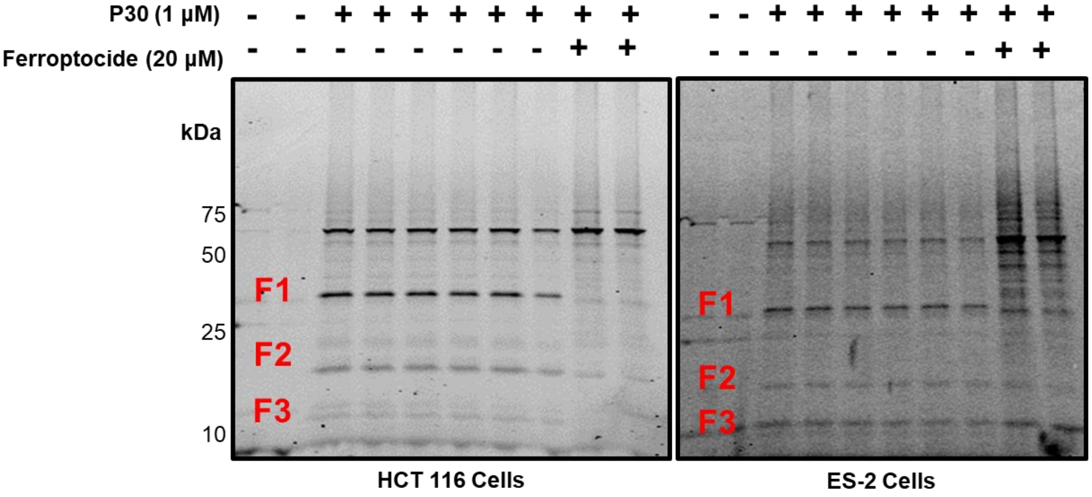

Figure 2.39. In-gel fluorescence studies coupled to chemical proteomics. Whole cells pre-treated with **ferroptocide** (20 µM, 30 min) followed by **P30** incubation (1 µM, 30 min) were subjected to mitochondrial fractionation and then analyzed via in-gel fluorescence assay. Fractions 1 and 2 were excised and submitted for LC–MS/MS analysis. n=2 biological replicates.

Table 2.3. Top-scored protein candidates identified from the 1D mitochondrial gel of HCT 116 and ES-2 cells.

12 Proteins in HCT116 (F1)	45 Proteins in ES-2 (F1)
Putative 553734	Unnamed protein product
ATP synthase, H+ transporting, mitochondrial F1 complex, gamma polypeptide 1	Chain A, Human Annexin V with Incorporated Methionine Analogue Azidohomoalanine
Unnamed protein product	Unnamed protein product
hCG2045732	Unnamed protein product, partial
GAS2-like protein 2	Unnamed protein product
HSPC303	hCG2028724
V12-13	Cytokeratin 9
Zinc finger protein 445	L-lactate-dehydrogenase B chain
synaptophysin	60S ribosomal protein L8
Tetratricopeptide repeat protein 28	Putative 553734
RecName: FAM201A	BBC1
Predicted: AT-rich interactive domain-containing protein 1B isoform X4	L-lactate-dehydrogenase A chain
60S ribosomal protein L13 isoform1	40S ribosomal protein S6
	ATP synthase, H+ transporting, mitochondrial F1 complex, gamma polypeptide 1

2.9.4 2D-gel target ID studies

A two-dimensional gel electrophoresis (2D-PAGE) strategy was incorporated to narrow down the number of candidate protein target(s) and improve the resolution of 1D in-gel analysis. 2D-PAGE is a robust method to readily detect changes in protein levels between different samples.[80,81] Proteins are initially separated by the isoelectric point (pI) in the first dimension, followed by molecular weight (MW) via SDS–PAGE in the second dimension; thus, only proteins with the same isoelectric point and molecular weight are present in an isolated spot of a 2D gel.

2.9.4.1 Fluorescence pattern in a 2D-gel

Attempting to exploit the high sensitivity of 2D-PAGE to separate proteins of the same molecular weight and pI, HCT 116 whole cell extracts were subjected to a 2D in-gel fluorescence analysis as shown in **Figure 2.40**. Gratifyingly, the pattern of fluorescence in the 2D gel is consistent with the 1D gel indicating that fluorescent analogue of **ferroptocide**, **P30**, is targeting specific proteins. Pre-treatment of HCT 116 cells with **ferroptocide** resulted in diminishment of only one of the fluorescent signals in the 2D gel suggesting non-specific compound labeling (**Fig. 2.40**) of the other two bands. Excision of the bands of interest (marked in red **Fig. 2.40**) followed by tryptic digestion and LC–MS/MS analysis (LTQ-Orbitrap in positive ionization mode) afforded a list of over 150 potential protein targets. Efforts to monitor the **P30**-induced chemical modification of the peptides of interest were unsuccessful potentially due to compound fragmentation and/or lack of sample ionization in the positive electrospray ionization (ESI) mode.

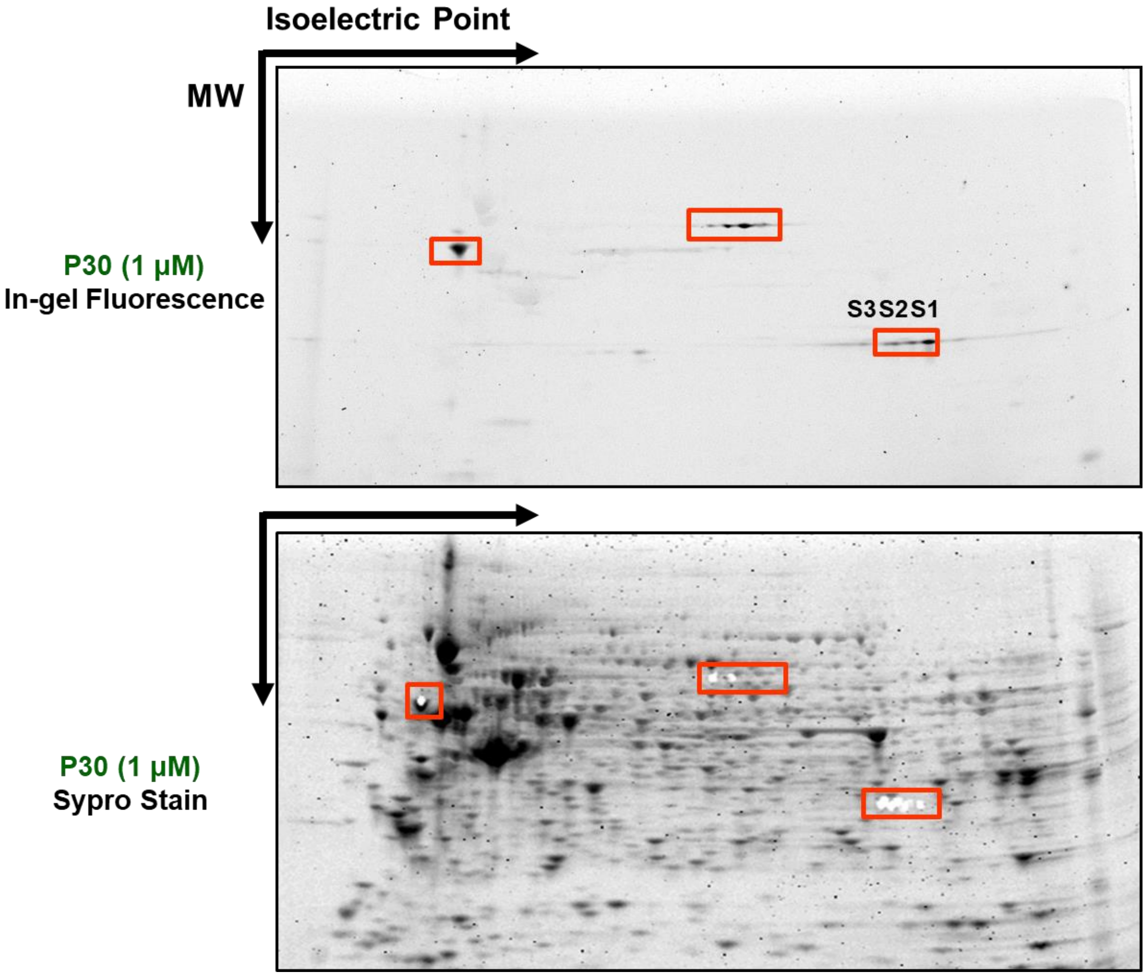

Figure 2.40. Separation of proteins from HC T116 cells treated with **P30** (1 µM, 30 min) by molecular and isoelectric point. The fluorescent gel was stained with Sypro Ruby and existed at the bands of interest (S1, S2, S3). Samples were subjected to trypsin digestion and analyzed via LC–MS/MS. n=1 biological replicate.

2.9.4.2 Compound fragmentation pattern in LC–MS/MS

To further explore this hypothesis, MS/MS analysis of compound alone (**P30**), and **P30** adduct with glutathione was monitored. This study revealed a unique fragmentation pattern where the α-chloroester is lost during LC–MS/MS analysis as shown in **Figure 2.41**, resulting in a 58 Da modification shift. Given the propensity of **ferroptocide** to react with nucleophilic amino-acids including cysteine, serine, tyrosine and threonine in a similar fashion as with glutathione, such residues were examined for a + 58 Da mass increment corresponding to compound reactivity.

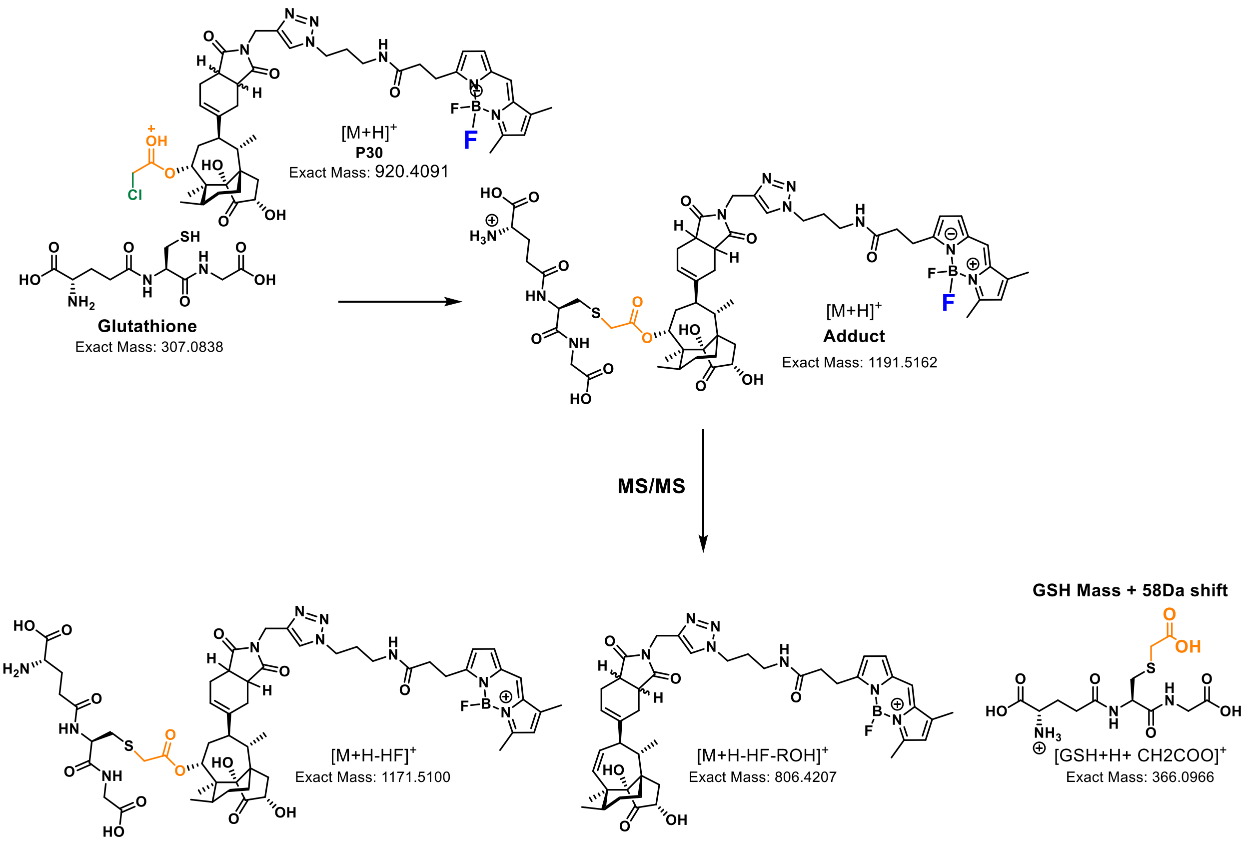

Figure 2.41. Compound (**P30**) fragmentation pattern in LC–MS/MS upon reactivity with glutathione for 24 hr.

2.9.4.3 Candidate protein targets from 2D-gel analysis

Investigation of proteins that contain a 58 Da modification in their cysteine residues resulted in identification of four potential candidate proteins (**Table 2.4**). From this selected list, electron-transport flavoprotein (*ETFA*), showed significantly higher spectral count scores in all three samples, and thus was further evaluated as a putative target. **Figure 2.42** showcases the 58 Da shift of a cysteine residue of *ETFA* as observed from LC–MS/MS analysis implying covalent modification of *ETFA* from the compound of interest. emPAI is a metric for measuring protein coverage while the ion score is a measure of how well the observed MS/MS spectrum matches the database peptide sequence. High emPAI and ion score values represent high confidence and significance of the data set. Comparison of the potential targets identified from the 2D gel analysis (**Table 2.4**) was inconsistent with the data set obtained from the mitochondria isolated bands in the 1D gel. Such discrepancies could be attributed to potential sample contamination during work up, different facilities, and drastically different staining methods and instrumentations.

Table 2.4. Top-scored protein candidates identified from the 2D gel of HCT 116.

Protein Name	**MW kDa**	**Ion Score**			**Isoelectric Point**	**emPAI**		
		S1	**S2**	**S3**		**S1**	**S2**	**S3**
Electron-transfer flavin alpha	33	61	58	3	8.62	8.77	3.58	2.55
Actin related 2/3 complex subunit	34	49	54	NA	6.84	13.76	20.29	2.40
Pyrroline-5-carboxylate reductase	33	19	NA	26	7.18	4.14	3.00	13.09
Guanine-nucleotide binding beta	35	10	34	22	7.60	3.74	6.65	4.34

NA (no modification)
S1: sample 1, **S2**: sample 2, **S3**: sample 3
emPAI: exponentially modified protein abundance index

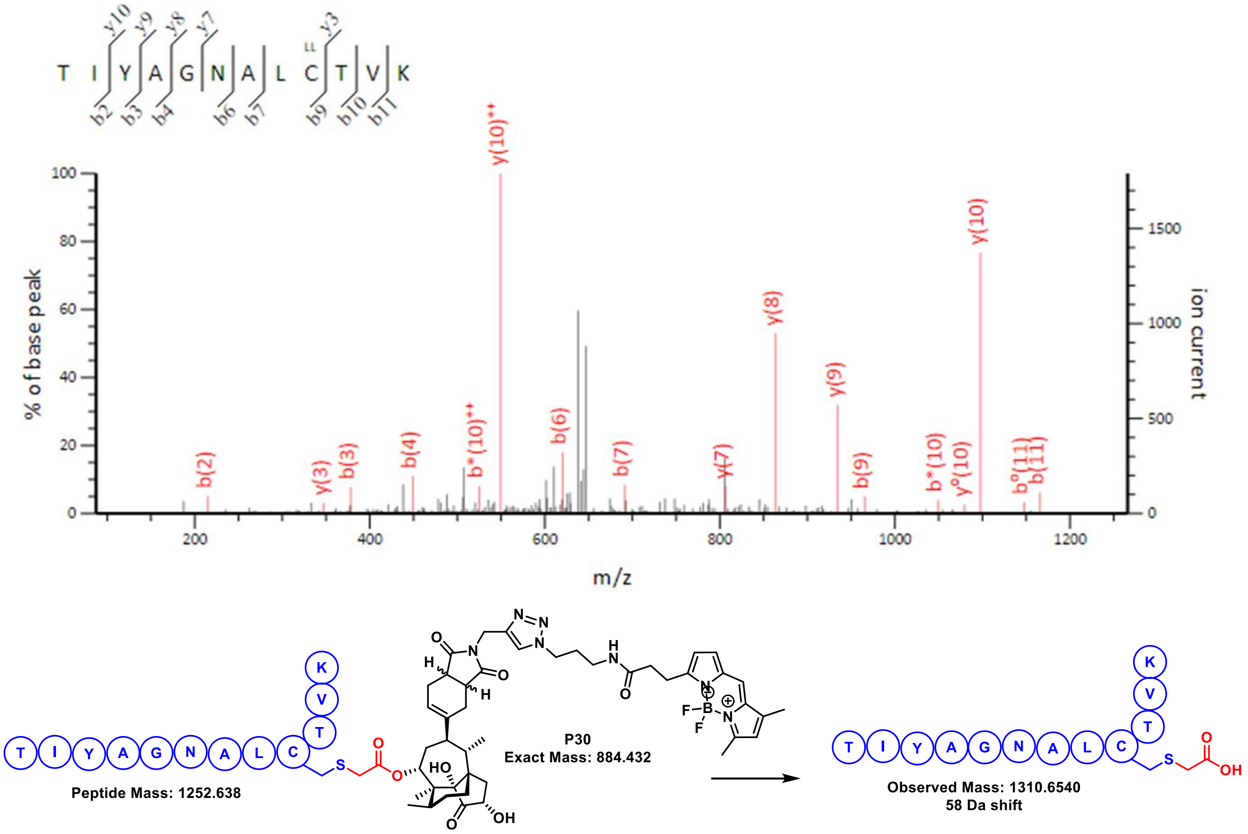

Figure 2.42. LC–MS/MS representative chromatogram of the 58 Da shift of the ETFA peptide at the cysteine residue as a result of the covalent modification by the compound of interest **P30**.

2.9.5 Target validation from 2D-gel analysis

2.9.5.1 Role of ETFA in Cells

ETFA is a 30 kDa subunit of the electron transfer flavoprotein (ETF), which is localized at a strategic position in the mitochondrial respiratory chain (**Fig. 2.43**) and shuffles electrons from 9 different binding partners such as acetyl-CoA, isovaleryCoA, Glutaryl-CoA, and Sarcosine dehydrogenase to the main mitochondrial respiratory chain via ETF-ubiquinone oxidoreductase.[82,83] *ETFA* is vital for the mitochondrial fatty acid oxidation and metabolism of normal amino acids. Mutations or deficiencies in *ETFA* (as well as the other subunit, ETFB) lead to an inherited metabolic disorder named glutaric aciduria type II, which impairs processing of proteins and fatty acids resulting in their buildup and metabolic acidosis (tissues and blood become too acidic).[84,85]

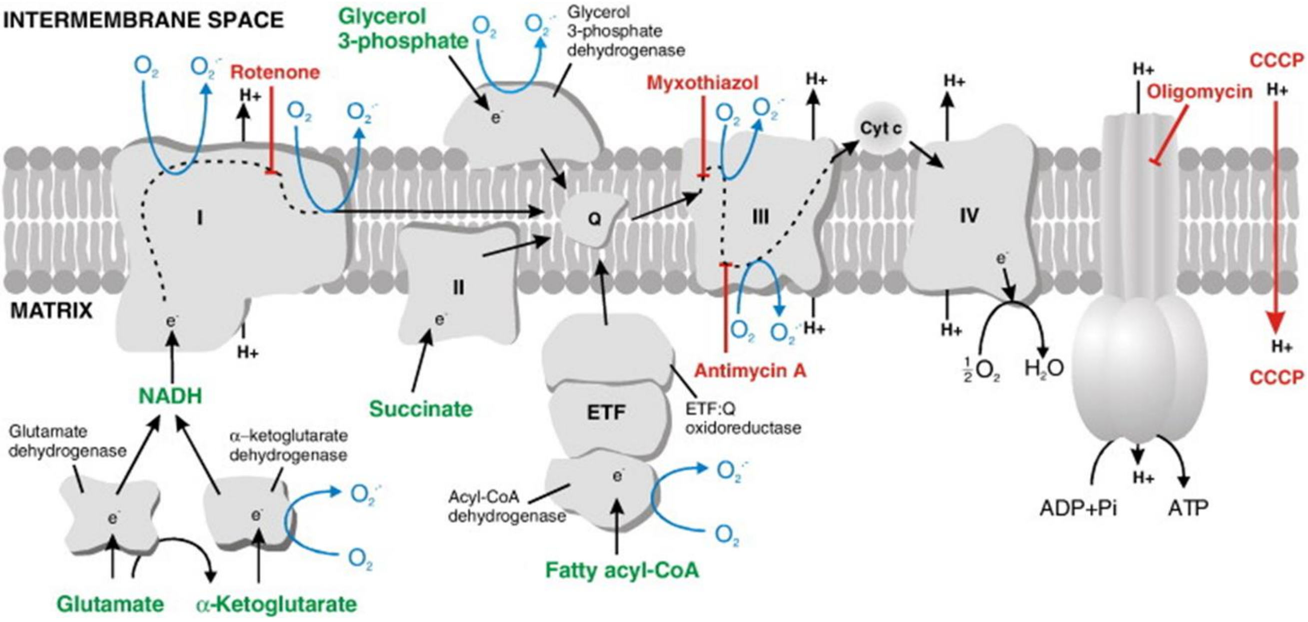

Figure 2.43. Schematic of the position and function of ETFA in the mitochondria respiratory chain.

2.9.5.2 Immunoprecipitation studies using BODIPY antibody

To investigate *ETFA* as a potential target of **P30**, immunoprecipitation studies were conducted (**Fig. 2.44**). In brief, HCT 116 and ES-2 cells were treated with DMSO, BODIPY azide, **P30** (1 µM, 30 min), lysed and exposed to magnetic beads pre-incubated overnight with a BODIPY antibody for 15–24 hr at 4 degrees. Upon elution of BODIPY antibody-compound-protein complex, samples were subjected to in-gel fluorescence studies followed by western blot analysis with an *ETFA* specific antibody. BODIPY azide served as a control for non-specific binding to the BODIPY fluorophore, while DMSO was a control for non-specific binding to Dynabeads (magnetic beads).

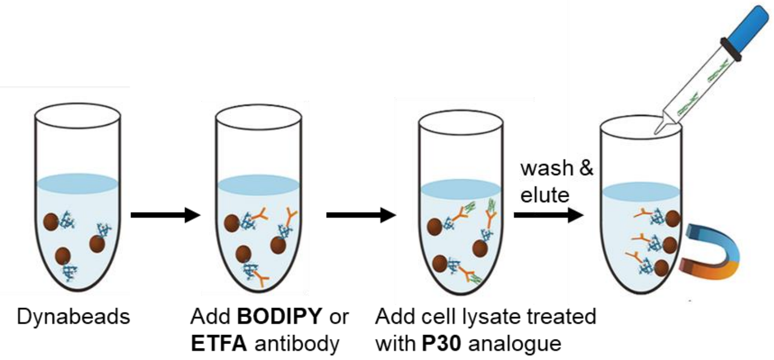

Figure 2.44. Schematic of pulldown studies with BODIPY antibody.

As observed in **Figures 2.45** and **2.46**, immunoprecipitation studies were successful in both cell lines without interference from non-specific binders. **Figure 2.46** displays the ability of a BODIPY antibody to pulldown *ETFA* from HCT 116 cells treated with **P30** suggesting modification of *ETFA* by our compound of interest. Competition pull down studies revealed competition of the specific band at 10 kDa but not at 25 kDa (a target different than *ETFA*). Nevertheless, investigation of the ability of *ETFA* antibody to colocalize with the fluorescent signal of compound **P30** were not successful, implying a weak *ETFA*–**P30** interaction.

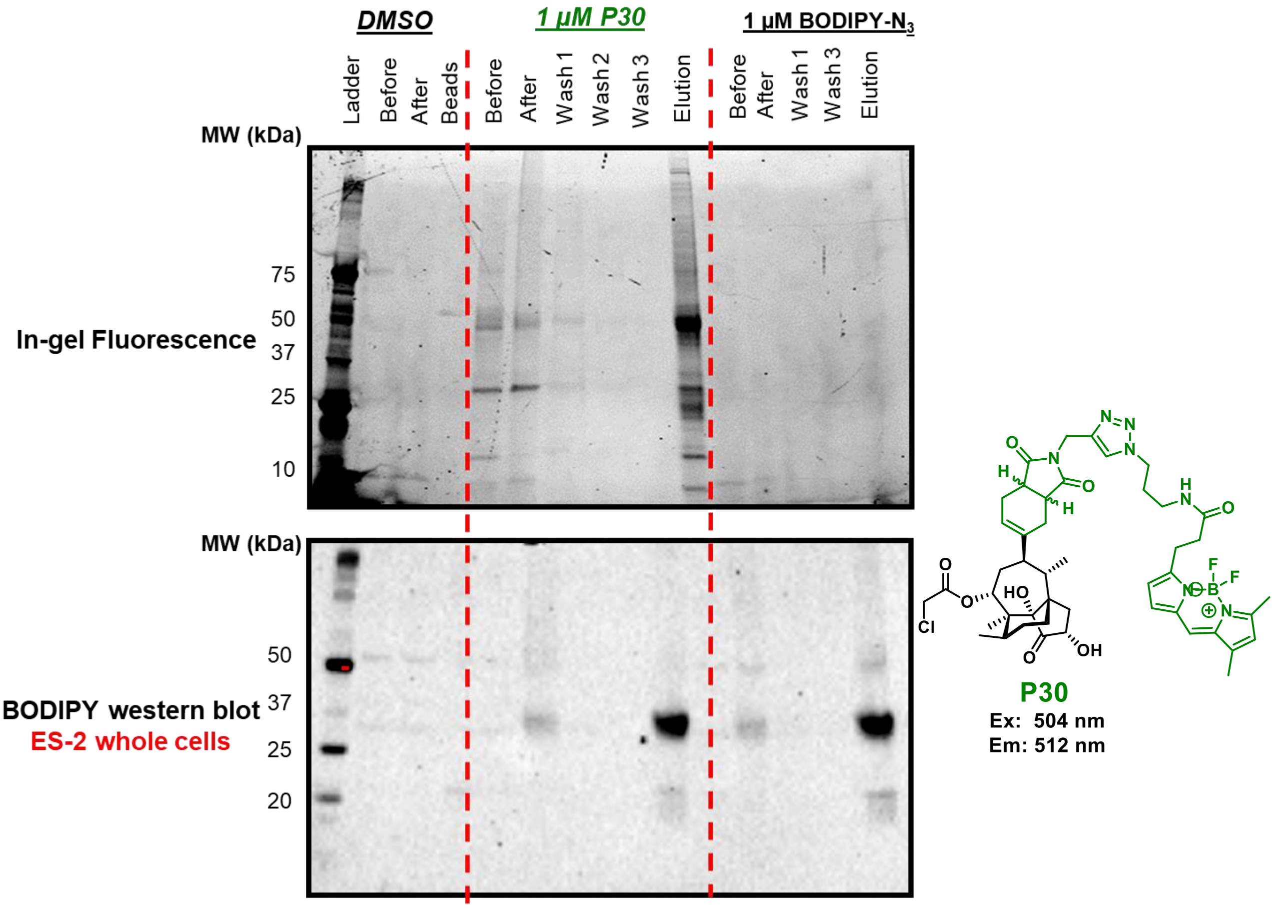

Figure 2.45. **Immunoprecipitation studies with a BODIPY antibody in ES-2 cells.** Upon 30 min treatment of cells with **P30** (1 µM), DMSO, BODIPY azide (1 µM), 100 µg protein samples were co-incubated with anti-rabbit IgG Dynabeads coated with BODIPY antibody and eluted for in-gel fluorescence studies and western blot analysis. The elution lane indicates successful pull down of proteins targeted by **P30**. Gel image is representative of three independent biological replicates.

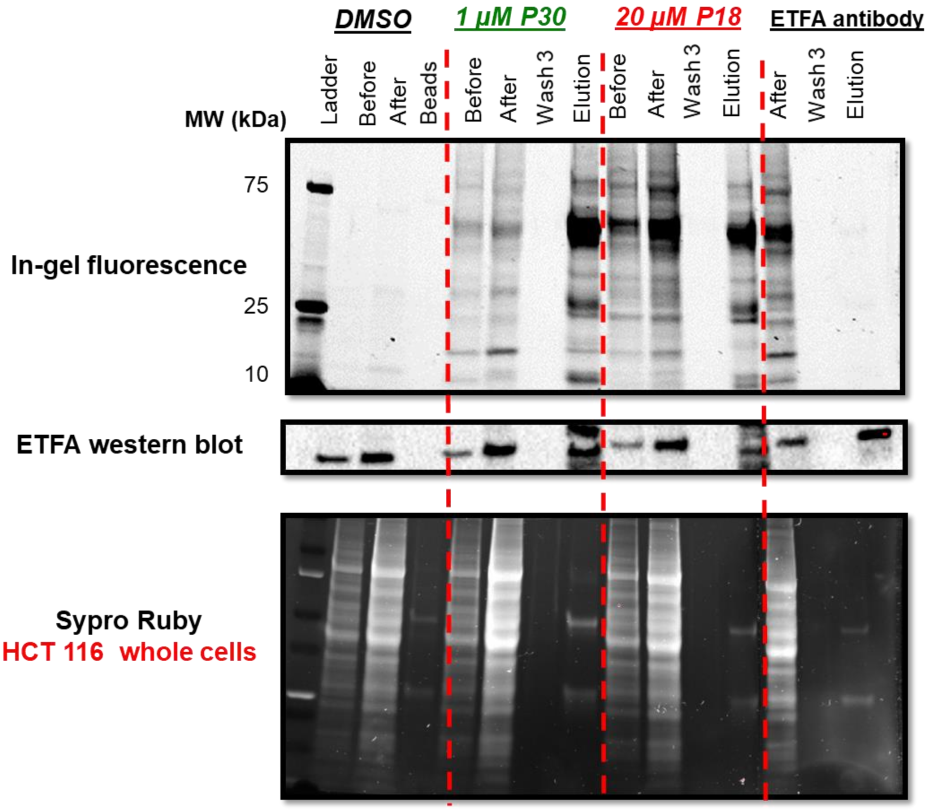

Figure 2.46. Immunoprecipitation studies with a BODIPY or ETFA antibody in HC T116 cells. Upon 30 min treatment of cells with **P18** (20 µM), DMSO followed by 30 min incubation with **P30** (1 µM), 100 µg protein samples were co-incubated with anti-rabbit IgG Dynabeads coated with BODIPY/ETFA antibody and eluted for in-gel fluorescence studies and western blot analysis. Fluorescent bands were observed with the BODIPY pulldown but not with ETFA suggesting weak binding between **P30** and ETFA. Gel image is representative of three independent biological replicates.

2.9.5.3 CETSA *ETFA* and Ferroptocide

Cellular thermal shift assay (CETSA) is a novel method used to monitor target engagement in cells. CETSA evaluates the change in melting temperature of the protein target in the presence or absence of the small molecule upon thermal denaturation.[86-88] This technique is based on the principal that binding of a compound to the protein of interest results in a conformational change which can stabilize the protein complex and protect it from thermal denaturation. Despite the initial promise for use of CETSA as a target identification method, its potential has only been demonstrated in validating well-known or hypothesized targets, which must not melt at high temperatures. In addition, this approach has yet to be optimized for membrane targets.

CETSA was performed to monitor the **ferroptocide**-*ETFA* target engagement in cells. Treatment of ES-2 cells with DMSO, **ferroptocide**, and inactive analogue **P24** resulted in a small 3 degrees difference in melting temperature values as shown in **Figure 2.47.** Actin levels were monitored for equal protein loading (LDHA protein is a more suited CETSA control since it melts at high temperatures, >90°). Given the insignificant change in the melting temperatures between DMSO & **ferroptocide**-treated samples, additional target validation studies needed to be pursued.

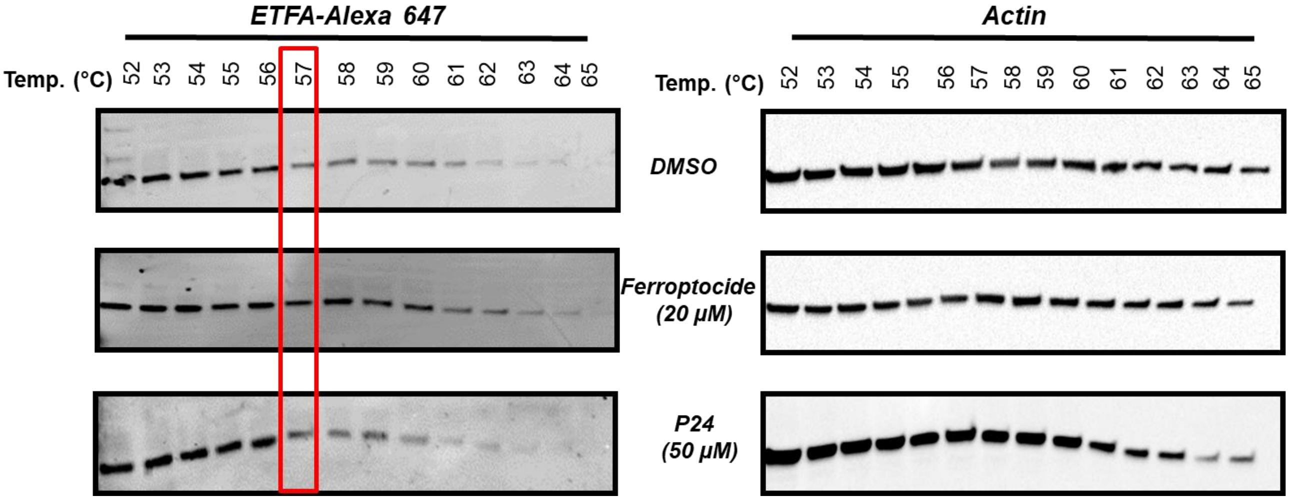

Figure 2.47. Ferroptocide weakly binds to ETFA in ES-2 cells to stabilize it against thermal denaturation. Cells were treated with DMSO, **ferroptocide** (20 μM), and inactive analogue **P24** (50 μM) for 30 min. Samples were subjected to 3 flash freezing cycles with liquid nitrogen in the presence of a protease inhibitor cocktail followed by western blot analysis with ETFA antibody. Actin protein was monitored for equal protein loading. Immunoblots are representative of n=2 out of 4 biological replicates.

2.9.5.4 siRNA and CRISPR KO ETFA studies

Another validation method are genetic knockdown studies using siRNA. Upon siRNA knockdown of *ETFA* in HCT 116 cells for 72 hr, cells were treated with DMSO or **ferroptocide** for 30 min followed by 30 min **P30**-treatment and assessed for changes in the fluorescent signal between wild type and siRNA transfected cells. Quantitative knockdown of *ETFA* in cells (> 80 %, **Fig. 2.48**) did not result in any fluorescent changes in the in-gel fluorescence studies, suggesting that *ETFA* is not the target of interest. Exposure of HCT 116 cells with knockdown levels of *ETFA* to **ferroptocide** in a time-course study (**Fig. 2.49**) yielded inconsistent results towards protection against compound-induced cell death, thus requiring further investigation.

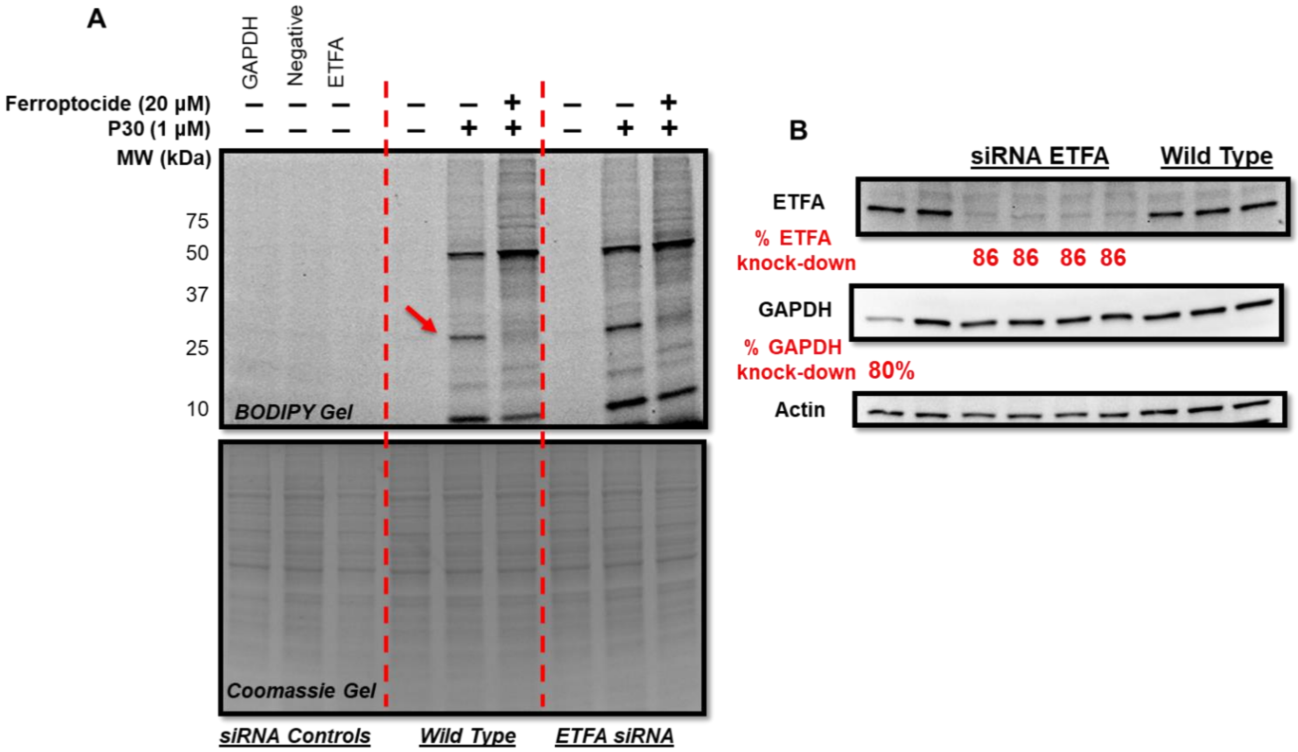

Figure 2.48. siRNA knockdown of ETFA in HCT 116 cells results in no change of the fluorescent labeling as shown by the red arrow. **(A)** Wild type and siRNA transfected cells were subjected to competition experiments with **ferroptocide** (20 μM) 30 min pre-treatment followed by **P30** (1 μM) 30 min treatment and in-gel analysis. Coomassie gel indicates equal protein loading. **(B)** Immunoblot of ETFA and GAPDH (siRNA positive control) of same cells shows a successful know down experiment. Data are representative of n=3 biological replicates.

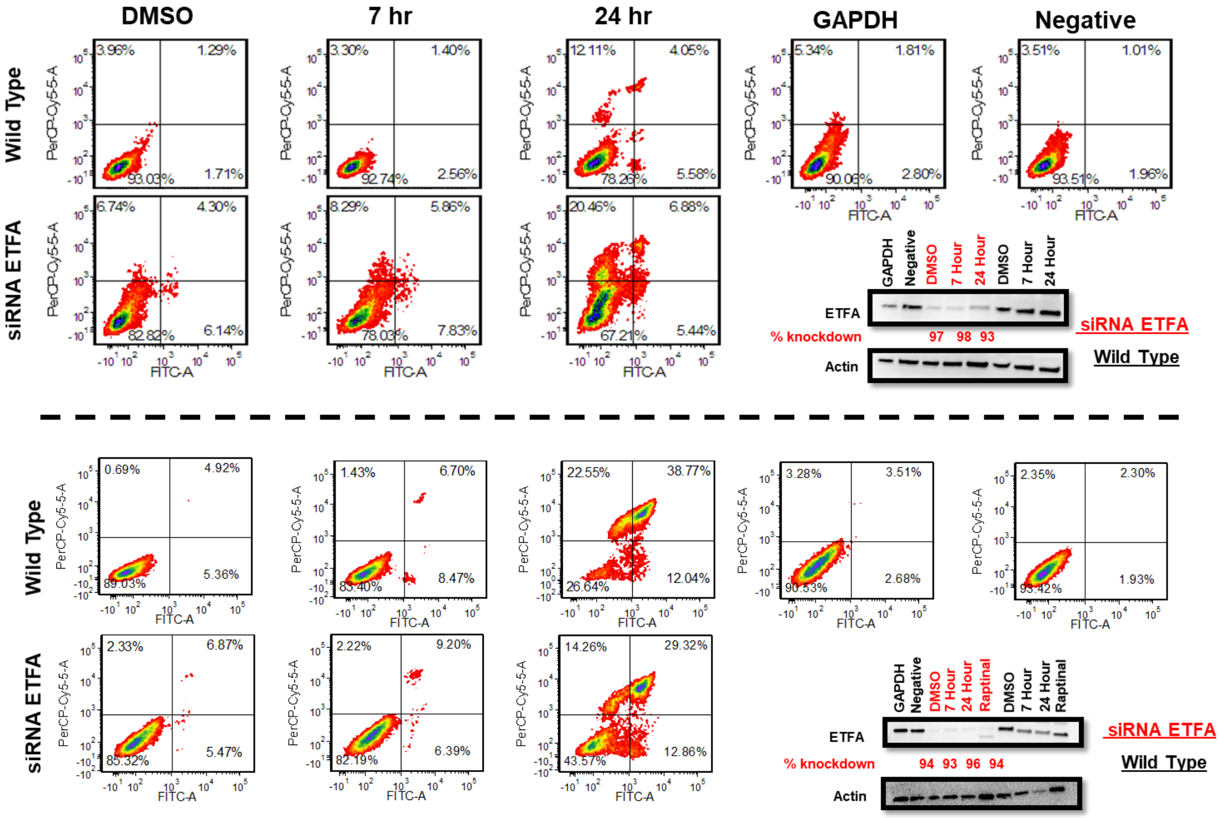

Figure 2.49. Monitoring the ability of siRNA transfected HCT 116 cells to protect against **ferroptocide**-induced (10 µM) cell death at the indicated time points. Annexin V/PI analysis was utilized to assess cell death via flow cytometry. Immunoblots of the same cells used for flow analysis assess the efficiency of siRNA knockdown. Data are representative of 4 biological replicates.

To confirm *ETFA* as a non-target of **ferroptocide**, we turned to CRISPR KO studies. The in-gel fluorescence studies with HCT 116 cells lacking the *ETFA* protein show no change in the fluorescent labeling pattern compared to studies in wild type cells, thus concluding that *ETFA* is not the target of interest, band B (**Fig. 2.50**). Cell death studies with CRISPR KO cells protect against **ferroptocide**-induced cell death as shown in **Figure 2.51.** This finding suggests that *ETFA* is an off-target protein that could mediate **ferroptocide**-induced cell death. There are no reports to date that implicate *ETFA* in ferroptosis. In retrospect, inability of an *ETFA* antibody to isolate the **P30** fluorescent signal and inconsistency of CETSA results support the hypothesis that *ETFA* is not the target of interest. Nonetheless, CRISPR KO studies provided the most conclusive evidence and must be prioritized in small molecule target validation efforts

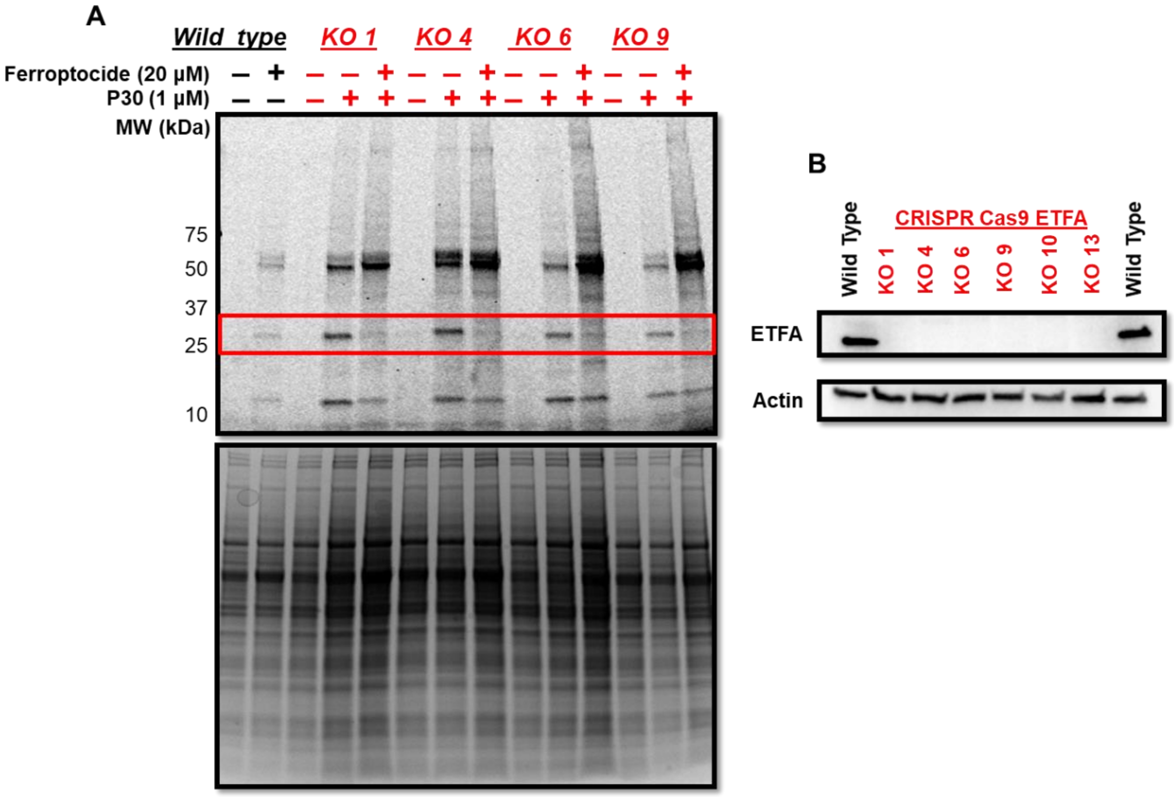

Figure 2.50. CRISPR knockout of ETFA in HCT 116 cells results in no change of the fluorescent labeling as shown by the red box. **(A)** Wild type and CRISPR KO cells were subjected to competition experiments with **ferroptocide** (20 μM) 30 min pre-treatment followed by **P30** (1 μM) 30 min treatment and in-gel analysis. Coomassie gel (botom gel) indicates equal protein loading. **(B)** Immunoblot of ETFA and Actin (loading control) of same cells confirms successful knockout of ETFA in cells. Data are representative of n=3 biological replicates.

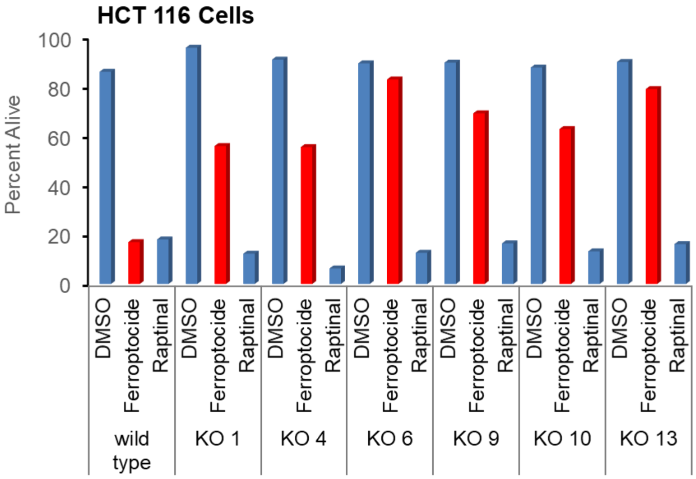

Figure 2.51. Monitoring the ability of ETFA KO clones to protect against 10 μM **ferroptocide**-induced cell death upon 24 hr incubation. Raptinal (10 μM) is used as a positive control. Annexin V/PI assessment was performed via flow cytometry. Data represents the average cell death of two biological replicates.

2.9.6 Target ID: Biotin-streptavidin pulldown

In an effort to identify the labeled protein(s), a biotin-streptavidin pulldown[78] (**Fig. 2.52 A**) was performed with the bioactive alkyne compound **P29** in collaboration with professor Eranthie Weerapana at Boston College. Briefly, HCT 116 cells were pre-treated with **ferroptocide** or DMSO, followed by treatment with **P29**. Upon incorporation of biotin using copper-catalyzed azide-alkyne cycloaddition (CuAAC) chemistry, **P29**-labeled proteins were enriched on streptavidin beads, subjected to an on-bead trypsin digestion and subsequent LC/LC–MS/MS analysis.

Protein identities were determined by database searches using the SEQUEST algorithm. Relative quantitation of proteins enriched in **ferroptocide** or DMSO pre-treated samples was achieved by spectral counting. The DMSO/ferroptocide spectral count ratio provides a relative measure of enriched proteins in the DMSO versus **ferroptocide** pre-treated samples (**Fig. 2.52B**). High-affinity targets from the HCT 116 cell line were then compared to targets identified in a second cell-line ES-2. Based on shared enrichment in both cell lines, as well as comparing protein molecular weights to the bands observed in in-gel fluorescent gel, nine proteins were selected for follow up characterization (**Table 2.5**).

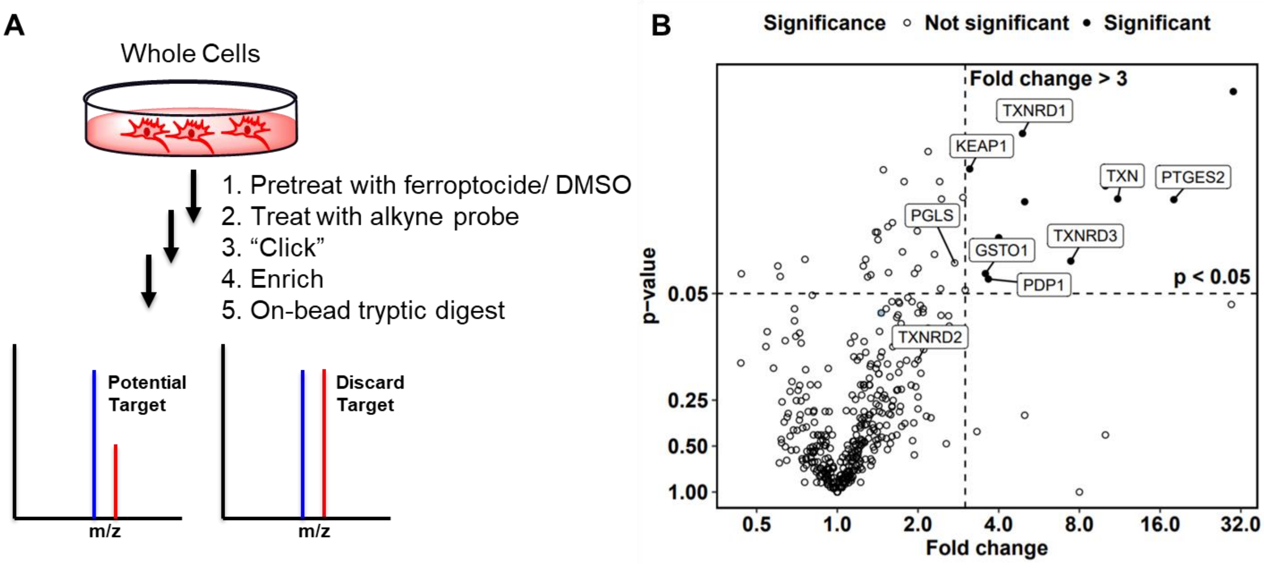

Figure 2.52. (A) Schematic of biotin-streptavidin pulldown method: Treatment of HCT 116 cells with ferroptocide (30 min) and **P29** (60 min) was followed by CuAAC reaction with biotin-azide and enrichment with streptavidin magnetic beads. On-bead trypsin digestion coupled to LC/LC–MS/MS provided a list of over 300 targets. **(B)** Enrichment of proteins based on p values (<0.05) and fold change (>3) in HCT 116 cells. Thioredoxin (TXN) was a top target candidate.

Table 2.5. Proteins identified for follow-up characterization that had shared enrichment in both HCT 116 and ES-2 cell lines, as well as molecular weights matching the bands observed by gel.

Protein	MW (kDa)	Fold Change
TXNRD3	76.4	7.4
TXNRD1	70.8	4.9
KEAP1	69.7	3.1
PDP1	61.1	3.7
TXNRD2	56.4	2
PTGES2	41.9	18
PGLS	27.5	2.7
GSTO1	27.5	3.6
TXN	11.7	11.1

2.9.7 siRNA and CRISPR KO studies of putative targets

In order to discriminate between on- and off- cytotoxicity-related targets, siRNA and CRISPR Cas9 strategies were employed. KEAP1 and GSTO1 proteins were targeted first since they possessed molecular weights similar to bands A and B respectively. Upon successful knockdown of these proteins (**Fig. 2.53B**), an assessment was made of how changes in protein expression affected band labeling in the in-gel fluorescence experiment. Comparison of cells with knockdown targets and wild type cells indicated no change in in-gel fluorescence (**Fig. 2.53A**), suggesting that KEAP1 and GSTO1 are off-pathway targets of **ferroptocide**.

CRISPR Cas9 technology was then used to rapidly investigate the remaining targets. We were able to successfully generate isogenic cell line pairs for seven knockout targets, with one target knockout leading to lethality. Knockout of six targets (PTGES2, PGLS, TXNRD1, TXNRD2, TXNRD3, and PDP1) did not diminish labeling of any of the fluorescent bands indicating that these proteins were not the targets of interest; the lethal target was thioredoxin protein (**Fig. 2.53C**).

Additionally, the same cell line pairs were subjected to cell viability studies using Annexin V/PI analysis upon 24 incubation with the compounds of interest. As shown in **Figure 2.54**, HCT 116 cells lacking thioredoxin reductase 2 (TXNRD2) and thioredoxin reductase 3 (TXNRD3) conferred modest protection against **ferroptocide**-induced cell death while cells without any PTGES2 protein afforded the highest degree of protection. These findings suggest that these targets could be relevant targets in the **ferroptocide**-elicited cell death pathway. The remaining targets such as PGLS, TXNRD1, and PDP1 appeared to have no effect in the **ferroptocide-**induced mode of cell death. Collectively, these results demonstrate that these targets are not implicated in the mechanism of action of ferroptocide; *TXN* must be evaluated.

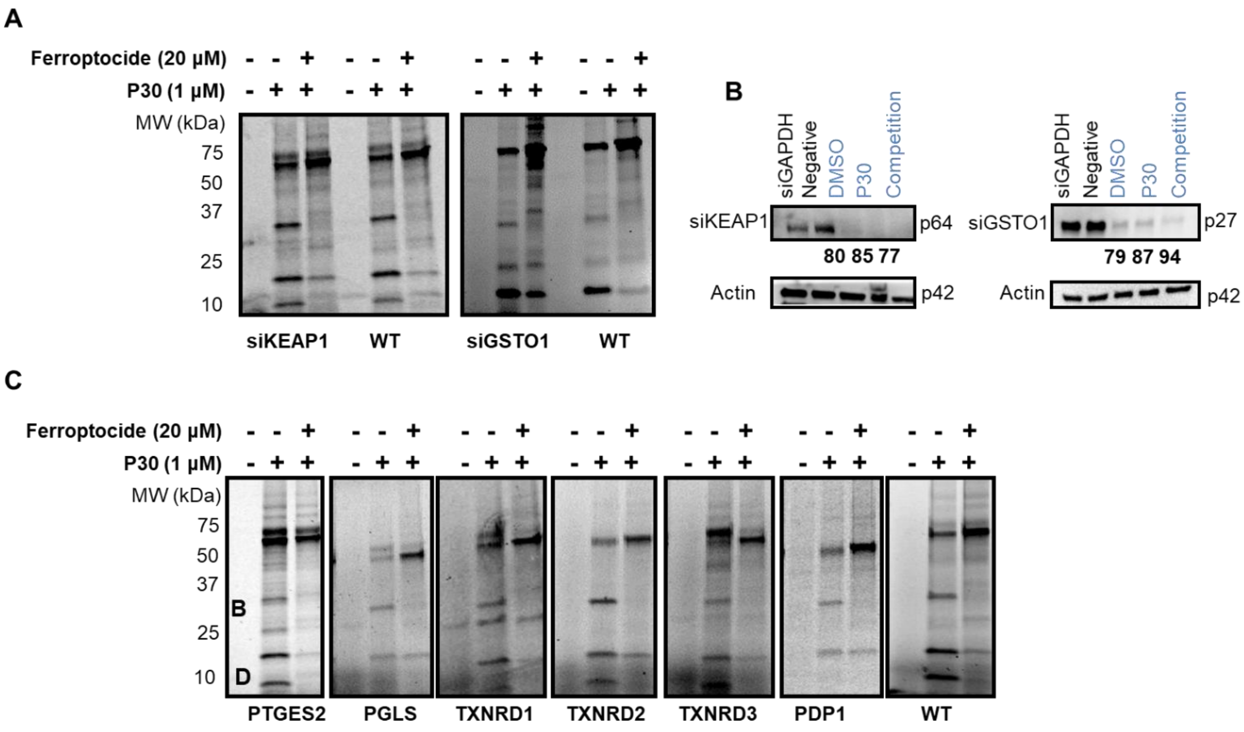

Figure 2.53. (A) Proteomic profiling of probe **P30** (1 µM, 30 min) upon pre-treatment with DMSO or ferroptocide (20 µM, 30 min) in HCT 116 cells after 72 hr siRNA transfection of GSTO1 and KEAP1 targets respectively. Coomassie stain of gels demonstrates equal loading (Supplementary Fig. 2.2). **(B)** Western blot analysis of siRNA knock-down efficiency. GAPDH is a positive control of transfection process and actin is a control of equal protein loading. **(C)** In-gel fluorescence scanning of CRISPR Cas9-generated isogenic cell lines for six targets in HCT 116 cells treated with DMSO or ferroptocide (20 µM, 30 min) followed by 30 min incubation with probe **P30** (1 µM) and separation of proteins via SDS-PAGE gel. Coomassie stain of gels demonstrates equal loading (Supplementary Fig. 2.2).

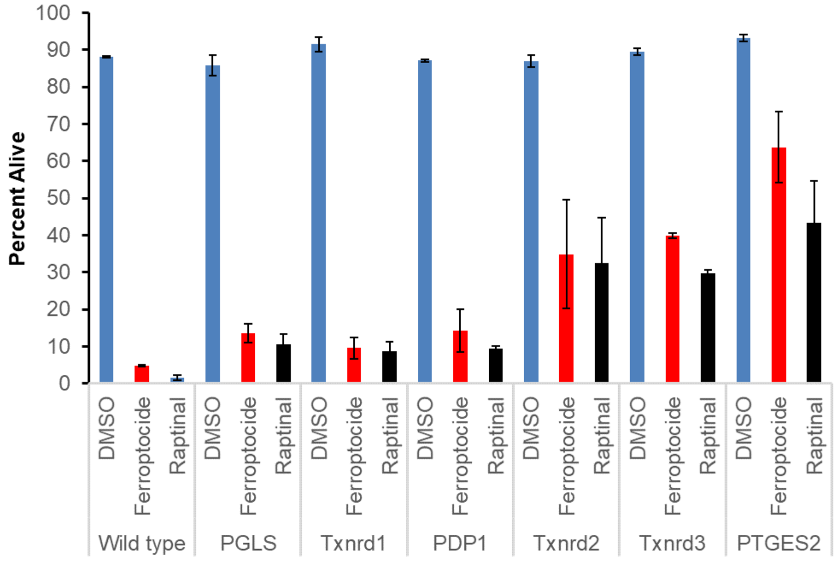

Figure 2.54. Protection studies with CRISPR KO clones of putative targets. HCT 116 cells lacking each of the specified proteins were treated with ferroptocide (10 µM), DMSO, and Raptinal (10 µM) for 24 hr. Cell viability was monitored via Annexin V/PI using flow cytometry. Data represent the average cell viability of 3 biological replicates.

2.9.8 Thioredoxin as a putative target of ferroptocide

Thioredoxin is a 12 kDa ubiquitous oxidoreductase that plays a key role in the thioredoxin antioxidant system comprised of thioredoxin, NADPH, and thioredoxin reductase. This enzyme contains 5 total cysteines and uses its active site cysteines (positions 32 and 35) to reduce the disulfide bonds of many binding partners such as transcription factors (NF-κB, AP-1, Ref-1), ribonucleotide reductases, peroxiredoxins, and glutathione peroxidases in addition to scavenging reactive oxygen species as shown in **Figure 2.55**.[89,90] In addition, thioredoxin is overexpressed in many cancers such as colon[91], gastric[92], renal[93], lung, mesothelioma[94] , non-small cell lung cancer[95], hepatocellular carcinoma[96], etc, so it is an attractive anticancer target in the clinic.

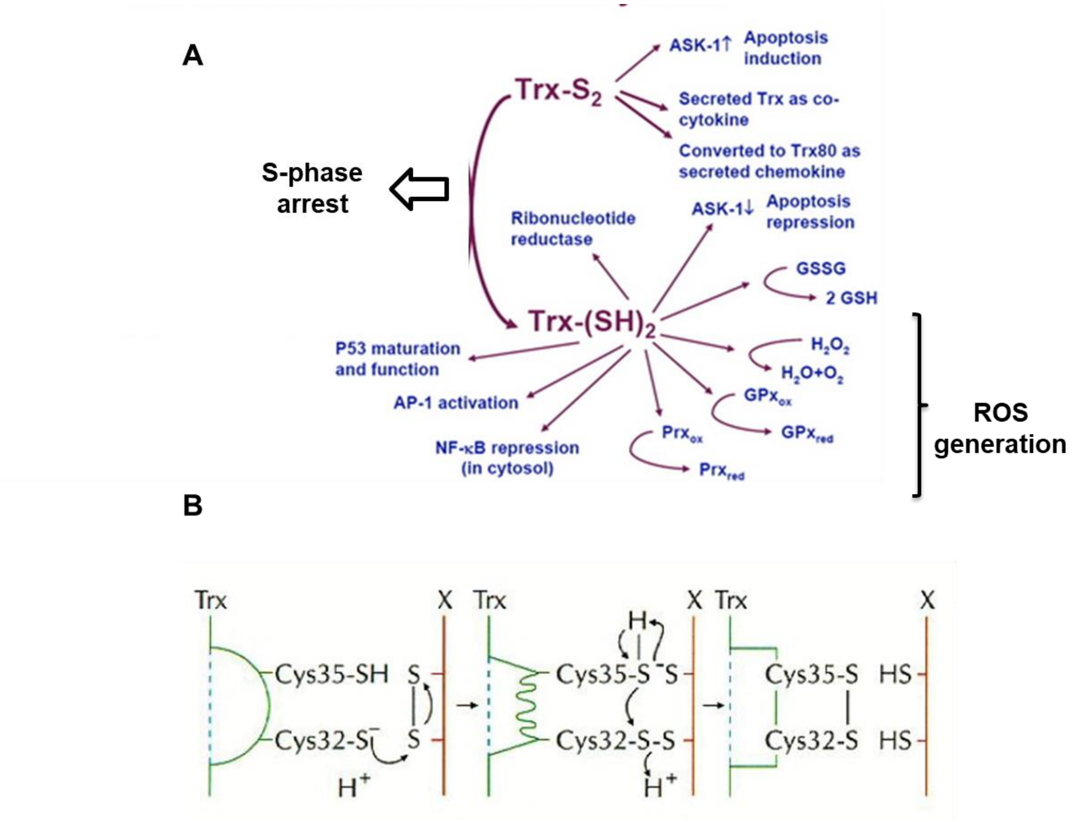

Figure 2.55. Role of thioredoxin in cells. (A) Thioredoxin is a key protein in the thioredoxin antioxidant system in cells that plays a critical role in many cellular processes upon reduction of multiple binding partners such as AP-1, NFκB, ribonucleotide reductase, peroxiredoxins (Prx), glutathione peroxidases (Gpx) etc. **(B)** Mechanism of disulfide bond reduction via thioredoxin. The first step involves nucleophilic attack by Cys 32 to afford an intermediate sulfide bridge between thioredoxin and the binding partner followed by extraction of an H atom from cysteine 35 that results in reduction of the target of interest and oxidation of thioredoxin.

2.9.8.1 TXN pulldown

To investigate thioredoxin as the potential target of **ferroptocide**, the alkyne probe was utilized to conduct a pulldown experiment. Treatment of HCT 116 cells with **P29**, coupled to biotin-streptavidin enrichment followed by immunoblotting yielded a band present only in compound treated sample as shown in **Figure 2.56**, suggesting that **ferroptocide** covalently modifies thioredoxin.

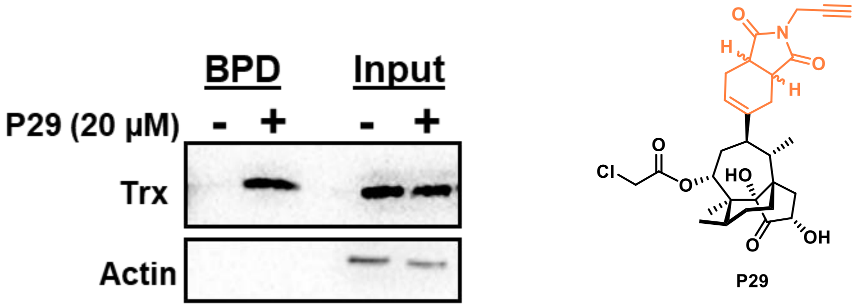

Figure 2.56. Immunoblot of thioredoxin pulldown upon treatment of HCT 116 cells with DMSO or **P29** (20 µM, 60 min) followed by CuAAC reaction with biotin-azide and enrichment with streptavidin magnetic beads. Thioredoxin appeared only in the **P29**-treated samples. BPD (biotin pulldown) and input (soluble cell lysate subjected to pulldown). Images are representative of three biological experiments.

2.9.8.2 TXN activity assay

A thioredoxin activity assay was then employed to assess the ability of **ferroptocide** to inhibit thioredoxin activity in cell lysate, and this compound significantly reduced the activity of thioredoxin within 30 min of treatment in HCT 116 cells to a greater extent than the two known inhibitors of thioredoxin (PMX464 and PX-12)[97-99] as shown in **Figure 2.57A**. Dose-response analysis confirmed that **ferroptocide** is also a more potent thioredoxin inhibitor than PMX464 and PX-12 in a biochemical (*in vitro*) assay (**Fig. 2.57B**).

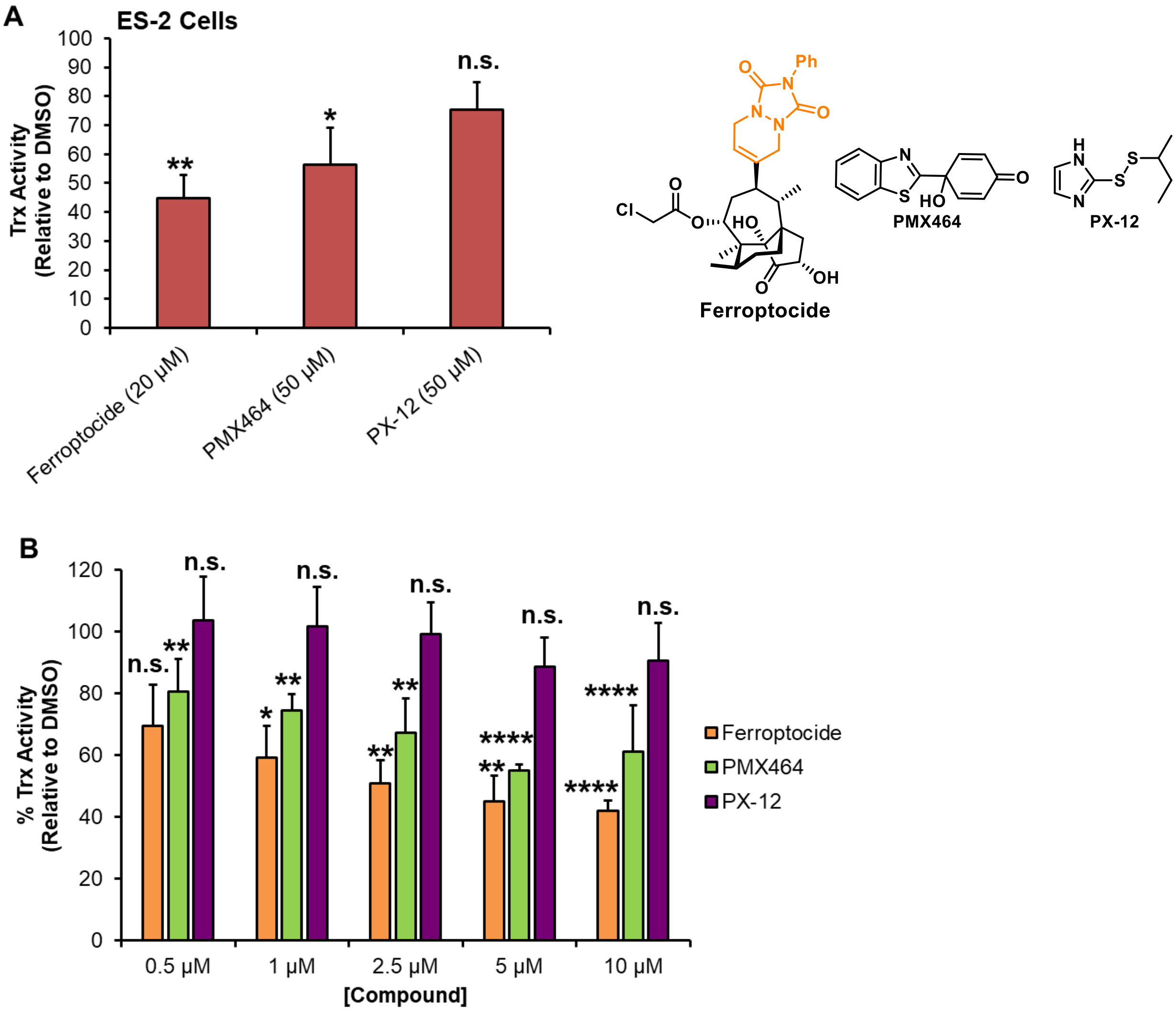

Figure 2.57. Ferroptocide inhibits thioredoxin activity in cells and in vitro. **(A)** Effect of ferroptocide (20 µM) and known inhibitors PMX464 and PX-12 (50 µM) on thioredoxin activity in ES-2 cells after 30 min incubation. p-values are relative to DMSO control. **(B)** Comparing in vitro activity of ferroptocide and known thioredoxin inhibitors, PX-12 and PMX464 to inhibit purified human thioredoxin in a dose-dependent manner after 30 min treatment using a thioredoxin activity kit. Data are plotted as the mean ± s.d., n=3 biologically independent samples. p values are relative to DMSO control, **** $p < 0.0001$, *** $0.0001 < p < 0.001$, ** $0.001 < p < 0.01$ * $0.01 \leq p < 0.05$, n.s. $p > 0.05$.

2.9.8.3 TXN overexpression

Generation of thioredoxin CRISPR KO cells is lethal; thus, to further assess the effect of **ferroptocide** on thioredoxin, thioredoxin fused to GFP (TXN-GFP, 37kDa) was overexpressed in HCT 116 cells as imaged in the GFP channel (**Fig. 2.58 A**). Treatment of these cells with the alkyne probe **P29**, followed by bioconjugation of the orthogonal fluorophore of Cy3, afforded a new band at 37 kDa corresponding to TXN-GFP as visualized in the Cy3 channel (**Fig. 2.58B**). This new band was competed upon pre-treatment with **ferroptocide** for 30 min followed by alkyne treatment suggesting compound specificity for this target and strengthening the hypothesis that thioredoxin is a target of **ferroptocide**.

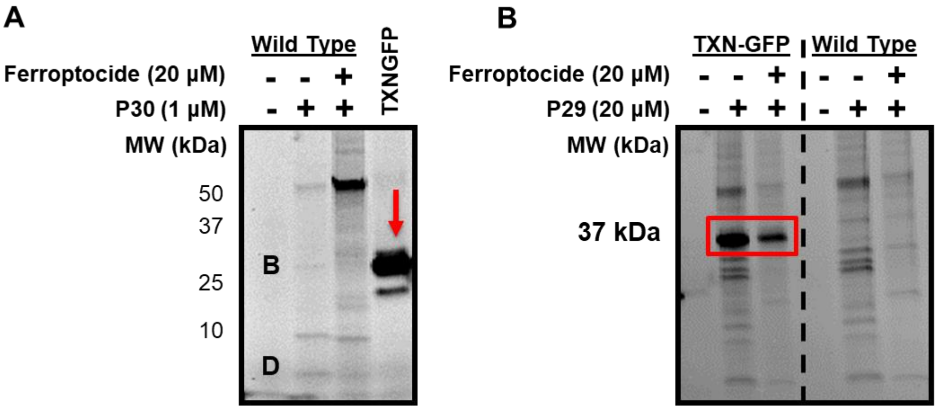

Figure 2.58. Ferroptocide and its analogues bind to thioredoxin in cells. (A) In-gel fluorescence scanning of HCT 116 cells overexpressing TXN-GFP shows a new band (red arrow) at 37 kDa, wild type are non-transfected cells, GFP channel. Coomassie stain of gel demonstrates equal loading (Figure S3). **(B)** Competition profile of thioredoxin labeling by probe **P29** (20 µM, 60 min) upon pre-treatment with DMSO or ferroptocide (20 µM, 30 min) followed by CuAAC with Cy3 azide in HCT 116 cells overexpressing TXN-GFP plasmid vs. non-transfected (wild type) cells, Cy3 channel. Red box indicates competition of the band of interest. Representative in-gel fluorescence images of n=3 biological replicates. Coomassie stain of gel demonstrates equal loading (Supplementary Fig. 2.3).

2.9.8.4 Site-directed mutagenesis

To identify the sites of modification of thioredoxin by **ferroptocide**, site-directed mutagenesis was used to introduce serine mutants of each of the five cysteines of TXN-GFP. The ability of **ferroptocide** to covalently modify these mutant proteins was assessed after transfection of mutant clones (C32S, C35S, C62S, C69S, and C73S, **Fig. 2.59A**) into HCT 116 cells, followed by pre-treatment of these cells with **ferroptocide** and subsequent alkyne treatment and Cy3 bioconjugation to evaluate band labeling via in-gel fluorescence assay. As shown in **Figure 2.59B**, the new band at 37 kDa is not present in the C32S and C35S mutants and has reduced labeling in the C73S mutant, suggesting that **ferroptocide** is modifying the active site cysteines and the adjacent cysteine 73 of thioredoxin as shown in the crystal structure (**Fig 1.59C**).

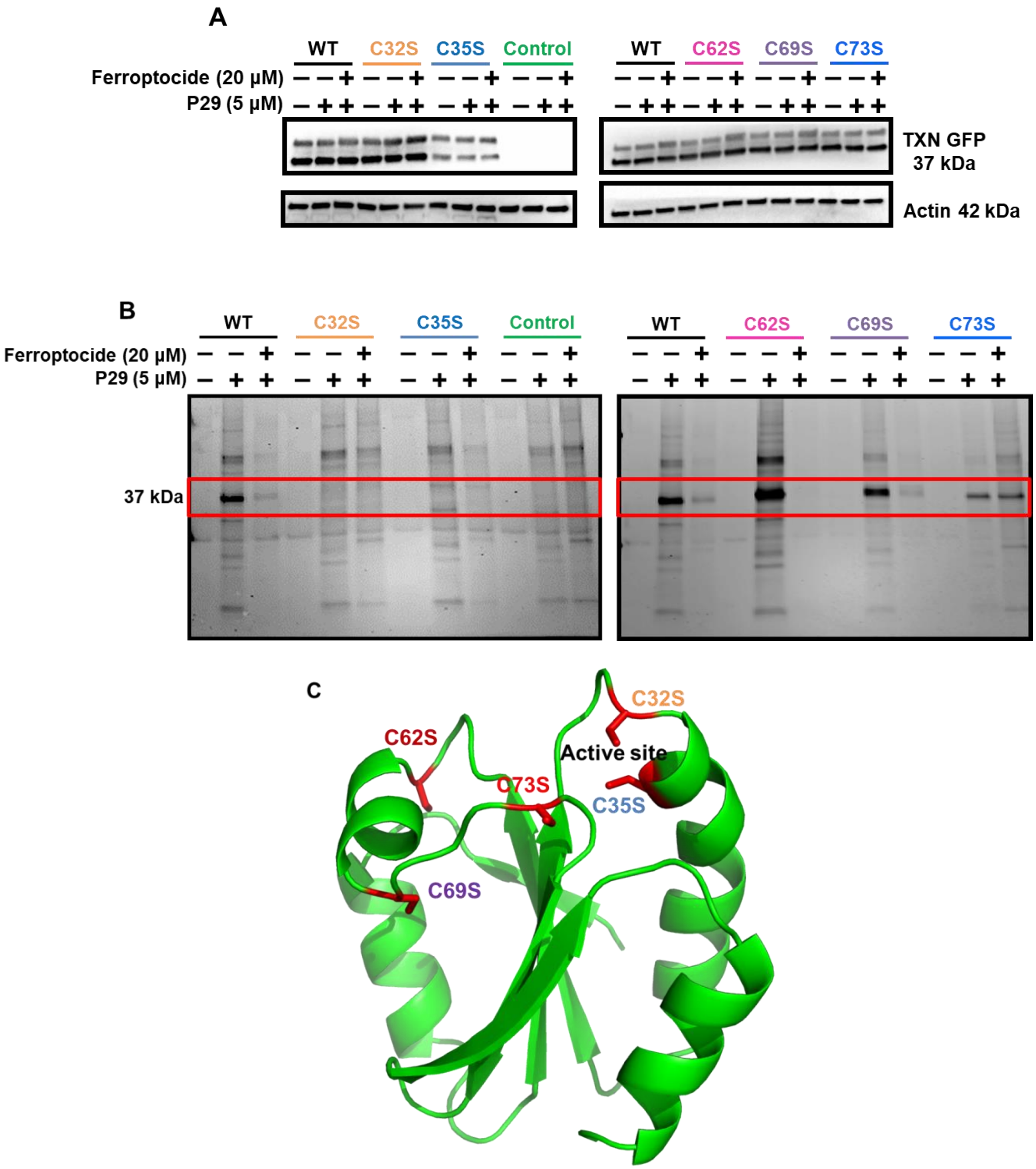

Figure 2.59. Ferroptocide modulates active site cysteines of thioredoxin. (A) Assessing transfection efficiency of HCT 116 cells overexpressing C32S, C35S, empty GFP vector, C62S, C69S, and C73S mutants. WT are non-transfected HCT 116 cells. Data are representative of n=3, biological triplicates. **(B)** Identification of ferroptocide labeling sites of thioredoxin. In-gel fluorescence scanning of HCT 116 cells overexpressing each thioredoxin-mutated cysteine plasmid. Cells were pre-treated with DMSO or ferroptocide (20 μM, 30 min) followed by incubation with **P29** probe (5 μM, 60 min) and then CuAAC reaction with Cy3 azide. The serine mutations of the active site cysteines 32, 35 and cysteine 73 diminished compound labeling. Data are representative of three independent experiments. Coomassie stain of gels demonstrates equal loading (Supplementary Fig. 2.4). **(C)** Crystal structure of thioredoxin with cysteine residues colored in red.

2.9.8.5 TXN and Ferroptosis

Together, these studies demonstrate that treatment with **ferroptocide** modifies critical residues needed for interaction of thioredoxin with its binding partners, and thus inhibiting its activity in cells. This inhibition presumably causes the observed phenotype of rapid ferroptotic cell death. Given that thioredoxin is a key component of a major antioxidant system, it is possible that its modulation renders cells susceptible to oxidative stress that causes lipid peroxidation and other imbalances in cellular processes, eventually leading to ferroptosis; other thioredoxin inhibitors have not been reported to induce ferroptosis.

To investigate this hypothesis, we assessed the cell phenotype upon genetic knockdown of thioredoxin. As shown in **Figure 2.60 A,B**, treatment of HCT 116 cells with siTXN, siGAPDH, and the scramble siRNA (siNeg) resulted in the generation of high levels of general ROS and lipid ROS only for the siTXN samples, supporting our previous hypothesis. The ferroptosis inhibitors (trolox, DFO, Fer-1) were unable to rescue cells from the siTXN-induced cell death potentially due to toxicity of these inhibitors (DFO), the long incubation time needed to genetically modulate the TXN gene in cells (72 hr), and the high levels of accumulated ROS (**Fig. 2.60C**). Furthermore, assessment of the combination of genetic knockdown of thioredoxin with **ferroptocide** resulted in sensitization of HCT 116 cells to compound treatment, leading to rapid cell death (50% cell death at 4 hr vs. 8 hr for siNeg control cells). Together, these data strongly suggest a direct effect of thioredoxin in ferroptocide-induced cell death (**Fig. 2.61**).

In conclusion, these studies implicate thioredoxin in ferroptosis—a new target in the spectrum of ferroptotic cell death—yet detailed future experiments are needed to investigate the role and molecular pathways involved upon thioredoxin-inhibition in ferroptosis.

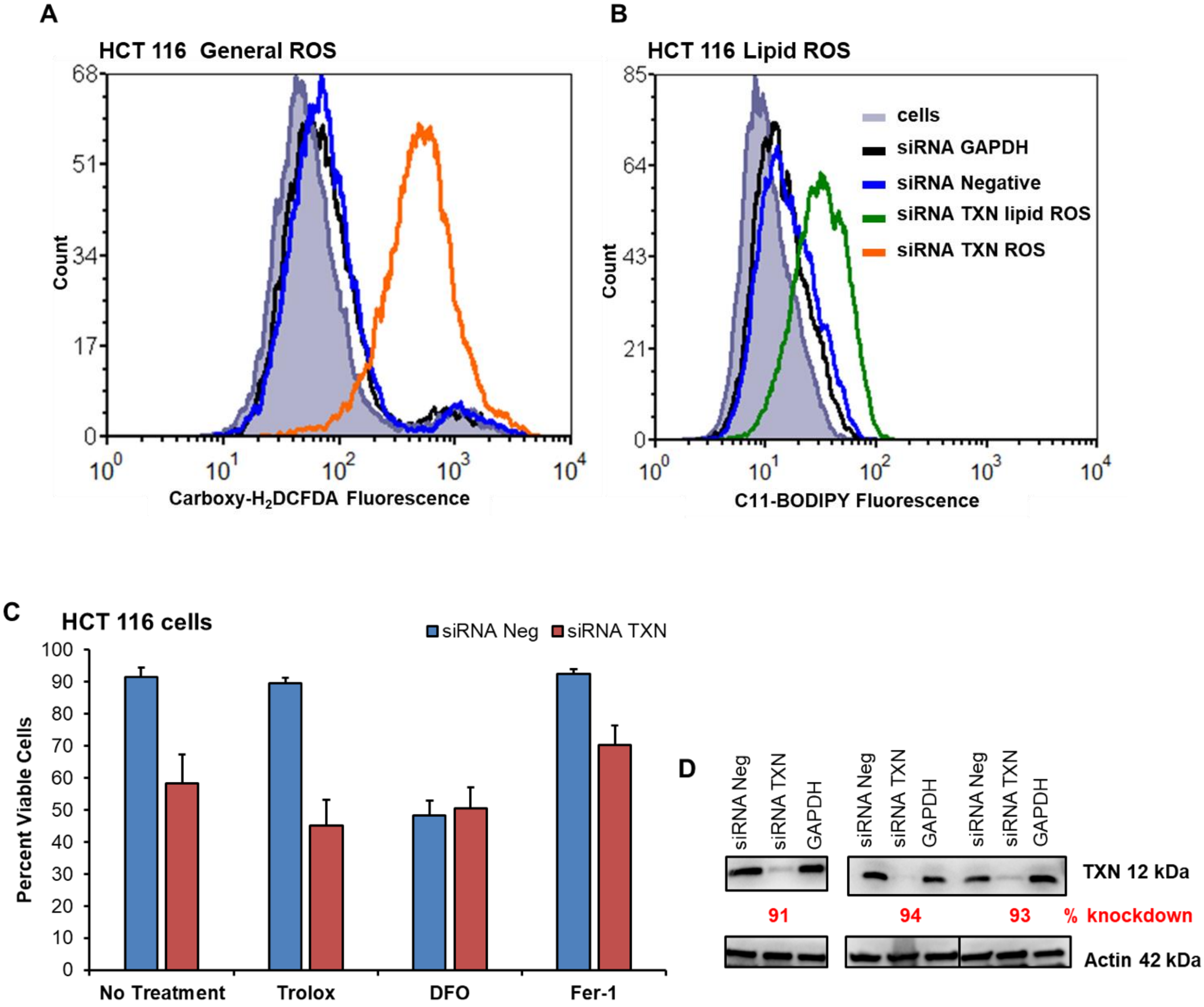

Figure 2.60. Genetic modulation of thioredoxin generates ROS. HCT 116 cells are treated for 72 hr with siRNA for thioredoxin, and the negative controls of GAPDH and scramble negative siRNA. **(A)** General ROS **(B)** lipid ROS were monitored via flow cytometry using carboxy-H2DCFDA and C11-BODIPY. **(C)** Monitoring the ability of ferroptosis inhibitors to rescue HCT 116 cells from cell death after 72 incubation of siTXN. **(D)** Western blot was used to assess the efficiency of the genetic knockdown for all three replicates. Data represent the mean ± s.e.m. are representative of n=3, biological triplicates.

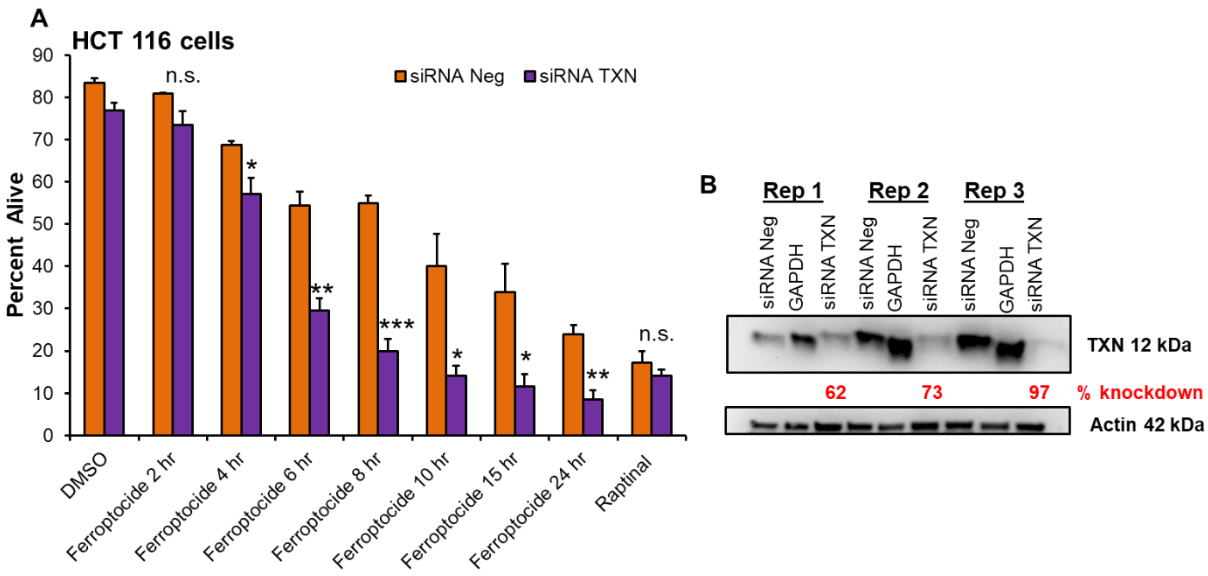

Figure 2.61. Sensitization of siTXN cells to ferroptocide treatmnet. (A) HCT 116 cells were treated for 48 hr with siRNA for thioredoxin, and the scramble negative control. Time course was assessed at the indicated time points after treatment with 10 µM ferroptocide and raptinal (negative control). AV/PI via flow cytometry. **(B)** Western blot was used to assess the efficiency of the genetic knockdown for all three replicates. Data represent the mean ± s.e.m. and are representative of n=3, biological triplicates.

2.10 Evaluation *in vivo*

2.10.1 MTD and PK studies

Given than **ferroptocide** demonstrated promising activity in cell culture, we set out to explore its activity in murine models. First, toxicity studies in C57BL/6 mice were conducted at single doses of 80 mg/kg and 100 mg/kg, which were concluded to be well-tolerated. Multiple-

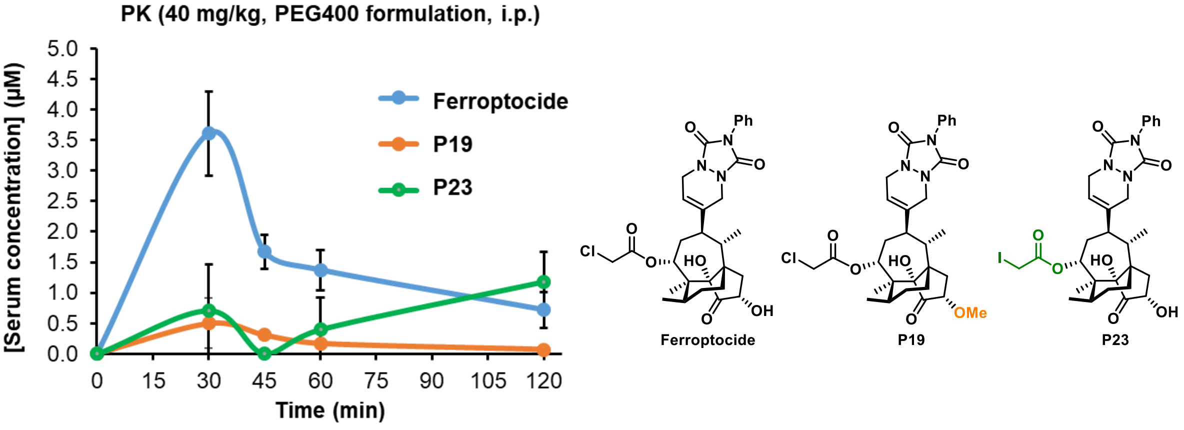

Figure 2.62. Ferroptocide displays the best pharmacokinetic profile. C57BL/6 mice were treated with ferroptocide, **P19**, and **P23** (40 mg/kg) via i.p. injection. Points: mean (n=3), bars: standard error

dose MTD was then established in the same model (3 mice/dose) given once daily (100 mg/kg) for 4 consecutive days. One mouse displayed signs of lethargy and thus was sacrificed on day 5. Upon establishment of a safe MTD (100 mg/kg), the pharmacokinetic (pK) profile of **ferroptocide** was assessed in C57BL/6 mice after intraperitoneal (i.p.) administration of 40 mg/kg of compound. Comparing **ferroptocide** to its **P19** and **P23** analogues (**Fig. 2.62**), **ferroptocide** possessed the best pK profile with a 50 µM C_{max} and half-life of 9.96 min.

Table 2.6. PK parameters of **ferroptocide** (40 mg/kg) in C57BL/6 mice calculated using GraphPad Prism V5.0.

Parameter	Estimate
AUC	422108.3 min*ng/mL
Half-life	9.96 min
Cmax	50 µM

2.10.2 Efficacy model in 4T1

To monitor the therapeutic relevance of **ferroptocide**, a subcutaneous murine model of 4T1 triple negative breast cancer cells in female Balb/c mice was performed. Potent activity of **ferroptocide** in 4T1 (**8.2 ± 0.5 µM**) cells favored their selection for efficacy studies. Upon

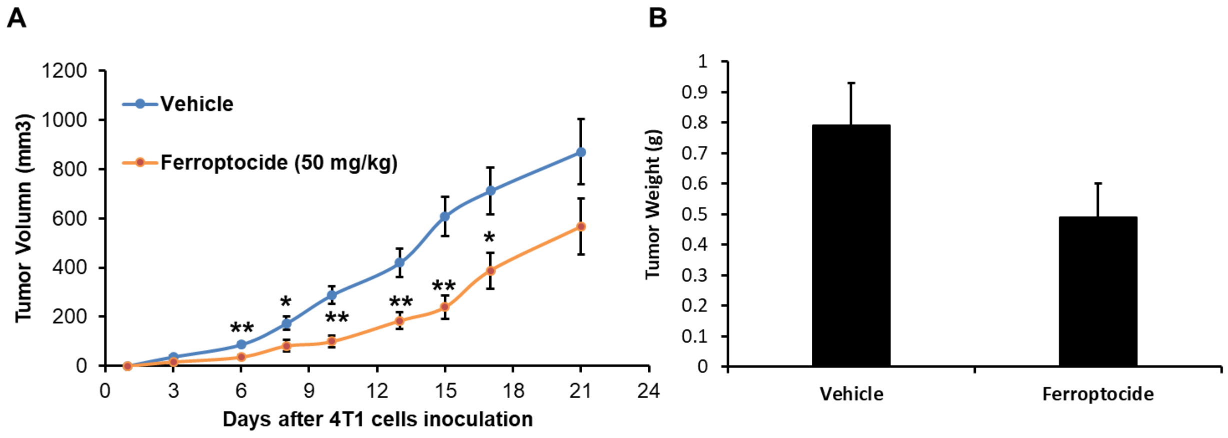

Figure 2.63. Compound inhibits 4T1 tumor growth in vivo as measured by tumor volume **(A)** and tumor mass **(B)** after tumor excision on day 21. Balb/c mice were administered with 50 mg/kg ferroptocide or vehicle. * $0.01 \le p < 0.05$, ** $p < 0.01$ relative to vehicle treatment.

tumor establishment, mice were dosed with 50 mg/kg for 5 doses and were consistently monitored for changes in tumor size and signs of toxicity. As shown in **Fig. 2.63**, treatment with **ferroptocide** retarded tumor growth compared to vehicle control in a statistically significant manner. In addition, there were no signs of toxicity after this dosing regimen.

2.10.3 Activity in immunocompetent and immunocompromised mice

The non-apoptotic nature of **ferroptocide** inspired exploration of its ability to modulate the immune system. Compounds that induce non-apoptotic mode of cell death are attractive anticancer agents, as they could potentially elicit an immune response.[100] We investigated the role of the immune system by assessing the efficacy of **ferroptocide** in a subcutaneous murine model of 4T1 triple negative breast cancer cells in immunocompetent (Balb/c) compared to immunocompromised (SCID) mice. Upon tumor establishment, mice were dosed with 50 mg/kg (twice a week) for five doses before being sacrificed (**Fig. 2.63**). Measurements of tumor volume indicated a 40% tumor growth retardation in compound-treated Balb/c mice compared to vehicle-treated animals. As shown in **Figure 2.64**, there was no effect of **ferroptocide** in immunocompromised mice suggesting that T and B cells play a critical role in the activity of **ferroptocide** in vivo. The potency of **ferroptocide** in this *in vivo* model is likely limited by poor pharmacokinetics in mice (**Table 2.6**).

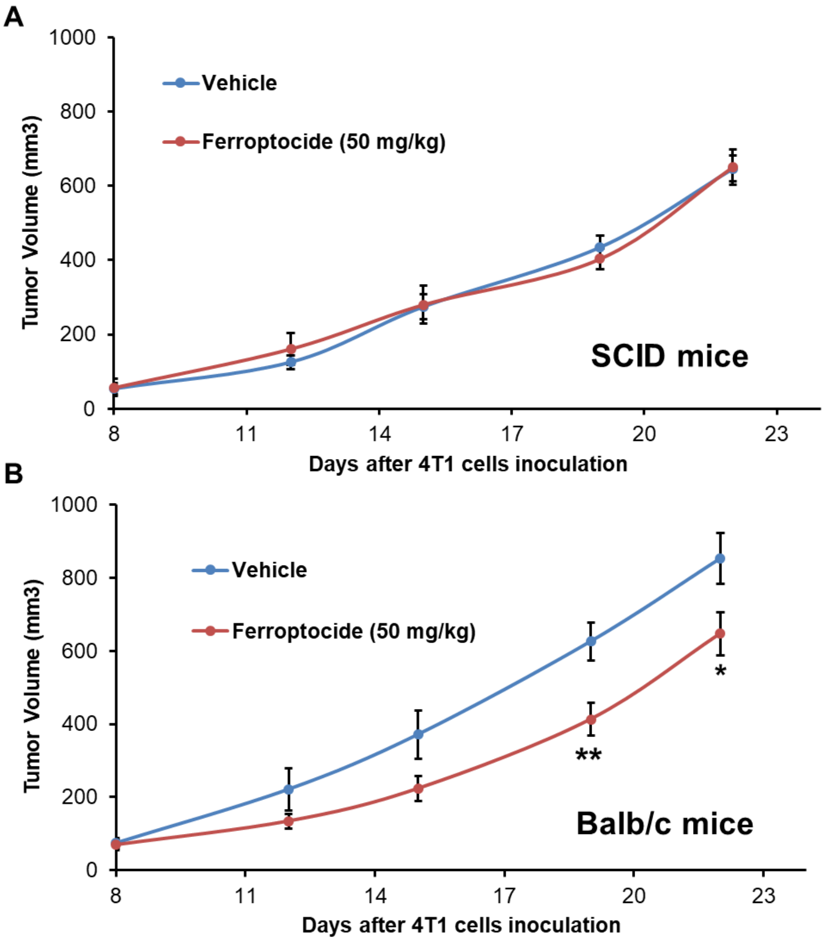

Figure 2.64. Ferroptocide retards tumor growth in immunocompetent mice. Ferroptocide inhibits subcutaneous 4T1 tumor growth in immunocompetent Balb/c mice **(A)** but not in immunodeficient SCID mice **(B)** as measured by tumor volume. Ferroptocide was administered intraperitoneally at 50 mg/kg, twice a week, five doses (n=7 mice per group). Data represent the mean ± s.e.m. p values are relative to vehicle control; ** $p < 0.01$, * $0.01 \leq p < 0.05$

2.11 Conclusions

In this chapter, I have highlighted the motivation, discovery, mechanistic and target identification/validation efforts of a novel tool compound named **ferroptocide**. A series of experiments suggested that **ferroptocide** induces non-apoptotic cell death, which was elucidated to be ferroptosis. Ferroptosis is a newly coined mode of cell death (2012) that has been the focus of many research groups. As described in chapter one, the current landscape of ferroptosis activators can be categorized in two classes including class I: compounds that inhibit system X_C^- and deplete glutathione levels in cells (erastin, sorafenib), and class II: compounds that inactivate GPX4, directly via covalent inhibition (RSL3), or indirectly via degradation (FIN56). **Ferroptocide** is distinct from these published probes as it targets a new target, thioredoxin, in an entirely different antioxidant system in cells.

Excitingly, genetic modulation of thioredoxin in cells caused a similar death profile to that of ferroptocide. Combination studies of genetic knockdown of thioredoxin in colon cancer cells followed by treatment with **ferroptocide** resulted in an increase in sensitization of these cells to compound treatment suggesting a role of thioredoxin in ferroptocide-mediated cell death. The data described herein implicate thioredoxin as a novel target in ferroptosis and call for more in-depth studies to elucidate the direct link between ferroptosis and thioredoxin antioxidant system.

Discovery of ferroptocide is important as it provides a new ferroptotic probe with broad utility regardless of the cell line type. The main issues with the gold standard compounds that are used to study ferroptosis (erastin and RSL3) reside in their limited bioactivity limited to specific cell systems and lack of quantitative cell death. **Ferroptocide** cause quantitative and rapid ferroptotic death, making it invaluable in the chemical biologist toolbox, as it can uravel new mechanistic insights about ferroptosis in cells and in animal models.

Furthermore, given that ferroptosis is a non-apoptotic mode of cell death, it would be of interest to explore if ferroptotic compounds can activate the immune system via the release of DAMP signals. We were able to perform limited experiments to this end, where we discovered that the activity of **ferroptocide** is dependent upon the presence of the immune system. Additional studies are needed to investigate the nature of compound interaction with the immune system, as it can offer insights for use of pro-ferroptotic compounds as a new anticancer strategy in the clinic.

2.12 Supplementary figures

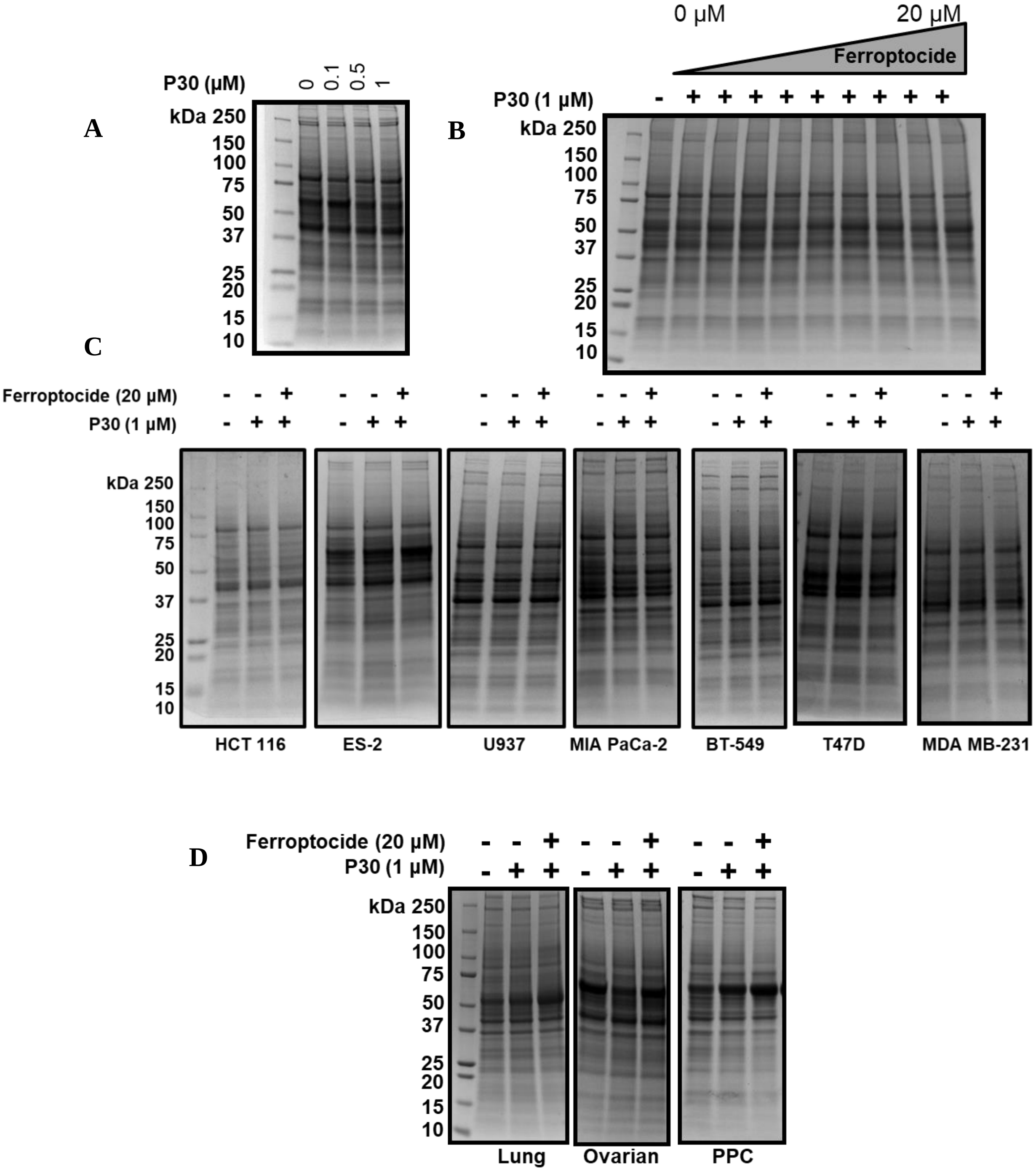

Supplementary Figure 2.1. Coomassie stain corresponding to fluorescence gels in **Fig. 2.35–2.36.**

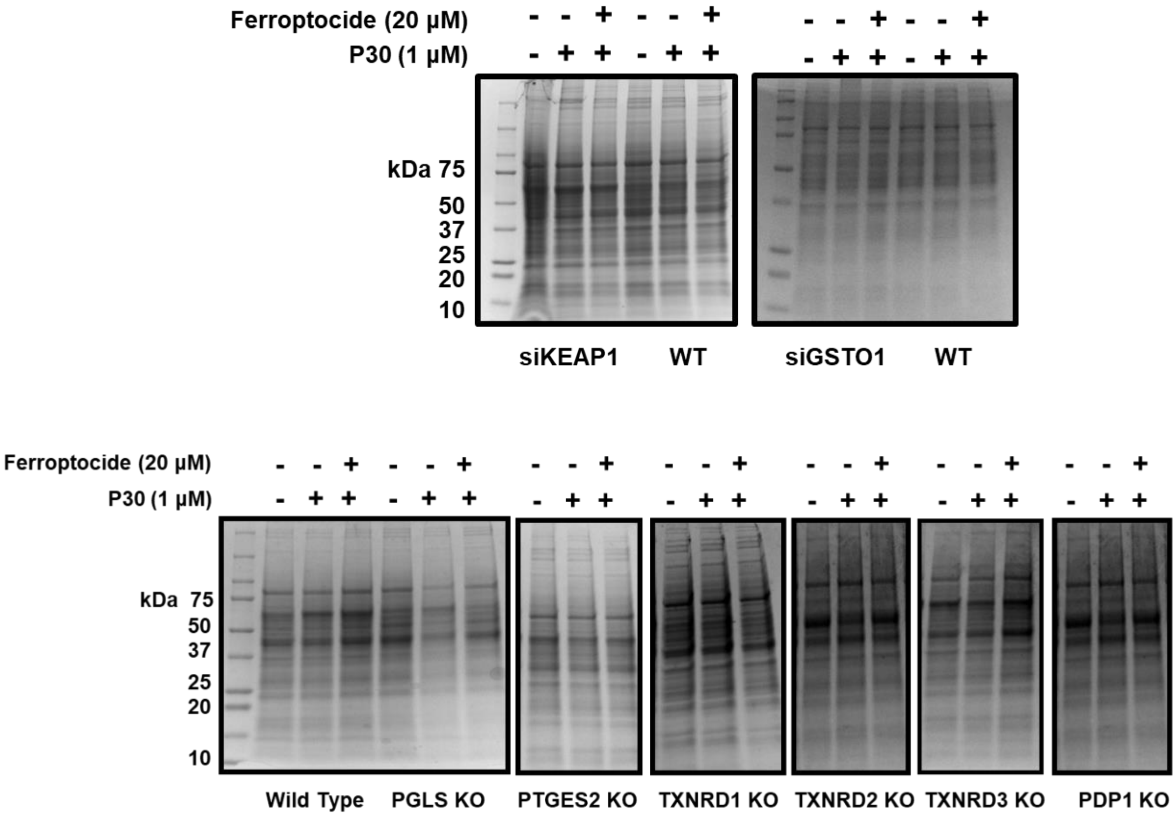

Supplementary Figure 2.2. Coomassie stain corresponding to fluorescence gels in **Fig. 2.53A,C** respectively.

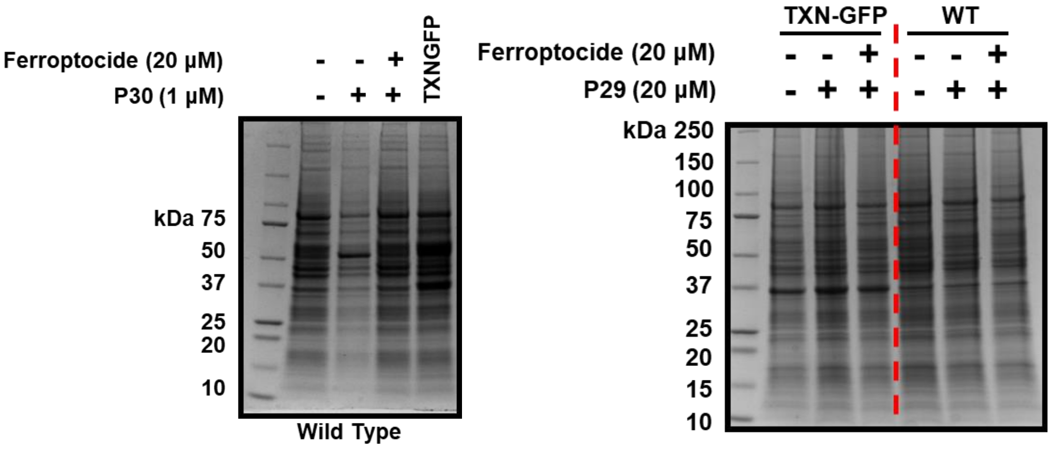

Supplementary Figure 2.3. Coomassie stain corresponding to fluorescence gel in **Fig. 2.58 A,B** respectively.

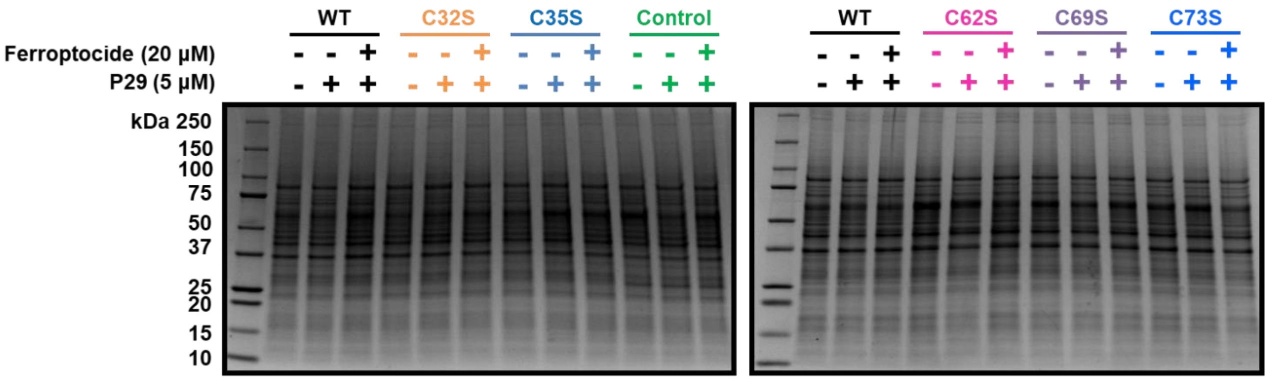

Supplementary Figure 2.4. Coomassie stain corresponding to fluorescence gels in **Fig 2.59B**.

Supplementary Table 2.1. Top 30 Upregulated genes after ferroptocide treatment of HT-29 cells (RNA-seq)

Symbol	Protein	Fold Change A549	FDR A549	Fold Change HT29	FDR HT29
HMOX1	heme oxygenase 1	2.4	2.68E-06	75.4	5.77E-10
NMRAL2P	NmrA like redox sensor 2, pseudogene	1.6	8.40E-03	38.0	1.54E-07
LOC107984862	uncharacterized LOC107984862	1.0	9.38E-01	24.0	1.43E-05
DDIT3	DNA damage inducible transcript 3	1.4	4.78E-04	22.5	7.75E-09
COL4A1	collagen type IV alpha 1 chain	-1.1	6.76E-01	12.8	5.24E-07
OSGIN1	oxidative stress induced growth inhibitor 1	1.4	4.15E-04	12.6	1.24E-08
SLC7A11-AS1	SLC7A11 antisense RNA 1	1.1	7.71E-01	11.7	1.02E-04
ATF3	activating transcription factor 3	1.1	2.76E-01	11.5	2.63E-07
DDIT4	DNA damage inducible transcript 4	1.3	2.54E-03	11.3	1.84E-08
RGPD1	RANBP2-like and GRIP domain containing 1	1.2	9.50E-01	10.3	1.88E-01
IQCJ-SCHIP1	IQCJ-SCHIP1 readthrough	14.7	9.19E-02	10.0	1.44E-01
CHAC1	ChaC glutathione specific gamma-glutamylcyclotransferase 1	2.0	1.50E-04	9.8	2.43E-07
LOC101927088	uncharacterized LOC101927088	1.1	8.19E-01	9.6	3.56E-05
LOC105379516	uncharacterized LOC105379516	1.4	1.54E-01	9.5	2.57E-05
AKR1C2	aldo-keto reductase family 1 member C2	-1.0	8.33E-01	9.4	2.39E-06
PPP1R15A	protein phosphatase 1 regulatory subunit 15A	1.3	7.31E-03	9.1	3.62E-08
GBP1	guanylate binding protein 1	1.0	9.31E-01	8.7	1.74E-05
CBR3	carbonyl reductase 3	-1.1	6.28E-01	8.5	1.73E-06
ULBP1	UL16 binding protein 1	1.9	1.11E-03	8.4	1.26E-06
ADGRE2	adhesion G protein-coupled receptor E2	1.2	9.05E-01	8.4	6.90E-02
HSPA1A	heat shock protein family A (Hsp70) member 1A	2.6	1.33E-05	8.2	1.97E-07
SLC7A11	solute carrier family 7 member 11	1.1	9.20E-02	8.1	3.84E-08
MTRNR2L9	MT-RNR2-like 9	1.2	8.20E-01	8.0	5.23E-03
LUCAT1	lung cancer associated transcript 1 (non-protein coding)	-1.0	8.77E-01	7.9	5.38E-06
LOC101928051	uncharacterized LOC101928051	1.1	7.32E-01	7.9	5.21E-05
SH3BP5	SH3 domain binding protein 5	-1.0	9.63E-01	7.8	4.80E-04
HSPA1B	heat shock protein family A (Hsp70) member 1B	2.6	1.02E-05	7.5	1.97E-07
LURAP1L	leucine rich adaptor protein 1 like	1.1	5.06E-01	7.5	5.43E-07
C14orf132	chromosome 14 open reading frame 132	1.2	9.04E-01	7.4	7.67E-02

FDR: false discovery rate

Supplementary Table 2.2. Top 25 downregulated genes in HT-29 cells after ferroptocide treatment

Symbol	Protein	Fold Change A549	FDR A549	Fold Change HT29	FDR HT29
ADRA2A	adrenoceptor alpha 2A	0.126528	1.4	0.22	-20.3
UBE2F-SCLY	UBE2F-SCLY readthrough (NMD candidate)	-0.5379	1.5	0.50	-16.7
IHH	indian hedgehog	-0.99957	1.0	0.94	-15.0
BDNF	brain derived neurotrophic factor	1.253589	-1.4	0.14	-14.4
LOC107985288	uncharacterized LOC107985288	-0.77767	27.8	0.00	-13.1
SLITRK6	SLIT and NTRK like family member 6	1.199831	-2.4	0.01	-9.8
CD200	CD200 molecule	0.01358	1.0	1.00	-8.6
HOXB8	homeobox B8	4.283369	-1.1	0.46	-8.2
HOXC6	homeobox C6	2.091793	-1.0	0.92	-8.0
SMUG1-AS1	SMUG1 antisense RNA 1	-0.34529	1.0	0.96	-7.6
ABCA1	ATP binding cassette subfamily A member 1	-0.04979	-1.2	0.48	-7.5
FGF19	fibroblast growth factor 19	-0.33648	1.9	0.02	-7.4
SPTBN5	spectrin beta, non-erythrocytic 5	0.489257	1.8	0.43	-6.6
RASL11A	RAS like family 11 member A	2.112077	-1.1	0.47	-6.4
LGR5	leucine rich repeat containing G protein-coupled receptor 5	-0.41022	-1.6	0.16	-6.4
KCNE3	potassium voltage-gated channel subfamily E regulatory subunit 3	1.197479	1.1	0.80	-6.2
SMIM11A	small integral membrane protein 11A	-0.86041	1.0	0.98	-6.0
SOSTDC1	sclerostin domain containing 1	-0.57191	1.2	0.58	-5.9
PRR15L	proline rich 15 like	0.613052	-1.8	0.17	-5.9
RASSF10	Ras association domain family member 10	2.791422	-1.4	0.03	-5.6
ENC1	ectodermal-neural cortex 1	6.727339	-1.2	0.00	-5.5
GPRIN3	GPRIN family member 3	2.717008	-1.5	0.01	-5.5
PKDCC	protein kinase domain containing, cytoplasmic	4.054862	-1.0	1.00	-5.5
HOXA13	homeobox A13	4.085672	-1.1	0.43	-5.5

FDR: false discovery rate

2.13 Materials and methods

Cell culture and reagents: Cells were grown at 37 °C under a humidified 5% CO_2 atmosphere, in a culture medium consisting of high-glucose (Life Technology) DMEM media for Mia PaCa-2, D54, U87, K7-M2, SK-MEL-5, and 3LL cells or RPMI for ES-2, HCT 116, MDA-MB-231, A549, T47D, B16-F10, and BT-549 cells or McCoy’s 5A media for HT29 cells. All media were supplemented with 10% FBS (Gemini), penicillin (50 IU/ml), streptomycin (50 μg/ml) and glutamine (2 mM) (Cellgro). Primary cells were isolated from pleural effusions of metastatic patients at Carle Foundation Hospital (IRB #15149) following a protocol as described previously.[101]

Anticancer screen: 40 µL of media was added to each well of a 384-well tissue culture-treated plate. 3x100 nL of compound in DMSO was then pin-transferred from compound storage plates (2 mM stocks) into media-containing wells using the Platemate Plus at the UIUC High Throughput Screening Facility. A 100,000 cells/mL suspension of ES-2 cells was prepared, and 10 µL was added to each well for a final concentration of 1000 cells/well. Doxorubicin (100 µM final) was used as a positive control. Plates were sealed with gas-permeable seals and incubated at 37 °C for 72 h. After incubation, 5 µL of Alamar blue (440 µM resazurin in sterile PBS) was added and allowed to incubate for 3-4 h, until visible color change occurred. Fluorescence was measured in a Molecular Devices SpectraMax 3 (Ex = 555 nm, emission = 585 nm, emission cutoff = 570 nm).

Dose response (IC_{50}) curves: To a 384-well plate, 40 µL of 1.25X compound dilution or 1.25% DMSO-containing media was added (final volume of 1% DMSO). Concentrations of compounds tested were 100 µM to 100 nM. On each plate at least 3 technical replicates were performed. Next, 10 µL of a 100,000 cells/mL suspension was added to each well, yielding a final concentration of 1,000 cells/well. To three wells in column 2 was added 1 µL of 10 mM doxorubicin (final concentration of 200 µM) as positive control of cell death. Plates were sealed with gas-permeable seals and incubated at 37 ˚C for 72 h. At that time, 5 µL of Alamar blue (440 µM resazurin in sterile PBS) was added and plates were incubated for 3-4 hours. Fluorescence was read on a Molecular Devices SpectraMax 3 (excitation = 555 nm, emission = 585 nm, emission cutoff = 570 nm). Wells were normalized to the average of untreated wells (0% cell death). The data were plotted as compound concentration versus percent dead cells and fitted to a logistic-dose response curve using OriginPro 2015 (OriginLab, Northampton, MA). The data were generated in triplicate, and IC_{50} values are reported as the average of three separate experiments with standard error of the mean.

Hemolysis assay: Whole human blood in citrate phosphate dextrose was obtained from Bioreclamation LLC, stored at 4 ˚C and used before expiration date. 100 µL of whole blood was combined with 500 µL saline (0.9% NaCl) and centrifuged for 5 min at 300xg. The supernatant was carefully removed from the erythrocyte pellet and the liquid was discarded. Washed pellet 3x in 500 µL saline. The erythrocyte pellet was resuspended in 800 µL of Red Blood Cell Buffer (10 mM Na_2HPO_4, 150 mM NaCl, 1 mM $MgCl_2$, pH 7.4). To a 0.5 mL eppendorf tube or a PCR plate was added 1.0 µL of 30X compound in DMSO and 19 µL RBC Buffer. For negative controls, 1.0 µL DMSO was combined with 19 µL RBC buffer. For positive controls, either 20 µL MilliQ H_2O or 1.0 µL 30% Triton X-100 were combined with 19 µL RBC Buffer. Tubes or plates were briefly centrifuged. Next, 10 µL of washed erythrocyte suspension was added to each tube, then sealed. After incubation at 37 ˚C for 2 h, samples were centrifuged for 5 min at 300xg, and 20 µL of supernatant was carefully removed and transferred to wells of a clear flat-bottomed 384-well plate. Absorbance was measured at 540 nm. The data were plotted as compound concentration versus percent hemolysis, and fitted to OriginPro (OriginLab, Northampton, MA).

Western botting. ES-2 and HCT 116 cells were treated with compound for the appropriate amount of time. Cells were harvested by centrifugation (3 min, 500xg), washed with PBS and resuspended in RIPA lysis buffer (50 mM Tris, 150 mM NaCl, 1% Triton X-100, 0.5% Na-deoxycholate, 0.1% SDS, pH = 7.4) containing 1X protease inhibitor cocktail, and 1 mM PMSF on ice. Whole cell lysates were normalized after determining their protein concentration using a

Bradford assay. Samples were resolved in a 4–20% gradient SDS-PAGE gel (Bio-Rad) at 120 V for 1 h, and then transferred to an activated PVDF membrane in Towbin transfer buffer (192 mM glycine, 25 mM Tris-HCl, 20% methanol, pH = 8.3) for 2 h at 45 V. Membranes were blocked overnight at 4 ˚C in 5% milk or bovine serum albumin in TBST (as per primary antibody manufacturer's instruction). Membranes were blotted for molecules of interest with primary antibody (1:1000 in 5% BSA in TBST) overnight at 4 ºC. The bound primary antibodies were detected after using the appropriate secondary HRP conjugated antibodies (1:5000 in TBST) for 1 hour at room temperature. The immunoblots were incubated for 3 min in SuperSignal West Pico Chemiluminescent Substrate (ThermoFisher) mixture before visualization in a ChemiDoc^{TM} Touch Imaging System (Bio-Rad) and processed using ImageLab software (Bio-Rad). Antibodies used: Thioredoxin (Cell Signaling #2429), KEAP-1 (Cell Signaling #8047), GSTO1 (Abcam #129106), Beta-Actin (Cell Signaling #5125), Anti-rabbit IgG HRP linked (Cell Signaling #7074) GAPDH (Cell Signaling #2118), PARP-1 (Cell Signaling # 9532).

Cell viability via flow cytometry: ES-2, HCT 116, Mia PaCa-2, A549, and 4T1 cells (1 x 10^5 cells/mL) were plated overnight in 12 well plates, prior to addition of compounds. For protection studies, samples were pre-treated with each protecting agent such as 25 µM Q-VD-OPh, 250 µM trolox, 2 µM ferrostatin-1, 5 mM NAC-1 (neutralized pH), or 100 µM deferoxamine (DFO) for two hours or 1 hr (NAC-1) before compound addition. Cells were incubated for the appropriate times and harvested for flow cytometry analysis. Cell pellets were resuspended in binding buffer (10 mM HEPES, pH 7.4, 140 mM NaCl, 2.5 mM $CaCl_2$) containing 2 µg/mL propidium iodide and 5 µL/mL Annexin V-FITC conjugate antibody and analyzed for cell viability after gating for forward and side scattering. Ten thousand events were collected per sample in BD LSR II Flow

Cytometer (BD Bioscience) and FCS express V6, De Novo software was used to perform experimental analysis.

Confocal microscopy: ES-2 cells (3 x 10^5 cell) were attached overnight in 1.5 mm petri dish plates containing 2 ml of RPMI media. Prior to imaging, cells were stained for 30 min with Mitotracker Red CMXRoss at 100 nM final concentration. Upon media replacement, samples were treated with 10 µM **P30** or 1 µM BODIPY azide for 30 min followed by a PBS wash. PBS or phenol free media was added to each dish and cells were stained with Hoechst 33342 (1µg/ mL). Samples were visualized and analyzed using Carl Zeiss LSM 700.

Confocal microscopy competition studies: ES-2 cells (3 x 10^5 cell) were attached overnight in 1.5 mm petri dish plates containing 2 ml of RPMI media. Prior to imaging, cells were stained for 30 min with Mitotracker Red CMXRoss at 100 nM final concentration. Upon media replacement, samples were pretreated with 3x IC_{50} of **ferroptocide**, **P27**, **L1**, **QQ1** for 30 min followed by treatment with 5 µM **P30** for an additional 30 min and a PBS wash. PBS or phenol free media was added to each dish and cells were stained with Hoechst 33342 (1µg/ mL). Samples were visualized and analyzed using Carl Zeiss LSM 700.

Transmission electron microscopy (TEM): ES-2 cells (2 x 10^5 cells/mL) were plated overnight in a 6-well plate. Compounds stocks were loaded in DMSO (0.05% final volume), and cells were incubated for 30 min. Following incubation, cells were pelleted at 500xg, for 3 min, and washed with Hank's buffered salt solution (HBSS). Karnovsky's fixative (0.5 mL) was added to cell pellets upon gently mixing and span at 500 xg, 3 min. Samples were stored at 4°C till analysis.

Preparation and imaging of samples was performed by the Center for Microanalysis of Materials of the Frederick Seitz Materials Research Laboratory Central Facilities, University of Illinois. Images of several cells in each sample were taken; displayed images are representative images.

Measurement of cellular ROS production: ES-2 and HCT 116 cells (3 x 10^5 cells/mL) were plated in 6-well plates. Cells were treated with DMSO, **ferroptocide** at the indicated concentrations, Etoposide (100 µM), TBHP (100 µM) for 1hr and 1.5 hr respectively. Cells were washed with HBSS and incubated in the dark for 25 min with 25 µM carboxy-H_2DCFDA probe. Cells were then washed 3x with HBSS and harvested at 1000xg, 3 min. After resuspension in 500 µl HBSS buffer, samples were subjected to flow cytometry to record ten thousand events per sample in FL1 channel in BD LSR II Flow Cytometer (BD Bioscience). FCS express V6 De Novo software was used to generate the histograms.

Measurement of cellular lipid ROS production: ES-2, HCT 116, and 4T1 cells (1 x 10^5 cells/mL) were plated in 12-well plates. Cells were pretreated for 2 hr with 100 µM deferoxamine followed by treatment with DMSO, 10 µM **ferroptocide**, 10 µM RSL3, or 100 µM TBHP for 1hr, 1.5 hr and 2,4,6 hr respectively. Cells were washed with HBSS and incubated in the dark for 20 min with 5 µM C11-BODIPY probe. Cells were then washed 2x with HBSS and harvested at 1000xg, 3 min. After resuspension in 500 µl HBSS buffer, samples were analyzed with flow cytometry to record ten thousand events per sample in FL1 channel in BD LSR II Flow Cytometer (BD Bioscience). FCS express V6 De Novo software was used to generate histograms.

Measurement of mitochondrial ROS production: ES-2 cells (1 x 10^5 cells/mL) were plated in 12-well plates and allowed to attach overnight. Cells were treated for 1 hr with DMSO, 10 and 25 µM **ferroptocide**, 5 µM IB-DNQ, and 10 µM rotenone. Cells were washed with HBSS and incubated in the dark for 10 min with 5 µM MitoSOX Red probe. Cells were then washed 2x with HBSS and harvested at 1000xg, 3 min. After resuspension in 500 µl HBSS buffer, samples were analyzed with flow cytometry to record ten thousand events per sample in PE channel in BD LSR II Flow Cytometer (BD Bioscience). FCS express V6 De Novo software was used to generate the histogram.

GPX4 LC-MS based activity assay: 1 million ES-2 cells/ well, 6 well plate were allowed to attach overnight and then treated with DMSO, 10 µM of each compound: ferroptocide, raptinal, and RSL3 for 1 hr. GPX4 enzymatic activity assay was performed with a GPX4 specific substrate, phosphatidyl choline hydroperoxide (PC-OOH) as described previously with minor modifications.[64] PCOOH was prepared as reported by Roveri and coworkers but using soybean lipoxidase type I-B (L7395, Milipore Sigma).[102] Cells were washed with PBS and lysed by liquid nitrogen freeze-thaw method in the assay buffer (137 mM NaCl, 2.7 mM KCl, 8 mM Na_2HPO_4, 2 mM KH_2PO_4, 1mM EDTA, 0.1 mM DFO; pH 7.4). Cell lysates were cleared by centrifugation at 14,000 rpm for 10 min at 4°C. Bradford assay was used to determine protein concentration; 200 µg of protein or assay buffer (PCOOH control sample) was mixed with 10 µL PC-OOH in methanol, 5mM reduced glutathione, and assay buffer to a final reaction volume of 500 µL. The reaction mixture was incubated at 37°C for 15 mins and extracted with 250 µL chloroform:methanol (2:1) solution. The lipid extract was evaporated under nitrogen and re-dissolved in 100% methanol before injecting into the LC-MS/MS for PCOOH detection.

In vitro glutathione assay: To an eppendorf tube added, 245 µL of 1X PBS, 5 µL of 10 mM DMSO stock of **ferroptocide** or **P23**, 250 µL of reduced GSH (5mM final concentration). Reactions were vortexed briefly and incubated at 37°C. Adduct formation was monitored at the indicated time points (0, 0.5, 1, 2, 3, 24 hr) by mixing an aliquot of 50 µL from the reaction mixture with 50 µL of MeOH before LC/MS analysis.

Cell Fractionation: Cells (ES-2, HCT 116) were grown to confluency in a T-25 flask (7 million cells), collected by centrifugation and washed with PBS. Cell fractionation was performed as instructed in the Cell Signaling Cell Fractionation kit (9038S).

Isolation of Mitochondria: Cells (ES-2, HCT 116) were grown to confluency in a T-75 flask (20 million cells), collected by centrifugation, and washed with PBS. Mitochondria were isolated using the ThermoScientific Mitochondria Isolation kit (#89874) as instructed.

Cell cycle studies: Cells (500k/ well, 12 well) were grown to confluency and treated with compound at the indicated concentrations. Samples were collected by centrifugation and washed with PBS. After aspirating off the media, cells were fixed with cold 70% ethanol (1mL) and saved at 4°C. Samples were span at 1700g, 7 min, washed with PBS, and incubated for 1 hr at r.t. with 50 µL of RNAse (1mg/ml). After addition of 300 µl of PI (50 µg/mL), samples were analyzed via flow cytometry. For cell synchronization studies, cells were cultured at 0.2% FBS (gradually).

ɣH2AX studies: Cells (200k/ well, 12 well) were treated with compounds at the indicated concentrations, fixed and permeabilized with 70% ethanol at 4°C. Samples were washed 2x with cell staining buffer (Biolegend, #420201) and PBS 1x. Upon addition of ɣ-H2AX-FITC at 1:20 ratio (Biolegend, #613403) in 500 µl of cell staining buffer for 1 hr at 4 degrees, samples were washed with PBS and treated with 300 µl of PI (50 µg/mL). Samples were analyzed via flow.

Antibody pulldown studies: 1 million cells (ES-2, HCT 116) were treated with compound (1 µM) for 30 min. Cells were lysed with 0.5% CHAPS in HEPES (with protease inhibitor) buffer and protein concentration was determined via Bradford assay. Dynobead magnetic beads (Thermofisher #11203D, activated per manufacturer's instructions) were incubated with 1 µl of BODIPY (Thermofisher #A-5770) or ETFA (Abcam #ab126131) antibody for 48 hr at 4°C in immunoprecipitation buffer (20 mM Tris, 150 mM NaCl, 1% NP-40, 1 mM EDTA, 5% glycerol, pH=7.5). 100 µg of protein were added to beads after 2x wash and incubated 48–72 hr in a shaker at 4°C. After incubation, supernatant was saved, beads were washed with buffer, and eluted with SDS laemmli dye. Samples were denatured at 95°C, 5 min and loaded without beads (15 µl) in a 4–20% gel. In-gel fluorescence labeling was monitored before and after the pulldown.

CETSA studies: Cells (ES-2, HCT 116) were grown to confluency (300k cells/tube), treated with DMSO or ferroptocide (20 µM) for 30 min, collected by centrifugation, and washed with PBS. CETSA protocol was followed as described by Molina and coworkers.[103] Briefly, upon addition of 40 µl of PBS containing protease inhibitor, samples were heated at the indicated temp for 3 min and cooled off at room temp. for another 3 min. Lysing was performed via liqiuid nitrogen flash-freezing method (3x), and soluble fraction was isolated after centrifugation at max speed for 20 min at 4°C. (Note: cell pellets can be saved at -80°C overnight after freezing with liquid nitrogen). Upon removal of 20 µl of each sample and addition of 5 µl of laemmli dye, samples were denatured at 70 °C for 10 min. Samples were then loaded in a 12% gel and subjected to western blot analysis as described here. ETFA antibody (1:3000) for >12 hr at 4 °C.

In-gel fluorescence. HCT 116 cells (3 x 10^5 cells/mL) were treated with DMSO or 20 µM **ferroptocide** for 30 min followed by 30 min treatment with 1 µM **P30** in 6-well plates (final DMSO concentration of 0.5%). Cells were harvested by centrifugation (500xg, 3 min), washed with PBS, and resuspended in RIPA lysis buffer (50 mM Tris, 150 mM NaCl, 1% Triton X-100, 0.5% Na-deoxycholate, 0.1% SDS, pH = 7.4) containing 1X protease inhibitor cocktail on ice. Protein concentration was determined by the Bradford assay and lysates were stored at -20 ˚C until further use. Samples were resolved in a 4–20% SDS-PAGE gel (Bio-Rad) at 120 V for 70 min. After PBS washes, each gel was scanned for fluorescence signal using a Molecular Dynamics Typhoon 9400 Multilaser Scanner at the Proteomics Center at UIUC (excitation at 526 nm, green laser, high sensitivity, 530 pmt). Gels were then treated with Coomassie Blue stain (Imperial Stain, ThermoFisher) via shaking for 45 min to stain for total protein content. Upon proteome labeling, gels were destained for 15 min–overnight on MilliQ H_2O followed by imaging in a Gel Dox XR+ from Bio-Rad (ex. 470 nm, UV High filter).

Biotin-streptavidin pulldown for target ID[78]: ES-2 and HCT 116 (20 x 10^6 cells/flask) were plated in T175 flasks and treated with DMSO or 20 µM **ferroptocide** for 1 hr followed by treatment with 20 µM **P29** for 1 hr. Cells were lysed via sonication (6500g, 4 min) in DPBS and the soluble proteome was isolated after ultrasonication (45000g, 45 min). Bradford assay was used to determine protein concentration. The soluble protein lysates in DPBS (pH 7.4) (500 µL, 2 mg/mL) were treated with biotin-azide (100 µM, 50X stock in DMSO), TCEP (1 mM, 50X fresh stock in water), TBTA ligand (100 µM, 17X stock in DMSO:t-butanol = 1:4), and copper(II) sulfate (1 mM, 50X stock in water) followed by incubation at r.t. for 1 hr. Samples were centrifuged (6500 g, 4 min, 4 °C) and the supernatant was discarded. The pellets were resuspended in cold methanol by sonication (2x) and then were solubilized in DPBS containing 1.2% SDS via sonication and heating (90 °C, 5 min). A final SDS concentration of 0.2% was achieved after addition of 5 mL of DPBS to the SDS-solubilized proteome samples. The solution was incubated overnight at 4 °C with 100 µL of streptavidin-agarose beads (ThermoFisher, washed 3X with DPBS to remove storage buffer). Samples were rotated at 22 °C for 2 hr before being washed by 5 mL 0.2 % SDS/DPBS, 3 X 5 mL DPBS, and 3 X 5 mL water. The beads were pelleted by centrifugation (1400 X g, 3 min) between washes.

On Bead trypsin digestion

The washed beads were suspended in 500 µL of 6 M urea/DPBS and 10 mM DTT (from 20X stock in water) and heated for 20 min on a 65 °C heat block. Upon addition of iodoacetamide (20 mM from 50X stock in water), samples were allowed to react at 37 °C for 30 min while shaking. Following reduction and alkylation, the beads were pelleted by centrifugation and resuspended in 200 µL of 2 M urea/DPBS, 1 mM $CaCl_2$ (100X stock in water), and sequencing-grade trypsin (2 µg). The bead digestion occured overnight at 37 °C while shaking. Next day, the beads were pelleted by centrifugation and washed with 2 X 50 µL water. The washes were combined with the supernatant from the trypsin digestion step, and after addition of formic acid (15 µL) to each sample, they were stored at -20 °C until mass spectrometry analysis.

Liquid Chromatography- Mass spectrometry Analysis

LC/LC-MS/MS analysis was performed on an LTQ-Orbitrap Discovery mass spectrometer (ThermoFisher) coupled to an Agilent 1200 series HPLC. Peptide digests were pressure loaded onto a 250 μm fused silica desalting column packed with 4 cm of Aqua C18 reverse phase resin (Phenomenex). The peptides were eluted onto a biphasic column (100 μm fused silica with a 5 μ, tip, packed with 10 cm C18 and 4 cm Partisphere strong cation exchange resin (SCX, Whatman) using a gradient 5-100% Buffer B in Buffer A (Buffer A: 95% water, 5% acetonitrile, 0.1% formic acid; Buffer B: 20% water, 80% acetonitrile, 0.1% formic acid). The peptides were then eluted from the SCX onto the C18 resin and into the mass spectrometer using 4 salt steps previously described.[104] The flow rate through the column was set to ~0.25 μL/min and the spray voltage was set to 2.75 kV. One full MS scan (FTMS) (400-1800 MW) was followed by 8 data dependent scans (ITMS) of the nth most intense ions. The tandem MS data were searched using the SEQUEST algorithm using a concatenated target/decoy variant of the human UniProt database. A static modification of +57.02146 on cysteine was specified to account for alkylation by iodoacetamide. MS2 spectra matches were assembled into protein identifications and filtered using DTASelect2.0 to generate a list of protein hits with a peptide false-discovery rate of 5%.

Generation of CRISPR-mediated knockout HCT 116 cell lines:

TXNRD3, TXNRD2, TXNRD1, PTGES2, PGLS, PDP1 KO cell lines were generated using CRISPR Cas9 nature protocol.[105] In brief, sgRNAs targeting TXNRD3, TXNRD2, TXNRD1, PTGES2, PGLS, PDP1, and TXN (described in table below) were designed, amplified, and cloned into P2-gRNA (from Perez lab) in a one-pot reaction as described previously.[106] Plasmid DNA was isolated using the QIAminiprep kit (QIAGEN cat # 27104) according to manufacturer's recommendation. HCT 116 cells (3 x10^5 cells/ mL) were transfected for 48 hr with specific plasmids (gene of interest [GOI] sgRNA, empty vector GFP, TV puro, TV hygro, Cas9, pAB059) using lipofectamine transfection agent following manufactures protocol. After 7-10 days of puromycin and hygromycin double selection, clonal cells were isolated, expanded and analyzed for KO efficiency of GOI using a three-way PCR as described previously[107] using GOI fwd primer, GOI rev primer, and GFP rev primer ww443. Desired clonal cells were used for downstream analysis as described in the in-gel fluorescence experiment above.

Supplementary Table 2.3. Sequences of sgRNAs used for generation of isogenic cell lines.

sgRNA	**Sequence**
TXNRD3 Fwd	CACCGACACTCAATCGTGCCCTCAC
TXNRD3 Rev	AAACGTGAGGGCACGATTGAGTGTC
TXNRD2 Fwd	CACCGATTAGGAGGGCGCTTCCGG
TXNRD2 Rev	AAACCCGGAAGCGCCCTCCTAATC
TXNRD1 Fwd	CACCGAGAACGGCGATGGCCGCCGT
TXNRD1 Rev	AAACACGGCGGCCATCGCCGTTCTC
PTGES2 Fwd	CACCGCGCCGTGTGGTACAGCCCC
PTGES2 Rev	AAACGGGGCTGTACCACACGGCGC
PGLS Fwd	CACCGCGTGCTCTCGGCGTGATCGA
PGLS Rev	AAACTCGATCACGCCGAGAGCACGC
PDP1 Fwd	CACCGAACGATTCTTCCCGACGAGG
PDP1 Rev	AA CCCTCGTCGGGAAGAATCGTT C
TXN Fwd	CACCGTACTTCAAGGAATATCACGT
TXN Rev	AAACACGTGATATTCCTTGAAGTAC

Supplementary Table 2.4. Sequences of primers used for generation of isogenic cell lines.

Primer	**Sequence**
TXNRD3 Fwd	TCA GAT TGC AGC GGG ATG TT
TXNRD3 Rev	GCT GTT AAA AAC CGG CCT CC
TXNRD2 Fwd	CCT ATC CCA GTG TTC CAC CC
TXNRD2 Rev	GAG ACC ACA GGT GCA GTC AG
TXNRD1 Fwd	TGG CCT GTG GGA CTT AAA TGG
TXNRD1 Rev	CGA GTA GCT GCG ACT ACA GG
PTGES2 Fwd	CTG CAG CTC GTA AGG GGA G
PTGES2 Rev	GGG GTG AGC CTA TAG TCC CA
PGLS Fwd	TTC TCG AGT TCC CAG GAG CT
PGLS Rev	TTG GCA TGA TAC CCA GTG GC
PDP1 exon 3 Fwd	CTC CCC TCC CAC TCG TCA
PDP1 exon 3 Rev	CCT CCC TGG AGC TCA CTC T
TXN Fwd	CCC ACA TTG AAA CAT GGG CC
TXN Rev	TGG TGA CTC CAT CAA GCC TAT G
ww443 GFP rev	TGCCCTTGTCTTGTAGTTTCC
Ab299 PuroR1	CCTGACTGTGGGCTTGTAT
Ab297 HygroR1	GCGGTGAGTTCAGGCTTTTT
T7 Primer	TAATACGACTCACTATAGGG

siRNA transfection: HCT 116 cells (1 x 10^5 cells/mL) were transfected for 72 hr with 5 nM of GSTO1 (silencer select #s18089, ThermoFisher), KEAP1 (silencer select #s18981 ThermoFisher), GAPDH as positive control (silencer select #4390849, ThermoFisher) or negative control siRNA (Qiagen, #1027280) following the Interferin polyplus transfection protocol. Cells were then pretreated for 30 min with DMSO or 20 μM **ferroptocide** followed by 30 min treatment with 1 μM **P30.** Cells were harvested, washed and subjected to in gel-fluorescence studies as described above. siRNA transfection efficiency was assessed via western blot analysis.

Studies with siRNA transfection of thioredoxin: HCT 116 cells (1 x 10^5 cells/mL) were transfected for 72 hr or 48 hr with 5 nM of TXN (silencer select #s1 4390824, ThermoFisher), GAPDH as positive control (silencer select #4390849, ThermoFisher) or negative control siRNA (Qiagen, #1027280) following the Interferin polyplus transfection protocol. Cells were then used to monitor general and lipid ROS accumulation or time course cell viability studies respectively using flow cytometry as described in this manuscript. In the time course studies, cells were treated with DMSO, 10 µM **ferroptocide,** 10 µM raptinal at the indicated time points, followed by AV/PI analysis.

In the case of protection studies, same transfection protocol was followed (72 hr, 5nM siTXN, siGAPDH, siNegative) after pretreatment of HCT 116 cells with 250 µM trolox, 100 µM deferoxamine (DFO), or 2 µM ferrostatin-1 for two hours. siRNA transfection efficiency for all experiments was assessed via western blot analysis.

Thioredoxin validation via pulldown: HCT 116 cells (1 x 10^6 cells/flask) in T25 flasks were treated with DMSO or 20 µM **ferroptocide** for 30 min followed by a 60 min treatment with 20 µM **P29**. Cells were lysed via sonication in PBS and the soluble proteome (100 µg) was subjected to click reactions with 400 µM biotin-azide, 1 mM TCEP freshly made, 100 µM THPTA, 1 mM $CuSO_4$ at r.t. for 60 min. Samples were quenched with 70% cold ethanol, centrifuged at 6500xg, 4 min and supernatant was discarded. The pellets were solubilized in 1.2% SDS/PBS solution by heating (90 °C, 5 min). Pierce streptavidin magnetic beads (50 µL) were activated per manufacturer's recommendation and added to each sample in addition to 500 µL of PBS to achieve a final 0.2% SDS concentration. After rotating for 12 hr at 4 °C, proteins of interest were eluted with 2x SDS laemmli dye. Proteins were resolved in 4-20% gradient SDS gel (120V, 60 min), transferred in activated immunoblot membranes, blocked in 5% BSA TBS-T, and incubated overnight with thioredoxin antibody (1:1000). Membranes labeled with the primary antibody thioredoxin (Cell Signaling # 229) and Beta-actin (Cell Signaling #5125) were then incubated with anti-rabbit HRP-conjugated antibody (Cell signaling #7074) diluted 1:3,000 for 60 min and washed with TBS-T for 2x10 min. Membranes were visualized using the Pico Plus Chemiluminescence Kit (#3477 ThermoFisher); images were captured using a ChemiDoc^{TM} Touch Imaging System (Bio-Rad) and processed using ImageLab software (Bio-Rad).

TXNGFP and TXNGFP mutants in-gel fluorescence: HCT 116 cells (3 x 10^5 cells/mL) at 80% confluency in 6 well plates, were transfected with 2.5 µg TXNGFP, empty vector GFP, or cysteine to serine mutant plasmid DNA for 24 hr (jetPRIME, Polyplus). Cells were then pretreated with DMSO or 20 µM **ferroptocide** followed by treatment with 20 µM **P29** for 1 hr. 50 µg of cell lysate was subjected to click conditions (freshly made 1mM TCEP, 100 µM THPTA, 1 mM $CuSO_4$) using 20 µM Cy3 azide fluorophore at r.t. for 1 hr. Reaction was stopped with 50 µL 2x SDS and proteins were resolve at 120 V for 1 hr. After a PBS wash, each gel was scanned for a fluorescence signal using a Molecular Dynamics Typhoon 9400 Multi-laser Scanner at the Proteomics Center at UIUC (excitation at 526 nm, green laser, high sensitivity, 530 pmt).

Site-directed mutagenesis: New England Biolabs (NEB) Q5 Site-directed mutagenesis kit protocol (#E0554) was used to generate cysteine to serine mutants for each of the five cysteines of thioredoxin in NEB highly efficient chemically competent cells by employing the primers shown below. Plasmid DNA was isolated using the QIAminiprep kit (QIAGEN cat # 27104), submitted for sequencing at Roy J. Carver Biotechnology center, and found to contain only the desired mutant. HCT 116 cells (3 x 10^5 cells/mL) were platted in 6 well plates. Upon reaching 80% confluency, cells were transfected for 24 hr with 1 µg plasmid DNA of each mutant or empty GFP vector. Next day, cells were treated with DMSO or 20 µM **ferroptocide** for 30 min, followed by 60 min treatment with 20 µM **P29**. Cells were harvested, washed 2x with PBS and lysed in RIPA buffer. Samples (50 µg) were then subjected to click chemistry conditions with Cy3-azide and in-gel fluorescence studies as described above.

Supplementary Table 2.5. Sequences of primers used in site-directed mutagenesis studies.

Primer	**Sequence**
C32Fwd	AGCCACGTGGTCTGGGCCTTGCA
C32Rev	GAGAAGTCAACTACTACAAGTTTATCACCTGC
C35Fwd	GTGTGGGCCTTCCAAAATGATCAAG
C35Rev	CACGTGGCTGAGAAGTCA
C62Fwd	TGTGGATGACTCTCAGGATGTTG
C62Rev	TCTACTTCAAGGAATATCAC
C69Fwd	TGCTTCAGAGTCTGAAGTCAAATG
C69Rev	ACATCCTGACAGTCATCC
C73Fwd	TGAAGTCAAATCCATGCCAACATTC
C73Rev	CACTCTGAAGCAACATCC

Thioredoxin activity assay: HCT 116 cells (1 x 10^6 cells/flask) were treated with DMSO, 10 µM **P18**, 50 µM PMX464, or 50 µM PX-12 for 30 min. Cells were harvested by centrifugation, resuspended in the assay buffer and lysed via sonication. For each condition, 20 µg of cell lysate was used to measure the activity thioredoxin activity following manufacturer' protocol (Cayman Chemical, Fluorescent Thioredoxin Activity Assay kit # 20039) in a 96-well black-walled plate. For in vitro studies, human thioredoxin (10 µL of 0.2 µM solution) was used in addition to thioredoxin reductase (10 µL of 1.0 µM solution), 1 µl of DMSO, **ferroptocide**, PMX44, or PX-12 at indicated concentrations, 5 µL of NADPH (diluted according to manufacturer's instructions), and assay buffer to a final volume of 75 µL. The plate was incubated at 37 °C for 30 min followed by immediate addition of 20 µL fluorescent substrate per each well (diluted as instructed in the kit). Fluorescence was then monitored over 1 hr at 520 nm after excitation at 480nm in a SpectraMax M3 (Molecular Devices) instrument at 37 °C.

RNA sequencing: Total RNA was extracted by RNeasy Kit (QIAGEN) and digested with DNase (QIAGEN) from n=3 samples per condition (DMSO, 10 µM **ferroptocide** cells treated for 6 hr). RNA quality was assessed with a 2100 Agilent Bioanalyzer prior to library preparation. The RNAseq libraries were prepared using the TruSeq Stranded mRNAseq Sample Prep kit (version 1) following manufacturer's instruction (Illumina). Libraries were then quantified, pooled, and sequenced by single-end 150 base pairs using the Illumina HiSeq 4000 platform at the Roy J. Carver Biotechnology center. FASTQ files were generated and demultiplexed with the bcl2FASTQ v2.17.1.14 Conversion Software (Illumina). Libraries were sequenced at an average depth of 40-50 million reads per sample. The spliced read aligner Salmon (v0.8.2) was used to align sequencing reads to NCBI's GRCh38.p11 transcriptome. Counts were summarized to the gene level (Annotation release 108) using tximport (v 1.6.0) and the "lengthScaledTPM" method. The counts were normalized using the TMM method from edgeR (v 3.20.5) and then transformed to log2 counts per million (logCPM) with prior.count = 3. TMM normalization was re-done after filtering and then limma's (v 3.34.5) voom method was used to find differentially expressed genes for the pairwise comparisons of treatment vs. control in two different cell lines (A549 and HT-29), and the interaction between treatment and cell lines. False discovery rate adjustment was performed for multiple hypothesis testing with the Benjamini-Hochberg method. Gene-level read counts were obtained based on ESGEA (v 1.6.1) gene annotation for the Gene Ontology BP, CC, and KEGG pathway.

Animal Studies

MTD of ferroptocide

The protocol was approved by the IACUC at the University of Illinois at Urbana-Champaign (Protocol Number: 14173). These studies used 10- to 12- week-old female C57BL/6 mice, that were purchased from Charles River. **Ferroptocide** was formulated in 100% PEG400 and given by i.p. All mice were monitored over the course of the study for signs of toxicity and weight loss.

Pharmacokinetic assessment of ferroptocide

The protocol was approved by the IACUC at the University of Illinois at Urbana-Champaign (Protocol Number: 14173). In these studies, 10- to 12- week-old female C57BL/6 mice (purchased from Charles River) were used. **Ferroptocide** was formulated in 100% PEG400. Mice were treated with **ferroptocide** (40 mg/kg) via i.p. with three mice per time point (15, 30, 45, 60, 120, 240, 480, and 1440 min). At specific time points, mice were sacrificed, and blood was collected, centrifuged; the serum was frozen at -80°C until analysis. The proteins in a 50 µL aliquot of serum were precipitated by the addition of 50 µL acetonitrile and the sample was centrifuged to remove the proteins. Serum concentrations of **ferroptocide** were determined by reverse phase HPLC (Shimadzu Corporation, Japan). PK parameters were determined using GraphPad Prism Version 5.00 for Windows.

4T1 syngeneic model

The protocol was approved by the IACUC at the University of Illinois at Urbana-Champaign (Protocol Number: 17192). 9-week old, female Balb/C or SCID mice (Charles River) were lightly sedated with i.p. xylazine/ketamine/saline solution. Following sedation, 4T1 murine breast cancer cells suspended in chilled HBSS (100 µL of 4 x 10^6 cells/mL) were injected subcutaneously into the right flank of shaved and sedated mice using an insulin syringe. On day 8 after inoculation, mice were randomized with 7 mice per group for vehicle or **ferroptocide** treatment. Vehicle (PEG400) or **ferroptocide** (50 mg/kg) was administered intraperitoneally as a PEG400 solution twice a week for 5 times. Tumor measurements were performed every 3 or 4 days using a caliper and tumor volume was calculated using the equation ($0.5 \times l \times w^2$). On day 23 after the 4T1 cells inoculation, mice were sacrificed. Tumors were then surgically removed, and their mass was measured.

Statistical analysis

All statistical analysis was performed using an unpaired, two-tailed student's t test where $p < 0.05$ values were considered statistically significant.

2.14 References

1 Swinney, D. C. & Anthony, J. How were new medicines discovered? *Nat. Rev. Drug Discov.* **10**, 507–519, (2011).

2 Swinney, D. C. The Contribution of Mechanistic Understanding to Phenotypic Screening for First-in-Class Medicines. *J. Biomol. Screen.* **18**, 1186–1192, (2013).

3 Moffat, J. G., Rudolph, J. & Bailey, D. Phenotypic screening in cancer drug discovery — past, present and future. *Nat. Rev. Drug Discov.* **13**, 588–602, (2014).

4 Schenone, M., Dančík, V., Wagner, B. K. & Clemons, P. A. Target identification and mechanism of action in chemical biology and drug discovery. *Nat. Chem. Biol.* **9**, 232–240, (2013).

5 Swinney, D. C. Phenotypic vs. Target-Based Drug Discovery for First-in-Class Medicines. *Clin. Pharmacol. Ther.* **93**, 299–301, (2013).

6 Chabner, B. A. & Roberts Jr, T. G. Chemotherapy and the war on cancer. *Nat. Rev. Cancer* **5**, 65–72, (2005).

7 Eder, J., Sedrani, R. & Wiesmann, C. The discovery of first-in-class drugs: origins and evolution. *Nat. Rev. Drug Discov.* **13**, 577–587, (2014).

8 Harrison, R. K. Phase II and phase III failures: 2013–2015. *Nat. Rev. Drug Discov.* **15**, 817–818, (2016).

9 Vincent, F. *et al.* Developing predictive assays: The phenotypic screening “rule of 3”. *Sci. Transl. Med.* **7**, 293ps215, (2015).

10 Wagner, B. K. The resurgence of phenotypic screening in drug discovery and development. *Expert Opin. Drug Discov.* **11**, 121–125, (2016).

11 Zheng, W., Thorne, N. & McKew, J. C. Phenotypic screens as a renewed approach for drug discovery. *Drug Discov. Today* **18**, 1067–1073, (2013).

12 Lovering, F., Bikker, J. & Humblet, C. Escape from flatland: Increasing saturation as an approach to improving clinical success. *J. Med. Chem.* **52**, 6752–6756, (2009).

13 Huigens III, R. W. *et al.* A ring-distortion strategy to construct stereochemically complex and structurally diverse compounds from natural products. *Nat. Chem.* **5**, 195–202, (2013).

14 Ciardiello, J. J. *et al.* A novel complexity-to-diversity strategy for the diversity-oriented synthesis of structurally diverse and complex macrocycles from quinine. *Bioorg. Med. Chem.* **25**, 2825–2843, (2017).

15 Rafferty, R. J., Hicklin, R. W., Maloof, K. A. & Hergenrother, P. J. Synthesis of complex and diverse compounds through ring distortion of abietic acid. *Angew. Chem. Int. Ed.* **53**, 220–224, (2014).

16 Garcia, A., Drown, B. S. & Hergenrother, P. J. Access to a structurally complex compound collection via ring distortion of the alkaloid sinomenine. *Org. Lett.* **18**, 4852–4855, (2016).

17 Tasker, S. Z., Cowfer, A. E. & Hergenrother, P. J. Preparation of Structurally Diverse Compounds from the Natural Product Lycorine. *Org. Lett.* **20**, 5894–5898, (2018).

18 Paciaroni, N. G. *et al.* A tryptoline ring-distortion strategy leads to complex and diverse biologically active molecules from the indole alkaloid yohimbine. *Chem. Eur. J.* **23**, 4327–4335, (2017).

19 Govindaraju, K. *et al.* Novel topologically complex scaffold derived from alkaloid haemanthamine. *Molecules* **23**, 255–263, (2018).

20 Charaschanya, M. & Aubé, J. Reagent-controlled regiodivergent ring expansions of steroids. *Nat. Commun.* **9**, 934–942, (2018).

21 Laurent, E. *et al.* A ring-distortion strategy from marine natural product ilimaquinone leads to quorum sensing modulators. *Eur. J. Org. Chem.* **2018**, 2486–2497, (2018).

22 Luca, L. *et al.* Discovery of novel cinchona-alkaloid-inspired oxazatwistane autophagy inhibitors. *Angew. Chem. Int. Ed.* **56**, 2145–2150, (2017).

23 Xu, H. *et al.* Identification of a diverse synthetic abietane diterpenoid library for anticancer activity. *Bioorg. Med. Chem. Lett.* **27**, 505–510, (2017).

24 Richter, M. F. *et al.* Predictive compound accumulation rules yield a broad-spectrum antibiotic. *Nature* **545**, 299–304, (2017).

25 Kavanagh, F., Hervey, A. & Robbins, W. J. Antibiotic Substances From Basidiomycetes: VIII. Pleurotus Multilus (Fr.) Sacc. and Pleurotus Passeckerianus Pilat. *Proc. Natl. Acad. Sci.* **37**, 570–574, (1951).

26 Poulsen, S. M., Karlsson, M., Johansson, L. B. & Vester, B. The pleuromutilin drugs tiamulin and valnemulin bind to the RNA at the peptidyl transferase centre on the ribosome. *Mol. Microbiol.* **41**, 1091–1099, (2001).

27 Hogenauer, G. The mode of action of pleuromutilin derivatives. *Eur. J. Biochem.* **52**, 93–98, (1975).

28 Davidovich, C. *et al.* Induced-fit tightens pleuromutilins binding to ribosomes and remote interactions enable their selectivity. *Proc. Natl. Acad. Sci.* **104**, 4291–4296, (2007).

29 Yang, L. P. & Keam, S. J. Retapamulin: a review of its use in the management of impetigo and other uncomplicated superficial skin infections. *Drugs* **68**, 855–873, (2008).

30 Ma, X. *et al.* Directed C–H bond oxidation of (+)-pleuromutilin. *J. Org. Chem.* **83**, 6843–6892, (2018).

31 Farney, E. P., Feng, S. S., Schäfers, F. & Reisman, S. E. Total synthesis of (+)-pleuromutilin. *J. Am. Chem. Soc.* **140**, 1267–1270, (2018).

32 Murphy, S. K., Zeng, M. & Herzon, S. B. A modular and enantioselective synthesis of the pleuromutilin antibiotics. *Science* **356**, 956–959, (2017).

33 Thirring, K., et al. & 12-epi-pleuromutilins. U.S. WO2015110481A1 patent (2015).

34 Gibbons, E. G. Total Synthesis of (+)-Pleuromutilin. *J. Am. Chem. Soc.* **104**, 1767–1769, (1982).

35 Paquette, L. A., Wiedeman, P. E. & Bulman-Page, P. C. (+)-Pleuromutilin synthetic studies. Degradative and de novo acquisition of a levorotatory tricyclic lactone subunit. *J. Org. Chem.* **53**, 1441–1450, (1988).

36 Liu, J., Lotesta, S. D. & Sorensen, E. J. A concise synthesis of the molecular framework of pleuromutilin. *Chem. Commun.* **47**, 1500–1502, (2011).

37 Birch, A. J., Holzapfel, C. W. & Rickards, R. W. The structure and some aspects of the biosynthesis of pleuromutilin. *Tetrahedron* **22**, 359–387, (1966).

38 Arigoni, D. Some studies in the biosynthesis of terpenes and related compounds. *Pure Appl. Chem.* **17**, 331–348, (1968).

39 Drews, J. *et al.* Antimicrobial activities of 81.723 hfu, a new pleuromutilin derivative. *Antimicrob. Agents Chemother.* **7**, 507–516, (1975).

40 Poulsen, S. M., Karlsson, M., Johansson, L. B. & Vester, B. The pleuromutilin drugs tiamulin and valnemulin bind to the RNA at the peptidyl transferase centre on the ribosome. *Molecular Microbiology* **41**, 1091-1099, (2001).

41 Yang, L. H. K., S. Retapamulin: a review of its use in the management of impetigo and other uncomplicated superficial skin infections. *Drugs* **68**, 855–873, (2008).

42 Bains, W. & Tacke, R. Silicon chemistry as a novel source of chemical diversity in drug design. *Curr. Opin. Drug Discov. Devel.* **6**, 526–543, (2003).

43 Barraza, S. J. & Denmark, S. E. Synthesis, Reactivity, Functionalization, and ADMET Properties of Silicon-Containing Nitrogen Heterocycles. *J. Am. Chem. Soc.* **140**, 6668–6684, (2018).

44 Barnes, M. J. *et al.* Trimethylsilylpyrazoles as novel inhibitors of p38 MAP kinase: A new use of silicon bioisosteres in medicinal chemistry. *Bioorg. Med. Chem. Lett.* **17**, 354–357, (2007).

45 Geyer, M. *et al.* Can Silicon Make an Excellent Drug Even Better? An in vitro and in vivo Head-to-Head Comparison between Loperamide and Its Silicon Analogue Sila-Loperamide. *ChemMedChem* **10**, 911–924, (2015).

46 Iovel, I. *et al.* Synthesis and Biological Activity of Some Trifluoromethyl Derivatives of 5-tert-Butyl-2-furylmethylideneanilines and Their Silyl Analogs. *Chem. Heterocycl. Compd.* **39**, 449–454, (2003).

47 Dahlin, J. L. *et al.* PAINS in the Assay: Chemical Mechanisms of Assay Interference and Promiscuous Enzymatic Inhibition Observed during a Sulfhydryl-Scavenging HTS. *J. Med. Chem.* **58**, 2091–2113, (2015).

48 Jöst, C. *et al.* Promiscuity and Selectivity in Covalent Enzyme Inhibition: A Systematic Study of Electrophilic Fragments. *J. Med. Chem.* **57**, 7590–7599, (2014).

49 Singh, J., Petter, R. C., Baillie, T. A. & Whitty, A. The resurgence of covalent drugs. *Nat. Rev. Drug Discov.* **10**, 307–317, (2011).

50 Johnson, D. S., Weerapana, E. & Cravatt, B. F. Strategies for discovering and derisking covalent, irreversible enzyme inhibitors. *Future Med. Chem.* **2**, 949–964, (2010).

51 Shannon, D. A. *et al.* Investigating the Proteome Reactivity and Selectivity of Aryl Halides. *J. Am. Chem. Soc.* **136**, 3330–3333, (2014).

52 Ben-David, U. *et al.* Genetic and transcriptional evolution alters cancer cell line drug response. *Nature* **560**, 325-330, (2018).

53 Botham, R. C. *et al.* Dual small-molecule targeting of procaspase-3 dramatically enhances zymogen activation and anticancer activity. *J. Am. Chem. Soc.* **136**, 1312–1319, (2014).

54 Parkinson, E. I., Bair, J. S., Cismesia, M. & Hergenrother, P. J. Efficient NQO1 substrates are potent and selective anticancer agents. *ACS Chem. Biol.* **8**, 2173–2183, (2013).

55 Palchaudhuri, R. *et al.* A small molecule that induces intrinsic pathway apoptosis with unparalleled speed. *Cell Rep.* **13**, 2027–2036.

56 Galluzzi, L. *et al.* Molecular mechanisms of cell death: Recommendations of the Nomenclature Committee on Cell Death 2018. *Cell Death Differ.* **25**, 486–541, (2018).

57 Bracci, L., Schiavoni, G., Sistigu, A. & Belardelli, F. Immune-based mechanisms of cytotoxic chemotherapy: Implications for the design of novel and rationale-based combined treatments against cancer. *Cell Death Differ.* **21**, 15–25, (2014).

58 Linkermann, A., Stockwell, B. R., Krautwald, S. & Anders, H.-J. Regulated cell death and inflammation: an auto-amplification loop causes organ failure. *Nat. Rev. Immunol.* **14**, 759–767, (2014).

59 Galluzzi, L., Senovilla, L., Zitvogel, L. & Kroemer, G. The secret ally: Immunostimulation by anticancer drugs. *Nat. Rev. Drug Discov.* **11**, 215–233, (2012).

60 Balaban, R. S., Nemoto, S. & Finkel, T. Mitochondria, Oxidants, and Aging. *Cell* **120**, 483–495, (2005).

61 Murphy, Michael P. How mitochondria produce reactive oxygen species. *Biochem. J* **417**, 1–13, (2009).

62 Stockwell, B. R. *et al.* Ferroptosis: A regulated cell death nexus linking metabolism, redox biology, and disease. *Cell* **171**, 273–285, (2017).

63 Dixon, Scott J. *et al.* Ferroptosis: An iron-dependent form of nonapoptotic cell death. *Cell* **149**, 1060–1072.

64 Yang, W. S. *et al.* Regulation of ferroptotic cancer cell death by GPX4. *Cell* **156**, 317–331, (2014).

65 Shimada, K. *et al.* Global survey of cell death mechanisms reveals metabolic regulation of ferroptosis. *Nat. Chem. Biol.* **12**, 497–503, (2016).

66 Gaschler, M. M. *et al.* FINO2 initiates ferroptosis through GPX4 inactivation and iron oxidation. *Nat. Chem. Biol.* **14**, 507‒515, (2018).

67 Yang, W. S. & Stockwell, B. R. Synthetic lethal screening identifies compounds activating iron-dependent, nonapoptotic cell death in oncogenic-RAS-harboring cancer cells. *Chem. Biol.* **15**, 234–245, (2008).

68 Adams, R., Steckel, M., Nicke, B. & D. Pohlenz, H. RNAi as a tool for target discovery in early pharmaceutical research. *Pharmazie* **71**, 35–42, (2016).

69 Gargiulo, G. *et al.* In vivo shRNA screens in solid tumors. *Nat. Protoc.* **9**, 2880–2902, (2014).

70 Neggers, J. E. *et al.* Target identification of small molecules using large-scale CRISPR-Cas mutagenesis scanning of essential genes. *Nat. Commun.* **9**, 502–515, (2018).

71 Moore, J. D. The impact of CRISPR–Cas9 on target identification and validation. *Drug Discov. Today* **20**, 450–457, (2015).

72 Wacker, S. A., Houghtaling, B. R., Elemento, O. & Kapoor, T. M. Using transcriptome sequencing to identify mechanisms of drug action and resistance. *Nat. Chem. Biol.* **8**, 235–237, (2012).

73 Subramanian, A. *et al.* A next generation connectivity map: L1000 platform and the first 1,000,000 profiles. *Cell* **171**, 1437–1452.

74 Dixon, S. J. *et al.* Pharmacological inhibition of cystine–glutamate exchange induces endoplasmic reticulum stress and ferroptosis. *eLife* **3**, e02523, (2014).

75 Shin, H.-J. *et al.* Doxorubicin-induced necrosis is mediated by poly-(ADP-ribose) polymerase 1 (PARP1) but is independent of p53. *Sci. Rep.* **5**, 15798, (2015).

76 Das, G. C., Holiday, D., Gallardo, R. & Haas, C. Taxol-induced cell cycle arrest and apoptosis: dose–response relationship in lung cancer cells of different wild-type p53 status and under isogenic condition. *Cancer Lett.* **165**, 147–153, (2001).

77 Takeuchi, T., Schumacker, P. T. & Kozmin, S. A. Identification of Fumarate Hydratase Inhibitors with Nutrient-Dependent Cytotoxicity. *J. Am. Chem. Soc.* **137**, 564–567, (2015).

78 Banerjee, R., Pace, N. J., Brown, D. R. & Weerapana, E. 1,3,5-Triazine as a modular scaffold for covalent inhibitors with streamlined target identification. *J. Am. Chem. Soc.* **135**, 2497–2500, (2013).

79 Abegg, D. *et al.* Proteome-Wide Profiling of Targets of Cysteine reactive Small Molecules by Using Ethynyl Benziodoxolone Reagents. *Angew. Chem. Int. Ed.* **54**, 10852–10857, (2015).

80 Lomenick, B., Olsen, R. W. & Huang, J. Identification of Direct Protein Targets of Small Molecules. *ACS Chem. Biol.* **6**, 34–46, (2011).

81 Person, M. D. *et al.* Protein Fragment Domains Identified Using 2D Gel Electrophoresis/MALDI-TOF. *J. Biomol. Tech.* **17**, 145–156, (2006).

82 Toogood, H. S., Leys, D. & Scrutton, N. S. Dynamics driving function−new insights from electron transferring flavoproteins and partner complexes. *FEBS J.* **274**, 5481–5504, (2007).

83 Tahara, E. B., Navarete, F. D. T. & Kowaltowski, A. J. Tissue-, substrate-, and site-specific characteristics of mitochondrial reactive oxygen species generation. *Free Radical Biol. Med.* **46**, 128–1297, (2009).

84 Freneaux, E. *et al.* Glutaric acidemia type II. Heterogeneity in beta-oxidation flux, polypeptide synthesis, and complementary DNA mutations in the alpha subunit of electron transfer flavoprotein in eight patients. *J. Clin. Invest.* **90**, 1679–1686, (1992).

85 Di Donato, S. & Taroni, F. in *Rosenberg's Molecular and Genetic Basis of Neurological and Psychiatric Disease* (eds Roger N. Rosenberg & Juan M. Pascual) 559–576 (Academic Press, 2015).

86 Molina, D. M. *et al.* Monitoring Drug Target Engagement in Cells and Tissues Using the Cellular Thermal Shift Assay. *Science* **341**, 84–87, (2013).

87 Jafari, R. *et al.* The cellular thermal shift assay for evaluating drug target interactions in cells. *Nat. Protocols* **9**, 2100-2122, (2014).

88 Franken, H. *et al.* Thermal proteome profiling for unbiased identification of direct and indirect drug targets using multiplexed quantitative mass spectrometry. *Nat. Protocols* **10**, 1567–1593, (2015).

89 Holmgren, A. Thioredoxin structure and mechanism: conformational changes on oxidation of the active-site sulfhydryls to a disulfide. *Structure* **3**, 239–243, (1995).

90 Nordberg, J. & Arnér, E. S. J. Reactive oxygen species, antioxidants, and the mammalian thioredoxin system. *Free Radical Biol. Med.* **31**, 1287–1312, (2001).

91 Ramanathan, R. K. *et al.* A phase I pharmacodynamic and pharmacokinetic study of a Ras inhibitor, PRLX 93936, in patients with advanced solid tumors. *J. Clin. Oncol.* **28**, e13042, (2010).

92 Grogan, T. M. *et al.* Thioredoxin, a putative oncogene product,is overexpressed in gastric carcinoma and associated with increased proliferation and increased cell survival. *Human Pathology* **31**, 475–481, (2000).

93 Lichtenfels, R. *et al.* Identification of metabolic enzymes in renal cell carcinoma utilizing PROTEOMEX analyses. *Biochim. Biophys. Acta* **1646**, 21–31, (2003).

94 Kahlos, K. *et al.* Up-regulation of thioredoxin and thioredoxin reductase in human malignant pleural mesothelioma. *Int. J. Cancer* **95**, 198–204, (2001).

95 Kakolyris, S. *et al.* Thioredoxin Expression Is Associated with Lymph Node Status and Prognosis in Early Operable Non-Small Cell Lung Cancer. *Clin. Cancer. Res.* **7**, 3087–3091, (2001).

96 Li, J. *et al.* Serum thioredoxin is a diagnostic marker for hepatocellular carcinoma. *Oncotarget* **6**, 9551–9563, (2015).

97 Mukherjee, A. *et al.* A cellular and molecular investigation of the action of PMX464, a putative thioredoxin inhibitor, in normal and colorectal cancer cell lines. *Br. J. Pharmacol.* **151**, 1167–1175, (2007).

98 Baker, A. F. *et al.* The antitumor thioredoxin-1 inhibitor PX-12 (1-methylpropyl 2-imidazolyl disulfide) decreases thioredoxin-1 and VEGF levels in cancer patient plasma. *J. Lab. Clin. Med.* **147**, 83–90, (2006).

99 Kirkpatrick, D. L. *et al.* Mechanisms of inhibition of the thioredoxin growth factor system by antitumor 2-imidazolyl disulfides. *Biochem. Pharmacol.* **55**, 987–994, (1998).

100 Casares, N. *et al.* Caspase-dependent immunogenicity of doxorubicin-induced tumor cell death. *J. Exp. Med.* **202**, 1691−1701, (2005).

101 Turin, I. *et al.* In vitro efficient expansion of tumor cells deriving from different types of human tumor samples. *Med. Sci.* **2**, 70–81, (2014).

102 Roveri, A., Maiorino, M. & Ursini, F. in *Methods Enzymol.* Vol. 233 202–212 (Academic Press, 1994).

103 Jafari, R. *et al.* The cellular thermal shift assay for evaluating drug target interactions in cells. *Nat. Protoc.* **9**, 2100–2122, (2014).

104 Weerapana, E., Speers, A. E. & Cravatt, B. F. Tandem orthogonal proteolysis-activity-based protein profiling (TOP-ABPP)—a general method for mapping sites of probe modification in proteomes. *Nat. Protoc.* **2**, 1414–1425, (2007).

105 Ran, F. A. *et al.* Genome engineering using the CRISPR-Cas9 system. *Nat. Protoc.* **8**, 2281–2308, (2013).

106 Brown, A., Woods, W. S. & Perez-Pinera, P. in *Enhancer RNAs: Methods and Protocols* 235–250 (Springer New York, 2017).

107 Brown, A., Woods, W. S. & Perez-Pinera, P. Multiplexed targeted genome engineering using a universal nuclease-assisted vector integration system. *ACS Synth. Biol.* **5**, 582–588, (2016).

Chapter 3: Personalized Therapy for Late-Stage Patients

3.1 Personalized medicine approaches

The ability to predict patient response to general cytotoxic or targeted therapeutics in the clinic remains a long sought but elusive goal. The overall objective in personalized medicine is to eradicate patient's cancer via control of the tumor burden, reduction of cancer-related symptoms, increase of progression free survival (PFS) and overall survival (OS). The current clinical methods of providing individualized treatment (also known as precision medicine—matching a drug to patient-specific features) encompass genomic and functional approaches.

3.1.1 Genomic precision medicine

The fundamental idea in genomic precision medicine involves identification of specific somatic alterations in cancer patients that can guide the development of targeted drugs for such abnormalities and improve patient's life. Somatic mutations are categorized as "driver" and "passenger" alterations and include point mutations, deletions, translocations, amplifications, and chromosomal aberrations.[1,4] Drugs that target these alterations have been successfully developed and demonstrated patient benefit, thus giving rise to a new translational strategy in the clinic. One of the earliest examples, is imatinib that targets BCR-ABL kinase fusion, a translocation product in patients with chronic myeloid leukemia (CML).[5] Lung cancers harboring epidermal growth factor receptor (EGFR) mutants are responsive to EGFR inhibitors such as erlotinib and gefitinib, as well as monoclonal antibodies.[6,7] A dual tyrosine kinase inhibitor, Lapatinib, interrupts the HER2/neu and epidermal growth factor receptor (EGFR) pathway. Melanoma patients carrying BRAF V600E mutation are treated with vemurafenib as first line of therapy.[8,9] Other "druggable" mutations include microsatellite instability as a biomarker for sensitivity against checkpoint blockers in colon cancer,[10] synthetic lethal pairs such as BRCA and PARP-1 inhibitors used in the clinic,[11,12] TP53 mutation and checkpoint regulators (WEE1 and CHK1)[13], synthetic lethality in KRAS mutant cancers,[14] and many more mutations reported recently by Zhao and coworkers[15] upon incorporation of a novel structural-genomics based strategy (SGDriver).

Despite the many genomic advances that identified "druggable" mutations and enabled development of effective targeted-therapeutics, very few patients benefit from these drugs and modest clinical benefit has been identified primarily via non-randomized retrospective studies.[16-19] For example, only one in five lung cancer patients harbor mutations in EGFR or ALK to respond to targeted-chemotherapy.[20-22] Multiple studies (SHIVA trial[23], NCI-MATCH trial, MD Anderson Cancer Center trial[24], and a more recent trial at Dana-Farber Cancer Institute[25]) have investigated the number of patients who bear an actionable mutation(s) and actually experienced an improved quality of life (QOL) upon enrollment in the targeted therapy arms. The results of these reports revealed that only 2.5% of 739- (NCI-

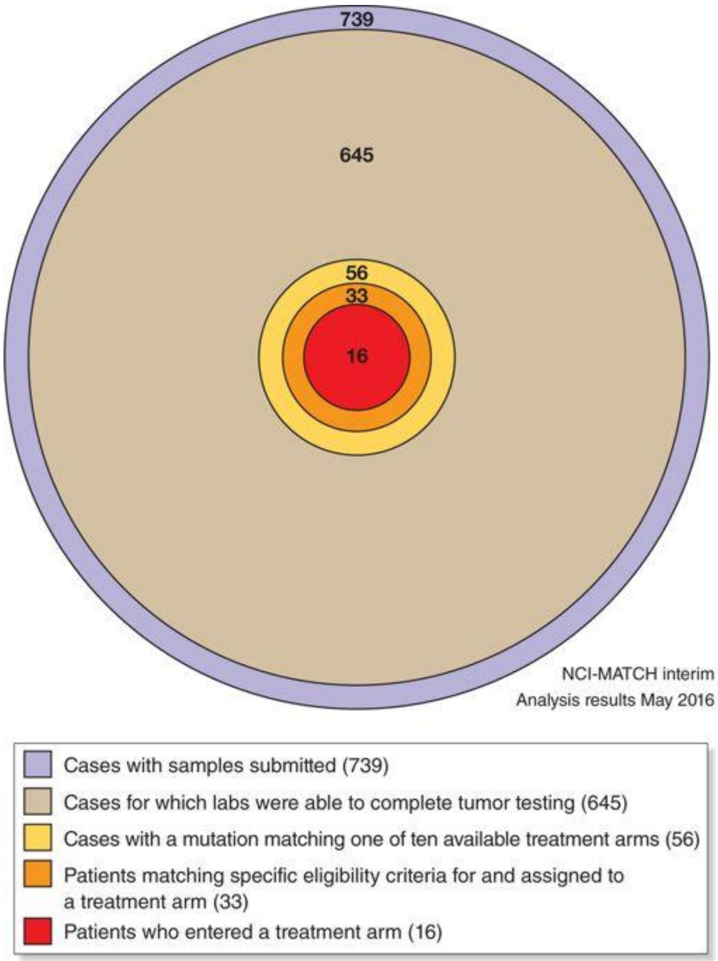

Figure 3.1. NCI-MATCH analysis of 739 submitted patient samples in May 2016.[1]

MATCH, **Fig. 3.1**) and 4.2% of 789- (MD Anderson Cancer Center) mutation-bearing patients, entered a genome-matched trial. While the reasons for these low patient enrollments change from trial to trial, all these reports emphasize the lack of and need for more potent targeted drugs. Notably, a large population of patients harbor numerous “non-druggable” aberrations that render them insensitive to targeted-drugs; thus, personalized treatment in the clinic cannot rely exclusively on genomic methods.

3.1.2 Functional precision medicine

Functional precision medicine is a complimentary approach to genomic medicine that involves monitoring of cancer cells upon exposure to a single drug or combination of drugs. Most of the commonly used chemotherapeutics in the clinic were discovered through some form of phenotypic-based observation, thus highlighting the importance and advantages of functional precision medicine.

3.1.2.1 Historical functional approaches

Initially developed in the 1960’s, chemosensitivity and chemoresistance assays (CSRA) were the first functional assays that attempted to predict tumor response.[26] CSRA consists of screening a panel of chemotherapeutics in primary tumor cells isolated from fresh biopsies or excised tumor samples. Since the

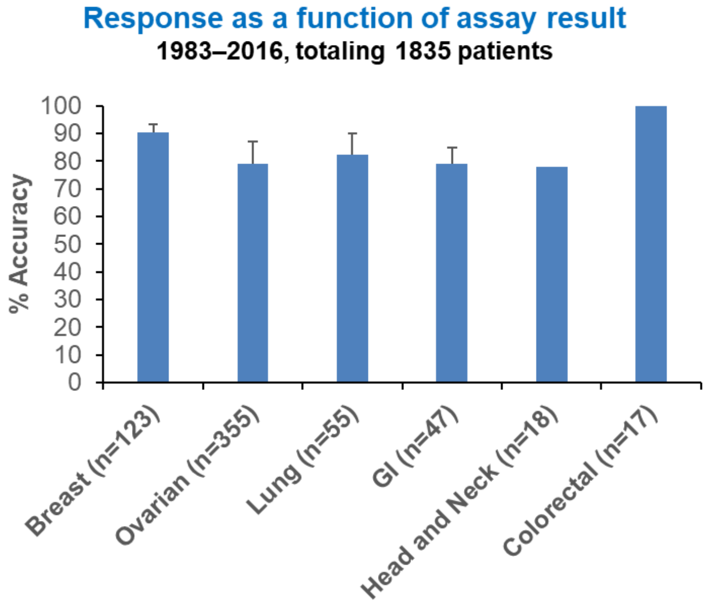

Figure 3.2. Chemosensitivity and resistance assays are good predictors of patient response to chemotherapy in the clinic. Analysis was performed with data collected from retrospective studies from 1983–2016.[2]

1980's, cytotoxicity assays have been incorporated in multiple platforms that are widely used by academic and clinical research groups to investigate the ability of CSRA to predict drug behavior in the clinic. These assays include: differential staining toxicity (DiSc), methyl thiazolyl-diphenyl-tetrazolium bromide (MTT), adenosine triphosphate bioluminescence (ATP), fluorescein diacetate assay (FMCA), and microculture kinetic assay (MicK).

According to a comprehensive 2017 meta-analysis that assessed all CSRA studies published from 1983–2016, there is a good correlation between CSRA results of different cell death assays and patient outcome (complete or partial remission) in the clinic. The prediction accuracy is as high as 90% for certain cancers (**Fig. 3.2**).[2] This result suggests that *ex vivo* assessment of drugs is a reliable predictor of drug efficacy in patients. Furthermore, CSRA assays are incorporated in routine hospital analysis by clinicians in Japan, Switzerland, and Sweden.[27-31] The analyses have helped guide treatment selection, improving overall survival, and lowering the cost of treatment for each patient by evading rounds of ineffective therapies.[32]

Despite this progress, there remain significant challenges for a widespread adoption of this technology: 1) difficulty of culturing primary cells *ex vivo,* 2) isolation of low numbers of cells, 3) low yielding assays, 4) inadequate turnaround time for clinical decisions, and 5) lack of randomized clinical trials. In addition, drug assessment is conducted in 384-well plates, which require 1000–3000 cells per well, extending the growth time of primary cells *in vitro* and limiting the number of compounds that can be tested per each patient. Long culture times of primary cells *ex vivo* renders them susceptible to contamination and high mutation loads[33,34] severely limiting the ability of these cells to represent the original tumors, resulting in choices that translate poorly to the clinic. Together, these challenges emphasize the need of new methods.

3.1.2.2 Recently developed functional assays

Various methods as indicated in **Table 3.1** have been developed to assess and measure drug exposure such that the information can be obtained in a clinically-relevant time frame. Despite the challenges described above, 2D cell culture models remain the mainstay of research and discovery. 3D cultures require weeks of expanding in culture—not favorable for clinical decision-making, and often select for viable clones thus lacking tumor representation.[35] PDX models are valuable tools that capture a wealth of information about tumor biology; yet, their challenges include cost, time of establishment (4–8 months), and heterogeneity in tumor engraftment.[36-38] BH3 profiling measures rapid induction of proapoptotic signals by drugs in a multiwell system and relates information within 48 hr of biopsy, thus circumventing the need for multiday culture of primary cancer cells.[39-42] Lastly, CIVO is a novel technology that enables exposure of drugs directly to the tumor *in vivo*, preserving the tumor microenvironment, but it is costly and only applicable to superficial tumors.[43-45]

In conclusion, genomic and functional methods complement each other and should be considered simultaneously when predicting the optimal drug regimen for cancer patients. Given that the clinical decision-making is time sensitive, only methods with a fast turnaround should be favored. However, genomic profiling is the only assessment currently used in the clinic in the US, while functional methods are still facing major obstacles despite their potential to identify the optimal drug regimen for cancer patients, especially those without a standard of care.

Table 3.1. Methods in functional precision medicine and their timeframe. Abbreviations: PDX, patient-derived xenografts; BH3, BH domain 3; CIVO, comparative in vivo oncology. Modified with permission from Letai and coworkers[1].

Methods	**Time until result**	**Specialized equipment/procedure**
2D culture	Days to weeks	No
3D culture	Weeks to months	No
PDX models	Months	Yes
Dynamic BH3 profiling	Hours to days	No
Mass accumulation rate	Days	Yes
Implantable devices	Days	Yes
CIVO	Days	Yes

3.2 Metastatic breast cancer no standard of care

Metastatic breast cancer (MBC) is responsible for 90% of breast cancer deaths and has an overall 5-year survival rate of 22%.[46] MBC is extremely challenging to treat due to tumor heterogeneity and the number/location of metastases. Regardless of the hormone receptor status, MBC patients are treated with cytotoxic chemotherapeutics (**Fig 3.3**). While several single–agent drugs have been approved for MBC, no clear consensus has emerged about which agent is superior or what drug to use for specific subtypes. Combination regimens have been extensively investigated, but due to overlapping toxicity

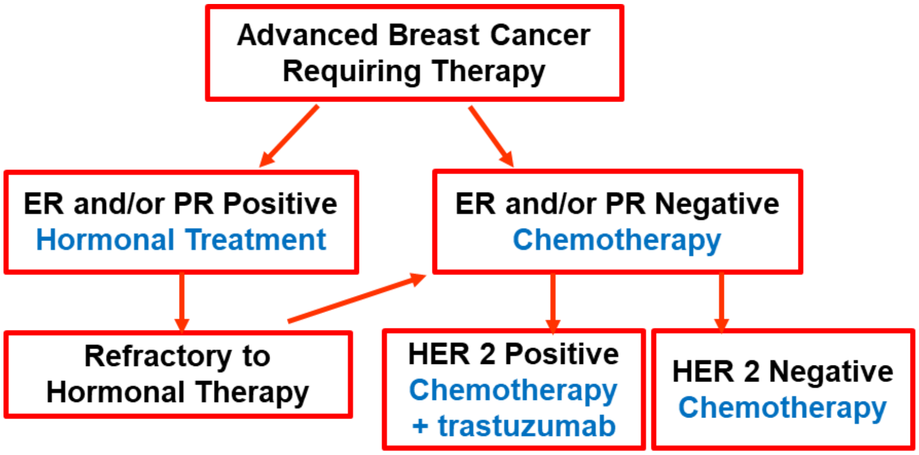

Figure 3.3. Chemotherapy is the backbone of treatment in breast cancer regardless of the receptor status.

profiles of candidate therapeutics, single–agent cytotoxic therapy remains the treatment of choice for MBC patients.[47-49] Because there exists no standard-of-care chemotherapeutic treatment for MBC, there is a *critical need* to determine the best drug for each patient and to develop novel effective combination therapies. To address this need, we set out to conduct a non-interventional study (NIS) in collaboration with Carle Foundation Hospital.

3.3 Non-interventional prospective study at Carle hospital

A non-interventional prospective study is a prospective trial, where tumor samples are collected as patients receive treatment, and the results of the study do not interfere with treatment selection, procedures, data and patient recruitment, which continue to follow hospital regulations. NIS is advantageous compared to a retrospective study, as patients are followed real time throughout the course of their treatment and clinical information is readily accessible. Given the poor prognosis of metastatic breast cancer, varying efficacy of single-agent therapeutics, we conducted a NIS to inform clinician's decisions about single–agent selection for treatment of each MBC patient at Carle hospital,

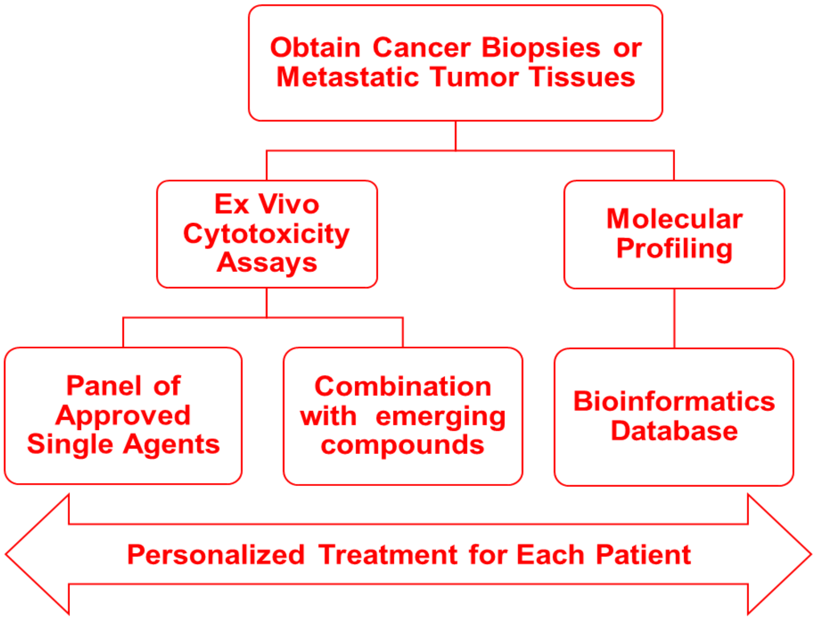

Figure 3.4. Treatment of metastatic tumor tissues in ex vivo cytotoxicity assays to determine the most sensitive agent or drug combination.

and to discover effective combination regimens that could have a strongly positive impact on advanced cancer treatment.

The project consisted of an *ex vivo* cytotoxic screen of patient-derived tumor samples with each of the drugs and drug combinations approved for MBC. Our *central hypothesis* is that single agents and drug combinations identified via a functional assay will provide information on the optimal drug regimen for MBC patients and extend their overall survival. In addition, we envisioned correlating drug toxicity with mutational status identified *via* molecular profiling by RNA sequencing of the tumor samples, which is routinely performed on all tumor biopsy specimens. This information would then be organized in a bioinformatics database in accordance with the Health Insurance Portability and Accountability Act (HIPAA) regulations. This database will correlate molecular profile patterns with drug effectiveness and help predict treatment for patients in the future, as outlined in **Fig 3.4**

While the primary focus of this project has been MBC, this strategy can also be extended to tumor samples from other metastatic diseases, specifically ovarian cancer (OC), which ranks fifth in cancer deaths among women. OC has poor prognosis, with 75%

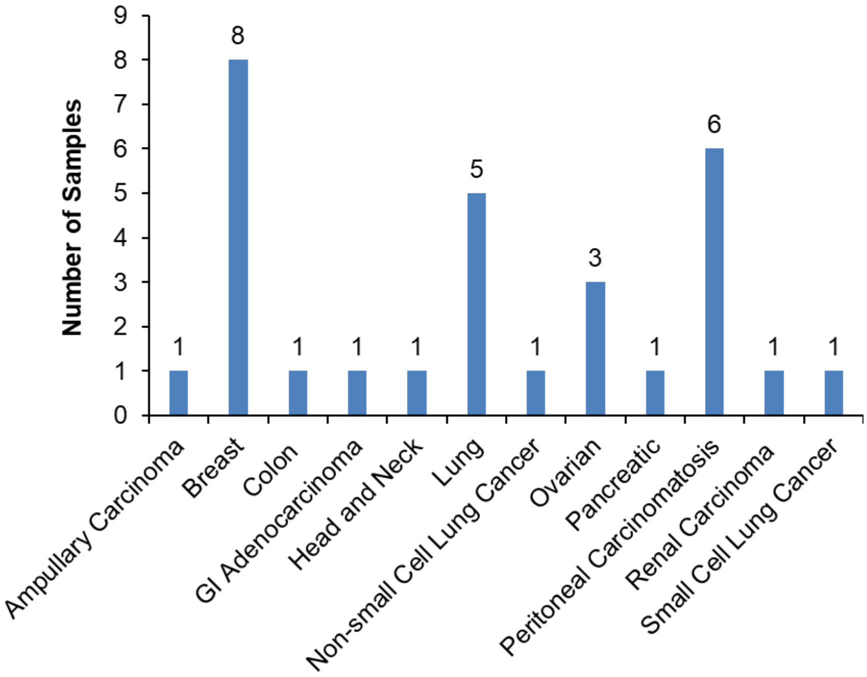

Figure 3.5. Types of samples collected from metastatic cancer patients at Carle hospital during 2016–2018 period.

of cases diagnosed in late stages and a 17% 5-year survival rate.[50] Clinicians rely on carboplatin and paclitaxel as the postoperative standard of care for these patients; however, platinum resistance is rapidly acquired.[51] Hence, clinicians still face the challenge of predicting the best chemotherapeutic out of several candidates. The fluorescent-based functional assay can support individualization of drug selection for these patients, thus resulting in higher response rates and improved overall survival.

3.4 Results and analysis

Recruitment of patients (>21 years old) for this study began in 2016 after obtaining an Institutional Review Board (IRB) approval. The cohort consisted of patients with solid tumors that had received specific procedures such as excisional biopsy/surgery, cytoreductive surgery, biopsy, thoracentesis, paracentesis, placement or draining of PleurX catheter.

At the 10-patient mark, the data revealed that each patient sample was sensitive to a specific drug as expected, so the study was extended to all tumors besides breast cancer (**Fig. 3.5**). To date, we have been able to access solid tumors and pleural effusion samples from 12 different cancers totaling 47 patients. Isolation of primary cancer cells was successful for 28 out of 47 patients due to the low number of isolated cells, 7–10 days *ex vivo* culturing needed to generate triplicate data, and high susceptibility of sample contamination.

A set of 9 drugs including FDA-approved drugs (5-fluorouracil [5-FU], cisplatin, etoposide, doxorubicin, gemcitabine, vinorelbine, taxol, and eribulin) and experimental drug PAC-1, was tested at 12 different concentrations in each of the isolated primary cancer cell lines. Cell viability was determined after 72 hr treatment using the Alamar Blue method, where resazurin dye converts to the fluorescent analogue, resorufin, in the presence of metabolically active cells. Half-maximum inhibitory concentration (IC_{50}) values were calculated for each compound and combined to build a training set, which can be utilized to determine compound sensitivity for future patients (**Fig.3.6**). This set will provide the benchmark of the average IC$_{50}$ value for each of these drugs in primary cancer cells. Comparison of results from future patients to this data set can potentially determine if a patient is a sensitive outlier or an inactive one for each of the tested drugs. Ideally, as the cohort expands, the training set can be modeled to each cancer type and ensure a higher prediction accuracy.

Retrospective analysis of the entire cohort deemed challenging due to the late-stage of the malignancy for these patients resulting in patient death (32 diseased). Nevertheless, monitoring of patient response for three patients suggests that this *ex vivo* assay can accurately predict patient response to therapy. Metastatic breast cancer patient 10 (ER$^-$PR$^-$Her2/neu$^+$) was

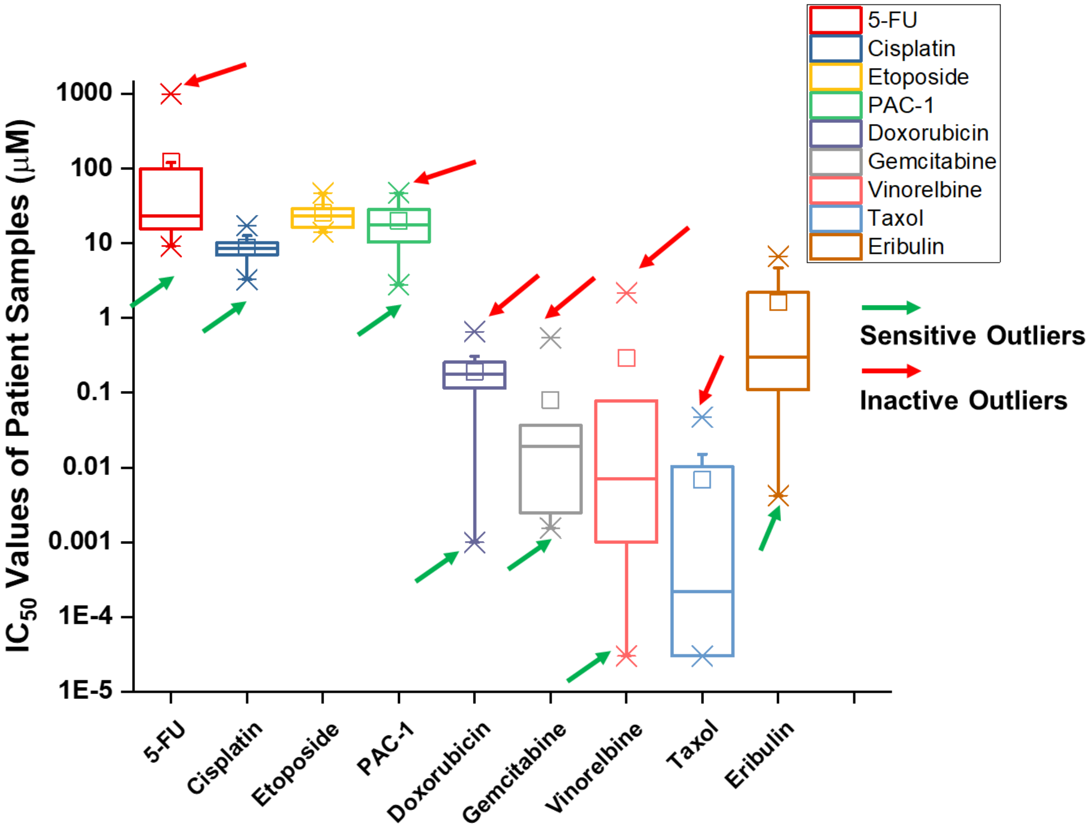

Figure 3.6. IC$_{50}$ data from 28 patients is used to build a training set. Cell viability was determined upon 72 hr treatment via Alamar Blue assay, 384 well. Red arrows indicate the inactive outliers while green arrows point at sensitive outliers. Data are representative of three biological replicates.

prescribed lapatinib (a dual tyrosine kinase inhibitor) and capecitabine (a 5-FU prodrug). The assay identified 5-FU as an inactive drug while taxanes, doxorubicin, vinorelbine, and PAC-1 were found to be responders, thus the patient experienced disease progression (**Fig 3.7 A**). In the case of patient 13 suffering from carcinoma of unknown primary, taxol and carboplatin were the first line of treatment followed by FOLFOX (oxaliplatin, 5-FU, folinic acid) and avastin (VEGF-A monoclonal antibody). The assay for this patient determined Pt-based compounds, doxorubicin and vinorelbine as the most active drugs; this patient displayed stable disease symptoms (**Fig 3.7 B**).

Lastly, patient 16 (peritoneal carcinomatosis) received the taxol/ carboplatin combination regimen and had an excellent response to therapy as shown in the CT scan images in **Figure 3.7 C**; the assay revealed Pt-compounds, and doxorubicin as the best drugs. This limited analysis suggests that Alamar blue assay is reliable and offers value to researchers in the clinic to investigate drug sensitivity for each cancer patients. However, due to practical challenges such as the need for large numbers of cells (1.5–3 million per plate, 5 compounds) that results in extended *ex vivo* culturing of cells, and the high susceptibility to contamination, this method requires coupling to a more robust technology to resolve these critical issues.

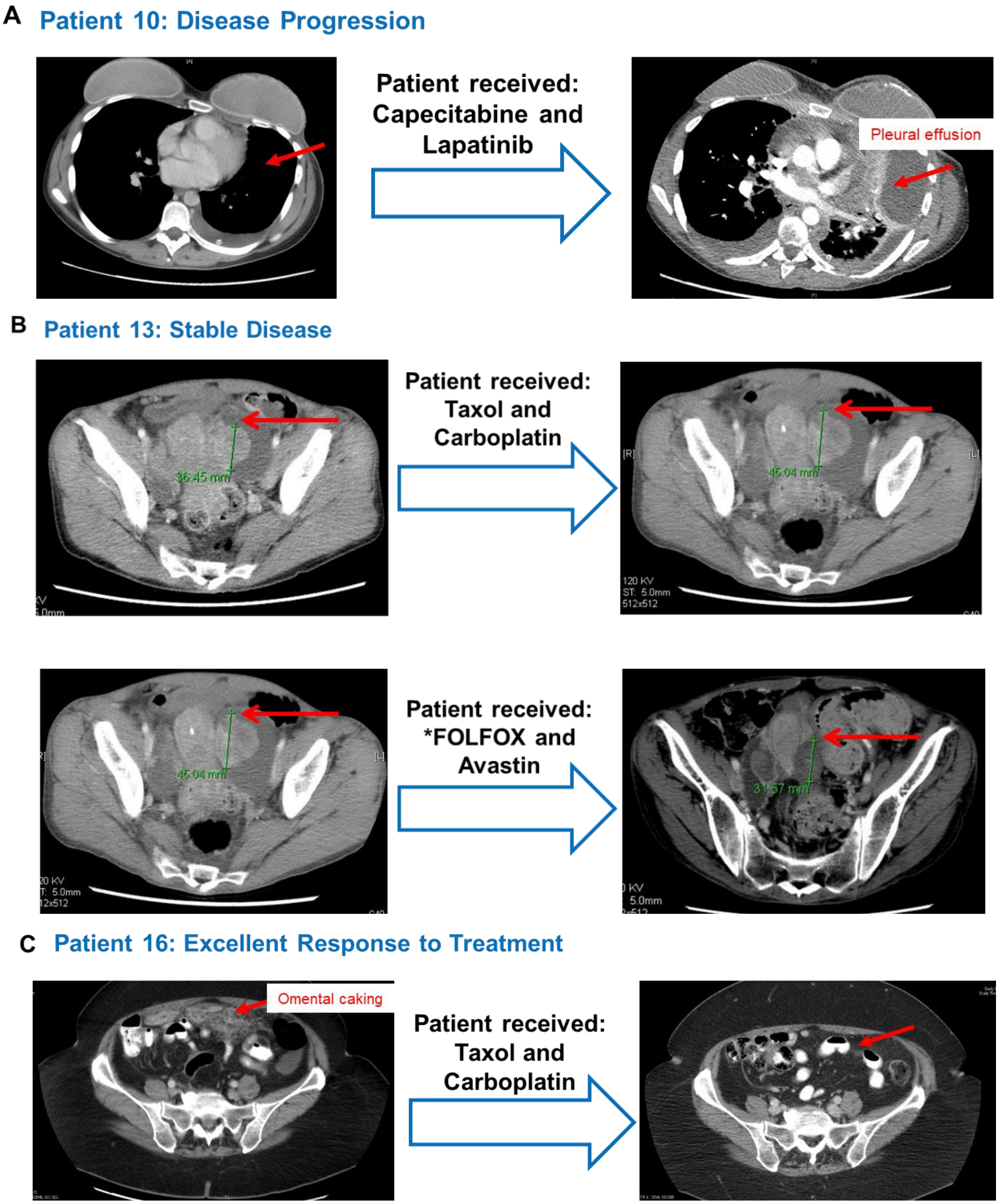

Figure 3.7. Monitoring patient response in the clinic. (A) MBC patient 10 experienced progression of disease on capecitabine and lapatinib. (B) Patient with carcinoma of unknown primary with stable disease on taxol/carboplatin regimen followed by FOLFOX/ avastin. (C) PPC patient 16 responded to taxol/carboplatin therapy. CT scan images were obtained from Carle Hospital. FOLFOX: 5-FU, oxaliplatin, folinic acid.

3.5 Future technology PCEM

One technology that could potentially address such a need is photonic crystal enhanced microscopy (PCEM), a label-free imaging technique, developed in the Cunningham lab. The PCEM instrument is a modified brightfield microscope that uses a line-scanning approach to measure the spatial distribution of peak wavelength value (PWV) across a photonic crystal (PC) surface with submicron spatial resolution for label-free imaging.[3,52] PCEM is a single cell technology that measures cell adhesion on the surface of a photonic crystal and represents the results in a heat map format. Initial proof of concept studies were conducted with adherent ES-2 (ovarian cancer) cells. Upon attachment, cells were subjected to treatment with a pro-apoptotic agent, Raptinal[53], and cell death was monitored over time. As shown in **Figure 3.8**, cell death begins as early as 25 min and concludes at 7 hr (100% cell death) as observed in bright field (BF) panel and the reduced heat capacity in the PWV channel. These promising results inspired us to further explore the use of PC biosensors as a novel functional assay. However, fabrication of a larger photonic crystal chip that would enable screening of multiple drugs at various concentrations has proven challenging. Ongoing efforts are aimed at

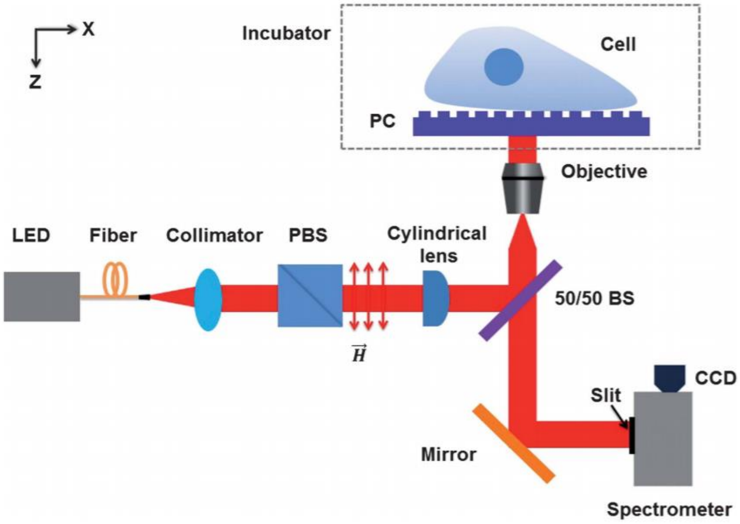

Figure 3.8. PCEM instrument schematic that incorporates parallel optical paths for broadband illumination with an LED for label-free imaging, and a laser diode for fluorescence imaging. Image is reported with permission from Chen and coworkers.[3]

troubleshooting the technical obstacles and optimizing the current process to implement this PCEM technology in the arsenal of *ex-vivo* functional assays.

3.6 Conclusion and outlook

This chapter focuses on historical and current methods available for personalized treatment medicine for cancer patients in the clinic. *Ex vivo* susceptibility assays are routinely used to inform selection of antibacterial therapy, thus the logical question remains as to why not utilize this strategy to cancer. The answer relies on the challenges of handling primary cancer cells: low cell numbers, *ex-vivo* culturing, tumor heterogeneity, and susceptibility to contamination. Regardless, there is an arsenal of genomic and functional approaches that address these challenges and have the potential to truly offer precision medicine in the clinic.

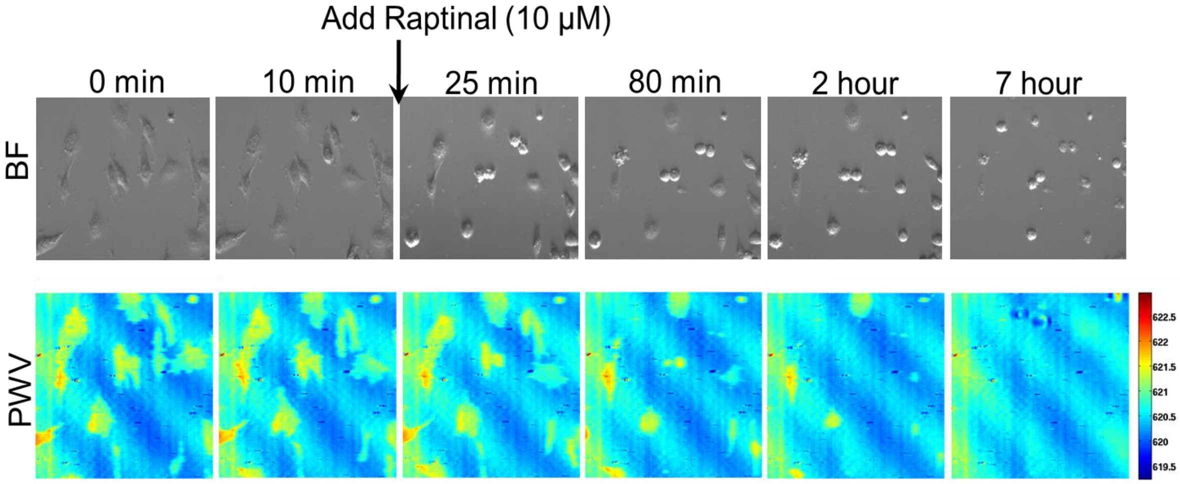

Figure 3.9. Proof of concept with PCEM technology. ES-2 ovarian cells were allowed to adhere to the chip surface and then treated with pro-apoptotic agent, raptinal (10 μM). Apoptosis was monitored over time. Data are representative images.

Genomic and functional precision medicine are complimentary to each other, and yet only genomic methods are widely incorporated in routine clinical analysis. Multiple studies indicate the small number of cancer patients that benefit from targeted-therapeutics and draw our attention to the lack of potent drugs for “actionable” mutations. While the use of these “driver” mutations in designing targeted-therapies has been successful for limited patient populations;

there is still an unmet need for the remaining majority of cancer patients. Functional methods can likely assist with these nonresponsive patients, but often lack the ability to yield information in a clinically-relevant time frame.

The use of 2D cultures to study tumor biology has been the mainstay of discovery for years, and a retrospective analysis of all 2D assays with primary cancer cells revealed how these functional assays can be good predictors of patient response in the clinic, regardless of tumor type. This information can be tremendously helpful in the case of oncological malignancies without standard of care such as metastatic breast cancer or cancers that rely on clinician's choice of treatment.

We aimed to inform oncologists on the optimal treatment regimen for late-stage patients in the clinic by collaborating with Carle hospital in a non-interventional study. This NIS trial enabled us to recruit 47 patients over the course of 2 years and collect data for 28 patients. Data consisted of IC_{50} values of a set of 8 FDA-approved drugs and an experimental compound (PAC-1) in primary cancer cells. The average IC_{50} values were then combined to build a training set that can serve as a benchmark of predicting patient sensitivity to each of this chemotherapeutics in the future. Furthermore, monitoring of a few patient outcomes revealed that the fluorescent-based functional assay could accurately determine patient response. This promising result encouraged us to search for novel technologies requiring fewer number of cells that would enable data collection for all patients. One such technology is the single-cell resolution, label-free imaging technology named PCEM (developed in the Cunningham lab at UIUC), which has demonstrated potential in initial studies. Ongoing efforts are focused on improving the high throughput screening ability of this technology and implementing it in primary cancer cell data collection.

In conclusion, advancements in genomics and technology have tremendously increased our understanding of tumor biology and precision medicine. However, providing personalized treatment for all cancer patients in the clinic requires the use of complimentary approaches (genomic and functional assays). The sooner we implement these strategies side-by-side, the more likely we are to improve the overall patient survival and their quality of life.

3.7 Methods and materials

Primary Cells from Tumors

Upon obtaining fresh solid tumor samples from Carle hospital (minimum size of 1.2 mm), tumor cells are obtained by enzymatic treatment with 0.1% collagenase and 50 U/ml dispase via incubation for 2 hours in a water bath. At the end of the incubation, cells are suspended in the appropriate growth media containing fetal bovine serum (FBS), and then filtered through a 85-µm nylon mesh cell strainer. Tumor cells are passed through filters to remove clusters and collected via centrifugation at 1000 rpm for 10 min. Trypan blue dye exclusion is used to check cell viability. Upon viability confirmation, cells are grown in the RMPI media containing 20% FBS, 2 mM L-glutamine, 100 U/ml penicillin, and 100 µg of streptomycin. These primary cells are then subjected to a fluorometric cytotoxicity assay based on resazurin reduction.

Primary Cells from Pleural and Peritoneal Effusions

Under sterile conditions, neoplastic effusions are transferred to 50 mL sterile tubes (Corning, Shiphol Rijk, The Netherlands) and centrifuged at 1200 rpm for 10 min. Once the supernatant is discarded, the cells are washed and re-suspended in complete medium. After evaluation of viability, the cells are seeded at a density of 3×10^6 cells/mL in 25 cm^2 tissue culture flasks (Corning) at 37 °C and 5% CO_2. Culture medium is changed as needed. When cultures reach sub-confluence, cells are subcultured at a dilution of 1:3 until they begin to grow rapidly, and then serially subcultured at a dilution of 1:5 every three days.

A Flurometric Cytotoxicity Assay

Resazurin is the active compound of the commercially available compound Alamar Blue.[5] The resazurin assay can be used to quantify cell proliferation and cytotoxicity since the substance becomes increasingly fluorescent in the presence of metabolically active cells.[6] To a 384-well plate, 40 µL of 1.25X compound dilution or 1.25% DMSO-containing media is added (final volume of 1% DMSO in all wells). Concentrations of compounds tested ranges from 100µM to 100 nM. On each plate at least 3 technical replicates are performed. Next, 10 µL of either a 100,000 cells/mL suspension are added to each well, yielding a final concentration of 1,000 cells/well. To three wells in column 2, 1 µL of 10 mM doxorubicin (final concentration of 200 µM) as positive control that should result in cell death are added. Plates are sealed with gas-permeable seals and incubated at 37 ˚C for 72 h. At that time, 5 µL of Alamar blue (440 µM resazurin in sterile PBS) are added, the plates are incubated for 3–4 hours. Fluorescence is read on an Analyst HT or a Molecular Devices SpectraMax 3 (excitation = 555 nm, emission = 585 nm, emission cutoff = 570 nm). Wells are normalized to the average of untreated wells (0% cell death). The data is plotted as compound concentration versus percent dead cells and fitted to a logistic-dose response curve using OriginPro (OriginLab, Northampton, MA). Hill Slope and E_{max} values can be obtained from curves fitted by OriginPro. The data is generated in duplicate or triplicate (dependent on cell numbers), and IC_{50} values, Hill slopes, and E_{max} values are reported as the average of three separate experiments along with standard error of the mean.

3.8 References

1 Letai, A. Functional precision cancer medicine—moving beyond pure genomics. *Nat. Med.* **23**, 1028, (2017).

2 Blom, K., Nygren, P., Larsson, R. & Andersson, C. R. Predictive Value of Ex Vivo Chemosensitivity Assays for Individualized Cancer Chemotherapy: A Meta-Analysis. *SLAS Technol.* **22**, 306–314, (2017).

3 Chen, W. *et al.* Photonic crystal enhanced microscopy for imaging of live cell adhesion. *Analyst* **138**, 5886–5894, (2013).

4 Martincorena, I. & Campbell, P. J. Somatic mutation in cancer and normal cells. *Science* **349**, 1483–1489, (2015).

5 Druker, B. J. *et al.* Efficacy and Safety of a Specific Inhibitor of the BCR-ABL Tyrosine Kinase in Chronic Myeloid Leukemia. *New Engl. J. Med.* **344**, 1031–1037, (2001).

6 Hutchinson, E. No longer in the dark. *Nat. Rev. Cancer* **4**, 415, (2004).

7 Paez, J. G. *et al.* EGFR Mutations in Lung Cancer: Correlation with Clinical Response to Gefitinib Therapy. *Science* **304**, 1497–1500, (2004).

8 Bollag, G. *et al.* Clinical efficacy of a RAF inhibitor needs broad target blockade in BRAF-mutant melanoma. *Nature* **467**, 596, (2010).

9 Flaherty, K. T. *et al.* Inhibition of Mutated, Activated BRAF in Metastatic Melanoma. *New Engl. J. Med.* **363**, 809–819, (2010).

10 Llosa, N. J. *et al.* The Vigorous Immune Microenvironment of Microsatellite Instable Colon Cancer Is Balanced by Multiple Counter-Inhibitory Checkpoints. *Cancer Discov.* **5**, 43–51, (2015).

11 Fong, P. C. *et al.* Inhibition of Poly(ADP-Ribose) Polymerase in Tumors from BRCA Mutation Carriers. *New Engl. J. Med.* **361**, 123–134, (2009).

12 Bryant, H. E. *et al.* Specific killing of BRCA2-deficient tumours with inhibitors of poly(ADP-ribose) polymerase. *Nature* **434**, 913, (2005).

13 Xu, C. *et al.* Functional Precision Medicine Identifies Novel Druggable Targets and Therapeutic Options in Head and Neck Cancer. *Clin. Cancer. Res.* **24**, 2828–2843, (2018).

14 Aguirre, A. J. & Hahn, W. C. Synthetic Lethal Vulnerabilities in KRAS-Mutant Cancers. *Cold Spring Harbor perspectives in medicine* **8**, a031518.

15 Zhao, J. *et al.* Systematic Prioritization of Druggable Mutations in ∼5000 Genomes Across 16 Cancer Types Using a Structural Genomics-based Approach. *Molecular & cellular proteomics : MCP* **15**, 642–656, (2016).

16 Kris, M. G., Johnson, B. E., Berry, L. D. & et al. Using multiplexed assays of oncogenic drivers in lung cancers to select targeted drugs. *JAMA* **311**, 1998–2006, (2014).

17 Tsimberidou, A.-M. *et al.* Personalized Medicine for Patients with Advanced Cancer in the Phase I Program at MD Anderson: Validation and Landmark Analyses. *Clin. Cancer Res.* **20**, 4827–4836, (2014).

18 Schwaederle, M. *et al.* Impact of Precision Medicine in Diverse Cancers: A Meta-Analysis of Phase II Clinical Trials. *J. Clin. Oncol.* **33**, 3817–3825, (2015).

19 Johannessen, C. M. & Boehm, J. S. Progress towards precision functional genomics in cancer. *Curr. Opin. Syst. Biol.* **2**, 74–83, (2017).

20 Barlesi, F. *et al.* Routine molecular profiling of cancer: results of a one-year nationwide program of the French Cooperative Thoracic Intergroup (IFCT) for advanced non-small cell lung cancer (NSCLC) patients. *Lancet* **287**, 1415-1426, (2016).

21 Majumder, B. *et al.* Predicting clinical response to anticancer drugs using an ex vivo platform that captures tumour heterogeneity. *Nat. Commun.* **6**, 6169, (2015).

22 Siena, S. *et al.* Biomarkers Predicting Clinical Outcome of Epidermal Growth Factor Receptor–Targeted Therapy in Metastatic Colorectal Cancer. *J. Natl. Cancer Inst.* **101**, 1308–1324, (2009).

23 Tsimberidou, A. M. & Kurzrock, R. Precision medicine: lessons learned from the SHIVA trial. *Lancet Oncol.* **16**, e579–e580, (2015).

24 Meric-Bernstam, F. *et al.* Feasibility of Large-Scale Genomic Testing to Facilitate Enrollment Onto Genomically Matched Clinical Trials. *J. Clin. Oncol.* **33**, 2753–2762, (2015).

25 Sholl, L. M. *et al.* Institutional implementation of clinical tumor profiling on an unselected cancer population. *JCI Insight* **1**, e87062–e87081, (2016).

26 Nygren, P. In Vitro Drug Sensitivity Testing of Tumor Cells From Patients with Non-Hodgkin's Lymphoma Using the Fluorometric Microculture Cytotoxicity Assay. *Int. J. Cancer* **56**, 127–131, (1994).

27 Frismantas, V. *et al.* Ex vivo drug response profiling detects recurrent sensitivity patterns in drug-resistant acute lymphoblastic leukemia. *Blood* **129**, e26–e37, (2017).

28 Yadav, B. *et al.* Quantitative scoring of differential drug sensitivity for individually optimized anticancer therapies. *Sci. Rep.* **4**, 5193, (2014).

29 Pemovska, T. *et al.* Individualized Systems Medicine Strategy to Tailor Treatments for Patients with Chemorefractory Acute Myeloid Leukemia. *Cancer Discov.* **3**, 1416–1429, (2013).

30 Akazawa, Y. *et al.* Impact of in vitro chemosensitivity test-guided platinum-based adjuvant chemotherapy on the surgical outcomes of patients with p-stage IIIA non-small cell lung cancer that underwent complete resection. *Mol. Clin. Oncol.* **7**, 327–335, (2017).

31 Lindhagen, E., Nygren, P. & Larsson, R. The fluorometric microculture cytotoxicity assay. *Nat. Protoc.* **3**, 1364–1369, (2008).

32 Plamadeala, V. *et al.* A cost-effectiveness analysis of a chemoresponse assay for treatment of patients with recurrent epithelial ovarian cancer. *Gynecol. Oncol.* **136**, 94–98, (2015).

33 Garnett, M. J. *et al.* Systematic identification of genomic markers of drug sensitivity in cancer cells. *Nature* **483**, 570–575, (2012).

34 Sharma, S. V., Haber, D. A. & Settleman, J. Cell line-based platforms to evaluate the therapeutic efficacy of candidate anticancer agents. *Nat. Rev. Cancer* **10**, 241–253, (2010).

35 Halfter, K. *et al.* Prospective cohort study using the breast cancer spheroid model as a predictor for response to neoadjuvant therapy – the SpheroNEO study. *BMC Cancer* **15**, 519–529, (2015).

36 Townsend, E. C. *et al.* The Public Repository of Xenografts Enables Discovery and Randomized Phase II-like Trials in Mice. *Cancer Cell* **29**, 574–586, (2016).

37 Bruna, A. *et al.* A Biobank of Breast Cancer Explants with Preserved Intra-tumor Heterogeneity to Screen Anticancer Compounds. *Cell* **167**, 260–274, (2016).

38 Roife, D. *et al.* Ex Vivo Testing of Patient-Derived Xenografts Mirrors the Clinical Outcome of Patients with Pancreatic Ductal Adenocarcinoma. *Clin. Cancer. Res.* **22**, 6021–6030, (2016).

39 Del Gaizo Moore, V. & Letai, A. BH3 profiling--measuring integrated function of the mitochondrial apoptotic pathway to predict cell fate decisions. *Cancer Lett.* **332**, 202–205, (2013).

40 Vo, T.-T. *et al.* Relative Mitochondrial Priming of Myeloblasts and Normal HSCs Determines Chemotherapeutic Success in AML. *Cell* **151**, 344–355, (2012).

41 Del Gaizo Moore, V. *et al.* Chronic lymphocytic leukemia requires BCL2 to sequester prodeath BIM, explaining sensitivity to BCL2 antagonist ABT-737. *J. Clin. Invest.* **117**, 112–121, (2007).

42 Pan, R. *et al.* Selective BCL-2 Inhibition by ABT-199 Causes On-Target Cell Death in Acute Myeloid Leukemia. *Cancer Discov.* **4**, 362–375, (2014).

43 Stevens, M. M. *et al.* Drug sensitivity of single cancer cells is predicted by changes in mass accumulation rate. *Nat. Biotechnol.* **34**, 1161–1167, (2016).

44 Jonas, O. *et al.* An implantable microdevice to perform high-throughput in vivo drug sensitivity testing in tumors. *Sci. Transl. Med.* **7**, 284ra257, (2015).

45 Chen, P.-L. *et al.* Analysis of Immune Signatures in Longitudinal Tumor Samples Yields Insight into Biomarkers of Response and Mechanisms of Resistance to Immune Checkpoint Blockade. *Cancer Discov.* **6**, 827–837, (2016).

46 Society, A. C. American Cancer Society Cancer Facts and Figures 2017. (2017).

47 Cardoso, F. *et al.* Second and subsequent lines of chemotherapy for metastatic breast cancer: what did we learn in the last two decades? *Ann. Oncol.* **13**, 197–207, (2002).

48 Di Lascio, S. & Pagani, O. Oligometastatic Breast Cancer: A Shift from Palliative to Potentially Curative Treatment? *Breast Care* **9**, 7–14, (2014).

49 Zeichner, S. B., Terawaki, H. & Gogineni, K. A Review of Systemic Treatment in Metastatic Triple-Negative Breast Cancer. *Breast Cancer* **10**, 25–36, (2016).

50 Society, A. C. Survival Rates for Ovarian Cancer by Stage (2004-2010).

51 Vita, D. *In Principles and Practices of Oncology*. 8 edn, Vol. 2 1568 (Lippincott Williams & Wilkins, 2008).

52 Zhuo, Y. & Cunningham, B. T. Label-Free Biosensor Imaging on Photonic Crystal Surfaces. *Sensors* **15**, 21613–21635, (2015).

53 Palchaudhuri, R. *et al.* A small molecule that induces intrinsic pathway apoptosis with unparalleled speed. *Cell Rep.* **13**, 2027–2036.